Bio-Butanol Dehydration and Butene Isomerization in Zeolites:
Ab Initio and Microkinetic Modelling

Bio-butanoldehydratatie en buteenisomerisatie in zeolieten:
ab initio en microkinetische modellering

Mathew John

Promotoren: prof. dr. M.-F. Reyniers, prof. dr. ir. G. B. Marin
Proefschrift ingediend tot het behalen van de graad van
Doctor in de ingenieurswetenschappen: chemische technologie

UNIVERSITEIT
GENT

Vakgroep Chemische Proceskunde en Technische Chemie
Voorzitter: prof. dr. ir. G. B. Marin
Faculteit Ingenieurswetenschappen en Architectuur
Academiejaar 2016 - 2017

ISBN 978-90-8578-938-3
NUR 952
Wettelijk depot: D/2016/10.500/70

Promotoren:

Prof. dr. ir. Guy B. **Marin**	Universiteit Gent
Prof. dr. Marie-Françoise **Reyniers**	Universiteit Gent

Andere leden van de examencommissie:

Prof. dr. Patrick **De Baets**	Universiteit Gent	Voorzitter
Prof. dr. ir. An **Verberckmoes**	Universiteit Gent	
Prof. dr. ir. Joris **Thybaut**	Universiteit Gent	Secretaris
Dr. ir. Konstantinos **Alexopoulos**	Universiteit Gent	
Prof. dr. Patrick **Bultinck**	Universiteit Gent	
Prof. dr. Johannes **Lercher**	Technische Universität München	
Prof. dr. ir. Dionisios G. **Vlachos**	University of Delaware	

This work was supported by the Long Term Structural Methusalem Funding by the Flemish Government – grant number BOF09/01M00409

Universiteit Gent

Faculteit Ingenieurswetenschappen en Architectuur

Vakgroep Chemische Proceskunde en Technische Chemie

Laboratorium voor Chemische Technologie

Technologiepark 914, B-9052 Gent, België

Contents

Contents ……... **i**

Notation ……..... **vii**

Summary …… **xi**

Samenvatting ……... **xv**

Chapter 1. Introduction ……..…… 1

1.1. Bio-alcohols - emergence of bio-butanol as a future source of energy and materials……..…… 2

1.2. Zeolites …… 6

1.3. Reaction mechanism ……..……. 8

1.3.1. Alcohol dehydration ……..…….. 8

1.3.2. Double bond isomerization…….…… 16

1.3.3. Skeletal isomerization…….…… 19

1.4. Ab initio microkinetic modelling……... 23

1.5. Scope …….. 24

1.6. Outline ……...…….. 25

1.7. References ……...…… 27

Chapter 2. Reaction path analysis for 1-butanol dehydration in H-ZSM-5 zeolite: ab initio and microkinetic modelling ……..... 33

2.1. Introduction …… 35

2.2. Theory……. ……... 37
2.2.1. Catalyst model…….. 37
2.2.2. Computational details……... 38
2.2.2.1. Electronic energy calculations…….. 38
2.2.2.2. Frequency calculations ……. 39
2.2.2.2. Statistical thermodynamics…….. 40
2.2.3. Microkinetic model…… 41
2.3. Results and discussion ……..…… 42
2.3.1. Adsorption of 1-butanol in H-ZSM-5…….. 42
2.3.1.1. Physisorbed 1-butanol……... 43
2.3.1.2. Protonated 1-butanol……. 44
2.3.1.3. Adsorbed butanol dimer…….. 45
2.3.2. Reaction pathways for 1-butanol dehydration in H-ZSM-5…… 46
2.3.2.1. Path A: dehydration of 1-butanol to 1-butene……. 50
2.3.2.2. Path B : Etherification reaction……..…… 58
2.3.2.3. Path C: Decomposition of di-1-butyl ether to 1-butene..... 63
2.3.2.4. Comparison of the different reaction pathways for 1-butanol dehydration……. 66
2.3.3 Microkinetic model and reaction path analysis…… 66
2.3.3.1. Effect of conversion……. 68
2.3.3.2. Effect of reaction temperature……. 70
2.3.3.3. Effect of partial pressure of 1-Butanol…… 72
2.3.3.4. Effect of partial pressure of water…….. 75
2.4. Conclusions ……..……..…….. 77
2.5. References ……..…….. 78

Chapter 3. First principles kinetic study on the effect of zeolite framework on 1-butanol dehydration ……..…….. 85
3.1. Introduction …… 87

3.2. Theory……. ……. 90
3.2.1. Zeolite models…….. 90
3.2.2. Computational details…….. 90
3.2.2.1. Electronic energy calculations…… 90
3.2.2.2. Frequency calculations …….. 91
3.2.2.2. Statistical thermodynamics…… 92
3.2.2.3. Microkinetic model…… 94
3.3. Results and discussion ……..……. 95
3.3.1. Reaction paths for zeolite-catalyzed butanol dehydration……. 95
3.3.1.1. Direct dehydration of 1-butanol to butene (path A)…… 98
3.3.1.2. Dehydration of 1-butanol to di-1-butyl ether (path B)…… 99
3.3.1.3. Di-1-butyl ether decomposition (path C)…… 99
3.3.2. Microkinetic modelling and reaction path analysis……... 100
3.3.2.1. Effect of site time and conversion……. 101
3.3.2.2. Effect of reaction temperature and butanol partial pressure. 109
3.4. Conclusions ……..……..…….. 120
3.5. References ……..…….. 121

Chapter 4. Mechanistic insights into formation of butene isomers from 1-butanol in H-ZSM-5: DFT based microkinetic modelling …….. 127

4.1. Introduction ……. 129
4.2. Theory……. ……. 131
4.2.1. Catalyst model……... 131
4.2.2. Computational details…… 132
4.2.2.1. Electronic energy calculations…… 132
4.2.2.2. Frequency calculations …….. 133
4.2.2.2. Statistical thermodynamics…… 133
4.2.2.3. Microkinetic model…… 135
4.3. Results and discussion ……..……. 136
4.3.1. Reaction paths for formation of butene isomers from 1-butanol

in H-ZSM-5…….. 136
4.3.1.1. Dehydration of 1-butanol to DBE and 1-butene…… 142
4.3.1.2. Formation of 2t-butene from adsorbed butanol and DBE 143
4.3.1.3. Double bond isomerization …… 147
4.3.1.4. Skeletal isomerization of linear butenes to isobutene….. 150
4.3.2 Microkinetic modelling and reaction path analysis: 1-butanol dehydration and butene isomerization…… 153
4.3.2.1. Effect of site time and conversion……. 154
4.3.2.2.. Effect of reaction temperature …….. 157
4.3.2.3. Effect of partial pressure of 1-butanol…….. 160
4.4. Conclusions ……..……..…….. 163
4.5. References ……..…….. 164

Chapter 5. Effect of zeolite framework on the conversion of 1-butanol to butene isomers: mechanistic insights from DFT-based microkinetic modelling…… 169
5.1. Introduction …… 171
5.2. Theory……. …….. 173
5.2.1. Catalyst models……. 173
5.2.2. Computational details…… 174
5.2.2.1. Electronic energy calculations…… 174
5.2.2.2. Frequency calculations …….. 175
5.2.2.2. Statistical thermodynamics…… 176
5.2.2.3. Microkinetic model…… 177
5.3. Results and discussion ……..…….. 178
5.3.1. Reaction paths for formation of butene isomers from 1-butanol in zeolites……. 178
5.3.2 Microkinetic modelling and reaction path analysis: 1-butanol dehydration and butene isomerization…… 192
5.3.2.1. Effect of site time ……. 192

5.3.2.2. Effect of conversion ……. 194

5.3.2.3. Effect of reaction temperature …….. 198

5.3.2.4. Effect of partial pressure of 1-butanol…… 202

5.4. Conclusions ……..……..…….. 205

5.5. References ……..…….. 206

Chapter 6. Conclusions and Prospects .....…… 211

List of Publications ..…… 217

Glossary ..……. 219

Appendices…… 223

Notations

Symbols

A	Arrhenius pre–exponential factor	s^{-1}
C_t	acid site concentration	mol H^+ kg^{-1}
E	electronic energy	kJ mol^{-1}
ΔE_{ads}	adsorption energy	kJ mol^{-1}
ΔE_r	reaction energy	kJ mol^{-1}
E_a	Arrhenius activation energy	kJ mol^{-1}
F_i	molar flow rate of component	mol s^{-1}
G	Gibbs free energy	kJ mol^{-1}
$\Delta G°_{ads}$	standard Gibbs free energy of adsorption	kJ mol^{-1}
$\Delta G°_r$	standard Gibbs free energy of reaction	kJ mol^{-1}
H	Enthalpy	kJ mol^{-1}
$\Delta H°_{ads}$	standard adsorption enthalpy	kJ mol^{-1}
$\Delta H°_r$	standard enthalpy of reaction	kJ mol^{-1}
h	Planck constant	J s

k_B	Boltzmann constant	J K^{-1}
k	rate coefficient	s^{-1}
K	equilibrium coefficient	-
N	number of particles	-
P	Pressure	Pa
$P_{BuOH,0}$	Feed butanol partial pressure	Pa
Q	total partition function	-
Q_{TS}	total partition function of transition state	-
Q_R	total partition function of reactant	-
q	molecular partition function	-
R	universal gas constant	kJ mol^{-1}
R_i	the net production rate of gas-phase species i	mol kg^1 s^{-1}
S	Entropy	J mol^{-1} K^{-1}
$\Delta S°_{ads}$	standard adsorption entropy	J mol^{-1} K^{-1}
$\Delta S°_{r}$	standard entropy of reaction	J mol^{-1} K^{-1}
T	Temperature	K
TOF_j	is the turnover frequency of elementary step j	mol mol_{H+}^{-1} s^{-1}
V	Volume	m^3
W	catalyst mass	kg
θ_k	fractional surface coverage of surface species k	mol mol_{H+}^{-1}
θ_*	the fractional coverage of free acid sites	mol mol_{H+}^{-1}
v_{ji}	stoichiometric coefficient of component i in the elementary step j	-

Subscripts and Superscripts

ads	adsorption
des	desorption
g, gas	gas phase
immobile	Immobile adsorbate
mobile	Mobile adsorbate
nD	n-dimensional
TS	transition state
TST	transition state theory

Abbreviations

BuOH	butanol
DFT	Density Functional Theory
D	dispersion
DFT-D2	Density Functional Theory calculations with dispersion corrections
GGA	Generalized Gradient Approximation
GHSV	Gas Hourly Space Velocity
IR	Infrared
HO	Harmonic Oscillator
MD	Molecular Dynamics
NEB	Nudged Elastic Band

PAW	Projector Augmented Wave method
PBE	Perdew-Burke-Ernzerhof
PHVA	Partial Hessian Vibrational Analysis
SCF	Self-Consistent Field
VASP	Vienna Ab initio Simulation Package

Summary

Growing environmental concerns and limited fossil reserves necessitate technological advancement towards the use of renewable resources such as biomass for the production of green fuels and chemicals. The catalytic conversion of bio-alcohols can serve as a sustainable means for the production of high-value chemicals. Butenes produced by dehydration of bio-butanol could serve as a building block for several essential compounds such as fuels and polymers. Use of zeolite catalyzed processes for conversion of bio-alcohols would allow to make use of the existing fossil fuel based industrial infrastructure, enabling a smooth transition from the petroleum based economy to a renewable-feed-based economy. Nevertheless, the selective conversion of the feed is the key to cost effectiveness and success of these processes. Theoretical simulations can be instrumental in revealing the dominant reaction mechanism and path, understanding the effect of the zeolite framework on catalytic activity and selectivity, thus guiding the prediction and development of improved catalysts.

In the present thesis, density functional theory (DFT) based microkinetic modeling is used to study 1-butanol conversion to butene isomers in a wide range of reaction conditions in different zeolite frameworks. This study emphasizes the role of reaction conditions in determining the dominant reaction path and mechanism. Moreover, different zeolite frameworks offer different stabilization for reaction intermediates and transition states, which can lead to significant differences in the preferred reaction mechanism and, hence, to changes in product selectivity. Such insights on the effect of the zeolite framework on the reaction rates and product selectivity can provide guidelines for rational catalyst design.

Chapter 1 presents an overview of the current status and the future prospects of utilizing bio-alcohols as means for sustainable production of green chemicals. In addition, it compares and reviews various catalytic options available for dehydration and further conversion of bio-alcohols to olefins, fuels and chemicals. The relevance and importance of first principles based microkinetic modeling used for the study is also discussed.

Chapter 2 provides a detailed insight into the reaction pathways for the dehydration of 1-butanol in H-ZSM-5. A comprehensive density functional theory study of plausible reaction mechanisms is used to gain fundamental insight into the dehydration process. The calculated reaction energetics clearly indicate the preference for the ether mediated path over the direct dehydration of 1-butanol to 1-butene. An ab initio based microkinetic model is used to explain the experimental trends reported in literature and to reveal the crucial role of reaction conditions in determining the dominant reaction mechanism and pathway. Reaction temperature and butanol partial pressure are found to have a significant impact on the surface coverages, turnover frequencies and product selectivity. Meanwhile, the presence of water is shown to have no significant influence on bio-butanol dehydration under industrially relevant conditions. Overall, our study allows us to reconcile the conflicting observations reported at different operating conditions.

Chapter 3 focuses on reaction paths and mechanisms for the dehydration of 1-butanol in different zeolites (viz. H-FAU, H-ZSM-5, H-ZSM-22 and H-FER). Ab initio based microkinetic simulations provide the first theoretical explanation for the experimental observation that H-FAU and H-FER, with significantly differing pore sizes, dimensionality and channel structure, yield a similar selectivity pattern and provide higher 1-butene selectivity as compared to H-ZSM-5 and H-ZSM-22. These results emphasize the pivotal role of confinement by the zeolite framework in defining the catalyst activity and product selectivity. This study also highlights the role of the reaction conditions in determining the

most abundant reaction intermediate, dominant reaction paths and underlying reaction mechanisms in all four zeolites.

Chapter 4 provides theoretical insights into the competing pathways for the formation of butene isomers (1-butene, cis/trans 2-butenes and isobutene) during dehydration of 1-butanol in H-ZSM-5. A new mechanism for direct formation of trans-2-butene from di-1-butyl ether (DBE) via E1 elimination is also envisaged along with the direct dehydration of 1-butanol to trans-2-butene. Concerted and 2-butoxide mediated stepwise double bond isomerization and alkoxide mediated monomolecular skeletal isomerization are also considered as mechanisms for the formation of butene isomers in H-ZSM-5. The skeletal isomerization mechanism involves a π-bonded propene-methyl carbocationic transition state for the transformation of 2-butoxide to iso-butoxide. The DFT based microkinetic simulation results show that, except for very low conversion levels where 2-butenes are produced via E1 elimination of 1-butanol from the protonated di-1-butyl ether (DBE*), the formation of 2-butenes occurs essentially via double bond isomerization with comparable contributions of the concerted and the 2-butoxide mediated stepwise mechanisms. Owing to the higher activation barrier for the skeletal isomerization, isobutene is not observed in the simulated temperature range of 450-500K. Simulation results indicate that low reaction temperature, low site time and high butanol pressure favor production of 1-butene and DBE, while high temperature and site time and low butanol pressure favor the consecutive reactions leading to production of butene isomers.

In **Chapter 5**, ab initio based microkinetic modeling of 1-butanol dehydration to butene isomers is used to obtain mechanistic insights into the effect of the zeolite framework on the reaction kinetics and product selectivity. A detailed microkinetic model including double bond isomerization, skeletal isomerization and mechanisms for direct formation of 2t-butene from 1-butanol dimer and DBE are considered for the dehydration study in H-ZSM-5, H-

ZSM-22 and H-FER. Simulated results show that H-FER has a higher preference for production of 2t-butene and H-ZSM-22 achieves the thermodynamic equilibrium composition for the linear butenes even at low conversion levels, while H-ZSM-5 exhibits an optimum conversion regime for maximizing 1-butene selectivity. Nevertheless, significant differences are observed in the underlying reaction mechanism leading to formation of 2t-butene. For H-ZSM-5 and H-ZSM-22, the formation of 2-butenes occurs via double bond isomerization of 1-butene produced from butanol dehydration. On the other hand for H-FER, 2t-butene is mainly produced from the butanol dimer via an E1 elimination accompanied by a 1,2-hydride shift. This in turn is attributed to an increase in enthalpic stabilization of the E1 elimination transition state for the direct formation of 2t-butene from 1-butanol dimer when moving from H-ZSM-5 to H-FER.

Chapter 6 discusses general conclusions and prospects for future work. This work emphasizes the understanding of the role of zeolite framework in defining its catalytic performance. It also highlights the pivotal role of the reaction conditions in determining the most abundant reaction intermediate, dominant reaction paths, and underlying reaction mechanisms. Furthermore, the extension of the microkinetic model with inclusion of oligomerization, cracking and hydride shift reactions would allow to simulate and obtain mechanistic insight at high temperature conditions. Finally, the presented approach can also be used for the study of conversion of other bio-based alcohols and polyols to value added chemicals. However, it would be interesting to study these reactions in the liquid/aqueous phase, where adsorption isotherms are first used to obtain the loading in the zeolite and molecular dynamics are then used to study the ensemble of possible reactants, transition states and products.

Samenvatting

Groeiende bezorgdheid over het milieu en de beperkte reserves van fossiele grondstoffen maken technologische vooruitgang in het gebruik van hernieuwbare energiebronnen zoals biomassa voor de productie van groene brandstoffen en chemicaliën noodzakelijk. De katalytische omzetting van bio-alcoholen kan een duurzaam alternatief vormen voor de productie van hoogwaardige chemicaliën. Butenen verkregen door dehydratatie van bio-butanol kunnen gebruikt worden als bouwstenen voor meerdere essentiële verbindingen zoals brandstoffen en polymeren. Het gebruik van zeoliet gekatalyseerde processen voor de omzetting van bioalcoholen laat toe om gebruik te maken van de bestaande industriële infrastructuur voor omzetting van fossiele grondstoffen en een een soepele overgang te maken van de aardolie gebaseerde economie naar een economie gebaseerd op hernieuwbare grondstoffen. Echter, de selectieve omzetting van de voeding vormt de sleutel tot de effectiviteit en het succes van deze processen. Theoretische simulaties kunnen als instrument dienen in het verwerven van inzicht in de dominante reactiemechanismen en reactiepaden, het begrijpen van het effect van het zeolietrooster op hun katalytische activiteit en selectiviteit en vormen een onmisbaar hulpmiddel voor een meer systematische aanpak in de ontwikkeling van optimale katalysatoren. .

In dit proefschrift wordt, op basis van quantumchemische berekeningen met dichtheidsfuctionaaltheorie, een microkinetisch model ontwikkeld voor het beschrijven en bestuderen van de omzetting van 1-butanol naar buteenisomeren in verschillende zeolietroosters (H-ZSM-5, H-FAU, H-FER, HZSM-22) in een breed bereik van industrieel relevante reactieomstandigheden. Deze studie benadrukt de rol van de reactieomstandigheden in het bepalen van het dominante reactiepad en reactiemechanisme. De verschillende zeolietrooster geven aanleiding tot verschillende stabilisatie voor intermediairen en

transitietoestanden wat leidt tot aanzienlijke verschillen in het geprefereerde reactiemechanisme en dus tot frapante verschillen in productselectiviteiten. Inzicht in het effect van zeolietrooster op de reactiesnelheden en productselectiviteiten laten toe om sturende richtlijnen voor rationeel katalysatorontwerp te formuleren.

Hoofdstuk 1 geeft een overzicht van de huidige toestand en de toekomstperspectieven van het gebruik van bio-alcoholen als grondstof voor de duurzame productie van groene chemicaliën. Bovendien worden verschillende katalytische mogelijkheden voor dehydratatie en verdere omzetting van bio-alcoholen tot alkenen, brandstoffen en chemicaliën vergeleken en beoordeeld. De relevantie en het belang van het gebruik van ab initio microkinetische modellering voor het onderzoek wordt eveneens besproken.

Hoofdstuk 2 geeft een gedetailleerd inzicht in de reactiepaden voor de dehydratatie van 1-butanol in H-ZSM-5. Een uitgebreide dichtheidsfunctionaaltheoriestudie van plausibele reactiemechanismen wordt gebruikt om fundamenteel inzicht in de dehydratatiereactie te verwerven. De berekende reactie-energieën tonen een voorkeur voor het ether-gemedieerde pad ten op zichtte van de rechtstreekse dehydratatie van 1-butanol tot 1-buteen. Ab initio gebaseerd microkinetische modellering wordt gebruikt om de experimentele trends in de literatuur te verklaren en de simulatieresultaten onthullen de cruciale rol van reactieomstandigheden in het bepalen van de dominante reactiemechanisme. Reactietemperatuur en butanol partieeldruk blijken een significant effect te hebben op de oppervlaktebedekkingen, de reactiesnelheden en de productselectiviteiten. Daarnaast is aangetoond dat de aanwezigheid van water geen significante invloed heeft op de bio-butanoldehydratie onder industrieel relevante voorwaarden. Algemeen laat dit onderzoek toe om de conflicterende waarnemingen gemeld bij verschillende werkomstandigheden te verzoenen.

Hoofdstuk 3 richt zich op reactiepaden en -mechanismen voor de dehydratatie van 1-butanol in verschillende zeolieten (nl. H-FAU, H-ZSM-5, H-ZSM-22 en H-FER). Ab initio gebaseerde microkinetische simulaties laten toe om voor het eerst een theoretische verklaring te geven voor de experimentele waarneming dat H-FAU en H-FER, met aanzienlijk verschillende poriegrootten, dimensionaliteit en kanaalstructuur, een soortgelijke selectiviteitspatroon vertonen en een hogere 1-buteenselectiviteit ten opzichte van H-ZSM-5 en H-ZSM-22 vertonen. Deze resultaten benadrukken de centrale rol van de stabilisatie door het zeolietrooster bij het bepalen van de activiteit en selectiviteit van de zeolietkatalysator. Deze studie benadrukt ook de rol van de reactieomstandigheden voor het bepalen van de belangrijkste reactie-intermediairen, de dominante reactiepaden en het onderliggende reactiemechanismen in de vier zeolieten.

Hoofdstuk 4 verschaft theoretisch inzicht in de concurrerende routes voor de vorming van buteenisomeren (1-buteen, cis/trans-2-butenen en iso-buteen) tijdens dehydratatie van 1-butanol in H-ZSM-5. Een nieuw mechanisme voor de directe vorming van trans-2-buteen uit 1-dibutylether (DBE) via E1 eliminatie samen met de rechtstreekse dehydratatie van 1-butanol tot trans-2-buteen wordt overwogen. Het geconcerteerde en het 2-butoxide gemedieerde stapsgewijze dubbele-binding-isomerisatiemechanisme zowel als de alkoxide gemedieerde monomoleculaire skeletisomerisatie worden tevens in overweging genomen voor de vorming van de buteenisomeren in H-ZSM-5. Het skeletisomerisatiemechanisme verloopt via een π-gebonden propeen-methyl carbokation als transitietoestand in de omzetting van 2-butoxide naar iso-butoxide. De DFT-gebaseerde microkinetische simulatieresultaten tonen aan dat, afgezien van bij zeer lage conversie waarbij 2-buteen gevormd wordt via E1 eliminatie van 1-butanol uit geprotoneerd di-1-butylether (DBE *), de vorming van 2-butenen hoofdzakelijk plaats grijpt via dubbele-binding-isomerisatie met nagenoeg een gelijke bijdrage van het geconcerteerde en het 2-butoxide gemedieerde stapsgewijze mechanisme.

Door de hogere activeringsbarrière voor de skeletisomerisatie wordt iso-buteen niet waargenomen in het gesimuleerde temperatuurbereik van 450 tot 500K. Simulatieresultaten geven aan dat lage reactietemperatuur, lage verblijftijd en hoge butanol druk de productie van 1-buteen en DBE begunstigen, terwijl hoge temperatuur, hoge verblijftijd en lage butanol druk de vervolgreacties die leiden tot de productie van buteenisomeren bevoordelen.

In **Hoofdstuk 5** wordt een ab initio gebaseerde microkinetische modellering van 1-butanol dehydratatie naar buteenisomeren uitgevoerd om mechanistisch inzicht te verkrijgen in het effect van zeolietrooster op de reactie kinetiek en selectiviteit. Een gedetailleerd microkinetische model inclusief dubbele-binding-isomerisatie, skeletisomerisatie en mechanismen voor de directe vorming van 2t-buteen uit 1-butanoldimeer en di-1-butylether (DBE) worden beschouwd voor de studie van de reactie in H-ZSM-5, H-ZSM-22 en H-FER. Simulatieresultaten tonen aan dat H-FER een grotere voorkeur voor de productie van 2t-buteen vertoont terwijl H-ZSM-22 het thermodynamisch evenwicht bereikt voor lineaire butenen zelfs bij lage omzettingen. H-ZSM-5 vertoont dan weer een optimaal conversieniveau waarbij de 1-buteenselectiviteit maximaal is. Toch zijn significante verschillen waarneembaar in het onderliggende reactiemechanisme leidend tot de vorming van 2t-buteen. In H-ZSM-5 en H-ZSM-22 grijpt de vorming van 2-butenen plaats via dubbele-binding-isomerisatie van 1-buteen geproduceerd vanuit de butanoldehydratatie. Anderzijds wordt H-FER 2t-buteen hoofdzakelijk gevormd uit het butanoldimeer via een E1 eliminatie met een simultane 1,2-hydride shift. Dit wordt op zijn beurt toegewezen aan een toename van de enthalpische stabilisatie van de E1 eliminatie transititiestoestand voor de directe vorming van 2t-buteen uit 1-butanoldimeer bij het variëren van het zeoliet rooster van H-ZSM-5 naar H-FER.

Hoofdstuk 6 bespreekt de algemene conclusies en mogelijkheden voor verder onderzoek. Dit werk legt de nadruk op het begrijpen van de rol van de zeolietrooster bij het verklaren van de katalytische werking van het zeoliet. Ook wijst het op de cruciale rol van de

reactieomstandigheden bij het bepalen van het meest voorkomende reactie-intermediair, de domninate reactiepaden, en de onderliggende reactiemechanismen. Bovendien zou de uitbreiding van het microkinetische model met oligomerisatie, krakingsreactie en hydride shiftreacties toelaten om een meer diepgaand mechanistisch inzicht te verkrijgen bij hoge temperaturen. Tenslotte kan de aanpak ook gebruikt worden voor de studie van de omzetting van andere bio-alcoholen en polyolen tot chemicaliën met toegevoegde waarde. Het zou interessant zijn om deze reacties te bestuderen in de vloeibare/waterfase, waarbij adsorptie-isothermen eerst worden gebruikt om de belading in het zeoliet te bepalen en om vervolgens gebruik te maken van moleculaire dynamica om het geheel van mogelijke reactanten, transitietoestanden en producten te bestuderen.

Chapter 1

Introduction

The ever-growing demand of fossil fuels and rising environmental concerns have attracted researchers across the globe towards sustainable energy resources. Renewable energy and materials are expected to play a major role in the development of a sustainable future. This has led to significant attention towards the use of biomaterials for fuel and chemical synthesis. Amongst these, the catalytic conversion of bio-alcohols to biofuels[1,2] and bio-chemicals[1,3,4] is of particular interest and can serve as a potential alternative to the non-renewable fossil fuels and petrochemicals. However, the economic viability of these processes is largely dependent on reducing the large capital costs associated with them. Utilizing the existing petroleum refining infrastructure for the transformation of biomass (see Figure 1) provides such an option[5]. Moreover, this will facilitate a smooth transition from the petroleum-based to a bio-based economy.

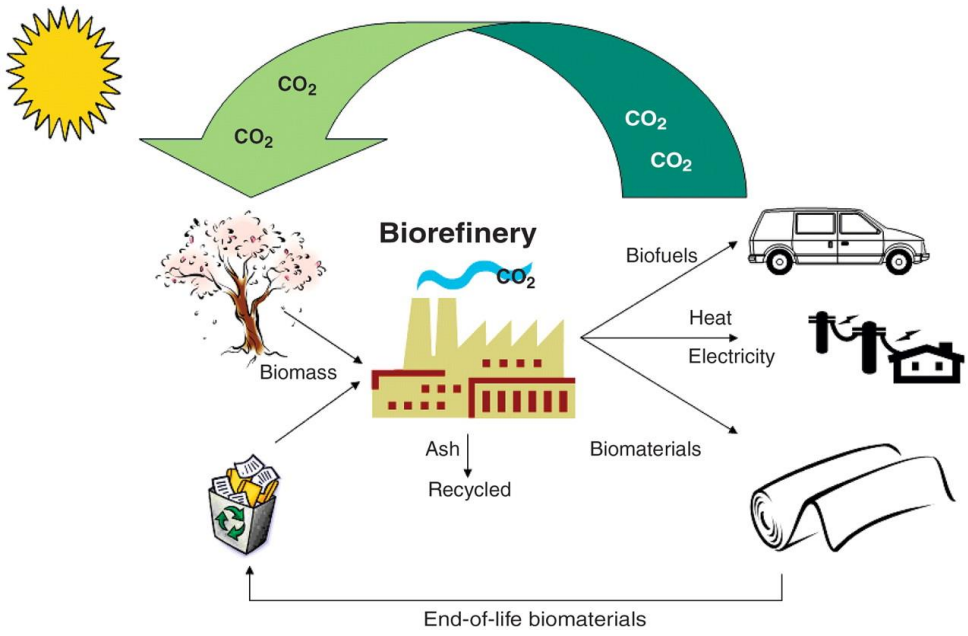

Figure 1. The fully integrated agro-biofuel-biomaterial-biopower cycle for sustainable technologies.[6]

This chapter presents an overview of the current status and the future prospects of utilizing bio-alcohols as means for sustainable production of green chemicals. In addition, it compares and reviews various catalytic options available for dehydration and further conversion of bio-alcohols to olefins, fuels and chemicals. Key research challenges associated with biomass catalytic conversion processes are also highlighted. This in turn points out the relevance and importance of the first principle based microkinetic modelling approach as an important complementary tool along with the experimental studies for catalyst and process design. The scope and outline of this doctoral thesis are also discussed at the end of this chapter.

1.1. Bio-alcohols - emergence of bio-butanol as a future source of energy and materials

Bio-alcohols such as bio-methanol, bio-ethanol, bio-propanol and bio-butanol are alcohols derived from biomass-based feedstocks. The use of bio-alcohols in the fuel sector was initially led by first generation fuels, essentially bioethanol, which is derived from sugar and carbohydrate based agricultural sources [7]. Although first generation fuels served to be an

attractive option in terms of ease of process and availability of mature technology, they had a direct impact on food availability and pricing. This led to the development of next generation bio-alcohols derived from feedstock obtained by conversion of lignocellulosic biomass and crop wastes. Lignocellulosic biomass is the most promising feedstock for biofuel production as it is renewable, easily available at low cost, and abundant in nature.[8,9] Bio-methanol is produced by gasification of biomass to syngas followed by catalytic conversion to methanol [10]. Apart from bio-methanol, the other three bio-alcohols (i.e. bio-ethanol, bio-propanol and bio-butanol) are mainly produced via fermentation processes. This production process involves sequential steps namely pretreatment (removal of lignin to ease hydrolysis), hydrolysis (conversion of polymers into simple sugars), detoxification, and fermentation [11].

Amongst the four bioalcohols, butanol has the highest energy density of 29.1 GJ/m^3 in comparison to 17.9, 23.3 and 26.9 GJ/m^3 for methanol, ethanol and propanol, respectively. Besides having a higher energy density, butanol has a lower vapor pressure, better compatibility with gasoline, lower water solubility and lower corrosion issues in comparison to ethanol[12]. These properties of butanol provide an easier storage, blending and transportation and a better engine life and overall vehicular mileage. As a consequence, much attention is being paid recently toward the usage of bio-butanol[13].

Traditionally, bio-butanol was produced by a natural process, catalyzed by *Clostridium acetobutylicum*, resulting in a mixture of acetone, 1-butanol and ethanol (the ABE process).[14] On the other hand, the use of genetically modified *E.coli* strains resulted in the selective production of iso-butanol.[15] Thus, with technological advancements, one could use appropriate microorganisms to produce n-butanol or iso-butanol. Alternatively, ethanol could be condensed into 1-butanol, which could be a promising route for the conversion of bio-ethanol to bio-butanol.[16] In addition, one could make use of the biomass gasification process

to produce syngas which is further used as feedstock for the Fischer – Tropsch synthesis where butanol is produced as a co-product.[17]

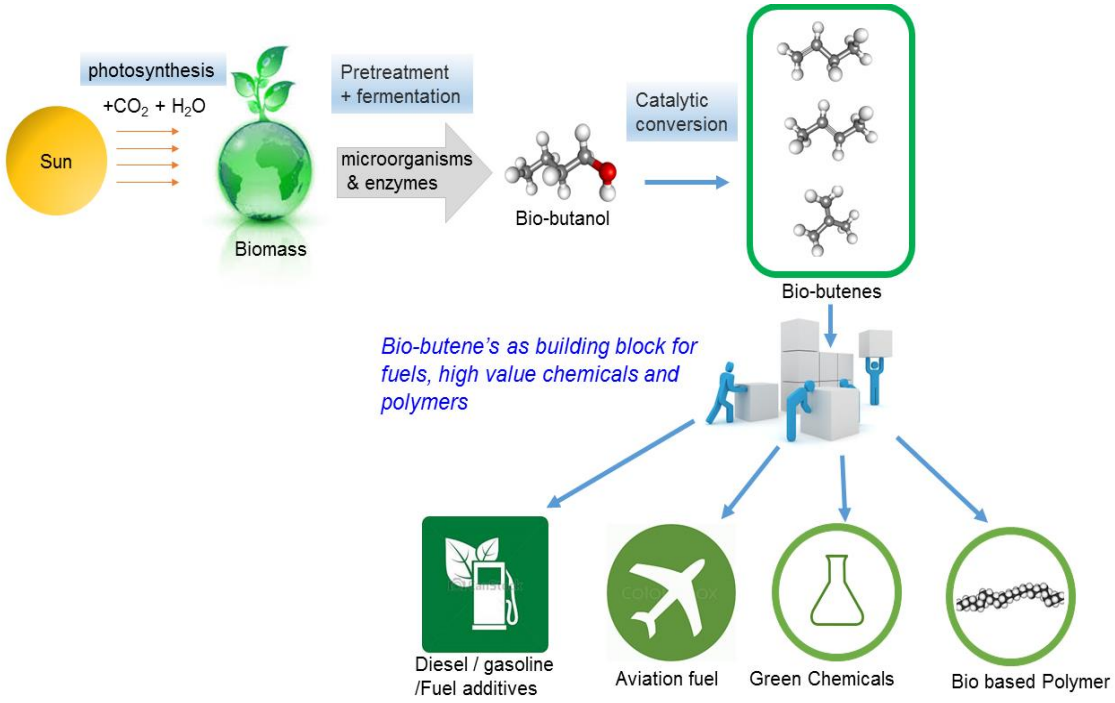

Figure 2. Bio-butene as a building block for production of renewable fuels, chemicals and polymers

Considering the future growth prospects of bio-butanol, it is imperative to look into the various aspects of chemicals synthesis using bio-butanol as a precursor. As shown in Figure 2, butenes produced by dehydration of bio-butanol can serve as building block for several essential compounds, fuels and polymers. Butene isomers have a diverse array of potential derivative markets. Some of them are direct while others branch out through other derivatives. An overview of these markets is provided in Figure 3. The 1-butanol dehydration process can be managed to give mainly 1-butene or a mixture of 1-butene and isomeric cis- and trans-2-butenes (2c-butene and 2t-butene). Collectively, these are referred to as linear butenes. Skeletal isomerization of linear butenes results in production of iso-butene which has a large variety of applications.[18-21] Likewise, 1-butene can be converted into butadiene and butane by oxidation and reduction reactions, respectively.

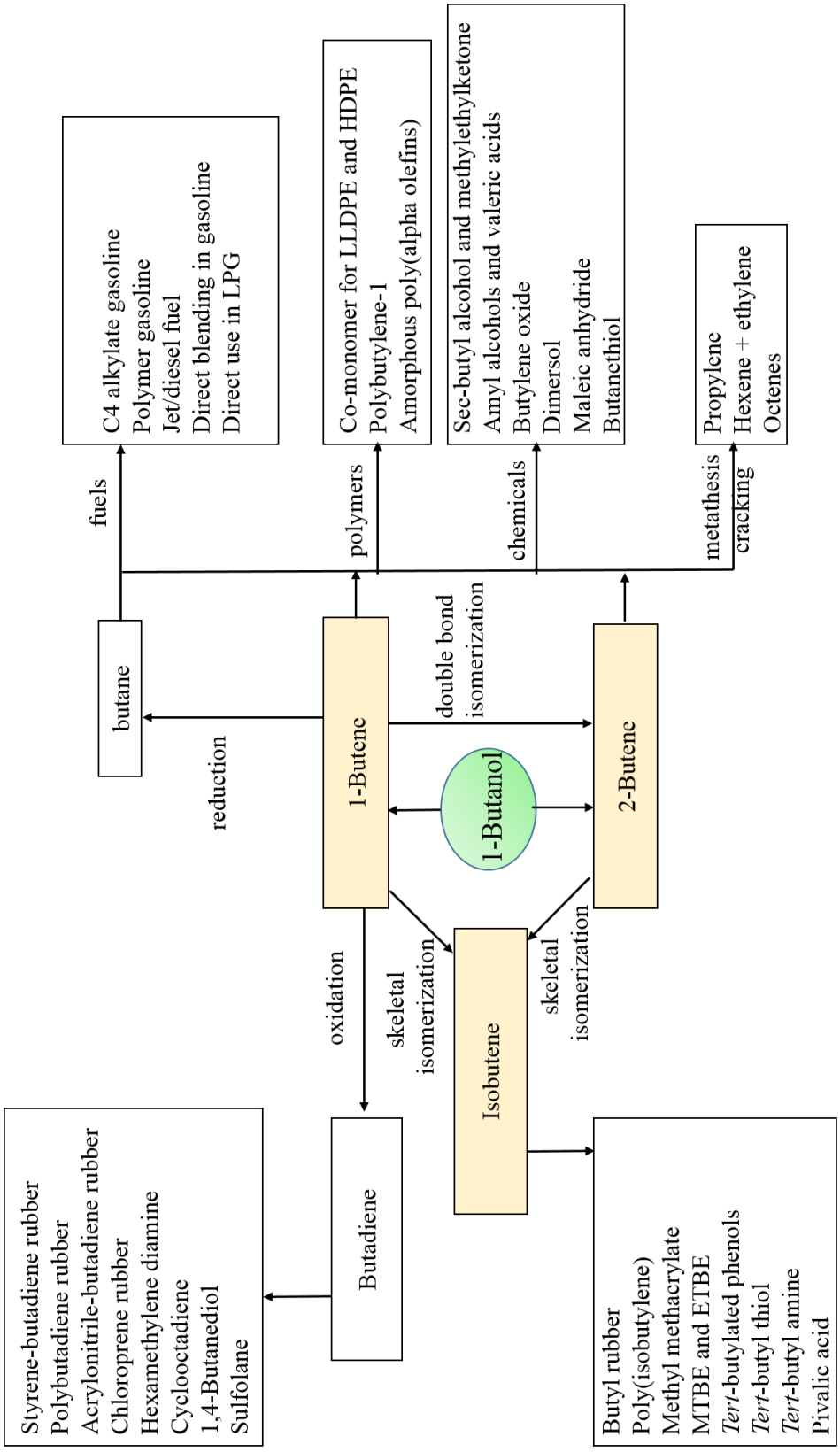

Figure 3. Dehydration of 1-butanol for production of renewable fuels, polymers and chemicals (applications for butene isomers from ref[1])

1.2. Zeolites

Zeolites are crystalline silicates and aluminosilicates linked through oxygen atoms, producing a three-dimensional network containing channels and cavities of molecular dimensions. The networks of well-defined micropores can act as reaction channels, whose activity and selectivity is enhanced by introducing active sites. The presence of strong electrostatic interactions and molecular confinement by the zeolite pores provides controllable adsorption properties and leads to its specific catalytic performance.

Typically, the selectivity of the desired product in a process is determined by the thermodynamic constraints, the operating parameters and the type of catalyst used in the reaction. Zeolites owing to their pore size and structure can serve as a way to tailor the product distribution, while their high acid strength is very much desirable for many of the catalytic reactions. These catalysts are well-known for providing shape selectivity and have been employed for several commercial processes, contributing to a hydrocarbon throughput of more than 70 million metric tons per year.[22] This makes them an ideal candidate for our bio-butanol conversion studies. Furthermore, as most of petrochemical reactions make use of zeolite based catalysts, the use of existing infrastructure for bio-butanol conversion will allow a smooth transition from the existing refining processes to the concept of bio-refinery, thus adding impetus towards the commercialization of these processes. In view of this, it is imperative to look into various zeolites for the selection of the best possible option for production of hydrocarbons, fuels and chemicals from renewable bio-resources.

The International Zeolite Association (IZA) recognizes 231 different zeolitic structures[23], which can be classified depending on the size of their pore openings determined by i) the number of tetrahedral atoms, i.e. Si or Al, forming the ring of the pore opening; e.g. large pore

zeolites have 12-membered-ring (12MR) apertures or ii) the number of dimensions (i.e. 1D, 2D, 3D) through which a molecule can diffuse within the crystals (see Figure 4).

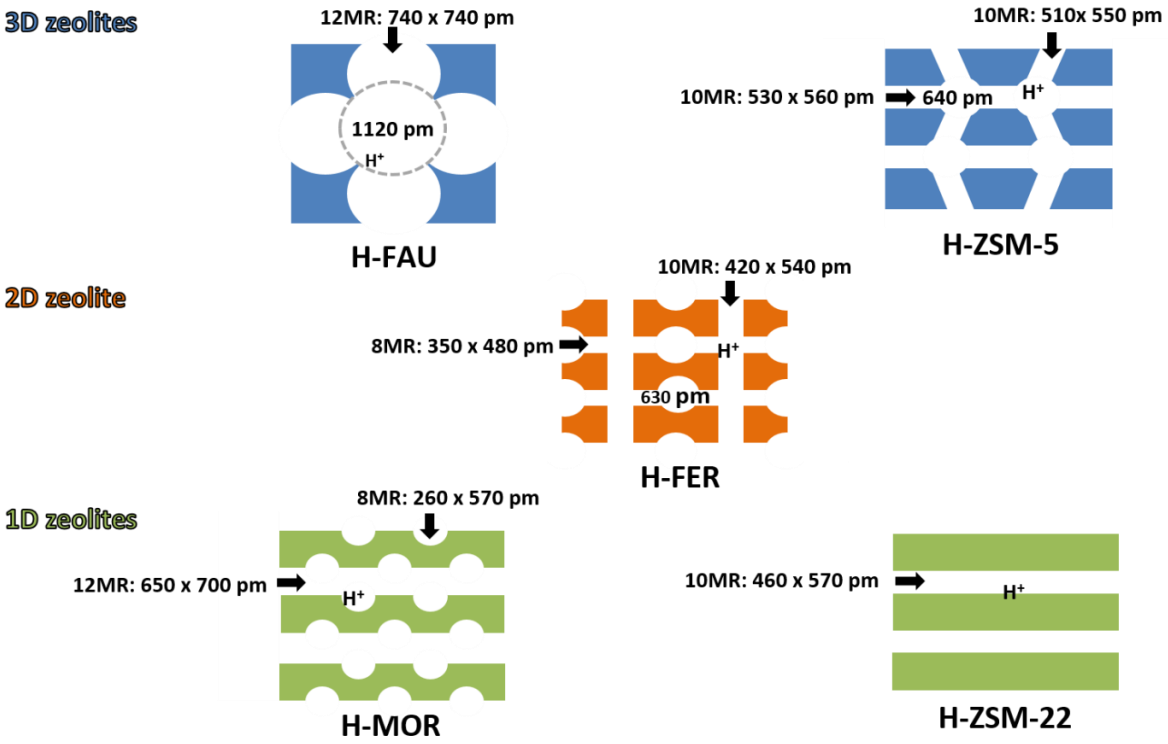

Figure 4. Examples of 3-D (H-FAU and H-ZSM-5), 2-D (H-FER) and 1-D (H-MOR, HZSM-22) zeolites.

Even though zeolites were extensively utilized in industry for several decades, an in-depth understanding for the design of shape selective catalysts was lacking owing to its huge dependence on rigorous time consuming experimentations. With the development of advanced computational facilities, researchers are now looking into a rational way towards the design of shape selective catalysts via the use of advanced computational modelling and simulation studies in conjunction with suitable material characterization techniques. [22] Hence, it is essential to look into the theoretical aspects for a better design of catalysts.

On the other hand, it is also desirable to have an idea of the experimentally observed product distribution and the reaction schemes that are used for explaining the obtained experimental data. Accordingly, the following section of this chapter will deal with the underlying reaction

mechanism and key observations from the experimental results for butanol dehydration and butene double bond and skeletal isomerization.

1.3. Reaction mechanism

1.3.1. Alcohol dehydration

Fundamental insight into the effect of catalyst properties on the underlying reaction mechanism can provide guidelines for the selection or rational design of an appropriate catalyst [24]. In general, alcohol dehydration can proceed via elimination and substitution reactions to yield alkenes and ether products. Elimination can occur via a step-wise E1 [25-31] or a concerted E2 mechanism [32-35] as shown in Figure 5a. An E1 elimination involves a heterolytic cleavage of the bond between the leaving group and the carbon atom leading to formation of a carbocation, followed by abstraction of an adjacent β-hydrogen by a base. On the other hand, E2 elimination can be relatively complex since it may involve a range of possible transition states owing to possible asynchronous breaking of C-O and C-H bonds[36]: pure E2 with synchronous breaking of the C-O and C-H_β bonds, E1-like E2 in which breaking of the C-O bond is more pronounced involving a transition state with a more or less pronounced carbenium ion character, and E1cb-like E2 with a more pronounced breaking of the C-H_β bond in the transition state that possesses a more or less pronounced carbanion character. Moreover, the concerted elimination requires the atoms or groups involved in the reaction to be in the same plane with an anti-periplanar or a syn-periplanar orientation characterized by torsional angles between leaving group and β-hydrogen of ~ 180° and 0°, respectively. The leaving group can also undergo a step-wise (S_N1) or a concerted (S_N2) nucleophilic substitution reaction, which lead to formation of an ether or alkoxide intermediate (see Figure 5b for a general scheme for nucleophilic substitution reaction). For S_N1 type substitution, the rate determining step involves cleavage of the bond between the

leaving group and the carbon atom leading to formation of a carbocation which undergoes nucleophilic attack to form the substituted product. On the other hand, S_N2 type nucleophilic substitution involves simultaneous bond breaking (between the carbon atom and leaving group) and bond formation (between carbon atom and the attacking nucleophile) via a transition state (TS) involving a penta-coordinated carbon atom with a trigonal bipyramidal geometry, having the incoming nucleophile and the leaving group occupying the axial positions (bond angle Nu--C--X ≈ 180°).

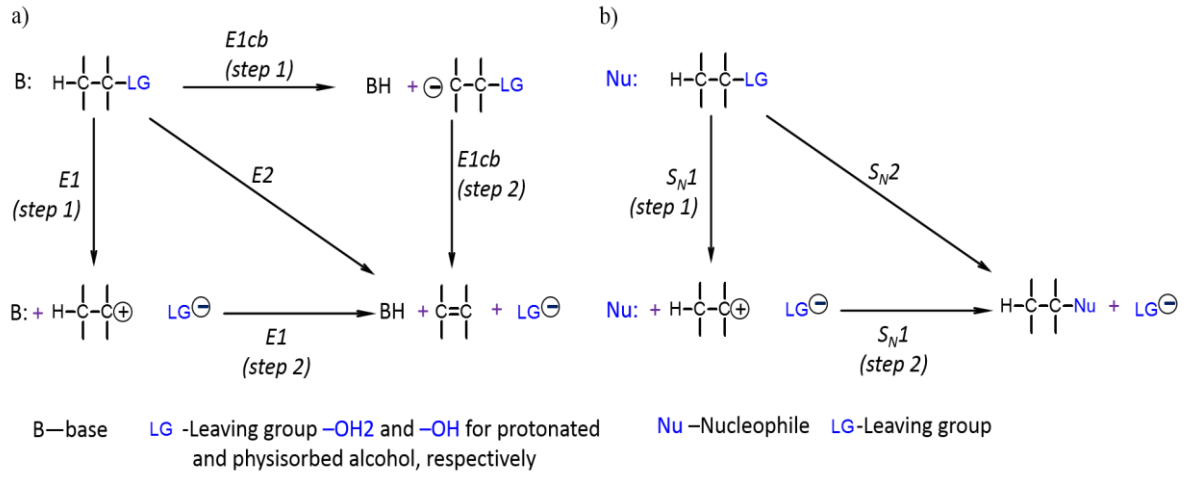

Figure 5. Scheme for different possible a) elimination[4] and b) nucleophilic substitution reaction mechanisms for alcohol dehydration.

Alcohol dehydration reactions can be catalyzed by acidic catalysts such as polyoxometalate (POM) [26-30], microporous SAPO [37,38], zeolites[39-46], and polyphosphoric acid or more basic catalysts such as alumina [47,48]. Knözinger [49] suggested a parallel-consecutive reaction scheme (see Figure 6) for the dehydration of alcohol over γ-alumina. Recent theoretical study by Christiansen et al.[50] provides mechanistic insights into competitive production of ethylene and diethyl ether from ethanol dehydration over γ-Al_2O_3

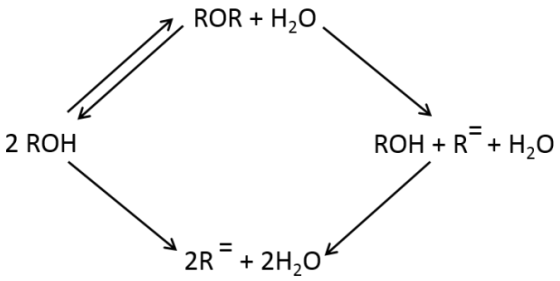

Figure 6. Parallel-consecutive reaction scheme for dehydration of alcohol (ROH) to ether (ROR) and alkene ($R^{=}$) [51].

Olaofe and Yue [31] carried out 1-butanol dehydration studies on zeolites (13X, 4A, ZNa) and proposed a reaction scheme for dehydration based on a E1 mechanism, where a 1-butyl carbonium ion undergoes Wagner-Meerwein rearrangement to form 2-butyl carbonium, which in turn gets converted into 1- and 2-butenes. Macht et al. suggested that the dehydration of 2-propanol and 2-butanol on POM [26-30] followed an E1 mechanism, which was corroborated by the observed secondary kinetic isotope effect (KIE) when the β-hydrogen was replaced by deuterium. Likewise, Vjunov et al. [25] confirmed an E1 mechanism for cyclohexanol dehydration in H-BEA based on ^{13}C -labeled scrambling experiments with in situ ^{13}C NMR analysis. DFT studies for dehydration of ethanol [34] and 2-propanol [32,35] in H-ZSM-5 reported a concerted (syn) elimination mechanism. On the other hand, Makarova et al. [39-46] through FTIR spectroscopy and kinetic studies at low pressures (< 1 kPa) and temperatures of 380 - 460 K suggested an alkoxide-mediated S_N2-type mechanism for conversion of 1-butanol to 1-butene and di-1-butyl ether (DBE) in H-ZSM-5. Similar alkoxide-mediated mechanisms were proposed for alkene formation for ethanol [52] and 1-propanol [53] dehydration in zeolites. The alcohol dehydration to ether can occur via an alkoxide-mediated and/or via an alcohol dimer-mediated mechanism[52]. Experimental and theoretical studies for methanol [54,55] and ethanol [52] dehydration in zeolites indicate that the ether is produced from the alcohol dimer via S_N2-type nucleophilic substitution.

Zhang et al. [37,38] studied the dehydration of 1-butanol to isobutene and other side products (linear butenes, butene oligomers and cracked products) over several zeolites (ZSM-5, ferrierite, SAPO-11, Theta-1/ZSM-22, ZSM-23 and Y) using a fixed bed reactor. They looked into the direct production of isobutene from 1-butanol dehydration. Their experimental conditions were much more severe as compared to Makarova et al. [40-44], since skeletal isomerization of linear butenes required higher acidity and temperature as compared to 1-butanol dehydration to linear butenes. The product distribution obtained for 1-butanol dehydration over different catalysts tabulated below (Table 1).

Table 1. Product distribution obtained for 1-butanol dehydration over different catalysts at 673K with 1:1 1-butanol : Ar mixture as feed and GHSV of 5200 hr^{-1}. 1-butanol conversion was 100% for all cases.

Catalyst	Si/Al	**i-$C_{4=}$**	**$C_{4=}$-1**	**$C_{4=}$-2 (*c* + *t*)**	**C3=**	**C5=**	**C_3^o + C_4^o**	**C6+**
Theta-1 [37]	31.5	31.7	9.0	27.9	6.7	7.1	3.7	13.7
FER [37]	10	33.8	11.8	36.9	5.0	9.6	2.4	6
ZSM-23 [37]	31.5	28.2	8.4	25.8	8.5	11.6	3.0	14.2
ZSM-5 [37]	25	11.3	3.1	10.3	18.1	19.1	7.8	28.5

The key parameters affecting the iso-butene yield were identified to be the zeolite framework structure, acidity, hydrothermal stability and the reactant partial pressure. Ten membered unidimensional zeolites (Theta-1 and ZSM-23) were shown to have a higher activity for butanol conversion. ZSM-5 had a low selectivity for iso-butene, while SAPO-11 and Y-zeolite depicted a loss in activity owing to lack of structural stability and excessive coke formation, respectively.

At higher conversions, formation of side products especially propene, pentene (C3 + C5 ~ 15%) and aromatics (8-15 %) was observed. [38] The carbenium ion based reaction mechanism involving dehydration, skeletal rearrangement, oligomerization, cracking and aromatization as described in Figure 7 was used to explain the product selectivity. The primary carbenium ion formed via dehydration of 1-butanol can undergo a hydride shift reaction to produce a

secondary carbenium ion, which in turn is converted into 1-butene / 2-butene through donation of a proton to the zeolite surface. Alternatively, the primary carbenium ion can undergo a methyl shift to produce a protonated cyclic intermediate, which is converted into a stable tertiary ion after a hydride shift.

Higher selectivity for 1- and 2- butenes was observed at lower temperatures, which shifts in favor of iso-butene with a slight increase in temperature, which is in turn accompanied by undesirable cracking reactions[37,38]. Zhang et al.[38] suggested that the formation of iso-butene occurs via both monomolecular (scheme 1, Figure 7) and bimolecular (scheme 2, Figure 7) mechanisms. However, the bimolecular mechanism could also lead to undesirable side reactions (schemes 3 and 4, Figure 7) as seen in the case of higher operating temperatures. On the other hand, a high isomer selectivity at lower conversion was linked to the predominance of isomerization reactions favoring the monomolecular mechanism.

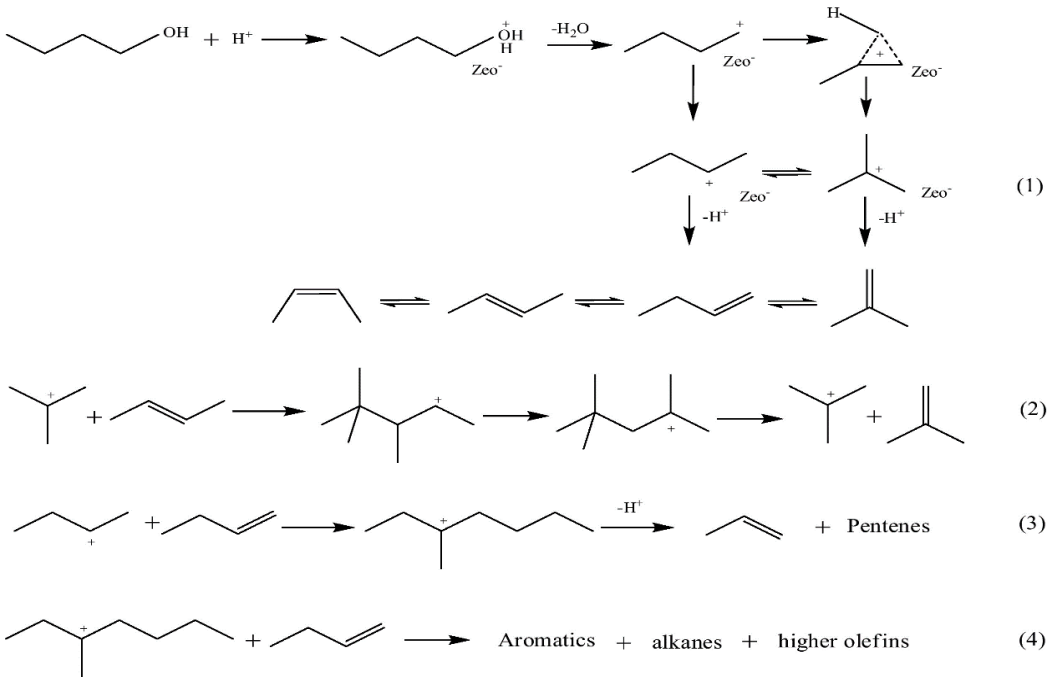

Figure 7. Reaction network of 1-butanol conversion over zeolite catalyst. (Zhang et al.[38]): 1) dehydration of 1-butanol to butene isomers, 2) bimolecular conversion to iso-butene, 3) bimolecular scheme producing cracked products, 4) other reactions producing aromatics, alkanes and higher olefins.

Likewise, a carbenium ion based mechanism was used by Taylor et al. to explain iso-butanol dehydration [56]. A schematic for the iso-butanol dehydration mechanism is shown in Figure 8. Iso-butanol first adsorbs on a Brønsted acid site, followed by elimination of a water molecule with formation of a carbenium ion, which could either desorb as iso-butene or undergo rearrangement to other butenes. An iso-butene yield of ~95% was reported for their experiments on alumina in a temperature range of 558-598 K and conversions between 35-98%. They found that the total pressure had a negative effect on the conversion values and this was accompanied by a slight increase in iso-butene selectivity. A comparison of their results for kinetic studies and their ASPEN simulated equilibrium data[56], clearly indicates that the reaction is far from equilibrium under the reported operating conditions.

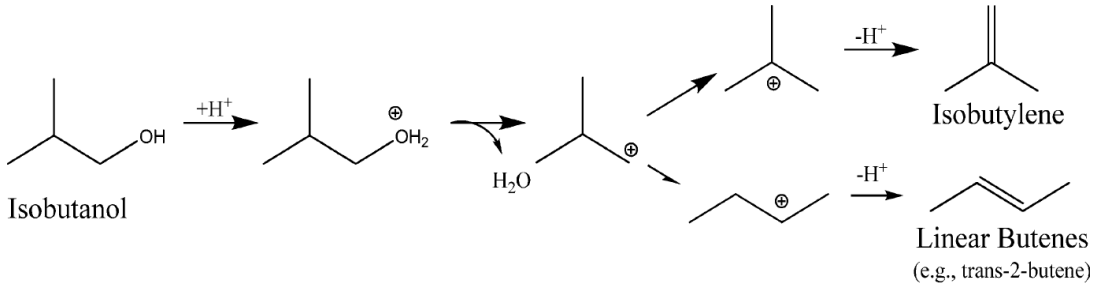

Figure 8. Iso-butanol dehydration mechanism [56].

Varvarin et al. [57] investigated the conversion of 1-butanol over H-ZSM-5, H-ZSM-11, H-L and H-Y zeolites in a temperature range of 573-673 K. They compared catalyst performances on the basis of gaseous and liquid product yields, with composition analysis for the liquid fraction. Under the same operating conditions, liquid product yields were found to be higher for medium pore zeolites in comparison to the large pore zeolites. H-ZSM-5 and H-ZSM-11 catalysts favored the formation of aromatic fractions (greater than 50% of the liquid fraction)

at temperatures above 598K, while it was in the range of 20-30% of the liquid fraction for large pore zeolites.

Although medium pore zeolites were described to function better than the large pore zeolites, some of them (for example, FER) could not maintain their initial activity during the course of the reaction. Jeong et al.[58] explored the use of a micro-mesoporous material synthesized by disassembling the ferrierite structure (MMZ-FER) for 1-butanol dehydration studies. They observed an increased stability and selectivity for butanol dehydration using their micro-mesoporous material.

Most of these studies focused on conversion of pure butanol. But as biobutanol is obtained via a fermentation process, it is essential to study the effect of water and other impurities on the dehydration process. Both 1-butanol and iso-butanol tend to form an azeotropic mixture with water, thus in order to make this process economically viable, it is very much desirable to carry out these reactions in the presence of water.

Talyor et al. [56] studied the dehydration of iso-butanol over alumina in the presence of water at two different temperatures. At 558 K, they found that the presence of water leads to a decrease in the overall conversion along with a slight increase in iso-butene selectivity. Experiments at 598 K presented similar selectivities and near complete conversion values for both dry and aqueous feed samples. Furthermore, they studied the effect of other possible impurities (iso-pentanol, ethanol, acetone, and iso-butyraldehyde) produced during the fermentation process. The presence of these impurities had no effect on the overall reaction performance in terms of conversion or selectivity.

West et al. [59] studied the effect of water in 2-butanol dehydration on zeolites and other solid oxide catalysts. Zeolite (HBEA, USY, ZSM-5) based catalysts, especially Y-zeolite, exhibited a significant drop in performance in the presence of water. Surprisingly, a higher catalyst

activity was seen for silica-alumina, niobium phosphate and niobic acid based catalysts in the presence of water, which they attribute to an increase in Brønsted acid sites on contact with liquid water.

A recent low temperature (413-443 K) experimental and theoretical study of 1-propanol dehydration in H-ZSM-5 indicated a reduction in dehydration rates in the presence of water [53]. The inhibition effect was attributed to differences in relative stabilization of elimination/substitution transition states with respect to the adsorbed intermediates in the presence of water.

The available literature data consists of a wide spectrum of experimental results corresponding to different catalysts and operating conditions and hence making a one to one comparison is quite a difficult task. A comparative study of activation energies over different catalysts could provide good insight into the effectiveness of the catalyst in reducing the activation energy barrier, hence increasing the reaction rate. The reported literature data associated with the dehydration of 1-butanol are tabulated in Table 2. Finally, the theoretically reported activation energy barrier for the same reaction in the gas-phase is 281 kJ/mol [60], which is much higher than that observed for the catalytic processes (see Table 2).

Table 2. Comparison of activation energies for 1-butanol dehydration over different catalysts

Catalyst	1-butanol dehydration to di-1-butyl ether (kJ/mol)	1-butanol dehydration to 1- and 2- butenes (kJ/mol)	Reference
13-X	142	159	[31]
4A	84	152	[31]
H-ZSM-5	92 ± 8	138 ± 8	[41]

On the other hand, there are very few theoretical studies on the adsorption/dehydration of butanol in zeolites. Nguyen et al.[61-63] studied adsorption of butanol isomers on H-ZSM-5 and of C1-C4 alcohols on H-FAU, H-MOR, H-ZSM-5 and H-ZSM-22, which gave an insight into

the significance of dispersive interactions and the better stabilization of molecules in zeolites with channel size close to that of the molecule. The predicted adsorption enthalpies and vibrational frequencies were in good agreement with the experimental results. Moreover, this study gave a better means to interpret the experimental IR spectra.[61,62] Their results indicated a comparable adsorption energy for physisorbed alcohol species (having two hydrogen bonds) and chemisorbed (protonated) alcohol species. The effect of the ZSM-5 channel topology was studied, and it was found that the strength of hydrogen bonding was higher in the zig-zag channel as compared to the straight one. This effect was more pronounced in the case of 2-butanol amongst all the butanol isomers. Steric constraints and dispersive van der Waals (vdW) interactions were found to have the foremost importance in determining the adsorption strength of the butanol isomers, with the 1-butanol molecule having the highest adsorption energy, followed by 2-, t-butanol and iso-butanol.[62] Moreover, it was found that the dispersive ion pair interaction terms increased with a decrease in pore size from H-FAU to H-ZSM-22 [63]. However, since all these theoretical studies remain confined to butanol adsorption, one needs to consider a more complete reaction scheme involving the formation of several products, in order to allow a comparison with experimental rates and selectivities.

1.3.2. Double bond isomerization

A possible mechanism explaining the formation of 2-butenes (cis and trans) during the dehydration of 1-butanol is double bond isomerization of 1-butene produced during the dehydration process [64]. Accordingly, this section focuses on the double bound isomerization of linear butenes.

Experimental [65,66] studies on deuterated solid catalysts were performed to explain the mechanism of double bond isomerization. Based on the incorporation of deuterium into both feed alkene and isomerized product, it was inferred that the double bond isomerization of alkenes proceeds via formation of a carbenium ion intermediate [65,66]. On the other hand,

Kazansky[67] proposed a mechanism involving the formation of a surface alkoxy group via proton addition from the zeolite to the double bond of butene, followed by the decomposition of the alkoxy intermediate as shown in Figure 9. The decomposition of the alkoxy group was found to be the rate determining step.[68]

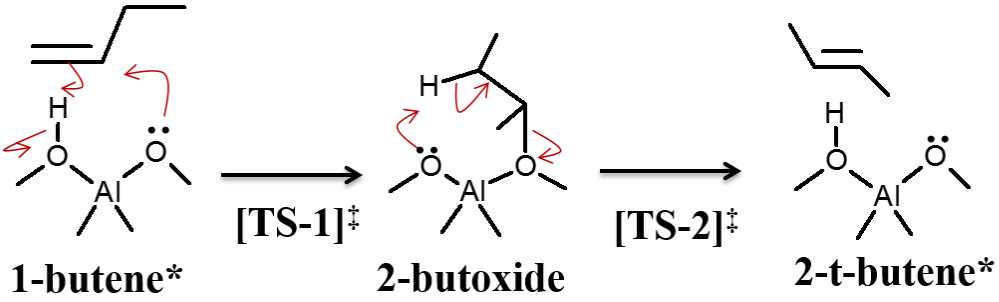

Figure 9. Mechanism for the double bond isomerization of butene via secondary alkoxide intermediate (adapted from ref [68])

An alternative mechanism was proposed by Kondo et al.[69,70] for temperatures below 230 K, where double bond isomerization proceeds via a π adsorption intermediate, instead of the protonated intermediate species, following a concerted mechanism as shown in Figure 10. They studied 1-butene isomerization to 2t-butene and 2c-butenes on D-ZSM-5 and D-MOR via FTIR experiments in a temperature range of 214-242 K and reported activation energy barriers of 49 ± 4 kJ/mol and 38 ± 8 kJ/mol respectively.

Stepanov et al. [71] studied the kinetics of 1-butene conversion on H-FER using ^{1}H , ^{2}H and ^{13}C MAS NMR spectroscopy. Their experimental results were in line with the mechanism proposed by Kondo et al.[69,70] They reported an activation energy barrier of 41 ± 5 kJ/mol for the reaction on H-FER.

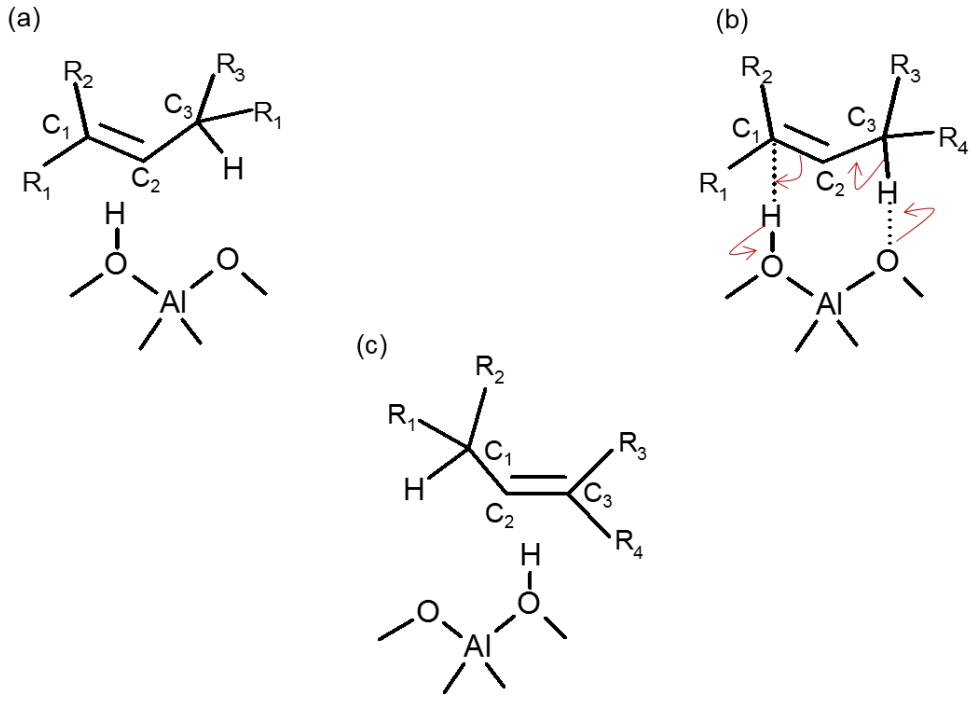

Figure 10. Concerted mechanism for the double bond isomerization of butene: a) adsorbed 1-alkene molecule, b) Transition state, c) adsorbed 2-alkene molecule [33].

Furthermore, concerted double bond isomerization has also been investigated via theoretical studies [33,72]. Density functional theory (DFT) was utilized by Boronat et al.[33] to unravel the mechanism associated with the double bond isomerization of butene. They made use of a cluster model with two Si and one Al atom to simulate the zeolite. Their study corroborates the concerted mechanism for the double bond isomerization reaction but slightly overestimates the activation energy barrier. A similar approach was employed by Li et al.[72] and their results further supported the concerted mechanism for isomerization of 1-butene to cis-2-butene. Although the activation energies for the forward and the backward reaction, calculated with respect to the adsorbed complexes, were 92 and 104 kJ/mol respectively, the apparent activation energy for the forward reaction is 63 kJ/mol. This predicted value is higher than the literature reported experimental value of 49 ± 4 kJ/mol.[69]

In addition, there are few other theoretical studies on butene double bond isomerization over homogeneous catalysts, such as 1-ethyl-3-methyl-imidazolium fluoride[73], which are associated though with very high activation energy barriers ~280 kJ/mol. Overall, although several theoretical calculations were reported in the literature, there are still discrepancies between the experimental and simulated values.

1.3.3. Skeletal isomerization

Butene skeletal isomerization is of both fundamental and technological interest and remains one of the important zeolite catalyzed reactions. The linear butenes produced from the dehydration of 1-butanol can undergo skeletal isomerization to produce isobutene, which is discussed in detail in this section.

Several zeolites (FER [74-84], ZSM-5[74-76], ZSM-22[74,77,78,85], ZSM-23[74,75] , etc.) have been studied for butene skeletal isomerization. A comparison of butene skeletal isomerization on small, medium and large pore zeolites is shown in Figure 11 [74]. This figure clearly depicts that medium pore zeolites AEL, FER and TON were far superior to other zeolites in terms of iso-butene selectivity. However, AEL type zeolites (SAPO-11, MeAPO-11) have stability issues under hydrothermal conditions, hence they cannot be used for the purpose of butanol dehydration and isomerization. FER and ZSM-22 have been studied extensively for butene skeletal isomerization. Although both of them showed comparable performance, the FER based catalyst was reported to have a lower apparent activation energy but its activity was found to decrease with time [77]. This decrease is often linked with an increase in iso-butene selectivity as a result of coking of non-selective sites.

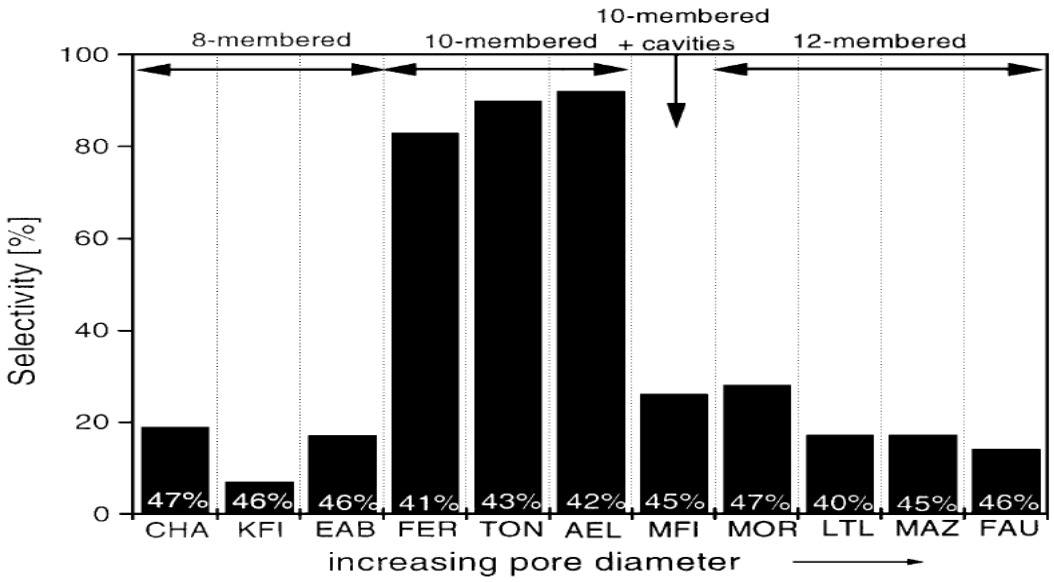

Figure 11. Comparison of various zeolite framework types for isobutene selectivity under identical operating conditions at conversions in the range of 41-47% [74] (numbers in the bars indicate conversion).

Concerning the effect of the Si/Al ratio on butene skeletal isomerization for FER, it was observed that an increase in Si/Al ratio led to an increase in selectivity and a decrease in conversion [78]. Thus, there is a tradeoff between the desired activity and selectivity which requires the selection of an optimum acidity.

The reaction mechanism for skeletal isomerization remains a topic of debate. The proposed reaction mechanisms can be classified into monomolecular [74,83-86] and bimolecular [76,78,87-89] reaction schemes. The monomolecular pathway starts with adsorption and protonation of 1-butene on the Brønsted acid site to give a primary butoxide intermediate, followed by the formation of a protonated cyclic transition state which decomposes into a iso-butoxide intermediate and finally rearranges into adsorbed iso-butene.

The bimolecular scheme can lead to two different possibilities: dimerization and co-dimerization mechanism. The former involves the dimerization of two linear butene molecules followed by isomerization and cracking to produce iso-butene and other alkenes.

[76,78,87,88]The co-dimerization mechanism is based on an autocatalytic principle as described in scheme 2 of Figure 7, where linear butene and iso-butene dimerizes to form tri-methyl-pentane and then crack to produce two iso-butene molecules.[89] Although, these reaction mechanisms allowed to explain some of the experimental results, none of them could fully explain the butene skeletal isomerization results for different zeolites.

An experimental study on the effect of pressure and temperature on isobutene yield gave insight into the underlying reaction mechanism[90]. It was observed that an increase in 1-butene pressure led to a decrease in the isobutene yield, whereas an increase in the reaction temperature led to an increase in the isobutene selectivity. Thus, it could be concluded that dimerization is favored at high pressures and low temperatures are responsible for the formation of by-products (as shown in the scheme 3 of Figure 7) and have minimal contribution towards iso-butene formation. On the other hand, Dokomos et al.[86] found a zero order dependence of isobutene yield on butene pressure, which was explained on the basis of a desorption limited monomolecular mechanism for the formation of isobutene. They reported an apparent activation energy barrier of 59 kJ/mol for 1-butene skeletal isomerization on H-FER. Nevertheless, both experimental studies indicated that the mono-molecular mechanism drives the conversion of butenes to iso-butenes.

More detailed insight in the reaction mechanism can be obtained via theoretical studies. Van Santen and co-workers [91] investigated the mechanism of butene skeletal isomerization in zeolites and liquid super acids using DFT cluster models. They found that the conversion of the surface alkoxy species proceeds via a corner protonated cyclopropane transition state, Boronat et al. [92] carried out DFT studies for butene skeletal isomerization over theta-1 zeolite. They considered a reaction mechanism involving three elementary steps (see Figure 12): the adsorbed 1-butene (I) undergoes protonation to form a 2-butoxide (III) intermediate, followed by conversion of the 2-butoxide into an iso-butoxide (V) via a protonated cyclic transition

state (with C_4 nearly equidistant from C_2 and C_3), which is further converted to an adsorbed iso-butene (VII). It was found that the geometry and stability of the alkoxide intermediates are strongly influenced by the local geometry of the active site, while the ionic transition states are mainly stabilized by electrostatic effects.

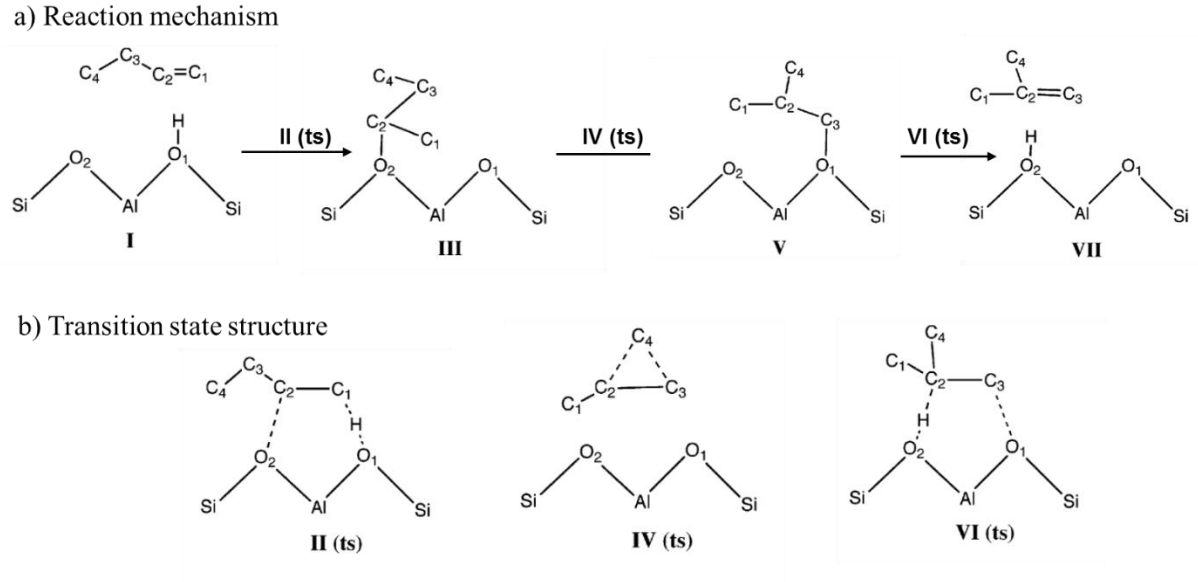

Figure 12. Monomolecular mechanism for conversion of 1-butene to iso-butene[92].

The monomolecular mechanism for skeletal isomerization of 1-butene to isobutene was also studied on H-FER using an ONIOM (MP2:M08-HX) approach by Wattanakit et al [93]. They modeled the FER structure using a 37T quantum cluster and could capture the confinement effect within the zeolite pore structure. Their results indicated a lower adsorption energy for iso-butene (-62 kJ/mol) as compared to 1-butene (-75 kJ/mol), which they attribute to the presence of steric constraints for isobutene in H-FER. Their study indicated that the conversion of isobutoxide to isobutene via a cationic transition state is the rate-determining step with an intrinsic activation barrier of 151 kJ/mol and an apparent activation energy barrier of 71 kJ/mol which was 13 kJ/mol higher than the experimentally observed value of 58 kJ/mol. In addition, a hybrid quantum/molecular mechanics model was used by Gleeson[94,95] to study the skeletal isomerization of cis-butene within the FER framework. They compared

the carbenium ion and the alkoxide mediated monomolecular reaction mechanisms using a 27T quantum cluster. The alkoxide intermediate was reported to be more stable than the carbenium ion intermediate, while the alkoxide based mechanism was 40 kJ/mol more activated than the carbenium ion based mechanism. The higher barrier for the former mechanism was attributed to the inherent stability of the alkoxide intermediates formed within FER. Likewise, they compared the monomolecular and bimolecular reaction mechanism for cis-butene skeletal isomerization. They supported the co-dimerization bimolecular scheme considering the fact that the activation energy barrier predicted via this route was much closer to the experimentally observed value [95].

Nevertheless, no fully periodic density functional theory calculations are available for butene skeletal isomerization, while most of the theoretical studies report only the 0 K electronic energies. Moreover, since entropic considerations can significantly alter the stability of adsorbed intermediates and transition states at higher temperatures, it is important to address these effects at industrially relevant reaction conditions.

1.4. Ab initio microkinetic modelling

Understanding the nature of transition states and adsorbed intermediates is of paramount importance for understanding chemical reactivity in heterogeneous catalysis. The transition state separates the reactant from the product, and the free energy required to reach it determines the kinetics of an elementary chemical reaction. In the same way, the stability of the reaction intermediate governs its surface coverage and hence the turnover frequency (TOF) of the elementary step involving this intermediate as a reactant or product.

Although advancement in experimental techniques allows to reveal several characteristics of adsorbed intermediate, the short lifetime of the TS makes it very difficult to be observed

experimentally. In this respect, quantum chemical modelling in the framework of density functional theory can provide a great deal of insight into the underlying reaction mechanism of zeolite-catalyzed processes. Density functional theory (DFT) is widely used to study such catalytic processes, as the investigated active sites and molecules are of considerable size and other theoretical methods are often not applicable due to unfavorable scaling properties. DFT-derived energetics combined with vibrational analysis and statistical thermodynamics can be used to obtain thermodynamic and kinetic parameters at relevant temperatures.

In order to translate insights at molecular level to the macroscale, DFT-based microkinetic simulations can be used to probe a wide range of reaction conditions. These simulations allow to capture changes in the coverage of key surface species, and in dominant reaction mechanisms and pathways with changes in reaction conditions. Typically, there can be significant differences in the reaction conditions of the experiments used for understanding different phenomena at different scales, which can lead to conflicting observations. Thus, mechanistic insights from DFT-based microkinetic simulations over a wide range of conditions can serve as a tool to reconcile such conflicting experimental observations.

1.5. Scope

The present ab initio based microkinetic modelling work investigates 1-butanol dehydration and butene isomerization kinetics in different industrially relevant zeolites. The key objectives of this work are as follows:

(1) investigating the reaction mechanism for 1-butanol dehydration in H-ZSM-5 zeolite aiming to provide mechanistic insights in the role of reaction conditions such as temperature, 1-butanol partial pressure and presence of water in determining butanol dehydration kinetics.

(2) elucidating the influence of the zeolite framework in defining the catalytic performance for 1-butanol dehydration kinetics. Here, the aim is twofold: i) to identify, under identical conditions, the most abundant reaction intermediates (MARIs), dominant reaction paths, and reaction mechanisms in different zeolites and ii) to explain these differences in terms of differences in stabilitization of intertermediates and/or transition states due to confinement in the zeolite.

(3) providing mechanistic insights into the competing reaction pathways for the formation of butene isomers (1-butene, cis/trans 2-butenes and iso-butene) during catalytic dehydration of 1-butanol in H-ZSM-5.

(4) probing the effect of zeolite framework on the production of butene isomers during the catalytic dehydration of 1-butanol in different industrially relevant zeolites and explaining the role of zeolite confinement in providing stabilization for reaction and TS intermediates.

1.6. Outline

Chapter 1 presents an up–to–date review for the catalytic conversion of bio-alcohols, mainly focusing on the zeolite catalyzed conversion of bio-butanol to “green” olefins, fuels and chemicals.

Chapter 2 deals with the DFT study of plausible reaction mechanisms for 1-butanol dehydration in H-ZSM-5. An ab initio based microkinetic model is used to explain the experimental trends reported in literature and to reveal the crucial role of reaction conditions in determining the dominant reaction mechanism and pathway. The effect of presence of water on 1-butanol dehydration under industrially relevant conditions is also investigated.

Chapter 3 focuses on the effect of zeolite framework on the underlying reaction mechanism, stability of surface intermediates, TOF and product selectivity for 1-butanol dehydration to 1-butene and di-1-butyl ether (DBE). The ab initio based microkinetic simulations provide unprecedented insights on how differences in dispersive stabilization and steric constraints govern catalytic activity and product selectivity.

Chapter 4 provides theoretical insights into the competing pathways for the formation of butene isomers (1-butene, cis/trans 2-butenes and isobutene) during dehydration of 1-butanol in H-ZSM-5. New mechanisms are proposed for the direct formation of trans-2-butene from 1-butanol or di-1-butyl-ether (DBE). The DFT-based microkinetic simulation results show that the formation of cis/trans 2-butenes in H-ZSM-5 essentially occurs via concerted and 2-butoxide mediated stepwise double bond isomerization. The possibility of tuning the reaction conditions for 1-butanol dehydration to maximize 1-butene yield is also discussed.

In **Chapter 5**, ab initio based microkinetic modelling of 1-butanol dehydration to butene isomers is used to obtain mechanistic insights into the effect of zeolite framework on reaction kinetics and product selectivity. The detailed microkinetic model for H-ZSM-5, H-ZSM-22 and H-FER includes double bond isomerization, skeletal isomerization and mechanisms for the direct formation of 2t-butene from 1-butanol dimer and di-1-butyl ether. Simulation results show that, unlike H-ZSM-5 and H-ZSM-22 where formation of cis/trans 2-butenes occurs via double bond isomerization, formation of trans-2-butene in H-FER occurs via direct dehydration of the 1-butanol dimer. The difference in the underlying reaction mechanism for different zeolites is rationalized on the basis of differences in the enthalpic stabilization of the transition state and reaction intermediate.

Finally, **Chapter 6** discusses general conclusions and prospects for future work, which would allow the application of the presented approach at even higher temperature conditions and for the conversion of other bio-based alcohols and polyols to value added chemicals.

1.7. References

(1) Mascal, M. *Biofuel Bioprod Bior* **2012**, *6*, 483.

(2) Luque, R.; Herrero-Davila, L.; Campelo, J. M.; Clark, J. H.; Hidalgo, J. M.; Luna, D.; Marinas, J. M.; Romero, A. A. *Energ Environ Sci* **2008**, *1*, 542.

(3) Haw, J. F.; Song, W. G.; Marcus, D. M.; Nicholas, J. B. *Accounts Chem Res* **2003**, *36*, 317.

(4) Sun, J.; Wang, Y. *Acs Catal* **2014**, *4*, 1078.

(5) Huber, G. W.; Corma, A. *Angew Chem Int Edit* **2007**, *46*, 7184.

(6) Ragauskas, A. J.; Williams, C. K.; Davison, B. H.; Britovsek, G.; Cairney, J.; Eckert, C. A.; Frederick, W. J.; Hallett, J. P.; Leak, D. J.; Liotta, C. L.; Mielenz, J. R.; Murphy, R.; Templer, R.; Tschaplinski, T. *Science* **2006**, *311*, 484.

(7) Cheng, C. L.; Che, P. Y.; Chen, B. Y.; Lee, W. J.; Lin, C. Y.; Chang, J. S. *Appl Energ* **2012**, *100*, 3.

(8) Taherzadeh, M. J.; Karimi, K. *Bioresources* **2007**, *2*, 472.

(9) Palmqvist, E.; Hahn-Hagerdal, B. *Bioresource Technol* **2000**, *74*, 25.

(10) Shamsul, N. S.; Kamarudin, S. K.; Rahman, N. A.; Kofli, N. T. *Renew Sust Energ Rev* **2014**, *33*, 578.

(11) Talebnia, F.; Karakashev, D.; Angelidaki, I. *Bioresource Technol* **2010**, *101*, 4744.

(12) Swana, J.; Yang, Y.; Behnam, M.; Thompson, R. *Bioresource Technol* **2011**, *102*, 2112.

(13) Savage, N. *Nature* **2011**, *474*, S9.

(14) Jones, D. T.; Woods, D. R. *Microbiol Rev* **1986**, *50*, 484.

(15) Alper, H.; Stephanopoulos, G. *Nat Rev Microbiol* **2009**, *7*, 715.

(16) Yang, C.; Meng, Z. Y. *J Catal* **1993**, *142*, 37.

(17) Karre, A. V.; Kababji, A.; Kugler, E. L.; Dadyburjor, D. B. *Catal Today* **2013**, *214*, 82.

\(18) Busca, G. *Chem Rev* **2007**, *107*, 5366.

(19) Wright, M. E.; Harvey, B. G.; Quintana, R. L. *Energ Fuel* **2008**, *22*, 3299.

(20) Gronowski, A. A. *J Appl Polym Sci* **2003**, *87*, 2360.

(21) Guan, J. Q.; Xu, C.; Wang, Z. Q.; Yang, Y.; Liu, B.; Shang, F. P.; Shao, Y. Q.; Kan, Q. B. *Catal Lett* **2008**, *124*, 428.

(22) Degnan, T. F. *J Catal* **2003**, *216*, 32.

(23) Baerlocher, C.; Meier, W. M.; Olson, D.; Meier, W. M. *Atlas of zeolite framework types*; 5th rev. ed.; Elsevier: Amsterdam ; New York, 2001.

(24) Norskov, J. K.; Bligaard, T.; Rossmeisl, J.; Christensen, C. H. *Nat Chem* **2009**, *1*, 37.

(25) Vjunov, A.; Hu, M. Y.; Feng, J.; Camaioni, D. M.; Mei, D. H.; Hu, J. Z.; Zhao, C.; Lercher, J. A. *Angew Chem Int Edit* **2014**, *53*, 479.

(26) Janik, M. J.; Macht, J.; Iglesia, E.; Neurock, M. *J Phys Chem C* **2009**, *113*, 1872.

(27) Macht, J.; Carr, R. T.; Iglesia, E. *J Am Chem Soc* **2009**, *131*, 6554.

(28) Macht, J.; Carr, R. T.; Iglesia, E. *J Catal* **2009**, *264*, 54.

(29) Macht, J.; Janik, M. J.; Neurock, M.; Iglesia, E. *J Am Chem Soc* **2008**, *130*, 10369.

(30) Macht, J.; Janik, M. J.; Neurock, M.; Iglesia, E. *Angew Chem Int Edit* **2007**, *46*, 7864.

(31) Olaofe, O.; Yue, P. L. *Collect Czech Chem C* **1985**, *50*, 1834.

(32) Konda, S. S. M.; Caratzoulas, S.; Vlachos, D. G. *Acs Catal* **2015**.

(33) Boronat, M.; Viruela, P.; Corma, A. *J Phys Chem A* **1998**, *102*, 982.

(34) Kim, S.; Robichaud, D. J.; Beckham, G. T.; Paton, R. S.; Nimlos, M. R. *J Phys Chem A* **2015**, *119*, 3604.

(35) Prestianni, A.; Cortese, R.; Duca, D. *React Kinet Mech Cat* **2013**, *108*, 565.

(36) Ensing, B.; Laio, A.; Gervasio, F. L.; Parrinello, M.; Klein, M. L. *J Am Chem Soc* **2004**, *126*, 9492.

(37) Zhang, D. Z.; Al-Hajri, R.; Barri, S. A. I.; Chadwick, D. *Chem Commun* **2010**, *46*, 4088.

(38) Zhang, D. Z.; Barri, S. A. I.; Chadwick, D. *Appl Catal a-Gen* **2011**, *403*, 1.

(39) Makarova, M. A.; Paukshtis, E. A.; Thomas, J. M.; Williams, C.; Zamaraev, K. I. *Catal Today* **1991**, *9*, 61.

(40) Makarova, M. A.; Paukshtis, E. A.; Thomas, J. M.; Williams, C.; Zamaraev, K. I. *Stud Surf Sci Catal* **1993**, *75*, 1711.

(41) Makarova, M. A.; Paukshtis, E. A.; Thomas, J. M.; Williams, C.; Zamaraev, K. I. *J Catal* **1994**, *149*, 36.

(42) Makarova, M. A.; Williams, C.; Romannikov, V. N.; Zamaraev, K. I.; Thomas, J. M. *J Chem Soc Faraday T* **1990**, *86*, 581.

(43) Makarova, M. A.; Williams, C.; Thomas, J. M.; Zamaraev, K. I. *Catal Lett* **1990**, *4*, 261.

(44) Makarova, M. A.; Williams, C.; Zamaraev, K. I.; Thomas, J. M. *J Chem Soc Faraday T* **1994**, *90*, 2147.

(45) Williams, C.; Makarova, M. A.; Malysheva, L. V.; Paukshtis, E. A.; Talsi, E. P.; Thomas, J. M.; Zamaraev, K. I. *J Catal* **1991**, *127*, 377.

(46) Williams, C.; Makarova, M. A.; Malysheva, L. V.; Paukshtis, E. A.; Zamaraev, K. I.; Thomas, J. M. *J Chem Soc Faraday T* **1990**, *86*, 3473.

(47) Dedecek, J.; Lucero, M. J.; Li, C. B.; Gao, F.; Klein, P.; Urbanova, M.; Tvaruzkova, Z.; Sazama, P.; Sklenak, S. *J Phys Chem C* **2011**, *115*, 11056.

(48) Tuma, C.; Sauer, J. *Phys Chem Chem Phys* **2006**, *8*, 3955.

(49) Nieminen, V.; Sierka, M.; Murzin, D. Y.; Sauer, J. *J Catal* **2005**, *231*, 393.

(50) Christiansen, M. A.; Mpourmpakis, G.; Vlachos, D. G. *Acs Catal* **2013**, *3*, 1965.

(51) Dai, W. L.; Wang, C. M.; Yi, X. F.; Zheng, A. M.; Li, L. D.; Wu, G. J.; Guan, N. J.; Xie, Z. K.; Dyballa, M.; Hunger, M. *Angew Chem Int Edit* **2015**, *54*, 8783.

(52) Chiang, H.; Bhan, A. *J Catal* **2010**, *271*, 251.

(53) Zhi, Y.; Shi, H.; Mu, L.; Liu, Y.; Mei, D.; Camaioni, D. M.; Lercher, J. A. *J Am Chem Soc* **2015**.

(54) Blaszkowski, S. R.; vanSanten, R. A. *J Am Chem Soc* **1996**, *118*, 5152.

(55) Blaszkowski, S. R.; vanSanten, R. A. *J Am Chem Soc* **1997**, *119*, 5020.

(56) Taylor, J. D.; Jenni, M. M.; Peters, M. W. *Top Catal* **2010**, *53*, 1224.

(57) Varvarin, A. M.; Khomenko, K. M.; Brei, V. V. *Fuel* **2013**, *106*, 617.

(58) Seo, G.; Jeong, H. S.; Lee, J. M.; Ahn, B. J. *Progress in Zeolite and Microporous Materials, Pts a-C* **1997**, *105*, 1431.

(59) West, R. M.; Braden, D. J.; Dumesic, J. A. *J Catal* **2009**, *262*, 134.

(60) Moc, J.; Simmie, J. M.; Curran, H. J. *J Mol Struct* **2009**, *928*, 149.

(61) Nguyen, C. M.; Reyniers, M. F.; Marin, G. B. *Phys Chem Chem Phys* **2010**, *12*, 9481.

(62) Nguyen, C. M.; Reyniers, M. F.; Marin, G. B. *J Phys Chem C* **2011**, *115*, 8658.

(63) Nguyen, C. M.; Reyniers, M. F.; Marin, G. B. *J Catal* **2015**, *322*, 91.

(64) Pines, H.; Haag, W. O. *J Am Chem Soc* **1961**, *83*, 2847.

(65) Ozaki, A.; Kimura, K. *J Catal* **1964**, *3*, 395.

(66) Misono, M.; Tani, N.; Yoneda, Y. *J Catal* **1978**, *55*, 314.

(67) Kazansky, V. B. *Accounts Chem Res* **1991**, *24*, 379.

(68) Corma, A. *Chem Rev* **1995**, *95*, 559.

(69) Kondo, J. N.; Domen, K.; Wakabayashi, F. *J Phys Chem B* **1997**, *101*, 5477.

(70) Kondo, J. N.; Shao, L. Q.; Wakabayashi, F.; Domen, K. *J Phys Chem B* **1997**, *101*, 9314.

(71) Stepanov, A. G.; Arzumanov, S. S.; Luzgin, M. V.; Ernst, H.; Freude, D. *J Catal* **2005**, *229*, 243.

(72) Li, H. Y.; Pu, M.; Liu, K. H.; Zhang, B. F.; Chen, B. H. *Chem Phys Lett* **2005**, *404*, 384.

(73) Pu, M.; Chen, B. H.; Fang, D. C. *Struct Chem* **2006**, *17*, 377.

(74) Houzvicka, J.; Hansildaar, S.; Ponec, V. *J Catal* **1997**, *167*, 273.

(75) Oyoung, C. L.; Pellet, R. J.; Casey, D. G.; Ugolini, J. R.; Sawicki, R. A. *J Catal* **1995**, *151*, 467.

(76) Bauer, F.; Chen, W. H.; Biiz, E.; Freyer, A.; Sauerland, V.; Liu, S. B. *J Catal* **2007**, *251*, 258.

(77) Kangas, M.; Kumar, N.; Harlin, E.; Salmi, T.; Murzin, D. Y. *Ind Eng Chem Res* **2008**, *47*, 5402.

(78) de Menorval, B.; Ayrault, P.; Gnep, N. S.; Guisnet, M. *Appl Catal a-Gen* **2006**, *304*, 1.

(79) Byggningsbacka, R.; Kumar, N.; Lindfors, L. E. *Catal Lett* **1998**, *55*, 173.

(80) Khitev, Y. P.; Ivanova, I. I.; Kolyagin, Y. G.; Ponomareva, O. A. *Appl Catal a-Gen* **2012**, *441*, 124.

(81) Domokos, L.; Lefferts, L.; Seshan, K.; Lercher, J. A. *J Mol Catal a-Chem* **2000**, *162*, 147.

(82) Onyestyak, G.; Valyon, J.; Pal-Borbely, G.; Rees, L. V. C. *Appl Surf Sci* **2002**, *196*, 401.

(83) Meriaudeau, P.; Tuan, V. A.; Le, N. H.; Szabo, G. *J Catal* **1997**, *169*, 397.

(84) Meriaudeau, P.; Naccache, C.; Le, H. N.; Vu, T. A.; Szabo, G. *J Mol Catal a-Chem* **1997**, *123*, L1.

(85) Simon, M. W.; Suib, S. L.; Oyoung, C. L. *J Catal* **1994**, *147*, 484.

(86) Domokos, L.; Lefferts, L.; Seshan, K.; Lercher, J. A. *J Catal* **2001**, *197*, 68.

(87) Guisnet, M.; Andy, P.; Gnep, N. S.; Benazzi, E.; Travers, C. *J Catal* **1996**, *158*, 551.

(88) Mooiweer, H. H.; Dejong, K. P.; Kraushaarczarnetzki, B.; Stork, W. H. J.; Krutzen, B. C. H. *Zeolites and Related Microporous Materials: State of the Art 1994* **1994**, *84*, 2327.

(89) Houzvicka, J.; Diefenbach, O.; Ponec, V. *J Catal* **1996**, *164*, 288.

(90) Asensi, M. A.; Corma, A.; Martinez, A. *J Catal* **1996**, *158*, 561.

(91) Frash, M. V.; Kazansky, V. B.; Rigby, A. M.; vanSanten, R. A. *J Phys Chem B* **1997**, *101*, 5346.

(92) Boronat, M.; Viruela, P.; Corma, A. *Phys Chem Chem Phys* **2001**, *3*, 3235.

(93) Wattanakit, C.; Nokbin, S.; Boekfa, B.; Pantu, P.; Limtrakul, J. *J Phys Chem C* **2012**, *116*, 5654.

(94) Gleeson, D. *J Phys Chem A* **2011**, *115*, 14629.

(95) Gleeson, D. *J Mol Catal a-Chem* **2013**, *368*, 107.

Chapter 2

Reaction path analysis for 1-butanol dehydration in H-ZSM-5 zeolite: ab initio and microkinetic modelling

The following pages include the paper:

M. John, K. Alexopoulos, M.-F. Reyniers and Guy B. Marin

Journal of Catalysis **330** (2015) 28 – 45.

Abstract

Dispersion corrected periodic density functional theory (DFT) is used to construct a microkinetic model for 1-butanol dehydration in H-ZSM-5. The latter is applied to determine the effect of reaction conditions on dehydration rates, product selectivity and dominant reaction pathway. The consecutive reaction scheme of 1-butanol dehydration to ether followed by ether decomposition offers lower energy barriers as compared to the direct conversion of 1-butanol to 1-butene. The direct dehydration of 1-butanol to 1-butene occurs via an E2 (anti) elimination at low1-butanol partial pressure and shifts to a 1-butanol assisted 1,2-syn-elimination with increasing1-butanol partial pressure. The ether formation reaction proceeds via an S_N2-type nucleophilic substitution mechanism, involving substitution of the -OH2 group of the protonated alcohol by 1-butanol, while ether decomposition predominantly occurs via a 1,2–syn-elimination mechanism. The effect of reaction conditions viz. reaction temperature, site time,1-butanol and water partial pressure is studied. The reaction conditions govern the coverage of key surface species which in turn has a significant role in determining the dominant reaction mechanism and product selectivity. Under industrially relevant conditions, the presence of water has no significant effect on 1-butanol conversion and product selectivity. A higher reaction temperature, higher site time and lower 1-butanol partial pressure favor a higher 1-butene selectivity.

Keywords: DFT, dispersion energy, bio-butanol, dehydration, zeolite, reaction mechanism, microkinetic modelling, reaction path analysis.

2.1. Introduction

Being a potential alternative to fossil fuels, biofuels are of prime interest for the development of a sustainable future[1]. First generation bio-fuels such as bio-ethanol are considered as harbingers to the growth in the area of bio-energy. With recent studies indicating health hazards[2,3] and drawbacks associated with the usage of ethanol as a fuel, much attention is being paid towards the usage of higher alcohols such as bio-butanol[4]. Considering the future growth prospects of bio-butanol, it is imperative to look into the various aspects of utilizing it as a feedstock for the chemical industry. Zeolite catalyzed selective dehydration of bio-butanol to butene could provide an ideal platform for the production of such an apt feedstock. Butene produced from butanol dehydration could serve as a building block for several specialty chemicals[5], commodity polymers[6] and fuel additives[7,8].

The catalytic dehydration of butanol has been extensively studied over Brønsted acid sites of several solid acid catalysts, such as zeolites[9-19], amorphous alumino-silicates[12,17] and polyoxometalate (POM) clusters[20-24]. The dehydration reaction is accompanied by side reactions such as oligomerization, cracking and aromatization[18]. Therefore design of a selective catalyst remains challenging. The first step towards catalyst design is to gain in-depth understanding of the underlying reaction mechanism. Earlier efforts to understand the reaction mechanism relied mostly upon experimental kinetic and FTIR studies. Based on their kinetic studies, Olaofe and Yue[9] proposed an E1 mechanism (involving Wagner-Meerwein rearrangement of a carbenium ion) for 1-butanol dehydration on zeolites. A similar carbenium ion based mechanism was used by Zhang et al.[19] to exemplify their reaction scheme for conversion of 1-butanol to iso-butene. On the other hand, Makarova et al.[17], through their FTIR spectroscopy and their kinetic studies at low pressures (less than 1 kPa) and temperatures (380 - 460 K), suggested a reaction mechanism involving butoxy intermediate for 1-butanol dehydration reactions in ZSM-5 zeolite. They observed formation of both di-

butyl ether and butene in their dehydration studies. Their kinetic experiments on ZSM-5 samples of different crystallite size (<0.1 to 20 μm) revealed absence of any diffusion limitation for the reactant and the product molecules. Their comparative study for dehydration of 1-butanol and di-1-butyl ether indicated similar rates for production of butene from both reactants. This could be associated with the possibility of the ether being an intermediate product in the path of dehydration of butanol to butene. Overall, there is a lack of consensus in literature on the butanol dehydration mechanism within the zeolite pores.

Theoretical studies could provide significant insight into the reaction mechanism but there are very few such studies reported for butanol dehydration in zeolites or over the Brønsted acid sites of other solid acid catalysts. Macht et al.[20,23,24] studied 2-butanol dehydration on POM clusters via both density functional theory (DFT) and experimental kinetic studies. Their DFT study corroborated the formation of a butoxy intermediate, which produces butene on deprotonation. They found that the reaction follows an E1 mechanism, with elimination of a water molecule via a carbenium ion like transition state. However, the dehydration reaction on the surface of the POM clusters doesn't involve confinement effects, as observed within the zeolite pore structure. Hence, one cannot disregard the possibility of an alternative reaction mechanism for the latter case. A recent DFT study by Prestianni et al.[25] indicated a concerted E2 β-elimination mechanism for the dehydration of 2-propanol on H-ZSM-5 and H-Y zeolite.

Owing to the disparity in the available literature regarding the underlying reaction mechanism, it is imperative to carry out a detailed investigation of possible reaction mechanisms. Herein, we present a DFT study of possible reaction mechanisms for 1-butanol dehydration in H-ZSM-5 zeolite. A comprehensive investigation of the effect of reaction conditions on the reaction rates and product selectivity is done using a reaction path analysis. Our study clearly elicits that the dominant reaction mechanism is strongly dependent on the reaction conditions.

2.2. Theory

2.2.1. Catalyst model

An orthorhombic H-ZSM-5 framework structure (*Pnma* symmetry, unit cell – $HAlSi_{95}O_{192}$) was used for the studies. The zeolite acid site was created by replacing a Si atom with an Al atom and adding a proton to the adjacent oxygen atom. The MFI orthorhombic unit cell has twelve different tetrahedral sites and the replacement of a Si atom requires selection of an appropriate site. The location of the Al atom in the unit cell was reported to be non-random[26] and to depend on the zeolite synthesis conditions[27]. Nevertheless, few other studies specify the T12 site to be a preferred location for the Al atom associated with the Brønsted acid site[28,29]. Moreover, when the Al atom is located at the T12 site, the Brønsted acid site is accessible to molecules located in both the straight and sinusoidal channels and could accommodate larger species. Accordingly, the T12 tetrahedral site was selected for the replacement of a Si atom with Al.

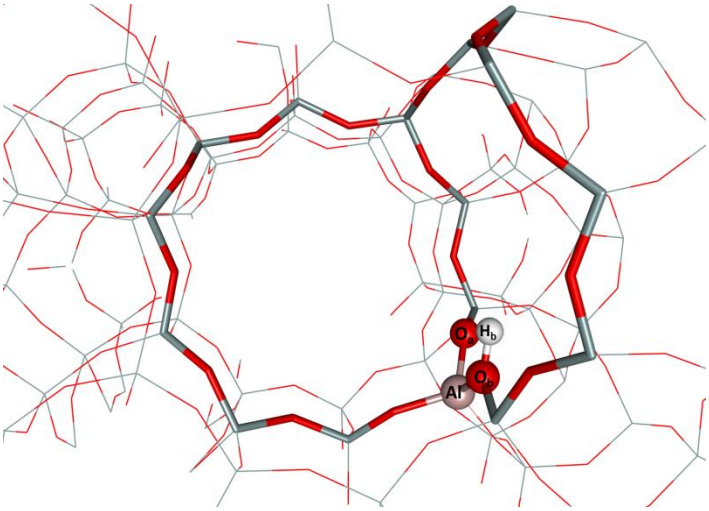

Figure 1. Location of the Brønsted acid site in the unit cell of the H-ZSM-5 structure.

Likewise, for the positioning of the proton one needs to select one of the oxygen atoms bound to the Al atom. The study by Svelle et al.[30] has shown that the proton prefers the oxygen atom (O_b) adjacent to the channel intersection rather than the oxygen atom (O_a) at the channel

intersection. Accordingly, the proton associated to the Brønsted acidity was placed at the oxygen atom (O_b) adjacent to the channel intersection as shown in Figure 1.

2.2.2. Computational details

2.2.2.1. Electronic energy calculations

Dispersion corrected periodic DFT calculations were performed with the Vienna Ab Initio Simulation Package (VASP) using plane wave basis sets[31-33]. The electron-ion interactions were described using the projector–augmented wave (PAW) method [34,35] with a plane-wave energy cut-off of 600 eV. The exchange correlation energies were calculated on the basis of the generalized gradient approximation (GGA) according to Perdew, Burke and Ernzerhof (PBE)[36]. Brillouin zone sampling was restricted to the Γ-point. A maximum force convergence criterion of 0.02 eV $Å^{-1}$ was used and each self-consistency loop was iterated until a convergence level of 10^{-8} eV was achieved. Dispersive corrections for the van der Waals interactions were included by adding a pairwise interaction term to the Kohn–Sham energy using the DFT-D2 approach proposed by Grimme[37] and extended by Kerber et al. [38] for periodic PBE calculations. Although systematic deviations may be observed due to the overestimation of the dispersion interaction [39-42], DFT-D2 has been widely applied for the theoretical investigation of adsorption [43-46] and reaction in zeolites [46,47] and is known to provide reasonably accurate results [40,48]. The electronic charge on atoms and fragments were calculated using Bader analysis [49] as implemented by Henkelman et al.[50]

Transition state search was performed using Nudged Elastic Band (NEB)[51] and dimer[52,53] calculations. The Nudged Elastic Band (NEB) method was used to find an initial guess for the minimal energy path (MEP), which was used as a starting point for the dimer calculations.

2.2.2.2. Frequency calculations

Normal mode analysis was performed using a Partial Hessian Vibrational Analysis (PHVA), relaxing the T5 cluster ($HAl(SiO_4)_4$) of the zeolite framework and the adsorbate molecule for the numerical Hessian calculation. Previous studies for physisorption and chemisorption in zeolite have shown that the partial hessian approach leads to a marginal difference in the result as compared to a Full Hessian Vibration Analysis (FHVA)[54]. Although very stringent optimization (maximum force criterion of 0.02 eV $Å^{-1}$) and electronic convergence (self-consistency loop convergence criterion of 10^{-8} eV and energy cut-off of 600 eV) criteria have been used, spurious imaginary frequencies were still present for very few cases, namely C4, TS-1, TS-6 and TS-9 attributed to loosely bonded species present in these complexes.

The low lying frequencies (<50 cm^{-1}) associated with the frustrated motions of the surface bound species (such as translation or rotation of the molecule within the zeolite pore structure) could lead to significant error in the entropy calculations [55-58]. A more accurate estimation of the entropic contributions could be obtained by accounting for anharmonicities by detailed scanning of the potential energy surface [59,60], but this would require significant computational efforts for large systems. Another approach to treat the low lying modes is the use of a frequency cutoff [43,55,56,61]. De Moor et al.[61] studied the entropy contributions of these frequencies for alkanes and alkenes in FAU zeolite and suggested the replacement of these spurious frequencies with 50 cm^{-1}. Therefore, in order to obtain consistent results, the spurious imaginary frequencies and low-lying frequencies were replaced by normal modes of 50 cm^{-1}. [61]

2.2.2.3. Statistical thermodynamics

Standard enthalpies, entropies, Gibbs free energies, adsorption and reaction equilibrium coefficients (K) are obtained from total partition functions by statistical thermodynamics calculations [62].

Reaction equilibrium coefficients, *K*, for elementary reactions are calculated as:

$$K(T) = \frac{\prod_i Q_i(N,V,T)}{\prod_j Q_j(N,V,T)} \exp\left(-\frac{\Delta E_r}{RT}\right) \qquad (1)$$

where *i* and *j* denote products and reactants respectively. ΔE_r is the change in electronic energy at 0 K (including the zero-point vibrational energy) of the reaction and *Q* the total partition function. The electronic energy from the DFT calculation along with the frequencies obtained from the vibrational analysis are used for the statistical thermodynamic calculation (see Appendix A). The partition functions for the gas-phase species included vibrational, rotational and translational degrees of freedom, while only the vibrational contributions were taken into account for the surface species.

The reaction rate coefficients of elementary reaction steps are calculated on the basis of transition state theory:

$$k_{TST}(T) = \frac{k_B T}{h} \frac{Q_{TS}(N,V,T)}{Q_R(N,V,T)} \exp\left(-\frac{E^{\ddagger}}{RT}\right) \qquad (2)$$

where k_B is Boltzmann constant, *h* is Planck constant and $E^{\ddagger}$ is the electronic activation barrier at 0 K (including the zero-point vibrational energy). Q_{TS} and Q_R denote the total partition functions of the transition and reactant state respectively. Arrhenius pre-exponential factors (*A*) and activation energies (E_a) are obtained by regression of Eq. 2 in the temperature range of 300 – 800 K.

The adsorption occurs without any activation barrier. Hence, the reaction rate coefficient for the adsorption step is calculated as $k_{ads} = k_B T/h$, while the reaction rate coefficient for the desorption step is calculated from thermodynamic consistency as $k_{des} = k_{ads}/K_{ads}$.

2.2.3. Microkinetic model

A microkinetic modelling approach has been used to carry out reaction path analysis and to study the effect of reaction conditions (temperature, site time and pressure). Here in, an isothermal plug flow reactor model was used for the reactor simulations. The following continuity equations were applied for the gas-phase components *i* and surface species *k* along with a site balance:

$$\frac{d\theta_k}{dt} = \sum_j \nu_{jk} TOF_j = 0 \qquad (3)$$

$$\theta_* + \sum_k \theta_k = 1 \qquad (4)$$

$$\frac{dF_i}{dW} = R_i = C_t \sum_j \nu_{ji} TOF_j \qquad (5)$$

with $F_i = F_{i,0}$ at $W = 0$

where TOF_j is the turnover frequency of elementary step *j* (mol mol_{H+}^{-1} s^{-1}), ν_{ji} the stoichiometric coefficient of component *i* in the elementary step *j*, θ_k the fractional coverage of surface species *k* (mol mol_{H+}^{-1}), θ_* the fractional coverage of free acid sites (mol mol_{H+}^{-1}), C_t the acid site concentration (mol_{H+} kg^{-1}), F_i the molar flow rate of gas-phase component *i* (mol s^{-1}), *W* the mass of the catalyst (kg), R_i the net production rate of gas-phase species *i* (mol kg^{-1} s^{-1}).

The microkinetic model assumes absence of any diffusion limitation for reactant and product species. The above mentioned set of ordinary differential equations is integrated using the

LSODA module of ODEPACK[63]. The steady state solution for coverages of surface species were obtained transiently by solving the differential equations of Eq. (3) till steady state is reached. The investigated reaction conditions are partial pressure of 1-butanol (0.01-100 kPa) and water (0-40 kPa), site time ($N_{H+}/F_{BuOH,0}$ = 0-200 mol H+ s / mol $BuOH_0$) and reaction temperature (400-460 K).

2.3. Results and discussion

2.3.1. Adsorption of 1-butanol in H-ZSM-5

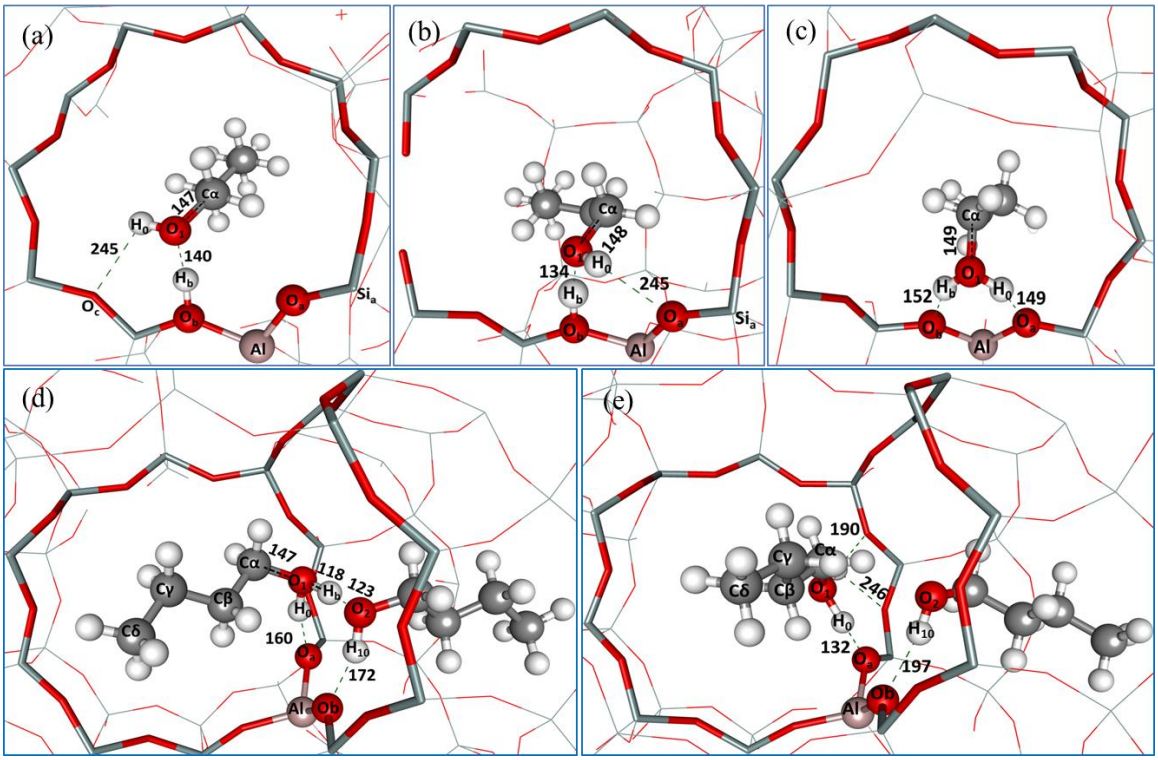

Figure 2. Adsorbed forms of 1-butanol in H-ZSM-5. (a) P1-physisorbed butanol configuration 1, (b) P2-physisorbed butanol configuration 2, (c) M1-protonated monomer, (d) D1-protonated dimer, (e) D2-protonated monomer next to physisorbed butanol. Color code: silicon-light blue, aluminum-pink, oxygen-red, hydrogen-white, carbon-grey, hydrogen bonds (distance < 250)

The adsorption of the 1-butanol molecule on the Brønsted acid site at the intersection of the channels is studied first. The butanol molecule can be adsorbed either in the straight or in the

sinusoidal channel of the H-ZSM-5 framework. Previous theoretical studies on physisorption and protonation of alcohols in H-ZSM-5 have shown that there is no energetic preference for adsorption of 1-butanol in the straight or sinusoidal channel of the zeolite[44,45]. Herein, for the adsorption of a single molecule of 1-butanol, the molecule is considered to be situated in the straight channel, while the second molecule is adsorbed in the sinusoidal channel. Representative physisorbed and protonated states for 1-butanol in H-ZSM-5 zeolite are depicted in Figure 2. The geometrical parameters and Bader charges (of the butanol molecule and the protonated butanol fragment) for the different adsorbed forms of 1-butanol are summarized in Table S1.

2.3.1.1. Physisorbed 1-butanol

During physisorption, the oxygen atom of the butanol molecule readily forms a strong hydrogen bond with the Brønsted acid site of the zeolite. As illustrated in Figure 2, depending on the orientation of the adsorbed molecule, it can form a second hydrogen bond with the oxygen (O_c) bridging two silica atoms, forming P1 or with the oxygen atom adjacent to the Al atom (O_a), forming P2. The standard adsorption enthalpy/entropy and adsorption equilibrium coefficients are reported in Table 1. The standard adsorption enthalpy for P2 is marginally higher than that of P1. Both P1 and P2 have similar values for adsorption entropy. According to the Bader analysis, the butanol fragment of P1 has a total charge of +0.11 as compared to +0.12 for P2. This can be rationalized on the basis of a strong hydrogen bond (bond length 133.8 pm) between the oxygen atom of butanol (O_1) and the zeolite proton (H_b) in P2, giving it partial characteristics of the protonated species as seen in the next section. On the other hand, a relatively weaker interaction of the alcohol with the zeolite Brønsted acid site leads to a lower partial charge on butanol in the P1 monomer. These results for physisorption are also in line with previous studies by Nguyen et al. [44,45].

Table 1. Thermodynamics for the adsorbed monomer and dimer forms of 1-butanol in H-ZSM-5 zeolite. ΔE_{DFT} - electronic adsorption energy at 0 K (kJ/mol), ΔE_D - dispersive contribution to adsorption energy (kJ/mol), ΔE_{DFT-D} - DFT-D adsorption energy at 0 K (kJ/mol), standard adsorption enthalpy (ΔH^o_{ads} in kJ/mol), adsorption entropy (ΔS^o_{ads} in J/mol/K), and equilibrium coefficient at 400K (K_{ads}^{400K} in 10^{-2} kPa^{-1} and 10^{-4} kPa^{-2} for the adsorption of one and two molecules of butanol, respectively)

	ΔE_{DFT}	ΔE_D	ΔE_{DFT-D}	ΔH^o_{ads}	ΔS^o_{ads}	K_{ads}^{400K}
P1	-70	-65	-135	-130	-178	$5.3\ 10^7$
P2	-65	-70	-135	-132	-178	$8.4\ 10^7$
M1	-77	-72	-149	-146	-192	$1.1\ 10^9$
D1	-110	-173	-283	-272	-375	$8.0\ 10^{15}$
D2	-87	-154	-241	-229	-378	$1.4\ 10^{10}$

2.3.1.2. Protonated 1-butanol

The protonation of the butanol molecule on the Brønsted acid site of the zeolite is a key step in the butanol dehydration reaction. The monomeric protonated form, M1, is hydrogen bonded to two zeolite oxygen atoms which are adjacent to the Al atom. This is a highly exothermic adsorption with a standard adsorption enthalpy (ΔH^o_{ads}) of -146 kJ/mol. The adsorption equilibrium coefficient (K_{ads}) at 400K for M1 is an order of magnitude higher than that for the physisorbed forms (P1 and P2). However, as seen from the Figure S1 of Appendix A the difference in stability of physisorbed and protonated monomer is somewhat more pronounced when using DFT-D2 as compared to vdW-DF2. The influences of electronic and dispersive forces along with enthalpy and entropy contributions for the adsorption of the butanol molecule are tabulated in Table 1. A significant contribution of dispersive forces in the stabilization of the adsorbed butoxonium is observed. The Bader charge on the protonated alcohol is found to be +0.77, with an equivalent negative charge on

the deprotonated zeolite framework. A stabilization effect by this ion pair interaction is thus observed in this study. These results are consistent with previous studies.[44,45]

Our results show that there is an elongation of the C_α - O_1 bond distance from 143.8 to 148.8 pm. The protonation of the alcohol molecule weakens the strength of the C-O bond and facilitates the heterolytic cleavage of the C-O bond. Similar results have been reported for alkyl halides (R-X), where the protonation was found to favor the heterolytic scission of the C-X bond[64]. As inferred by the elongation of the C-O bond, the protonated alcohol molecule is a more suitable candidate for the elimination and substitution reactions that follow.

2.3.1.3. Adsorbed butanol dimer

If a second 1-butanol molecule is adsorbed at the sinusoidal channel, there is a complete abstraction of the zeolite proton, which is shared by the two butanol molecules. This adsorption is also highly exothermic (ΔH^o_{ads} = -272 kJ/mol) and leads to the formation of the dimer D1, stabilized by strong hydrogen bonds between the two molecules and with the zeolite surface. The strong binding with the zeolite surface leads to a significant entropy loss (ΔS^o_{ads} = -375 J/mol/K). The formation of such stable dimer intermediates on Brønsted acid sites has been reported by Macht et al. [20,23,24]. As illustrated in Figure 2, the dimer D1 can undergo a re-arrangement via cleavage of the hydrogen bond between the protonated alcohol and the butanol molecule to form a thermodynamically less favorable configuration, D2 (see Table 1). A significant fraction of the overall adsorption energy comes from the dispersive contribution, since the bulky dimer molecules (D1 & D2) feel a large dispersive stabilization. A comparison can be made based on the energetics of the different species reported in Table 1. The dimer D1 has an adsorption equilibrium coefficient which is a few orders of magnitude higher than all the other adsorbed reactant species ($K_{adsD1} >> K_{adsD2} \sim K_{adsM1} > K_{adsP2} \sim K_{adsP1}$).

2.3.2. Reaction pathways for 1-butanol dehydration in H-ZSM-5

The adsorbed 1-butanol molecule can undergo a direct dehydration reaction producing 1-butene (path A) or react in a sequential manner to yield di-1-butyl ether (path B) which can further decompose to 1-butene and 1-butanol (path C) as shown in Figure 3.

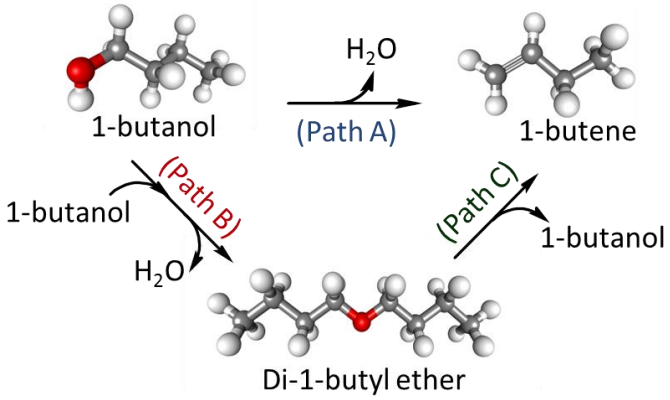

Figure 3. Reaction scheme for dehydration of 1-butanol to 1-butene (path A), dehydration of 1-butanol to di-1-butyl ether (path B) and ether decomposition (path C).

An overview of the reaction network consisting of all the elementary steps considered for the dehydration of butanol in H-ZSM-5 zeolite is depicted in Figure 4. This reaction network consists of 10 different mechanisms that are involved in the aforementioned three reaction pathways as shown in Table 2. A detailed electron flow diagram for each mechanism is shown in Figure S2 of Appendix A. A brief definition of the investigated elimination and substitution mechanisms is available in Appendix A. Any further reference to a specific reaction step of the network is done as per the numbering used in Figure 4. The standard reaction enthalpy (ΔH_r^o), reaction entropy (ΔS_r^o), Arrhenius activation energies and pre-exponential factors, forward reaction rate coefficients and equilibrium coefficients for each elementary step are tabulated in Table 3, while the corresponding reaction energies and activation barriers at 0K are reported in Table S4 of Appendix A.

.

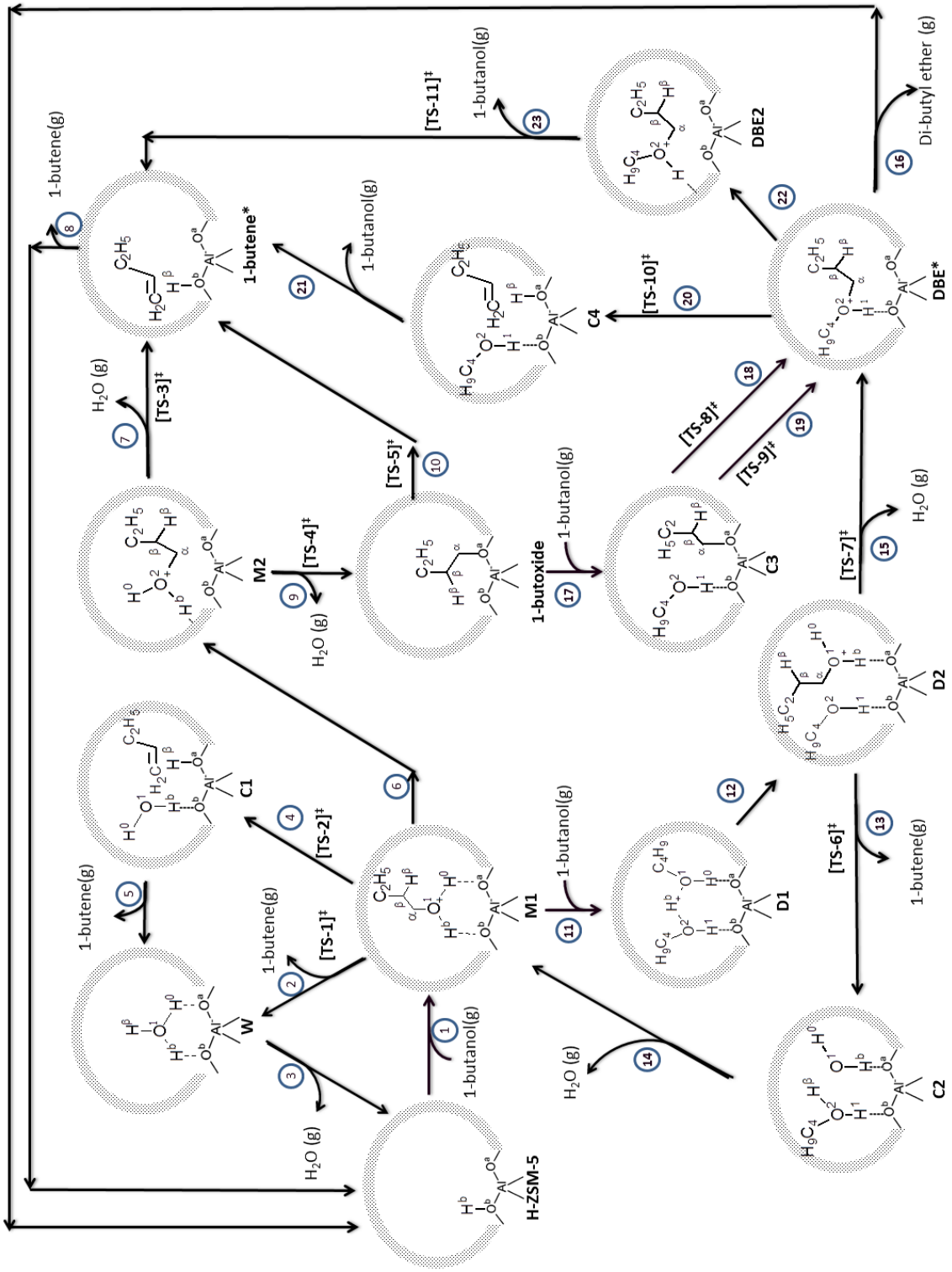

Figure 4. Detailed reaction network for dehydration of butanol in H-ZSM-5

Table 2. Elementary steps and reaction mechanisms for the butanol dehydration reaction. Non-equilibrated steps are indicated with bold stoichiometric numbers.

		Path A					**Path B**			**Path C**	
	Mechanism #	*1*	*2*	*3*	*4*	*5*	*6*	*7*	*8*	*9*	*10*
1	1-BuOH(g) + ∗ ↔ M1	1	1	1	1	0	1	1	1	0	0
2	M1 ↔ W + 1-Butene$_{(g)}$	**1**	0	0	0	0	0	0	0	0	0
3	W ↔ H2O(g) + *	1	1	0	0	0	0	0	0	0	0
4	M1 ↔ C1	0	**1**	0	0	0	0	0	0	0	0
5	C1 ↔ W + 1-Butene$_{(g)}$	0	1	0	0	0	0	0	0	0	0
6	M1 ↔ M2	0	0	1	1	0	0	1	1	0	0
7	M2↔ 1-Butene*+ H2O$_{(g)}$	0	0	**1**	0	0	0	0	0	0	0
8	1-Butene* ↔ 1-Butene$_{(g)}$+ ∗	0	0	1	1	0	0	1	1	1	1
9	M2↔ Butoxy + H2O$_{(g)}$	0	0	0	**1**	0	0	**1**	**1**	0	0
10	Butoxy ↔ 1-Butene*	0	0	0	**1**	0	0	0	0	0	0
11	M1 + BuOH$_{(g)}$↔ D1	0	0	0	0	1	1	0	0	0	0
12	D1 ↔ D2	0	0	0	0	1	1	0	0	0	0
13	D2↔ C2+1-Butene$_{(g)}$	0	0	0	0	**1**	0	0	0	0	0
14	C2 ↔ M1 + H2O$_{(g)}$	0	0	0	0	1	0	0	0	0	0
15	D2 ↔ DBE* + H2O$_{(g)}$	0	0	0	0	0	**1**	0	0	0	0
16	DBE* ↔ DBE$_{(g)}$+ ∗	0	0	0	0	0	1	1	1	-1	-1
17	Butoxy + BuOH$_{(g)}$↔ C3	0	0	0	0	0	0	1	1	0	0
18	C3↔ DBE* (S_N2)	0	0	0	0	0	0	**1**	0	0	0
19	C3↔ DBE* (S_N1)	0	0	0	0	0	0	0	**1**	0	0
20	DBE* ↔ C4	0	0	0	0	0	0	0	0	**1**	0
21	C4 ↔ 1-Butene*+ BuOH$_{(g)}$	0	0	0	0	0	0	0	0	1	0
22	DBE* ↔ DBE2	0	0	0	0	0	0	0	0	0	1
23	DBE2↔ 1-Butene*+ BuOH$_{(g)}$	0	0	0	0	0	0	0	0	0	**1**

Path A	(mechanism # *1-5*)	**1-BuOH$_{(g)}$ ↔ 1-Butene$_{(g)}$+H2O$_{(g)}$**
Path B	(mechanism # *6-8*)	**1-BuOH$_{(g)}$+1-BuOH$_{(g)}$ ↔ DBE$_{(g)}$+H2O$_{(g)}$**
Path C	(mechanism # *9-10*)	**DBE$_{(g)}$ ↔ 1-Butene$_{(g)}$+1-BuOH$_{(g)}$**

Table 3. Standard reaction enthalpy (kJ/mol), reaction entropy (J/mol/K), activation energy (kJ/mol), pre-exponential factor (s^{-1}), forward reaction rate coefficient k_f (s^{-1}) at 400K and equilibrium coefficient at 400K (10^{-2} kPa^{-1}, 10^{2} kPa or dimensionless for adsorption, desorption and surface transformation, respectively) for the elementary steps (numbered as indicated in Figure 4).

	Elementary steps	**ΔH_r^o**	**ΔS_r^o**	**$E_{a(f)}$**	**A_f**	**$k_{f\,(400K)}$**	**$K_{eq\,(400K)}$**
(R1)	1-$BuOH_{(g)}$ + ∗ ↔ M1	-146	-192	-	-	-	1.1 10^{9}
(R2)	M1 ↔ W + 1-$Butene_{(g)}$	107	200	176	1.1 10^{15}	1.1 10^{-8}	2.7 10^{-4}
(R3)	W ↔ $H_2O_{(g)}$ + ∗	85	150	-	-	-	5.0 10^{-4}
(R4)	M1 ↔ C1	74	78	139	2.9 10^{14}	1.9 10^{-4}	2.9 10^{-6}
(R5)	C1 ↔ W + 1-$Butene_{(g)}$	34	122	-	-	-	9.3 10^{1}
(R6)	M1 ↔ M2	82	-5	-	-	-	1.1 10^{-11}
(R7)	M2↔ 1-Butene*+ $H_2O_{(g)}$	28	199	53	9.0 10^{14}	1.2 10^{8}	5.7 10^{6}
(R8)	1-Butene* ↔ 1-$Butene_{(g)}$ + ∗	83	155	-	-	-	2.2 10^{-3}
(R9)	M2↔ Butoxy + $H_2O_{(g)}$	22	165	49	3.4 10^{14}	1.3 10^{8}	5.1 10^{5}
(R10)	Butoxy ↔ 1-Butene*	6	35	93	3.7 10^{13}	2.3 10^{1}	1.1 10^{1}
(R11)	M1 + $BuOH_{(g)}$ ↔ D1	-126	-183	-	-	-	7.4 10^{6}
(R12)	D1 ↔ D2	43	-3	-	-	-	1.7 10^{-6}
(R13)	D2 ↔ C2+1-$Butene_{(g)}$	69	165	118	2.8 10^{14}	9.8 10^{-2}	4.5 10^{-1}
(R14)	C2 ↔ M1 + $H_2O_{(g)}$	61	179	-	-	-	2.5 10^{1}
(R15)	D2 ↔ DBE* + $H_2O_{(g)}$	15	157	92	1.4 10^{14}	1.4 10^{2}	1.5 10^{6}
(R16)	DBE* ↔ $DBE_{(g)}$ + ∗	191	209	-	-	-	1.1 10^{-14}
(R17)	Butoxy + $BuOH_{(g)}$ ↔ C3	-95	-173	-	-	-	2.0 10^{3}
(R18)	C3↔ DBE* (S_N2)	-77	-16	61	3.1 10^{12}	3.4 10^{4}	1.8 10^{9}
(R19)	C3↔ DBE* (S_N1)	-77	-16	111	9.2 10^{13}	2.8 10^{-2}	1.8 10^{9}
(R20)	DBE* ↔ C4	102	51	140	2.5 10^{14}	1.3 10^{-4}	2.2 10^{-11}
(R21)	C4 ↔ 1-Butene*+ $BuOH_{(g)}$	76	173	-	-	-	1.4 10^{-1}
(R22)	DBE* ↔ DBE2	63	9	-	-	-	1.9 10^{-8}
(R23)	DBE2↔1-Butene*+ $BuOH_{(g)}$	115	215	84	1.6 10^{13}	3.0 10^{-6}	3.1 10^{-12}

2.3.2.1. Path A: dehydration of 1-butanol to 1-butene

Five different reaction mechanisms are considered for the direct conversion of 1-butanol to 1-butene in H-ZSM-5, of which four are monomolecular and one is bi-molecular. The reaction mechanisms are classified based on the geometric and electronic features of the transition state intermediate. The transition state structures for the different reaction mechanisms associated with the direct dehydration of 1-butanol to 1-butene are shown in Figure 5.

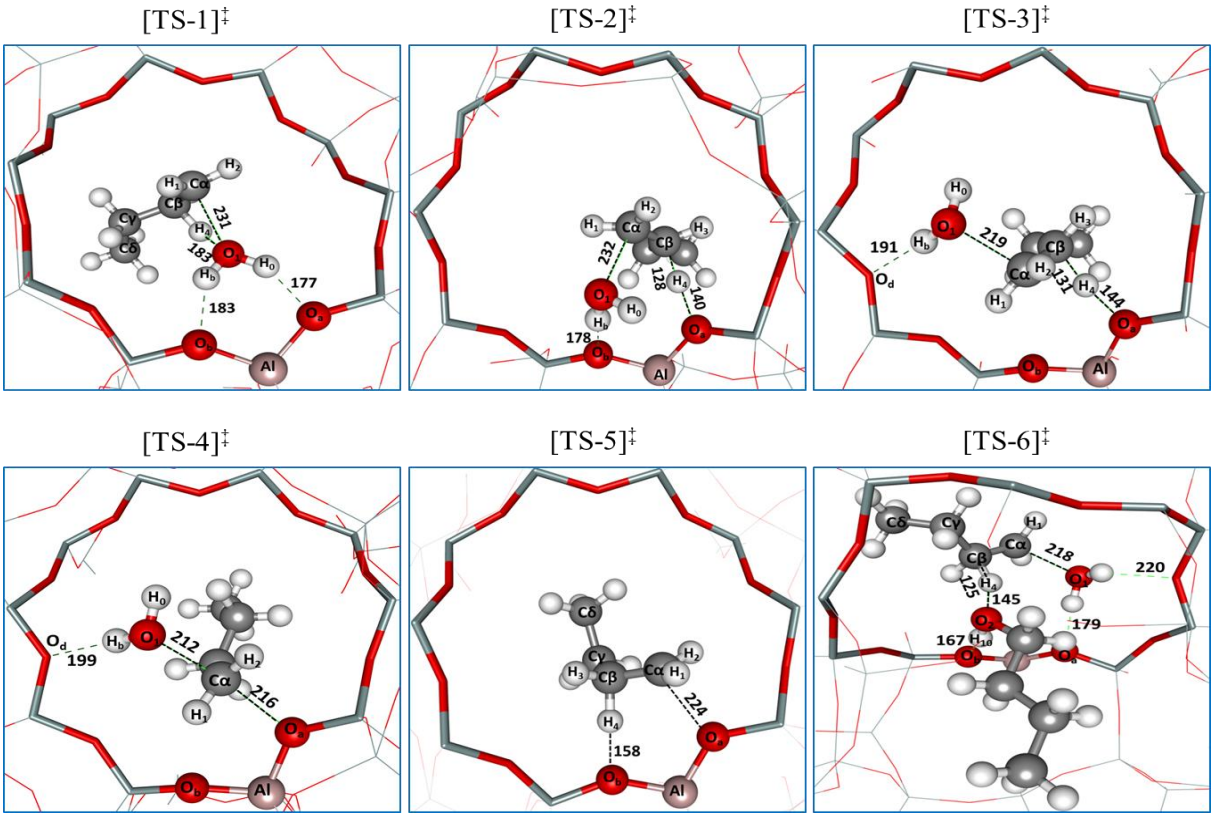

Figure 5. Transition state structures (views along the sinusoidal channel) for 1-butanol dehydration to 1-butene (path A): 1) TS-1, 4-ring E1-like transition state 2) TS-2, syn–elimination 3) TS-3, E-2 (anti) elimination 4) TS-4, S_N2 substitution 5) TS-5, deprotonation/decomposition of 1-butoxide 6) TS-6, butanol assisted syn elimination . Color code: silicon – light blue, aluminum – pink, oxygen – red, hydrogen – white, carbon – grey, hydrogen bonds – green dashed lines, bond breaking/forming – black dashed lines. Important interatomic distances are shown in pm.

Reaction mechanism 1 (E1-like): This mechanism consists of the sequence of elementary steps 1, 2 and 3 as illustrated in Figure 4. In step 2, the crucial step of the mechanism, the

adsorbed monomer M1 undergoes a heterolytic cleavage of the C-O bond forming a 4-ring (O_1-C_α-C_β-H_4) transition state (TS-1), involving a carbenium ion like [C4H9] fragment and a water molecule (see TS-1, Figure 5). Both hydrogen atoms of the water molecule are hydrogen bonded to the zeolite oxygen atoms (O_a and O_b) adjacent to the Al atom. Meanwhile the atom (O_1) of the adsorbed water molecule attacks the β-hydrogen (H_4) of the C_4H_9 fragment leading to the formation of a physisorbed 1-butene and an adsorbed hydronium ion (W). Thereafter, the butene molecule desorbs leaving the adsorbed hydronium ion. The hydronium undergoes deprotonation and the desorption of a water molecule regenerates the zeolite Brønsted acid site. The step leading to the formation of butene and hydronium from M1 is an activated process with an activation energy of 176 kJ/mol.

In the transition state (TS-1, Figure 5) geometry, C_α-O_1 and C_β-H_4 bond lengths are 231 and 118 pm, respectively. Herein, the C-O bond is completely broken while the C_β- H_4 still remains intact indicating an E1-like mechanism. Although a carbenium ion like TS is observed, formation of a stable carbocation intermediate characteristic of a pure E1 mechanism is not observed. This can be attributed to the high reactivity of the primary carbocation. Overall, a late transition state is evident from the fact that the geometric configuration (e.g. extent of C_α-O_1 bond breakage and other bond distances/angles) of the transition state is much closer to the product (see Appendix A, Table S2).

Further insight into the nature of the transition state was obtained via a Bader charge analysis. The Bader charge for the [C4H9] fragment and the water molecule were found to be +0.80 and +0.07 respectively, while the zeolite framework had an overall charge of -0.87. The charge on the [C4H9] fragment is comparable with the one reported for the cationic fragment (+0.85) in a DFT study on E1 elimination of 2-butanol in POM.[23]

Reaction mechanism 2 (syn-elimination): This dehydration mechanism consists of steps 1, 4, 5 and 3 as illustrated in Figure 4. The formation of adsorbed monomer M1 (step 1) is followed by an activated step (step 4), involving a concerted mechanism, wherein there is a simultaneous cleavage of the C_α-O_1 bond along with an abstraction of the β-hydrogen by the zeolite basic oxygen (O_a). For this concerted reaction to occur, the M1 monomer has to reorient itself by breaking the H_0-O_a hydrogen bond and aligning the β-hydrogen towards O_a (NEB shown in Appendix A, Figure S4). The simultaneous cleavage of C_α-O_1 and C_β-H_4 (step 4) has an activation energy of 139 kJ/mol. This step is followed by a subsequent desorption of 1-butene (step 5) and water (step 3) respectively.

In the transition state (TS-2, Figure 5) structure, the β-hydrogen (H_4) and the leaving group (water) have a near syn-coplanar configuration with a O_1-C_α-C_β-H_4 dihedral angle of 17.3°. The α- and β-carbon have a near planar configuration with the α-carbon being closer to planarity than the β-carbon (see Appendix A, Table S2). The extent of C_α-O_1 bond breakage is found to be more prominent as compared to that of the C_β-H_4 cleavage. As described above, the protonation of butanol to form the adsorbed monomer M1 leads to an elongation of the C-O bond making it easier to break the C-O bond as compared to the C-H bond and this gives the mechanism an E1-like character.

The total Bader charge on the [C4H9] fragment is +0.67, but the major fraction of this charge is associated with the β-hydrogen (+0.39) which has nearly broken its bond with the β-carbon (C_β). Moreover, the formal charge on the [C4H9] fragment is much lower than the literature reported values for an E1-type mechanism [23]. Thus, the results of the Bader analysis confirm that although the TS has some E1 character, it essentially represents a one step 1,2-syn-elimination reaction.

Reaction mechanism 3 (E2 elimination): This dehydration mechanism consists of steps 1, 6, 7 and 8. It occurs via an E2-type elimination that requires the atoms or groups involved in the reaction to be in the same plane, with antiperiplanar orientation of the leaving group and the β-hydrogen. To achieve this configuration, the protonated monomer (M1) undergoes a re-orientation (step 6), breaking two strong hydrogen bonds and forming a new weaker hydrogen bond with the oxygen atom (O_d) bridged between two Si atoms, to form a loosely adsorbed monomer M2, having the required antiperiplanar configuration. The M2 monomer has a higher positive formal charge of +0.86 as compared to +0.77 for the protonated M1 monomer, indicating that the zeolite proton is more strongly associated to the M2 monomer. On rearrangement to M2, the C-O bond distance is elongated to 154 pm as compared to 149 pm for M1 facilitating the removal of the -OH2 species. M2 is less stable as compared to M1 with a free energy difference of ~80 kJ/mol. Thus, M2 represents a high energy metastable intermediate that fulfills the stereochemistry required for the following elimination reaction.

The M2 monomer undergoes an elimination through a concerted mechanism (step 7), involving simultaneous cleavage of the C-O bond and abstraction of the β-hydrogen by the zeolite basic oxygen (O_a). This step is an activated process and has an activation energy of 53 and 135 kJ/mol, considering M2 and M1 as reference states, respectively. Due to the hydrogen abstraction, the zeolite regains its proton and the loosely bound water molecule desorbs leaving 1-butene physisorbed over the Brønsted acid site. Desorption of butene (step 8) regenerates the Brønsted acid site.

In the transition state (TS-3, Figure 5) geometry, the β-hydrogen (H_4) points towards the bridge oxygen atom (O_a) and the leaving –OH2 group is positioned opposite to it, making a dihedral angle (O_1-C_α-C_β-H_4) of 180.9°. Looking at the bond angles, it is evident that both the α- (C_α) and β-carbon (C_β) have a near planar configuration with the α-carbon being closer to planarity than the β-carbon (see Appendix A, Table S2). The C_α-O_1 and C_β -H_4 bond length in

the transition state are 223 and 130 pm respectively. The extent of C-O bond breakage is more pronounced than that of the β-carbon (C_β) and β-hydrogen (H_4). The E1 character in the transition state could be explained by the significant elongation of the C-O bond in the reactant M2, making it easier to break the C-O bond as compared to the C-H bond during the reaction step. TS-3 has a C_α-C_β bond distance of 138 pm, which is similar to that of the physisorbed 1-butene and indicates a late transition state. Thus, we can conclude that this mechanism follows a one step 1,2-anti-elimination (E2) reaction with E1 character.

Comparing anti- and syn-elimination (TS-3 vs TS-2), the β-carbon (C_β) is closer to planarity in the anti-elimination. The anti-elimination has an activation energy of 135 kJ/mol (with respect to M1) which is slightly lower than that for syn-elimination.

Reaction mechanism 4 (1-butanol to 1-butoxide via S_N2 *type reaction, followed by deprotonation to butene):* In this mechanism, the protonated alcohol undergoes a nucleophilic substitution with the zeolite oxygen atom (O_a) to form 1-butoxide, which then undergoes deprotonation to give 1-butene. The mechanism involves a sequence of elementary steps 1, 6, 9, 10 and 8, of which two steps (9 and 10) are activated. The S_N2-type substitution reaction has also specific stereochemical requirements as was the case for the E2 anti-elimination reaction. Moreover, it requires simultaneous bond breaking (i.e. C-OH2 bond of the protonated alcohol) and bond forming (between C_α and O_a of zeolite). The formation of the new bond eases the breaking of the existing bond. To minimize the repulsion of the electronic clouds of the approaching and departing species, the nucleophile (O_a) and the leaving group (-OH2) should align themselves in a direction opposite to each other (dihedral angle close to 180^o) forming a trigonal bi-pyramidal structure. The M2 monomer described earlier meets these stereochemical requirements associated with the S_N2 back-side attack.

In this mechanism, M1 rearranges to M2 (step 6), which then undergoes a nucleophilic substitution reaction to form a surface bound 1-butoxide (step 9). Herein, the basic oxygen (O_a) of the zeolite surface acts as a nucleophile and attacks the primary carbon (C_α). The primary carbon atom C_α breaks its bond with the leaving group (-OH2) and concurrently forms a new C_α-O_a bond with the zeolite surface. A detailed analysis of the transition state structure (TS-4, Figure 5) reveals that the C_α carbon atom is equidistant from O_1 and O_a and assumes a penta-coordinated trigonal bi-pyramidal state, characteristic of a S_N2-type substitution reaction.

In the subsequent step (step10), the 1-butoxide undergoes a de-protonation reaction, in which the zeolite oxygen atom (O_b) attacks the β-hydrogen (H_4), while the primary carbon atom breaks its bond with the zeolite oxygen (O_a). There is a simultaneous elongation and cleavage of the C_α-O_a and C_β-H_4 bond. In the transition state geometry (TS-5, Figure 4), the α- and β-carbon have a near-planar configuration with the α-carbon being closer to planarity than the β-carbon. The C_α-O_a and C_β-H_4 bond length in the transition state are 224 and 119 pm respectively. Again, a late transition state is evident, as the TS structure is close to the product rather than the reactant (see Appendix A, Table S2).

The Bader charge analysis for TS-4 and TS-5 shows a cationic nature of the transition state fragments. The Bader charge analysis allocated a total charge of +0.76 on the [C4H9-H2O] fragment of the TS-4 transition state, with the [C4H9] fragment and [H2O] fragment having Bader charges of +0.64 and +0.12 respectively. The charge on the [C4H9] fragment of TS-5 is +0.6916, but the major fraction of this charge is associated with the β–hydrogen (+0.32). The large positive charge on the β–hydrogen atom (H_4) is associated with the elongation of the C_β-H_4 bond and the formation of a new bond of β-hydrogen (H_4) with the zeolitic oxygen (O_b).

Reaction mechanism 5 (butanol-assisted syn-elimination):

In this mechanism, the adsorption of another butanol molecule on the protonated M1 (step 11) leads to formation of an adsorbed butanol dimer D1, which undergoes a reorientation (step 12) to form D2. This is followed by an activated elimination reaction with desorption of 1-butene (step 13) and a subsequent water desorption (step 14). In step 13, the protonated alcohol of the reoriented adsorbed butanol dimer (D2) undergoes a concerted elimination reaction, similar to the monomolecular 1,2-syn-elimination reaction (reaction mechanism 2). Herein, the β-hydrogen abstraction is done by the oxygen atom (O_2) of the physisorbed butanol molecule instead of the basic zeolitic oxygen. This provides a bimolecular route for the production of butene without involving ether as an intermediate product.

In the transition state (TS-6, Figure 5) structure, the β-hydrogen (H_4) and the leaving group (water) have a syn-coplanar configuration with O_1-C_α-C_β-H_4 dihedral angle of 0.4°. The α- and β- carbon both have a near planar configuration with α-carbon being slightly more planar than the β-carbon (see Appendix A, Table S3). Here again, the extent of C-O bond (bond distance 218 pm) breakage is found to be more prominent as compared to that of the β-carbon and hydrogen cleavage (125.6 pm).

The physisorbed butanol and water molecule have a minor charge of +0.12 and +0.08 respectively, while the zeolite framework has a charge of -0.86. The charge on the [C4H9] fragment is +0.66, but a major fraction of this charge is associated with the β–hydrogen (+0.37) which has nearly broken its bond with the β-carbon (C_β). Based on the geometrical aspects and results of the Bader charge analysis, one can conclude that the key step of this reaction mechanism follows a one step 1,2-syn-elimination with E1 character.

Comparison of the reaction mechanisms for the direct dehydration of 1-butanol to 1-butene

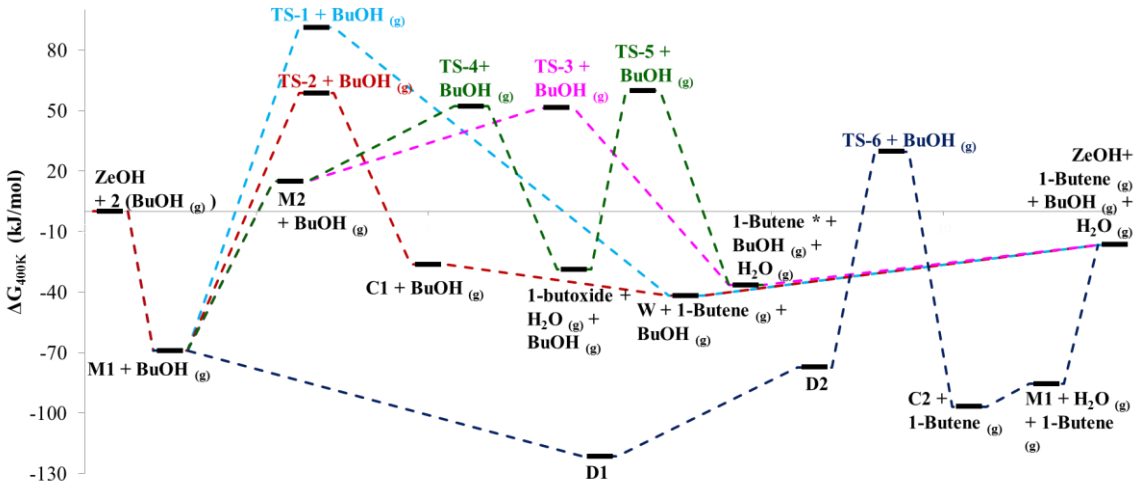

Figure 6. Gibbs Free Energy profile for different plausible mechanisms of the direct dehydration of 1-butanol to 1-butene in H-ZSM-5 at 400K.

The Gibbs free energy profile for the five different reaction mechanisms for the direct dehydration of 1-butanol to 1-butene (path A) at 400K is shown in Figure 6. The reaction mechanism having a 4-ring transition state (TS-1) with E1 character was found to have the highest free energy barrier. The 1,2-anti-elimination (TS-3) is seen to be favored over the 1,2-syn-elimination (TS-2) reaction. The reaction mechanism involving the butoxide intermediate has two transition states, namely TS-4 and TS-5. Here, the reaction of 1-butoxide to 1-butene via TS-5 has a slightly higher free energy barrier as compared to the reaction of the protonated butanol monomer (M2) to 1-butoxide via TS-4. With an increase in the temperature, the entropic contributions make significant changes to the Gibbs free energy profile and the free energy barrier at 500K becomes higher for TS-4 as compared to TS-5 (see Figure S5 of Appendix A). Amongst the monomolecular mechanisms for path A (i.e. mechanisms 1 to 4), the one step 1,2-anti-elimination via TS-3 provides the lowest free energy barriers with an apparent $\Delta G^{\ddagger}$ of 51 kJ/mol at 400K (with respect to the gas phase

butanol and the zeolite). The conversion of the butanol dimer D2 to C2 (co-adsorbed butanol and water) and gas-phase 1-butene provides a bimolecular mechanism for the direct dehydration of 1-butanol to 1-butene. This butanol-assisted syn-elimination reaction offered the lowest free energy barrier (apparent $\Delta G^{\ddagger}$ of 30 kJ/mol at 400K) as compared to all other path A mechanisms. It is pertinent to note that although the butanol-assisted syn-elimination offers a lower free energy barrier at 400K, it becomes less favorable with an increase in temperature (see Figure S5 of Appendix A).

For comparison with the experimental results of Makarova et al.[17], the activation energy for the activated steps was calculated with respect to the adsorbed state M1, since this is expected to be the most abundant reaction intermediate at the low pressure conditions used by Makarova et al.[17]. Relative to M1, the anti-elimination (via TS-3) has an activation energy ($E_{a,(TS3-M1)}$) of 135 kJ/mol, which is in rather good agreement with the experimentally reported value of 138 ± 8 kJ/mol [17].

2.3.2.2. Path B : Etherification reaction (dehydration of 1-butanol to di-1-butyl ether)

Makarova et al.[17] observed significant formation of di-1-butyl ether in their 1-butanol dehydration studies in H-ZSM-5. In view of this, three possible mechanisms for the conversion of 1-butanol to di-1-butyl ether have been envisaged. One mechanism proceeds via the dehydration of the butanol dimer while the other two mechanisms involve the reaction of physisorbed butanol with surface bound butoxide species. The transition state structures for the different reaction mechanisms associated with the dehydration of 1-butanol to di-1-butyl ether are shown in Figure 7.

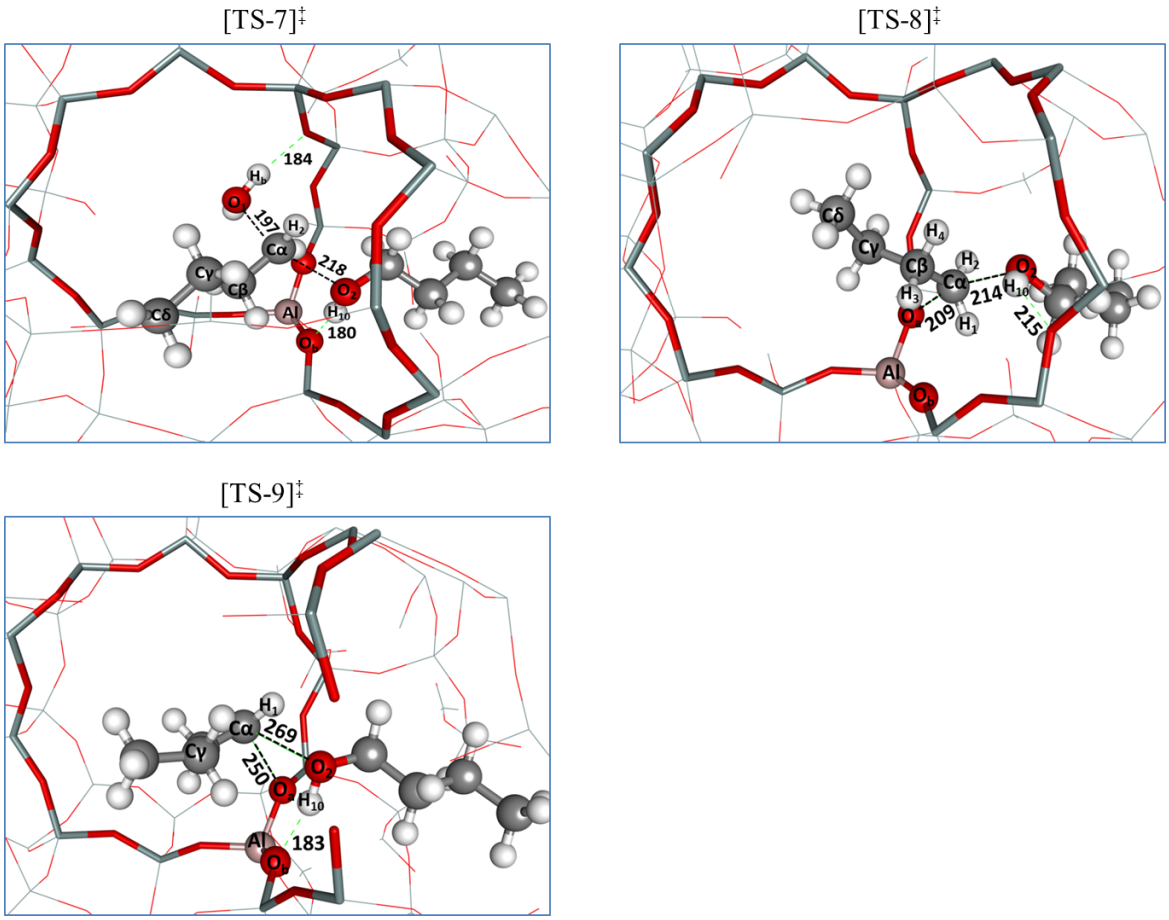

Figure 7. Transition state structures (views at the channel intersection) for the etherification reaction (path B): 1) TS-7, S_N2 substitution reaction (mechanism 6, 1-butanol dimer (D2) to di-1-butyl ether) 2) TS-8, S_N2 substitution reaction (mechanism 7, 1-butoxide and 1-butanol to dibutyl ether) 3) TS-9, S_N1 like substitution reaction (mechanism 8, 1-butoxide and 1-butanol to di-1-butyl ether) Color code: silicon - light blue, aluminum - pink, oxygen - red, hydrogen - white, carbon - grey, hydrogen bonds (distance < 250 pm) - green dashed lines, bond breaking/forming - black dashed lines.

Reaction mechanism 6 (butanol dimer to ether and water via S_N2 *type reaction)*: This reaction mechanism consists of a sequence of steps, namely, formation of adsorbed 1-butanol dimer D1 (step 11), reorientation of D1 to D2 (step 12), a nucleophilic substitution reaction leading to the formation of protonated ether (step 15) and the desorption of ether (step 16). In step 15, the protonated alcohol part of D2 undergoes a nucleophilic substitution of the -OH2 group with the physisorbed butanol molecule to form a protonated di-butyl ether and a water molecule. During this etherification reaction, the protonated alcohol breaks one of its H-bond (O_a-H_0) and reorients itself to place the α-carbon (C_α) between the oxygen atoms of the

leaving group (-OH2) and the physisorbed butanol molecule. This is an activated step and the transition state structure is shown in Figure 7 (TS-7).

The transition state (TS-7) has a trigonal bipyramidal configuration with the C_α carbon in a penta-coordinated state, which is characteristic of a S_N2-type substitution reaction. The β-carbon (C_β) remains in a tetrahedral state. The bond distance between C_α-O1 and C_α-O2 is 197 and 218 pm respectively with C_α placed near the center of O_1 and O_2. The O_1-C_α-O_2 angle for the transition state structure is 162.7°. This orientation of O_1-C_α-O_2 in the transition state largely depends on the stabilization of the leaving water molecule by hydrogen bonding with the zeolite oxygen.

The Bader charge on [H2O-C4H9-C4H9OH] is +0.88, with the [C4H9] fragment, the [H2O] molecule and the physisorbed alcohol having +0.58, +0.19 and +0.11 respectively. In case of a S_N1 kind of mechanism, we would have expected the net charge on the [C4H9] fragment to be comparable to its value for an E1 mechanism (i.e. +0.80, see mechanism 1). This further corroborates that the reaction step is following an S_N2 mechanism as inferred from the geometric conformation of the transition state.

Reaction mechanism 7 (formation of di-1-butyl ether from 1-butoxide and 1-butanol via S_N2 *type reaction):* 1-Butoxide produced as an intermediate in mechanism 4 (steps 1-6-9, via TS-4) can react with another butanol molecule leading to the formation of protonated ether (DBE*) and water. This reaction mechanism involves a sequence of elementary steps, namely, the physisorption of 1-butanol (step 17) alongside the surface bound butoxide species, the nucleophilic substitution reaction leading to the formation of protonated ether (step 18) and the deprotonation and desorption of di-1-butyl ether (step 16). In step 18, the oxygen atom (O_2) of butanol attacks the α-carbon atom (C_α) of the butoxide, which is accompanied by the concurrent cleavage of the C_α-O_a bond of the butoxide forming

protonated ether adsorbed on the zeolite. This is an activated step and the transition state (TS-8) geometrical parameters are tabulated in Table S3 of Appendix A.

In the transition state structure (TS-8, Figure 7), it is seen that the bond between C_α-O_a is elongated and C_α is placed near the center of O_2 and O_a. The bond distance between C_α-O_2 and C_α-O_a is 214.3 and 208.5 pm respectively. The α-carbon (C_α) acquires a trigonal bipyramidal structure which is characteristic of a S_N2-type substitution reaction while the β–carbon (C_β) remains in a tetrahedral state. The O_2-C_α-O_a angle in the transition state configuration is 160°. The Bader charge on the [C4H9-OH-C4H9] fragment is +0.75, with the [C4H9] fragment and the physisorbed alcohol having +0.59 and +0.16 respectively. The charge on the [C4H9] fragment is consistent with that of the S_N2 reaction (mechanism 6, step 15) for the conversion of D2 to protonated ether.

Reaction mechanism 8 (formation of di-1-butyl ether from 1-butoxide and 1-butanol via S_N1 *type reaction):* This reaction mechanism follows a sequence of elementary steps similar to that of mechanism 7, except that the back side S_N2 nucleophilic substitution (step 18) is replaced by a S_N1 like substitution reaction (step 19). Herein, the reaction proceeds via the heterolytic cleavage of the C_α-O_a bond leading to the formation of a carbenium ion like C4H9 fragment which undergoes a nucleophilic attack by the oxygen atom (O_2) of the butanol. However, as seen from Table 3, the activated step 19 has a significantly higher activation energy compared to step 18 of the S_N2 mechanism 7.

In the transition state structure (TS-9, Figure 7), it is seen that the bond between C_α-O_2 is not formed yet with an interatomic distance of 269 pm, while the C_α-O_a bond is already broken (C_α-O_a = 250 pm). Herein, the [C4H9] fragment is stabilized via hydrogen bonds formed by α-hydrogen atoms (H_1 and H_2) with the oxygen atoms of the physisorbed alcohol (O_2) and the zeolite framework (O_a) respectively. The results of the Bader charge analysis indicate a higher

positive charge of +0.71 on the [C4H9] fragment as compared to +0.59 for the S_N2 mechanism 7. The presence of a carbenium-like fragment, having a pronounced positive charge, is indicative of a S_N1-like mechanism.

Comparison of the reaction mechanisms for the etherification reaction of 1-butanol

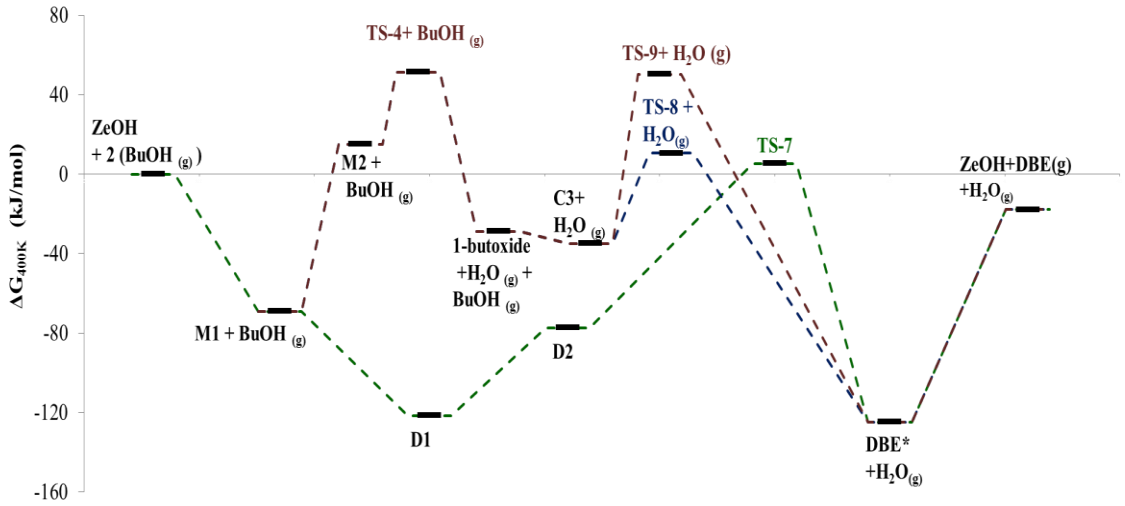

Figure 8. Gibbs Free Energy profile for the dehydration of 1-butanol to dibutyl ether (DBE) in H-ZSM-5 at 400K.

The Gibbs free energy profile for the three different mechanisms of the dehydration of 1-butanol to dibutyl ether (path B) is shown in Figure 8. Amongst the three plausible mechanisms, the conversion of the dimer D2 to protonated di-1-butyl ether and water via a S_N2 reaction (TS-7) offered the lowest free energy barrier with an apparent $\Delta G^{\ddagger}$ of 5 kJ/mol at 400Kwith respect to the gas phase butanol and the zeolite). The energetic preference for the dimer mediated route over the alkoxide mediated route for ether formation reaction, has also been reported for dehydration of methanol [65,66] and ethanol [67] in zeolites. The free energy diagram suggests that the conversion of monomer M2 to 1-butoxide (via S_N2 substitution reaction, TS-4) having the highest apparent free energy barrier, would be critical for the butoxide-mediated conversion of alcohol to ether (mechanism 7 and 8). For the further conversion of 1–butoxide to ether, the S_N2 type nucleophilic substitution (via TS-8) offers a

much lower free energy barrier as compared to the S_N1 like nucleophilic substitution (via TS-9). The protonated ether molecule that is formed can either undergo further reaction (see path C) or get deprotonated and desorb. Although, the desorption of ether is highly endothermic (ΔH^o = 191 kJ/mol), the overall conversion of two molecules of 1-butanol to ether and water is exothermic and hence, should be favored at low temperatures.

2.3.2.3. Path C: Decomposition of di-1-butyl ether to 1-butene

The experimental study by Makarova et al. [17] indicated a decrease in ether yield with increasing site time, which was credited to the ether decomposition reaction. Moreover, the observation of similar reaction rates for dehydration of butanol to butene and for ether decomposition to butene indicates that butene formation can proceed via an ether-mediated route. In view of this, two plausible mechanisms for the decomposition of ether to butene have been studied. Herein, the ether decomposition mechanism involves either a syn- or an anti- (E2) elimination reaction as described in the case of direct dehydration of butanol to butene. The transition state structures associated with these two mechanisms are shown in Figure 9.

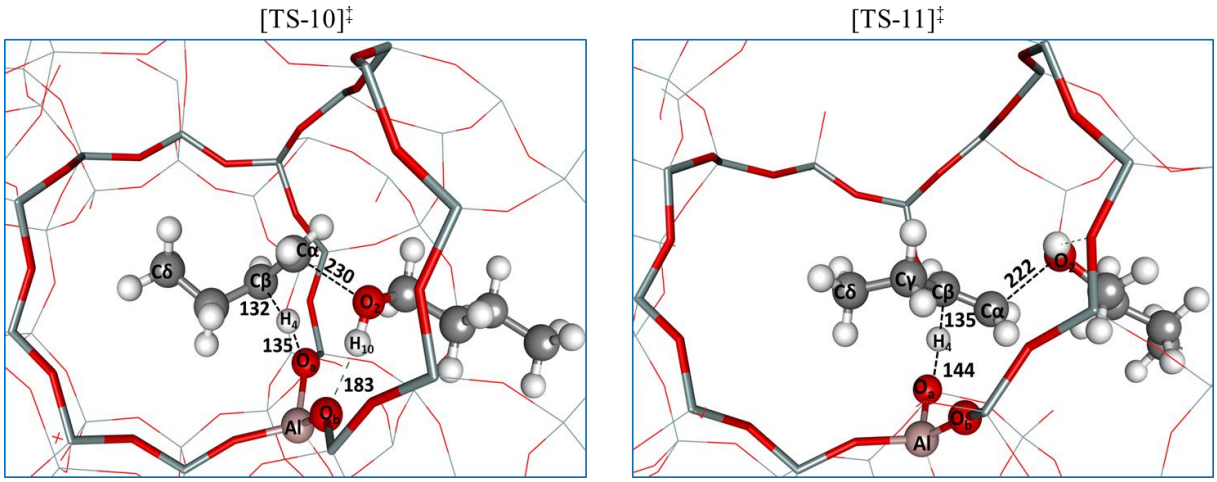

Figure 9. Transition state structures (views at the channel intersection) for the ether decomposition reaction (path C): 1) TS-10, syn-elimination (mechanism 9) 2) TS-11, anti-elimination (mechanism 10). Color code: silicon - light blue, aluminum - pink, oxygen - red, hydrogen - white, carbon - grey, hydrogen bonds (distance < 250 pm) - green dashed lines, bond breaking/forming - black dashed lines

Reaction mechanism 9 (decomposition of ether to butene and butanol via syn elimination):
This reaction mechanism involves the decomposition of the protonated ether produced via the re-adsorption of dibutyl ether (reverse of step 16), in a sequence of elementary steps 20, 21 and 8. In step 20, the protonated ether undergoes a cleavage of a C-O bond and a concurrent abstraction of a β-hydrogen by the zeolite basic oxygen. This elementary step is activated (TS-10) and has an activation energy of 140 kJ/mol (Table 3), considering DBE* as reference state. This is in good agreement with the experimentally reported value of 138 ± 8 kJ/mol for decomposition of ether to butene [17]. The elementary step 20 leads to the formation of a co-adsorbed species C4, having both butanol and butene adsorbed on the acid site of the zeolite. Further desorption of butanol (step 21) and butene (step 8) restores the Brønsted acid site.

In the transition state (TS-10, Figure 9) structure, the β-hydrogen (H_4) and the leaving group (butanol) have a near syn-coplanar configuration with a O_2-C_α-C_β-H_4 dihedral angle of -21.6°. The α-carbon is completely planar, while the β-carbon is approaching a planar state (see Appendix A, Table S3). The extent of the C_α-O_2 bond scission is larger than that of the C_β-H_4 bond, giving the syn-elimination an E1 character. Moreover, the interatomic distances show that the C_α-O_2 (229.9 pm) and C_β-H_4 (131.1 pm) bonds are nearly broken, which is indicative of a late transition state.
The physisorbed butanol molecule has a minor charge of +0.10, while the zeolite framework has a charge of -0.75. The charge on the [C4H9] fragment is +0.65, but the major fraction of this charge is associated with the β–hydrogen (+0.4113) which has nearly broken its bond with the β-carbon (C_β). Based on the geometrical aspects and the results of the Bader charge analysis, one can conclude that the key step of this reaction mechanism follows a one step 1,2-syn-elimination reaction with E1 character.

Reaction mechanism 10 (decomposition of ether to butene and butanol via E2 (anti) elimination): This reaction mechanism is similar to mechanism 9, but proceeds via an anti-

elimination route instead of the syn-elimination. The protonated ether undergoes a sequence of elementary steps, namely, reorientation (step 22) to an antiperiplanar configuration DBE2, butanol elimination (step 23) to form physisorbed 1-butene and desorption of 1-butene (step 8) to restore the zeolite Brønsted acid site. The elementary step 23 is activated (TS-11) and has an activation energy of 84 and 147 kJ/mol, considering DBE2 (Table 3) and DBE* as reference states, respectively. In this step, the protonated ether molecule undergoes an elimination through a concerted mechanism, involving simultaneous cleavage of the C_α-O_2 bond and abstraction of the β-hydrogen (H_4) by the zeolite basic oxygen (O_a).

In the transition state (TS-11, Figure 9) geometry, the β-hydrogen (H_4) points towards the bridge oxygen atom (O_a) and the leaving group (butanol) is positioned opposite to it, having a dihedral angle (O_2-C_α-C_β-H_4) of 181.4°.The α- and β-carbon have a near planar configuration with the α-carbon being closer to planarity than the β-carbon (see bond angles in Appendix A, Table S3). The C_α-O_2 and C_β-H_4 bond length in the transition state are 222 and 135 pm respectively. The extent of C-O bond breakage is more pronounced than that of the β-carbon (C_β) and β-hydrogen (H_4).

The physisorbed butanol molecule has a minor charge of +0.12, while the zeolite framework has a charge of -0.81. The charge on the [C4H9] fragment is +0.69, but the major fraction of this charge is associated with the β–hydrogen (+0.38) which has nearly broken its bond with the β-carbon (C_β). Based on the geometrical aspects and the results of the Bader charge analysis, one can conclude that the key step of this reaction mechanism follows an 1,2-anti-elimination reaction.

Comparison of the reaction mechanisms for the decomposition of ether: The Gibbs free energy profile for the two plausible mechanisms of the ether decomposition to 1-butene (path C) is shown in Figure 10. Amongst the syn- (TS-10) and anti-elimination (TS-11), the syn-

elimination offered a lower free energy barrier (apparent $\Delta G^{\ddagger}$ of 4 kJ/mol at 400K with respect to the gas phase butanol and the zeolite).

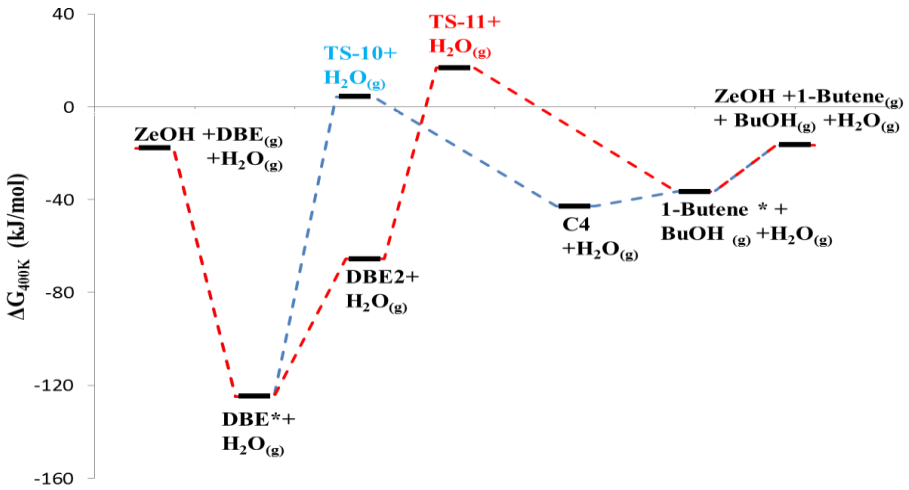

Figure 10. Gibbs Free Energy profile for the decomposition of ether to 1-butene in H-ZSM-5 at 400K (Gibbs free energy of zeolite with two gas-phase 1-butanol molecules was considered as the reference zero)

2.3.2.4. Comparison of the different reaction pathways for 1-butanol dehydration

Comparison of the free energy profiles for path A, B, and C, indicates that etherification (via TS7, S_N2 substitution, see Figure 8) and ether decomposition (via TS-10, syn-elimination, see Figure 10) to be energetically more favorable as compared to any of the mechanisms associated with path A (see Figure 6). However, as the actual reaction rate is a complex function of reaction conditions and feed concentrations, it is imperative to carry out a detailed reaction path analysis to arrive at a conclusive result regarding the dominant reaction mechanism in actual reaction conditions.

2.3.3 Microkinetic model and reaction path analysis:

A detailed microkinetic model involving 10 different reaction mechanisms, consisting of 23 elementary steps (as seen in Figure 4 and Table 2) has been considered without making any

assumption for the rate determining step. The effect of reaction conditions, viz., partial pressure of 1-butanol (0.01-100 kPa) and water (0-40 kPa), site time ($N_{H+}/F_{BuOH,0}$ = 0-200 mol H^+ s / mol $BuOH_0$) and reaction temperature (400-460 K), is studied.

A comparison of the forward, reverse and net reaction rates for the different elementary steps over a wide range of reaction conditions has been used to determine the rate determining and the equilibrated/non-equilibrated steps along each mechanism. For the direct conversion of butanol to butene (path A), the elementary steps R2 (TS-1), R4 (TS-2), R7 (TS-3) and R13 (TS-6) are found to be the rate determining steps along mechanism 1 (via E1-like elimination), mechanism 2 (via syn-elimination), mechanism 3 (via anti-elimination) and mechanism 5 (butanol-assisted syn-elimination), respectively. On the other hand, mechanism 4 (butoxide-mediated dehydration of butanol to butene) involves two non-equilibrated steps, namely step R9 (TS-4) and R10 (TS-5). For the conversion of butanol to ether (path B), the elementary step R15 (TS-7) is the rate determining step for mechanism 6 (butanol dimer to ether via S_N2 reaction), while for both the butoxide-mediated etherification mechanisms (7 via S_N2 and 8 via S_N1), two non-equilibrated steps (step R9 (TS-4) and R18 (TS-8) for mechanism 7 and R9 (TS-4) and R19 (TS-9) for mechanism 8) are identified. For the ether decomposition reaction (path C), elementary steps R20 (TS-10) and R23 (TS-11) are found to be the rate determining steps along mechanism 9 (via syn-elimination) and 10 (via anti-elimination), respectively. All other reaction steps in the microkinetic model are found to be quasi-equilibrated.

To validate the results of our ab initio based microkinetic model, a comparison is made with the experimental result of Makarova et al.[17]. The microkinetic model was used to simulate their experimental conditions and the turnover frequency (TOF) for the production of dibutyl ether and butene were compared at identical site times. The experimentally reported reaction rates were converted to TOF by accounting for the number of Brønsted acid sites per gram of

catalyst (see Appendix A for details). Table 4 provides a comparison between our theoretical and literature reported experimental results.

Table 4. Comparison between theoretical and experimental TOFs for production of dibutyl ether (DBE) and butene at 400K, butanol feed mole fraction 0.7%, total pressure of 1 bar and site time of 36.6 mol_{H+} s mol^{-1}.

			This work	Experimental [#]
1	TOF for production of Butene	(mol /mol H+ /s)	$2.5\ 10^{-6}$	$4.1\ 10^{-5}$
2	TOF for production of DBE	(mol /mol H+ /s)	$1.7\ 10^{-4}$	$5.1\ 10^{-4}$
3	Conversion	(mol %)	1.8	~ 2

[#] Experimental result of Makarova et al.[17]

The ab initio based microkinetic model captures the experimental observation of a considerably larger ether formation compared to butene formation under the investigated conditions. The theoretical results predict reasonably well the rate of production of ether but under-predict the rate of formation of butene by an order of magnitude. This can be attributed to deficiencies of GGA functionals (e.g. overpolarization effects [48]), inaccuracies in describing dispersive interactions [39-42] and the inaccuracy associated with the harmonic oscillator approximation in predicting the entropic contributions for the gas-phase butene molecule [68] and loosely bonded transition states [69]. Nevertheless, this deviation from the experimental result for butene formation is of the order of the expected accuracy for the harmonic oscillator approximation [68,69]. Moreover, the total rate of butanol dehydration is comparable as decribed by the similar conversion values. Overall, the simulated results are in good agreement with the experimentally observed results and the model can be used to identify dominant reaction mechanisms and to provide a reliable insight in the effect of reaction conditions.

2.3.3.1. Effect of conversion

The influence of conversion on product yields, TOFs and surface coverages is studied by systematically increasing the site time at constant temperature and pressure, thus increasing

the conversion of butanol. The butene yield was found to increase steadily with increasing site time, while the ether yield was found to pass through a maximum as a function of site time (see Figure 11a). The simulated results are in line with the experimentally observed trends for the butene and ether yield [17]. The decrease in ether yield at higher site time is attributed to the decomposition of ether to butene.

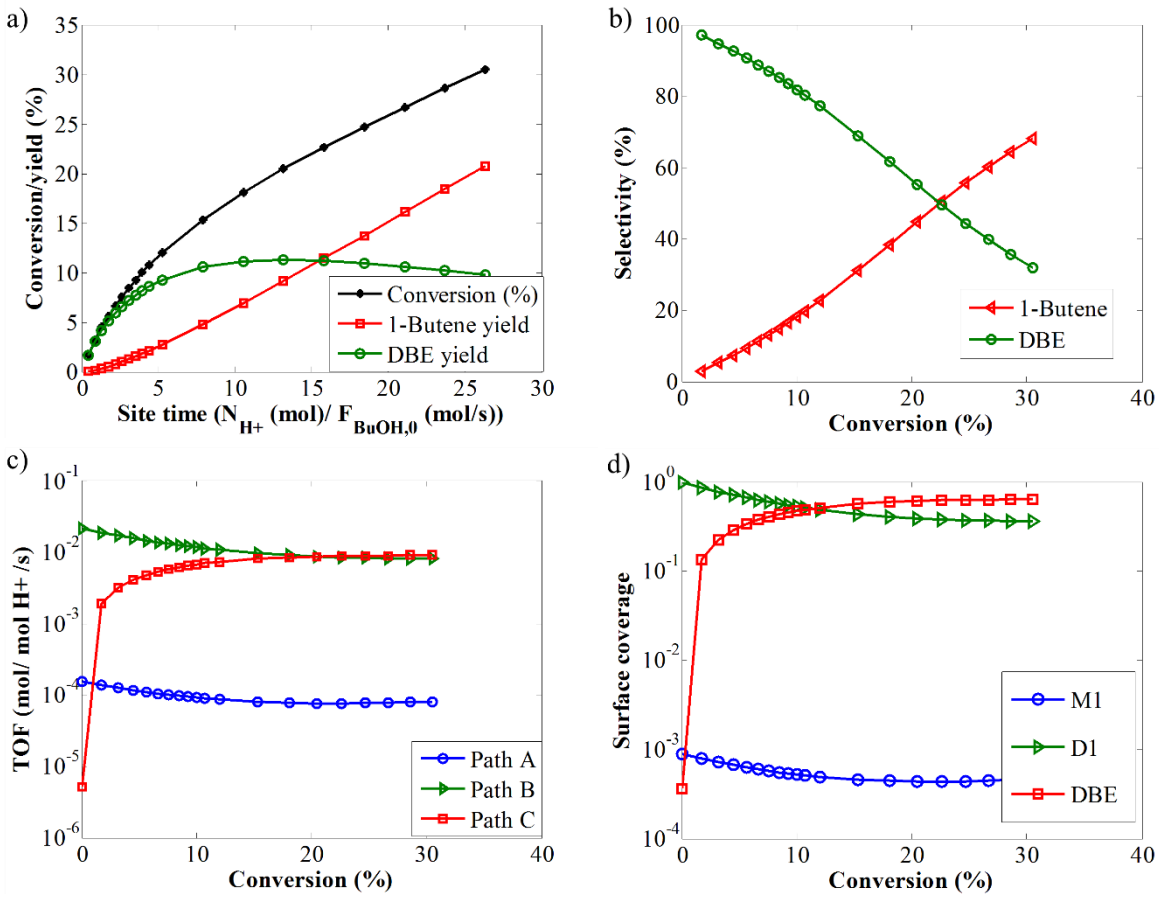

Figure 11. a) Butanol conversion and product (1-butene and DBE) molar yield as a function of site time, b) 1-butene and DBE selectivity as a function of conversion, c) Turnover frequencies (TOF) for different reaction pathways as a function of conversion, d) Coverages for surface species. Reaction conditions: 450K, butanol feed partial pressure of 1 kPa and site time varied between 0 – 30 ($N_{H+(mol)}/F_{BuOH,0\ (mol/s)}$).

Figure 11c shows the effect of conversion on the TOFs for the different reaction pathways. Here, the TOF value for each reaction pathway is calculated by summing up the TOF values for each of the contributing reaction mechanism. The detailed contribution of the TOF values of each reaction mechanism to the corresponding reaction pathway at 450K and 1kPa feed

butanol pressure is shown in Figure S6 of Appendix A. Reaction path A proceeds predominantly via reaction mechanism 3 (E2 elimination) and mechanism 5 (butanol-assisted syn-elimination), while reaction paths B and C occur primarily via mechanism 6 (S_N2 substitution of butanol dimer to ether) and mechanism 9 (syn-elimination), respectively. Overall, it is seen that reaction path B remains the dominant one up to 10% conversion, while path C starts gaining importance with an increase in conversion.

Butene selectivity is found to increase with increasing conversion (see Figure 11b). As seen in Figure 11c, the production of butene predominantly occurs via decomposition of ether (path C), except for very low conversions, where it occurs via direct dehydration of butene (path A). This can be explained on the basis of the change in the surface coverages with an increase in conversion (see Figure 11d). At a very low conversion, the adsorbed dimer (D1) is the most abundant species, followed by protonated monomer (M1) and protonated ether (DBE*), and the production of butene occurs via path A. With an increase in conversion, DBE* becomes the most abundant surface species and butene is produced via ether decomposition.

The simulated surface coverages (see Figure 11d) indicate a large abundance of adsorbed dibutyl ether (DBE*) and dimeric species (D1) over the zeolite active sites. TGA studies[70] for 1-butanol adsorption on H-ZSM-5 indicated an occupancy of two molecules of alcohol per Al site. In addition, IR studies[71] for adsorption of 1-butanol on H-ZSM-5 indicated that the surface dominant species have a stoichiometry close to that of DBE.

2.3.3.2. Effect of reaction temperature

The effect of temperature on product selectivity, surface coverage and TOFs is investigated at a temperature range of 400-460 K. An increase in the reaction temperature is also associated with an increase in the conversion which has a significant impact on the overall product

selectivity. Therefore, when comparing selectivities at different temperatures, the conversion needs to be fixed in order to decouple the temperature effect from the conversion effect. The temperature of the study was limited to 460K in order to avoid reaction conditions which would lead to further conversion of butene to higher hydrocarbon and cracked products.

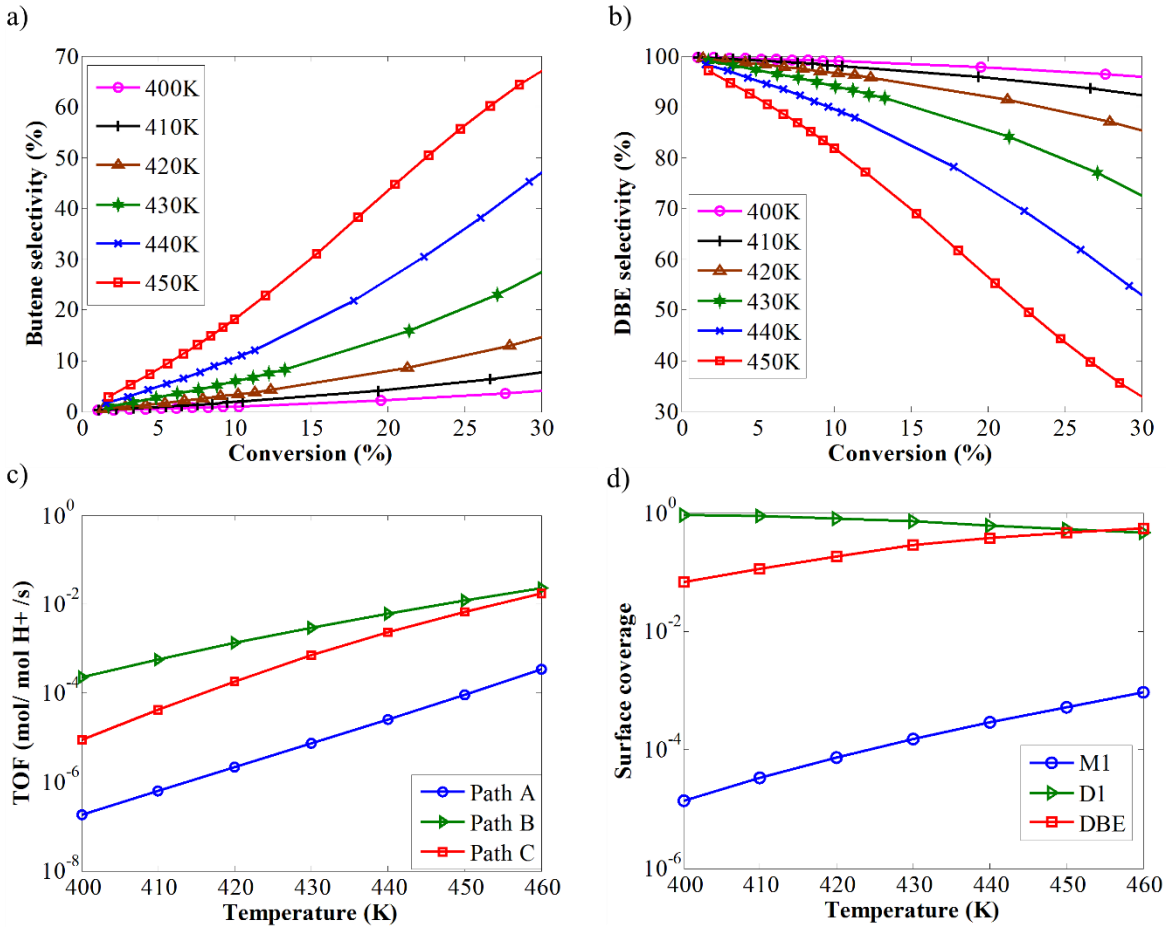

Figure 12. Effect of reaction temperature on (a) 1-butene selectivity and (b) DBE selectivity as a function of conversion. (c) turnover frequencies (TOF) for different reaction pathways at x= 10% and (d) surface coverages compared at a constant butanol conversion (x) of 10%. Inlet partial pressure of butanol: 1 kPa, site time adjusted in the range of 0 – 200 ($N_{H+(mol)}/F_{BuOH,0\ (mol/s)}$) so as to attain similar conversion levels.

Figures 12a and 12b show the effect of temperature variation on product selectivity at constant inlet pressure (1 kPa) of butanol. At low temperatures (below 400K), ether remains the key product in agreement with the low temperature (368-409 K) experimental results of

Chiang and Bhan [67]. On the other hand, selectivity shifts towards the production of butene with an increase in temperature, which is consistent with high temperature (673-773K) experimental results where formation of an ether fraction is not observed [18,19].

Figure 12c shows the effect of temperature on TOFs compared at a conversion level of 10%. In the temperature window of 400-460 K, the rate of production of butene occurs essentially via an ether-mediated consecutive reaction scheme (i.e. path B followed by path C). This is consistent with the conclusion drawn on the basis of comparison of the free energy diagrams for the different reaction pathways (Section 3.2.4.).

Finally, temperature plays a key role in defining the dominant reaction mechanism within each reaction pathway. The detailed contribution of the TOF values of each reaction mechanism to the corresponding reaction pathway is shown in Figure S7 of Appendix A. For path A, there is a shift in the dominant mechanism from mechanism 5 (butanol-assisted syn-elimination) to mechanism 3 (E2 elimination) with an increase in temperature. On the other hand, reaction mechanism 6 (S_N2 butanol dimer to ether) and 9 (syn-elimination) remain dominant for path B and C, respectively.

2.3.3.3. Effect of partial pressure of 1-butanol

The effect of butanol partial pressure on the butene and ether selectivity has been examined using microkinetic simulations in the butanol inlet partial pressures range of 0.001-100 kPa at 450K. The butanol partial pressure is varied by keeping the same butanol flow rate and varying the inert gas flow rate to match the desired inlet partial pressure value. The effect of inlet butanol partial pressures on the product selectivity is compared at different conversion levels (Figures 13a and 13b).

An increase in butanol feed partial pressure leads to a decrease in butene selectivity (see Figure 13a). This is attributed to the decrease in the TOF of path A and path C (see Figure

13c). This is in turn ascribed to the increased preference for adsorption of butanol to form the adsorbed dimer (as compared to protonated ether or adsorbed butanol monomer) at higher butanol partial pressures (see Figure 13d).

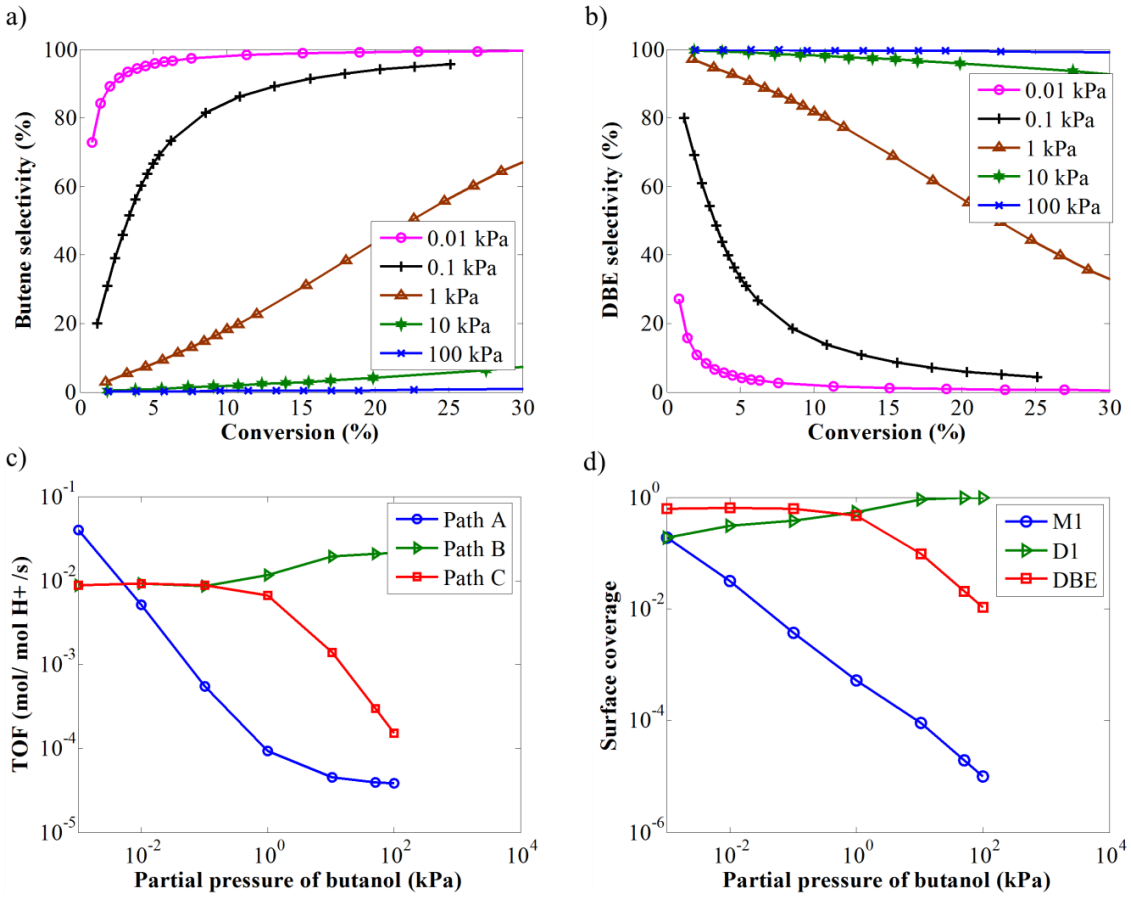

Figure 13. Effect of butanol partial pressure in the feed on (a) 1-butene selectivity and (b) DBE selectivity as a function of conversion. (c) turnover frequencies (TOF) for different reaction pathways at x= 10% and (d) surface coverages compared at a constant butanol conversion (x) of 10%. Reaction temperature: 450 K, site time is varied between 0 – 30 ($N_{H+(mol)}/F_{BuOH,0\ (mol/s)}$) in order to attain similar conversion levels.

Figure 13c depicts a shift in dominant path with inlet butanol pressure. For extremely low values of inlet butanol pressure ($P_{BuOH,0}$ less than 0.01 kPa) path A is dominant. With an increase in pressure ($P_{BuOH,0}$ in the range of 0.1-10 kPa), butanol dehydration essentially proceeds via path B and C. For pressures greater than 10 kPa, path B becomes the dominant

reaction pathway. Hence, one should be careful when comparing results obtained from low pressure experiments (such as FTIR or Temporal Analysis of Products) to that of the high pressure experimentation carried out in a micro-reactor or an industrial scale reactor.

Further insight into the pressure dependence of TOFs for each reaction pathway is obtained by looking into the TOFs for the individual reaction mechanisms (see Figure S8 of Appendix A). For path A, the increase in butanol partial pressure is associated with a decrease in the TOFs for mechanisms 1-4 and an increase in the TOF for mechanism 5. This leads to a shift in the dominant mechanism from E2 elimination (mechanism 3) to butanol-assisted syn-elimination (mechanism 5) with an increase in butanol partial pressure. For path B, the increase in butanol partial pressure is associated with an increase in the TOF for mechanism 6 and a decrease in the TOFs for mechanisms 7 and 8. The reaction mechanism 6 (S_N2, butanol dimer to ether) remains dominant except at very low partial pressures (less than 0.001 kPa), where mechanism 7 (S_N2 butoxide-mediated etherification) tends to gain importance. For path C, both mechanisms 9 and 10 depict a zero-order pressure dependence until butanol feed partial pressure of 1 kPa, while shifting to a negative order pressure dependence at higher butanol partial pressures. Thus, for experimentally relevant conditions (above 1kPa) one would observe a negative order dependence with respect to butanol partial pressure. Reaction mechanism 9, i.e. ether decomposition via syn-elimination, remains dominant throughout the complete pressure range for path C.

The pressure dependence and shift in the dominant reaction path can be explained on the basis of changes in the surface coverage with reaction conditions. The simulated surface coverages (see Figure 13d) depict a large abundance of adsorbed dibutyl ether (DBE*) and dimeric species (D1) over the zeolite active sites especially at high pressures. Since the surface coverages of D1 and DBE* are much higher than M1 at high butanol pressures, this leads to prevalence of path B and path C mechanisms at these conditions. On the other hand, the M1

intermediate is found to have a significant surface coverage only at low partial pressures of butanol, where path A prevails.

Although the present study infers that the alcohol dimer can undergo further reaction, it is pertinent to note that formation of these dimer species reduces the overall rate of production of alkenes (see Fig 13c/d). Our simulations indicate a decrease in TOFs for path A and path C which leads to formation of butene with increase in butanol partial pressure (associated with increase in dimer coverage). A decrease in ethylene yield was also observed in ethanol dehydration over H-MOR [67], with increase in ethanol pressure.

2.3.3.4. Effect of partial pressure of water

The effect of the partial pressure of water on the butanol dehydration reaction is of prime interest for the production of alkenes from bio-butanol. The fermentation process used for production of bio-butanol, utilizes water as a solvent and involves production of acetone and ethanol in addition to 1-butanol. Typically, an azeotropic distillation process[72] is used to recover an aqueous butanol stream from the clarified fermentation broth. The 1-butanol – water mixture has an azeotropic composition of 24.8 and 75.2 mol % of butanol and water, respectively. Since further concentration of 1-butanol is energy intensive, it would be ideal to feed the water-butanol azeotrope for the dehydration process[73].

Inhibition effects due to presence of water can be ascribed to several different factors such as competitive adsorption and co-adsorption, solvation effect by water (where water stabilizes the reactant better than the transition state structure), or hydrothermal deactivation due to change in catalyst structure (for instance hydrothermal dealumination in zeolites). Moreover,

at higher water partial pressure thermodynamic limitations can also play a role. The present study essentially focuses on the competitive adsorption and co-adsorption of a water molecule.

In order to investigate the effect of water on butanol dehydration within H-ZSM-5, a wide range of inlet water partial pressures ($P_{H2O,0}$ - 0.1 to 40 kPa) has been studied at a constant inlet butanol partial pressure of 1kPa and reaction temperature of 450K as shown in Figure 14. Interestingly, the presence of water in the feed does not have any significant impact on the butanol conversion and the overall product selectivity even at partial pressure ratios much higher than that corresponding to the azeotropic composition ($P_{H2O,0}$ /$P_{BuOH,0}$ $|_{azeotrope}$ ~ 3). This is also evident from the negligible change in the TOFs (see Figure 14a) with an increase in partial pressure of water indicative of a zero order dependence with respect to water. Although, this seems to be in contrast with the experimental observation for the dehydration of 2-butanol over POM cluster [20] and ethanol dehydration over γ-alumina [74], it has been reported in literature [75,76] that water has no inhibiting effect on the dehydration of ethanol in H-ZSM-5. The observation that the partial pressure of water has practically no effect on the rates can be explained by the marginal increase of the water coverage with increasing partial pressure of water (see Figure 14b) which is related to the higher adsorption strength for the butanol dimer (D1) and ether (DBE) in H-ZSM-5 as compared to the water (W) and the co-adsorbed butanol-water species (C2). A similar reasoning was proposed by Corma and Perezpariente [77] to explain the absence of a water inhibition effect for the ethanol dehydration reaction over an acidic sepiolite catalyst. The higher adsorption strength of 1-butanol in H-ZSM-5 as compared to water and other lower alcohols (methanol/ethanol/1-propanol/2-propanol) is also consistent with the experimental observation of Aronson et al. [78] that lower alcohols were unable to displace adsorbed butanol in the zeolite.

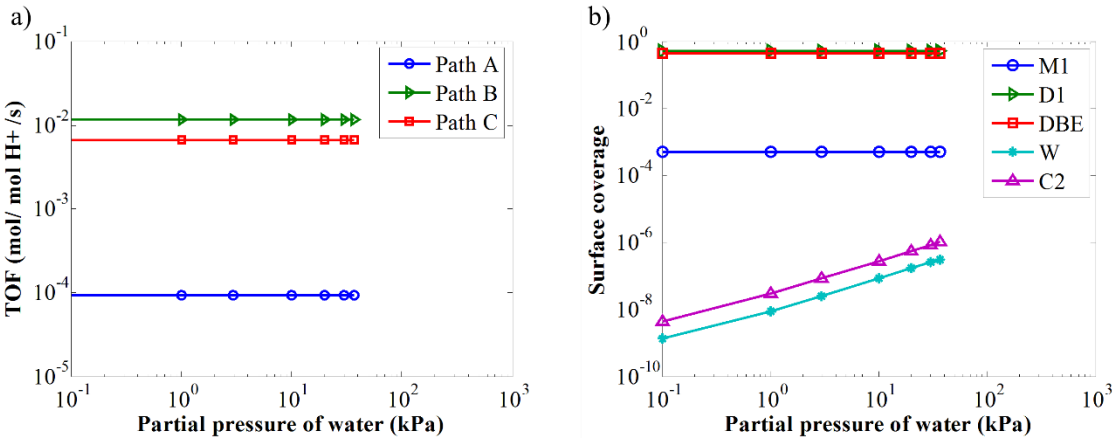

Figure 14. Effect of partial pressure of water on (a) turnover frequencies (TOF) for different reaction pathways at x= 10% and (b) surface coverages compared at a constant butanol conversion (x) of 10%. Reaction temperature: 450K, inlet partial pressure of butanol: 1 kPa, site time adjusted in the range of 0 – 30 ($N_{H+(mol)}/F_{BuOH,0\ (mol/s)}$) so as to attain similar conversion levels.

4. Conclusions

This study provides a detailed insight into the plausible reaction mechanisms for dehydration of 1-butanol in H-ZSM-5 zeolite. A first principles microkinetic model is used to obtain a predictive guidance on the effect of reaction conditions on reaction rates and product selectivity. Useful insights into the dominant reaction mechanism and its dependence on reaction conditions are derived using a reaction path analysis.

Our study reveals the importance of the alcohol protonation by the Brønsted acid site, which helps in the advancement of the reaction as it leads to an elongation of the C-O bond, facilitating the cleavage of C-O bond in the later steps. The reasonable agreement between the simulated and literature reported experimental values, demonstrate the reliability of the DFT based microkinetic model in providing directional information on reaction kinetics. An increase in conversion leads to an increase in butene yield. Lower temperatures favor ether formation, while higher temperatures lead to preferential production of butene. Higher

butanol partial pressures favor dehydration of butanol to ether, followed by a temperature dependent ether decomposition. The reaction path analysis reveals that, except for extremely low butanol pressures, the production of butene occurs essentially via an ether mediated route. The butanol partial pressure has a prominent role in determining the dominant reaction mechanism. For the direct dehydration of butanol to butene (path A), mechanisms involving an E2 (anti) elimination reaction remain dominant at low butanol partial pressures (below 0.01 kPa) and shift to butanol-assisted syn-elimination at higher butanol pressures (greater than 1 kPa). The ether formation (path B) can occur via S_N2 mechanisms following two possible routes, from physisorbed dimer (D2) or from 1-butanol and 1-butoxide. Ether formation predominantly occurs via the former route, except at very low partial pressures where it can occur via both routes. The ether decomposition (path C) occurs primarily via a 1,2-syn-elimination. The shift in the dominant reaction mechanism can be explained on the basis of changes in surface coverages. This shift in the preferred reaction mechanism can help to reconcile conflicting observations reported at different reaction conditions. Last but not least, the absence of a water inhibition effect makes the dehydration of aqueous bio-butanol an attractive option for the production of bio-butenes, which can serve as a feedstock for the chemical industry.

5. References

(1) Luque, R.; Herrero-Davila, L.; Campelo, J. M.; Clark, J. H.; Hidalgo, J. M.; Luna, D.; Marinas, J. M.; Romero, A. A. *Energ Environ Sci* **2008**, *1*, 542.

(2) Jacobson, M. Z. *Environ Sci Technol* **2007**, *41*, 4150.

(3) Cook, R.; Phillips, S.; Houyoux, M.; Dolwick, P.; Mason, R.; Yanca, C.; Zawacki, M.; Davidson, K.; Michaels, H.; Harvey, C.; Somers, J.; Luecken, D. *Atmos Environ* **2011**, *45*, 7714.

(4) Savage, N. *Nature* **2011**, *474*, S9.

(5) Guan, J. Q.; Xu, C.; Liu, B.; Yang, Y.; Ma, Y. Y.; Kan, Q. B. *Catal Lett* **2008**, *126*, 301.

(6) Gronowski, A. A. *J Appl Polym Sci* **2003**, *87*, 2360.

(7) Busca, G. *Chem Rev* **2007**, *107*, 5366.

(8) Wright, M. E.; Harvey, B. G.; Quintana, R. L. *Energ Fuel* **2008**, *22*, 3299.

(9) Olaofe, O.; Yue, P. L. *Collect Czech Chem C* **1985**, *50*, 1834.

(10) Williams, C.; Makarova, M. A.; Malysheva, L. V.; Paukshtis, E. A.; Zamaraev, K. I.; Thomas, J. M. *J Chem Soc Faraday T* **1990**, *86*, 3473.

(11) Williams, C.; Makarova, M. A.; Malysheva, L. V.; Paukshtis, E. A.; Talsi, E. P.; Thomas, J. M.; Zamaraev, K. I. *J Catal* **1991**, *127*, 377.

(12) Makarova, M. A.; Williams, C.; Zamaraev, K. I.; Thomas, J. M. *J Chem Soc Faraday T* **1994**, *90*, 2147.

(13) Makarova, M. A.; Williams, C.; Thomas, J. M.; Zamaraev, K. I. *Catal Lett* **1990**, *4*, 261.

(14) Makarova, M. A.; Williams, C.; Romannikov, V. N.; Zamaraev, K. I.; Thomas, J. M. *J Chem Soc Faraday T* **1990**, *86*, 581.

(15) Makarova, M. A.; Paukshtis, E. A.; Thomas, J. M.; Williams, C.; Zamaraev, K. I. *Catal Today* **1991**, *9*, 61.

(16) Makarova, M. A.; Paukshtis, E. A.; Thomas, J. M.; Williams, C.; Zamaraev, K. I. *Stud Surf Sci Catal* **1993**, *75*, 1711.

(17) Makarova, M. A.; Paukshtis, E. A.; Thomas, J. M.; Williams, C.; Zamaraev, K. I. *J Catal* **1994**, *149*, 36.

(18) Zhang, D. Z.; Al-Hajri, R.; Barri, S. A. I.; Chadwick, D. *Chem Commun* **2010**, *46*, 4088.

(19) Zhang, D. Z.; Barri, S. A. I.; Chadwick, D. *Appl Catal a-Gen* **2011**, *403*, 1.

(20) Macht, J.; Janik, M. J.; Neurock, M.; Iglesia, E. *J Am Chem Soc* **2008**, *130*, 10369.

(21) Macht, J.; Janik, M. J.; Neurock, M.; Iglesia, E. *Angew Chem Int Edit* **2007**, *46*, 7864.

(22) Macht, J.; Carr, R. T.; Iglesia, E. *J Am Chem Soc* **2009**, *131*, 6554.

(23) Janik, M. J.; Macht, J.; Iglesia, E.; Neurock, M. *J Phys Chem C* **2009**, *113*, 1872.

(24) Macht, J.; Carr, R. T.; Iglesia, E. *J Catal* **2009**, *264*, 54.

(25) Prestianni, A.; Cortese, R.; Duca, D. *React Kinet Mech Cat* **2013**, *108*, 565.

(26) Olson, D. H.; Khosrovani, N.; Peters, A. W.; Toby, B. H. *J Phys Chem B* **2000**, *104*, 4844.

(27) Dedecek, J.; Balgova, V.; Pashkova, V.; Klein, P.; Wichterlova, B. *Chem Mater* **2012**, *24*, 3231.

(28) Lonsinger, S. R.; Chakraborty, A. K.; Theodorou, D. N.; Bell, A. T. *Catal Lett* **1991**, *11*, 209.

(29) Mentzen, B. F.; Sacerdoteperonnet, M. *Mater Res Bull* **1994**, *29*, 1341.

(30) Svelle, S.; Tuma, C.; Rozanska, X.; Kerber, T.; Sauer, J. *J Am Chem Soc* **2009**, *131*, 816.

(31) Kresse, G.; Hafner, J. *Phys Rev B* **1993**, *47*, 558.

(32) Kresse, G.; Hafner, J. *Phys Rev B* **1994**, *49*, 14251.

(33) Kresse, G.; Furthmuller, J. *Comp Mater Sci* **1996**, *6*, 15.

(34) Blochl, P. E. *Phys Rev B* **1994**, *50*, 17953.

(35) Kresse, G.; Joubert, D. *Phys Rev B* **1999**, *59*, 1758.

(36) Perdew, J. P.; Chevary, J. A.; Vosko, S. H.; Jackson, K. A.; Pederson, M. R.; Singh, D. J.; Fiolhais, C. *Phys Rev B* **1992**, *46*, 6671.

(37) Grimme, S. *J Comput Chem* **2006**, *27*, 1787.

(38) Kerber, T.; Sierka, M.; Sauer, J. *J Comput Chem* **2008**, *29*, 2088.

(39) Tuma, C.; Sauer, J. *Phys Chem Chem Phys* **2006**, *8*, 3955.

(40) Goltl, F.; Gruneis, A.; Bucko, T.; Hafner, J. *J Chem Phys* **2012**, *137*.

(41) Vener, M. V.; Rozanska, X.; Sauer, J. *Phys Chem Chem Phys* **2009**, *11*, 1702.

(42) Chiu, C. C.; Vayssilov, G. N.; Genest, A.; Borgna, A.; Rosch, N. *J Comput Chem* **2014**, *35*, 809.

(43) Nguyen, C. M.; Reyniers, M. F.; Marin, G. B. *J Catal* **2015**, *322*, 91.

(44) Nguyen, C. M.; Reyniers, M. F.; Marin, G. B. *Phys Chem Chem Phys* **2010**, *12*, 9481.

(45) Nguyen, C. M.; Reyniers, M. F.; Marin, G. B. *J Phys Chem C* **2011**, *115*, 8658.

(46) Bučko, T.; Hafner, J. *J Catal* **2015**, *329*, 32.

(47) Leydier, F.; Chizallet, C.; Costa, D.; Raybaud, P. *J Catal* **2015**, *325*, 35.

(48) Grimme, S.; Antony, J.; Ehrlich, S.; Krieg, H. *J Chem Phys* **2010**, *132*.

(49) Bader, R. F. W. *Atoms in molecules : a quantum theory*; Clarendon Press: Oxford, 1990.

(50) Henkelman, G.; Arnaldsson, A.; Jonsson, H. *Comp Mater Sci* **2006**, *36*, 354.

(51) Henkelman, G.; Jonsson, H. *J Chem Phys* **2000**, *113*, 9978.

(52) Henkelman, G.; Jonsson, H. *J Chem Phys* **1999**, *111*, 7010.

(53) Heyden, A.; Bell, A. T.; Keil, F. J. *J Chem Phys* **2005**, *123*.

(54) De Moor, B. A.; Ghysels, A.; Reyniers, M. F.; Van Speybroeck, V.; Waroquier, M.; Marin, G. B. *J Chem Theory Comput* **2011**, *7*, 1090.

(55) Zhao, Y.; Truhlar, D. G. *Phys Chem Chem Phys* **2008**, *10*, 2813.

(56) Ribeiro, R. F.; Marenich, A. V.; Cramer, C. J.; Truhlar, D. G. *J Phys Chem B* **2011**, *115*, 14556.

(57) Grimme, S. *Chem-Eur J* **2012**, *18*, 9955.

(58) Jensen, J. H. *Phys Chem Chem Phys* **2015**, *17*, 12441.

(59) Piccini, G.; Sauer, J. *J Chem Theory Comput* **2014**, *10*, 2479.

(60) Piccini, G.; Alessio, M.; Sauer, J.; Zhi, Y. C.; Liu, Y.; Kolvenbach, R.; Jentys, A.; Lercher, J. A. *J Phys Chem C* **2015**, *119*, 6128.

(61) De Moor, B. A.; Reyniers, M. F.; Marin, G. B. *Phys Chem Chem Phys* **2009**, *11*, 2939.

(62) Cramer, C. J. *Essentials of computational chemistry : theories and models*; 2nd ed.; Wiley: Chichester Hoboken, NJ, 2004.

(63) Hindmarsh, A. C. *IMACS transactions on scientific computation* **1983**, *1*, 55.

(64) Boyd, S. L.; Boyd, R. J.; Bessonette, P. W.; Kerdraon, D. I.; Aucoin, N. T. *J Am Chem Soc* **1995**, *117*, 8816.

(65) Blaszkowski, S. R.; vanSanten, R. A. *J Am Chem Soc* **1996**, *118*, 5152.

(66) Jones, A. J.; Iglesia, E. *Angew Chem Int Edit* **2014**, *53*, 12177.

(67) Chiang, H.; Bhan, A. *J Catal* **2010**, *271*, 251.

(68) Van Speybroeck, V.; Van der Mynsbrugge, J.; Vandichel, M.; Hemelsoet, K.; Lesthaeghe, D.; Ghysels, A.; Marin, G. B.; Waroquier, M. *J Am Chem Soc* **2011**, *133*, 888.

(69) Reyniers, M. F.; Marin, G. B. *Annu Rev Chem Biomol* **2014**, *5*, 563.

(70) Aronson, M. T.; Gorte, R. J.; Farneth, W. E. *J Catal* **1986**, *98*, 434.

(71) Aronson, M. T.; Gorte, R. J.; Farneth, W. E. *J Catal* **1987**, *105*, 455.

(72) Ramey, D.; Yang, S.-T. *final report to the US Department of Energy, Contract No.: DE-F-G02-00ER86106* **2004**.

(73) D'Amore, M.; Manzer, L.; Miller, E.; DiCosimo, R.; Knapp, J.; Google Patents: 2007.

(74) DeWilde, J. F.; Chiang, H.; Hickman, D. A.; Ho, C. R.; Bhan, A. *Acs Catal* **2013**, *3*, 798.

(75) Phillips, C. B.; Datta, R. *Ind Eng Chem Res* **1997**, *36*, 4466.

(76) Moser, W. R.; Thompson, R. W.; Chiang, C. C.; Tong, H. *J Catal* **1989**, *117*, 19.

(77) Corma, A.; Perezpariente, J. *Clay Miner* **1987**, *22*, 423.

(78) Aronson, M. T.; Gorte, R. J.; Farneth, W. E.; White, D. *Langmuir* **1988**, *4*, 702.

Chapter 3

First principles kinetic study on the effect of zeolite framework on 1-butanol dehydration

The following pages include the paper:

M. John, K. Alexopoulos, M.-F. Reyniers and Guy B. Marin

ACS Catalysis **6** (2016) 4081 – 4094.

Abstract

Understanding the role of zeolite topology in defining its catalytic performance is of prime importance for the development of catalytic processes. Herein, a first principle based microkinetic study of 1-butanol dehydration is used to illustrate the effect of different zeolites (i.e. H-FAU, H-ZSM-5, H-ZSM-22 and H-FER) on the dehydration activity and product selectivity. Under identical reaction conditions, microkinetic simulations show significant variation in dehydration rates and butene/ether selectivity profile within the different zeolites. H-ZSM-5 has the highest catalytic activity, whereas H-FAU and H-FER exhibit a higher butene selectivity. In the large pore H-FAU, the weaker dispersive stabilization of the dimer makes the butene formation by monomolecular direct dehydration via a concerted anti-elimination compete with n-dibutyl ether formation. In H-FER, steric constraints due to partial confinement of the protonated n-dibutyl ether in the 8-MR channel decrease its stability favoring its further decomposition to butene via a concerted syn-elimination of butanol. On the other hand, the higher ether selectivity in H-ZSM-5 and H-ZSM-22 is rationalized on the basis of a higher stability for adsorbed ether and a higher activation barrier for ether decomposition. Next to the effect of zeolite framework, this study further highlights the pivotal role of the reaction conditions in determining the most abundant reaction intermediate, dominant reaction paths and underlying reaction mechanisms. In general, for all four zeolites, an increase in reaction temperature and a decrease in butanol feed partial pressure favors direct dehydration of butanol to butene (via butanol monomer). Whereas a decrease in reaction temperature and increase in butanol feed partial pressure favors dimer mediated dibutyl ether formation. An increase in conversion favors direct dehydration and dibutyl ether decomposition to butene.

Keywords: DFT, bio-butanol, dehydration, zeolite, confinement, reaction path, mechanism, microkinetic modelling.

3.1. Introduction

The development of a sustainable energy based economy relies essentially on the transformation from the existing petroleum-based infrastructure to renewable biomass-based technologies[1,2]. Bio-alcohol based processes have emerged as one such alternative[3]. Most of the recent research has focused on the conversion of lower alcohols such as methanol and ethanol to olefins and higher hydrocarbons[4,5]. Higher alcohols such as bio-butanol are expected to play a significant role as a future fuel and for other energy related applications[6,7]. Amongst these, the catalytic conversion of bio-butanol to biofuels and bio-chemicals is of particular interest[7]. The key to the success of such a process relies on the catalytic advancement of selective and energy efficient conversion of the feedstock.

Zeolites are extensively used in refining and petrochemical industry, since they are renowned for providing shape selectivity owing to their well-defined pore size and structure, while their high surface area and acid strength are very desirable for many catalytic reactions[8]. For this purpose, zeolites are an ideal candidate for bio-alcohol conversion processes.

The catalytic activity and selectivity in zeolite catalyzed reactions are primarily governed by zeolite acid strength and host-guest interactions [9-11] . Makarova et al.[12] studied the effect of confinement by comparing dehydration of 1-butanol in H-ZSM-5 and aluminosilicate, indicating that the confined environment of H-ZSM-5 favored ether formation. Differences in zeolite topology could also alter the dominant reaction path by stabilizing or destabilizing reaction intermediates and/or transition states. Chiang and Bhan[13] studied low temperature (368-409 K) ethanol dehydration in H-FER, H-ZSM-5 and H-MOR and observed a preferential production of diethyl ether (DEE) in H-ZSM-5 and H-FER, while both DEE and ethene were produced in H-MOR. The preferred formation of ethene in H-MOR was

attributed to the presence of small 8–membered ring (8–MR) side pockets which prevented formation of bulky dimer species, favoring monomolecular dehydration producing ethene. Phung et al. [14]reported substantial variation in turn over frequency (TOF) and product selectivity in ethanol dehydration at 453-573 K in H-FER, H-ZSM-5, H-MOR, H-BEA and H-FAU. Interestingly, both large pore H-FAU (12-MR) and medium/small pore H-FER (10-MR/8-MR) displayed a higher selectivity for ethene. On the other hand, H-MOR (12MR/8-MR) and H-ZSM-5 (10-MR), with average pore diameter in between these of H-FAU and H-FER, favored DEE formation. These results indicate that there is no straightforward correlation between product selectivity /activity and zeolite properties such as zeolite pore size.

A fundamental insight into the effect of zeolite properties on the underlying reaction mechanism can provide guidelines for the selection or rational design of an appropriate catalyst[15]. In general, alcohol dehydration can proceed via elimination and substitution reactions to yield alkene and ether products. Elimination reaction within a zeolite catalyst can occur via a step-wise E1 or/and a concerted E2 mechanisms[5]. Macht et al. suggested that the dehydration of 2-propanol and 2-butanol on POM [16-18] followed an E1 mechanism, which was corroborated by the observed secondary kinetic isotope effect (KIE) when β-hydrogen was replaced by deuterium. Likewise, Vjunov et al. [19] confirmed an E1 mechanism for cyclohexanol dehydration in H-BEA based on ^{13}C -labeled scrambling experiments with in situ ^{13}C NMR analysis. An E2 type of elimination can be relatively complex since it may involve a range of possible transition states owing to possible asynchronous breaking of C-O and C-H bonds[20]: pure E2 with synchronous breaking of the C-O and C-H_β bonds, E1-like E2 in which breaking of the C-O bond is more pronounced involving a transition state with a more or less pronounced carbenium ion character and E1cb-like E2 with a more pronounced breaking of the C-H_β bond in the transition state that possesses a more or less pronounced

carbanion character. Moreover, the concerted elimination requires the atoms or groups involved in the reaction to be in the same plane with an anti-periplanar or a syn-periplanar orientation characterized by torsional angles between leaving group and β-hydrogen of ~ 180° and 0°, respectively. DFT studies for dehydration of ethanol[21] and 2-propanol[22,23] in H-ZSM-5 reported a concerted (syn) elimination mechanism. Additionally, DFT-based microkinetic study of 1-butanol dehydration in H-ZSM-5 suggested an E1-like E2 anti-elimination at low 1-butanol partial pressures[24]. On the other hand, Makarova et al.[12,25-28] through FTIR spectroscopy and kinetic studies at low pressures (< 1 kPa) and temperatures of 380 - 460 K suggested an alkoxide-mediated S_N2-type mechanism for conversion of 1-butanol to 1-butene and di-1-butyl ether (DBE) in H-ZSM-5. Similar alkoxide-mediated mechanisms were proposed for alkene formation for ethanol[13] and 1-propanol [29] dehydration in zeolites. The alcohol dehydration to ether can occur via a alkoxide-mediated and/or via a alcohol dimer-mediated mechanism. Experimental and theoretical studies for methanol[30,31], ethanol [13] and 1-butanol [24] dehydration in zeolites indicate that the ether is produced from the alcohol dimer via S_N2-type nucleophilic substitution. A detailed comparison of all the aforementioned reaction mechanisms for 1-butanol dehydration in H-ZSM-5 is reported in previous work[24].

In this work, we present a dispersion-corrected periodic density functional theory (DFT) study for 1-butanol dehydration in four different zeolite frameworks i.e. H-FAU, H-ZSM-5, H-ZSM-22 and H-FER. A rigorous DFT-based microkinetic modelling and reaction path analysis is used to assess the effect of reaction conditions on the reaction rates and product selectivity for the different zeolites. The difference in catalytic performance of the investigated zeolites is rationalized on the basis of differences in stabilization of the reaction intermediates and transition state structures within the zeolite framework.

3.2. Theory

3.2.1. Zeolite models

The geometries of the zeolite structures were taken from the database of the International Zeolite Association (IZA) [32] and were further optimized after substitution of one Si atom with an Al atom and addition of a proton to the adjacent oxygen atom. H-FAU is a three-dimensional large-pore zeolite, characterized by supercages with diameter 1300 pm that are interconnected by 12 membered rings (12-MR) with dimensions 740 pm × 740 pm. The acid site is located at the Al1O1 position [33-35] and the primitive cell composition is $Si_{47}AlO_{96}H$ (Si/Al = 47). H-ZSM-5 is a three-dimensional medium-pore zeolite with intersecting straight (540 pm × 560 pm) and sinusoidal or zigzag (510 pm × 540 pm) 10-MR channels. The acid site is chosen to be located at the Al12O24 intersecting position [24,36,37] leading to a unit cell composition of $Si_{95}AlO_{192}H$ (Si/Al = 95). H-ZSM-22 is a one-dimensional medium-pore zeolite with straight channels in the *c* direction with dimensions 460 pm × 570 pm. The small primitive cell is tripled in the *c* direction to ensure sufficient separation of the adsorbed species. The acid site is located at the Al3O3 position, and the resulting unit cell composition is $Si_{35}AlO_{72}H$ (Si/Al = 35)[34,35]. H-FER is a two-dimensional medium-pore zeolite with intersecting 10-MR and 8-MR straight channels of 420 pm × 540 pm and 350 pm × 480 pm, respectively. The acid site is chosen to be located at the Al1O2 intersecting position [38,39] leading to a unit cell composition of $Si_{71}AlO_{144}H$ (Si/Al = 71). The zeolite unit cell parameters are provided in Table S1 of the Appendix B.

3.2.2. Computational details

3.2.2.1. Electronic energy calculations

Dispersion corrected periodic DFT calculations were performed with the Vienna Ab Initio Simulation Package (VASP) using plane wave basis sets[40-42]. The electron-ion interactions

were described using the projector–augmented wave (PAW) method [43,44] with a plane-wave energy cut-off of 600 eV. The exchange correlation energies were calculated on the basis of the generalized gradient approximation (GGA) according to Perdew, Burke and Ernzerhof (PBE)[45]. Brillouin zone sampling was restricted to the Γ-point. All the structures were fully relaxed to a maximum force convergence criterion of 0.02 eV $Å^{-1}$ and each self-consistency loop was iterated until a convergence level of 10^{-8} eV was achieved. Dispersive corrections for the van der Waals interactions were included by adding a pairwise interaction term to the Kohn–Sham energy using the DFT-D2 approach proposed by Grimme [46] and extended by Kerber et al. [47] for periodic PBE calculations. Although systematic deviations may be observed due to the overestimation of the dispersion interaction[48-51], DFT-D2 has been widely applied for the theoretical investigation of adsorption [34,52-54] and reaction in zeolites [24,54,55] and is known to provide reasonably accurate results [49,56]. The electronic charge on atoms and fragments were calculated using Bader analysis [57] as implemented by Henkelman et al.[58] Transition state search was performed using Nudged Elastic Band (NEB)[59] and dimer calculations[60-62]. The Nudged Elastic Band (NEB) method was used to find an initial guess for the minimal energy path (MEP), which was used as a starting point for the dimer calculations.

3.2.2.2. Frequency calculations

Normal mode analysis was performed using a Partial Hessian Vibrational Analysis (PHVA), relaxing the T5 cluster ($HAl(SiO_4)_4$) of the zeolite framework and the adsorbate molecule for the numerical Hessian calculation. Previous studies for physisorption and chemisorption in zeolite have shown that the partial hessian approach leads to a marginal difference in the result as compared to a Full Hessian Vibration Analysis (FVHA)[63]. Although very stringent optimization (maximum force criterion of 0.02 eV $Å^{-1}$) and electronic convergence (self-consistency loop convergence criterion of 10^{-8} eV and energy cut-off of 600 eV) criteria have been used, spurious imaginary frequencies were still present for very few cases.

The low lying frequencies (<50 cm^{-1}) associated with the frustrated motions of the surface bound species (such as translation or rotation of the molecule within the zeolite pore structure) could lead to significant error in the entropy calculations[64-67]. A more accurate estimation of the entropic contributions could be obtained by accounting for anharmonicities by detailed scanning of the potential energy surface [68,69], but this would require significant computational efforts for large systems. Another approach to treat the low-lying modes is the use of a frequency cutoff [34,64,65,70]. De Moor et al.[70] studied the entropy contributions of these frequencies for alkanes and alkenes in FAU zeolite and suggested the replacement of these spurious frequencies with 50 cm^{-1} when using the immobile adsorbate approach. Therefore, in order to obtain consistent results, the immobile adsorbate approach was used for all surface species and spurious imaginary and low-lying frequencies were replaced by normal modes of 50 cm^{-1} [70].

3.2.2.3. Statistical thermodynamics

Standard enthalpies, entropies, Gibbs free energies, adsorption and reaction equilibrium coefficients (K) are obtained from total partition functions by statistical thermodynamics calculations[71].

Reaction equilibrium coefficients, *K*, for elementary reactions are calculated as:

$$K(T) = \frac{\prod_i Q_i(N,V,T)}{\prod_j Q_j(N,V,T)} \exp\left(-\frac{\Delta E_r}{RT}\right) \qquad (1)$$

where *i* and *j* denote products and reactants respectively. ΔE_r is the electronic reaction energy at 0 K (including the zero-point vibrational energy) and *Q* the total partition function. The electronic energy from the DFT calculation along with the frequencies obtained from the vibrational analysis are used for the statistical thermodynamic calculation (see section S2 of Appendix B). The partition functions for the gas-phase species included vibrational, rotational and translational degrees of freedom, while only the vibrational contributions were taken into

account for the surface species. As observed from ^{2}H NMR studies on the dynamics of adsorbed t-butanol[72,73] and i-butanol[74] in H-ZSM-5, the presence of hydrogen bonds with the Brønsted acid site and zeolite oxygen tends to significantly reduce the mobility of adsorbed oxygenate species. Thus, one may use the vibrational contributions alone to calculate the total partition function of adsorbed oxygenates[34]. This assumption may not be valid for loosely bound surface species such as physisorbed 1-butene[70] and can lead to differences in mobility of these species within small and large pore zeolites. However, under the low temperature and low conversion regime considered in the present study (acid sites completely occupied by the adsorbed alcohol and ether), using the mobile adsorbate approach[70] for physisorbed 1-butene doesn't significantly alter the overall results (see Figure S2 of Appendix B).

The reaction rate coefficients of elementary reaction steps are calculated on the basis of transition state theory:

$$k_{TST}(T) = \frac{k_B T}{h} \frac{Q_{TS}(N,V,T)}{Q_R(N,V,T)} \exp\left(-\frac{E^{\ddagger}}{RT}\right) \qquad (2)$$

where k_B is Boltzmann constant, h is Planck constant and $E^{\ddagger}$ is the electronic activation barrier at 0 K (including the zero-point vibrational energy). Q_{TS} and Q_R denote the total partition functions of the transition and reactant state respectively. Arrhenius pre-exponential factors (A) and activation energies (E_a) are obtained by regression of Eq. 2 in the temperature range of 300 – 800 K.

The adsorption occurs without any activation barrier. Hence, the reaction rate coefficient for the adsorption step is calculated as $k_{ads} = k_B T/h$, while the reaction rate coefficient for the desorption step is calculated from thermodynamic consistency as $k_{des} = k_{ads}/K_{ads}$.

It is pertinent to note that although all the catalytic cycles are thermodynamically consistent (i.e. sum of reaction enthalpy/entropy for all the elementary steps along a catalytic cycle should match the gas phase reaction enthalpy/entropy), the inherent error associated with DFT

calculation[75] and the harmonic oscillator approximation leads to deviations between the calculated and experimental gas-phase thermochemistry[76]. This errors were accounted for by distributing the total error in the free energy term over the adsorption/ desorption steps as explained in more detail in section S3 of the Appendix B.

3.2.3. Microkinetic modelling

A microkinetic modelling approach has been used to carry out reaction path analysis and to study the effect of reaction conditions (temperature, site time and pressure). Here in, an isothermal plug flow reactor model was used for the reactor simulations. The following continuity equations were applied for the gas-phase components *i* and surface species *k* along with a site balance:

$$\frac{d\theta_k}{dt} = \sum_j \nu_{jk} TOF_j = 0 \qquad (3)$$

$$\theta_* + \sum_k \theta_k = 1 \qquad (4)$$

$$\frac{dF_i}{dW} = R_i = C_t \sum_j \nu_{ji} TOF_j \qquad (5)$$

with $F_i = F_{i,0}$ at $W = 0$

where TOF_j is the turnover frequency of elementary step *j* (mol mol_{H+}^{-1} s^{-1}), ν_{ji} the stoichiometric coefficient of component *i* in the elementary step *j*, θ_k the fractional coverage of surface species *k* (mol mol_{H+}^{-1}), θ_* the fractional coverage of free acid sites (mol mol_{H+}^{-1}), C_t the acid site concentration (mol_{H+} kg^{-1}), F_i the molar flow rate of gas-phase component *i* (mol s^{-1}), *W* the mass of the catalyst (kg), R_i the net production rate of gas-phase species *i* (mol kg^{-1} s^{-1}).

The microkinetic model assumes absence of any diffusion limitation for reactant and product species. The above mentioned set of ordinary differential equations is integrated using the

LSODA module of ODEPACK[77]. The investigated reaction conditions are partial pressure of 1-butanol (10^{-3}-10^{2} kPa), site time ($N_{H+}/F_{BuOH,0}$ = 0-200 mol H^+ s / mol $BuOH_0$) and reaction temperature (400-460 K).

3.3. Results and discussion

3.3.1. Reaction paths for zeolite-catalyzed butanol dehydration

An overview of the reaction network consisting of all the elementary steps considered for the dehydration of 1-butanol in the four zeolites is depicted in Figure 1. This reaction network consists of 10 different mechanisms (m_1 to m_{10}) which are given in Table 1. The adsorbed 1-butanol molecule can undergo a direct dehydration producing 1-butene (path A) or react in a sequential manner to yield di-1-butyl ether (path B) which can further decompose to 1-butene and 1-butanol (path C)[24]. The direct dehydration of butanol to 1-butene (path A) can procced via E1 elimination (m_1), syn-elimination (m_2), anti-elimination (m_3), butoxide formation (m_4) and dimer mediated syn-elimination (m_5). The ether formation (path B) can occur via dimer mediated S_N2 type substitution (m_6), butoxide mediated S_N1 type substitution (m_7) and butoxide mediated S_N2 type substitution (m_8). The ether decomposition (path C) can occur via syn-elimination (m_9) and anti-elimination (m_{10}). Henceforth, reference to any of the elementary reaction steps and mechanisms is done using the numbering scheme presented in Figure 1 and Table 1. A summary of standard reaction enthalpy (ΔH_r^o), reaction entropy (ΔS_r^o), Arrhenius activation energies and pre-exponential factors for each of the elementary steps in H-FAU, H-ZSM-5, H-ZSM-22 and H-FER is listed in Appendix B, Tables S6, S7, S8 and S9, respectively. The structure of all the transition states for all four zeolites are shown in Figure S4-14 of the Appendix B.

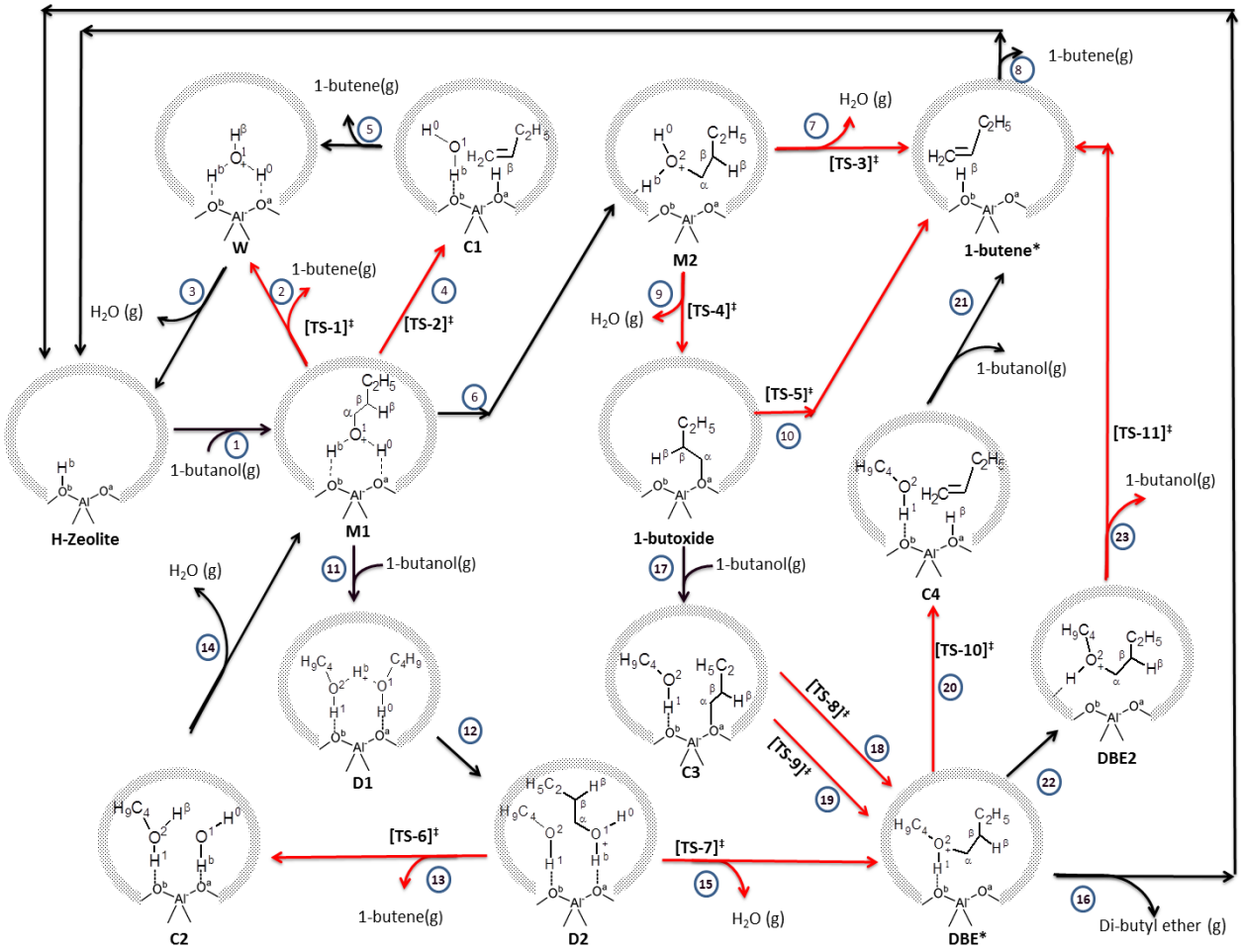

Figure 1: Reaction scheme for conversion of 1-butanol to di-1-butyl ether and 1-butene (adapted from reference[24]). Reaction mechanism and corresponding elementary steps in {}: m_1 -{1,**2**,3}, m_2-{1,**4,**5,3}, m_3-{1,6,**7**,8}, m_4 - {1,6,**9,10,**8}, m_5 - {11,12,**13,**14}, m_6-{1,11,12,**15**,16}, m_7 -{1,6,**9**,17,**18**,16}, m_8 -{1,6,**9**,17,**19**,16}, m_9 -{16,**20**,21,8}, m_{10} -{16,22,**23**,8}. Transition state (TS): TS-1 (E1 elimination), TS-2 (syn-elimination), TS-3 (anti-elimination), TS-4 (S_N2 substitution), TS-5 (deprotonation), TS-6 (butanol-assisted syn-elimination), TS-7 (S_N2 substitution), TS-8 (S_N1 substitution) , TS-9 (S_N2 substitution), TS-10 (syn-elimination) , TS-11 (anti-elimination). All the elementary steps are considered reversible. The black and red arrows represent the non-activated and activated steps, respectively.

Table 1. Elementary steps (step 1- step 23) and reaction mechanisms (m_1-m_{10}) for the butanol dehydration reaction. Non-equilibrated steps are indicated with bold stoichiometric numbers[24].

		Path A					Path B			Path C	
	Mechanism #	m_1	m_2	m_3	m_4	m_5	m_6	m_7	m_8	m_9	m_{10}
1	1-BuOH(g) + ∗ ↔ M1	1	1	1	1	0	1	1	1	0	0
2	M1 ↔ W + 1-Butene$_{(g)}$	**1**	0	0	0	0	0	0	0	0	0
3	W ↔ H2O(g) + *	1	1	0	0	0	0	0	0	0	0
4	M1 ↔ C1	0	**1**	0	0	0	0	0	0	0	0
5	C1 ↔ W + 1-Butene$_{(g)}$	0	1	0	0	0	0	0	0	0	0
6	M1 ↔ M2	0	0	1	1	0	0	1	1	0	0
7	M2↔ 1-Butene*+ H2O$_{(g)}$	0	0	**1**	0	0	0	0	0	0	0
8	1-Butene* ↔ 1-Butene$_{(g)}$+ ∗	0	0	1	1	0	0	1	1	1	1
9	M2↔ Butoxy + H2O$_{(g)}$	0	0	0	**1**	0	0	**1**	**1**	0	0
10	Butoxy ↔ 1-Butene*	0	0	0	**1**	0	0	0	0	0	0
11	M1 + BuOH$_{(g)}$↔ D1	0	0	0	0	1	1	0	0	0	0
12	D1 ↔ D2	0	0	0	0	1	1	0	0	0	0
13	D2↔ C2+1-Butene$_{(g)}$	0	0	0	0	**1**	0	0	0	0	0
14	C2 ↔ M1 + H2O$_{(g)}$	0	0	0	0	1	0	0	0	0	0
15	D2 ↔ DBE* + H2O$_{(g)}$	0	0	0	0	0	**1**	0	0	0	0
16	DBE* ↔ DBE$_{(g)}$+ ∗	0	0	0	0	0	1	1	1	-1	-1
17	Butoxy + BuOH$_{(g)}$↔ C3	0	0	0	0	0	0	1	1	0	0
18	C3↔ DBE* (S_N2)	0	0	0	0	0	0	**1**	0	0	0
19	C3↔ DBE* (S_N1)	0	0	0	0	0	0	0	**1**	0	0
20	DBE* ↔ C4	0	0	0	0	0	0	0	0	**1**	0
21	C4 ↔ 1-Butene*+ BuOH$_{(g)}$	0	0	0	0	0	0	0	0	1	0
22	DBE* ↔ DBE2	0	0	0	0	0	0	0	0	0	1
23	DBE2↔ 1-Butene*+ BuOH$_{(g)}$	0	0	0	0	0	0	0	0	0	**1**

Path A	(mechanism # m_1-m_5)	**1-BuOH$_{(g)}$ ↔ 1-Butene$_{(g)}$+H2O$_{(g)}$**
Path B	(mechanism # m_6-m_8)	**1-BuOH$_{(g)}$+1-BuOH$_{(g)}$ ↔ DBE$_{(g)}$+H2O$_{(g)}$**
Path C	(mechanism # m_9-m_{10})	**DBE$_{(g)}$ ↔ 1-Butene$_{(g)}$+1-BuOH$_{(g)}$**

3.3.1.1. Direct dehydration of 1-butanol to butene (path A)

Five possible reaction mechanisms are envisaged for the direct dehydration of 1-butanol to 1-butene (path A), of which four are monomolecular (m_1, m_2, m_3 and m_4) and one is bi-molecular (m_5). All the path A mechanisms start with the adsorption and protonation of butanol in the zeolite (step 1), forming chemisorbed butanol monomer M1[24]. The first reaction mechanism m_1 consists of the sequence of steps 1, 2 and 3. Step 2 of mechanism m_1 is activated and follows an E1 type elimination with heterolytic cleavage of the C_α–O bond followed by a deprotonation at the β-carbon and involves formation of a carbenium ion like transition state (see TS-1, Figure S4 of Appendix B). The second reaction mechanism m_2 consists of steps 1, 4, 5 and 3, of which step 4 is activated and occurs via a syn-elimination with concerted cleavage of the C_α–OH_2 and C_β–H_β bonds (see TS-2, Figure S5 of Appendix B). The third mechanism m_3 consists of steps 1, 6, 7 and 8, of which steps 7 is activated and follows a concerted anti-elimination (see TS-3, Figure S6 of Appendix B). The fourth reaction mechanism m_4 consists of steps 1, 6, 9,10 and 8, of which steps 9 (via TS-4) and 10 (via TS-5) are activated. Step 9 involves a S_N2 type nucleophilic substitution of the –OH2 group of the protonated butanol monomer by the zeolite oxygen leading to the formation of surface-bound butoxide, which deprotonates in step 10 to form physisorbed 1-butene (see TS-4 and TS-5, Figure S7 and S8 of Appendix B). The fifth reaction mechanism m_5 involves formation of butanol dimer (step 11) and consists of steps 11, 12, 13 and 14, of which steps 13 is activated and follows a butanol assisted concerted syn-elimination (see TS-6, Figure S9 of Appendix B). All elimination steps were found to have a late transition states with pronounced E1 character, i.e. the extent of C_α –O bond breakage is more pronounced than C_β–H_β bond breakage[24]. A detailed comparison of the standard free energy diagram for the five path A reaction mechanisms is available in Appendix B (Figures S16, S19, S22 and S25 for H-FAU , H-ZSM-5, H-ZSM-22 and H-FER, respectively).

3.3.1.2. Dehydration of 1-butanol to di-1-butyl ether (path B)

Three possible reaction mechanisms (m_6, m_7 and m_8) are considered for the DBE formation path (path B). DBE formation can occur via the butanol dimer-mediated mechanism m_6 or via the butoxide mediated mechanisms m_7 and m_8. The reaction mechanism m_6 involves formation of butanol dimer (step 11) and consists of the sequence of steps 1, 11, 12, 15 and 16, of which step 15 is activated and follows an S_N2 type nucleophilic substitution (see TS-7, Figure S10 of the Appendix B) leading to formation of protonated DBE (DBE*). The butoxide mediated mechanism m_7 consists of the sequence of steps 1, 6, 9, 17, 18 and 16, of which steps 9 and 18 are activated. The activated step 9 leading to formation of butoxide (via TS-4) is also involved in mechanism m_4 (see section 3.1.1.). The activated step 18 follows an S_N2 type nucleophilic substitution (see TS-8, Figure S11 of the Appendix B), where the oxygen atom (O_2) of the protonated butanol attacks the primary carbon atom (C_α) of the butoxide leading to formation of protonated DBE (DBE*). Another butoxide mediated mechanism m_8 consists of the sequence of steps 1, 6, 9, 17, 18 and 16 and is similar to mechanism m_7 except that it involves an S_N1 type nucleophilic substitution (step 19, see TS-8, Figure S12 of the Appendix B) instead of the S_N2 type nucleophilic substitution (step 18) of m_7. A detailed comparison of the standard free energy diagrams for path B mechanisms is available in the Appendix B (Figures S17, S20, S23 and S26 for H-FAU , H-ZSM-5, H-ZSM-22 and H-FER, respectively).

3.3.1.3. Di-1-butyl ether decomposition (path C)

For the DBE decomposition (path C) two possible mechanisms m_9 and m_{10} are considered. Mechanism m_9 consists of the steps 16, 20, 21 and 8, of which step 20 is activated and follows a concerted syn-elimination (see TS-10, Figure S13 of Appendix B). Mechanism m_{10} involves steps 16, 22, 23 and 8, of which step 23 is activated and follows a concerted anti-elimination (see TS-11, Figure S14 of Appendix B). A comparison of the standard free energy diagrams

for path C mechanisms is available in the Appendix B (Figures S18, S21, S24 and S27 for H-FAU, H-ZSM-5, H-ZSM-22 and H-FER, respectively).

3.3.2 Microkinetic modelling and reaction path analysis:

A detailed microkinetic model involving the 10 different mechanisms, consisting of 23 elementary steps (see Figure 1) has been considered without making any assumption for the rate determining step. Model parameters are given in Tables S6, S7, S8 and S9, for H-ZSM-5, H-FAU, H-ZSM-22 and H-FER, respectively. The effect of reaction conditions, viz., partial pressure of 1-butanol (10^{-3}-10^{2} kPa), site time ($N_{H+}/F_{BuOH,0}$ = 0-200 mol H^+ s / mol $BuOH_0$) and reaction temperature (400-460 K), is studied. The studied conversion range is limited to 30% since at higher conversions butane isomerization might occur which is not included in the current microkinetic modelling.

A comparison of the forward, reverse and net reaction rates for the different elementary steps over a wide range of reaction conditions has been used to identify rate limiting, quasi-equilibrated and non-equilibrated steps along each mechanism. The same quasi-equilibrated and non-equilibrated steps were found for all four zeolites as indicated in Table 1 and are consistent with the theoretical results for 1-butanol dehydration in H-ZSM-5[24]. In order to verify the reliability of the DFT calculations, a comparison is made with the experimental observation for 1-butanol dehydration in H-ZSM-5 [12]. The activation barrier for 1-butanol dehydration and DBE decomposition in H-ZSM-5 with respect to adsorbed intermediates (M1 and DBE*) are found to be 135 and 140 kJ/mol [24] as compared to experimentally reported value of 138 ± 8 kJ/mol [12] for both reactions. Moreover, a direct comparison of the TOF for the production of DBE and butene in H-ZSM-5 indicate a good agreement with the experimental observations[12] (see Table S2 of Appendix B).

Different zeolite frameworks can offer a different environment for stabilization of intermediates and transition states, which can lead to differences in reaction rates, MARI and

dominant reaction mechanism. In what follows, detailed microkinetic simulations and reaction path analysis are used to identify the dominant reaction mechanisms and to provide insight in the effect of reaction conditions on 1-butanol dehydration in the different zeolites.

3.3.2.1. Effect of site time and conversion

The influence of zeolite framework on its catalytic activity is studied at identical site time, while the effect of zeolite framework on product selectivity, TOFs and surface coverages is compared at identical conversion. The difference in zeolite performance is compared at several conversion levels by systematically varying the site time at constant temperature (450 K) and inlet butanol partial pressure (10 kPa). As seen from Figure 2, the investigated zeolites show significant differences in catalytic activity and product selectivity. The turn over frequency (TOF) for consumption of 1-butanol increases in the order H-FER < H-FAU < H-ZSM-22 < H-ZSM-5 (see Figure 2a and 2b). The higher TOF for H-ZSM-5 is in agreement with experimental results[14] for ethanol dehydration on different zeolites (H-FER, H-ZSM-5, H-MOR, H-BEA, H-Y and H-USY). All four zeolites show an increase in butene selectivity with increase in site time/conversion (see Figure 2 c). At extremely low conversion ($X \rightarrow 0$), H-ZSM-5, H-ZSM-22 and H-FER tend to selectively produce DBE (see Figure 2 d). Interestingly, 1-butanol dehydration in H-FAU depicts a significant butene selectivity even at extremely low conversion level ($X \rightarrow 0$). This is indicative of a difference in underlying reaction mechanism for H-FAU as compared to the other three zeolites. In general, H-ZSM-5 and H-ZSM-22 favor the production of DBE, while H-FER and H-FAU provide higher selectivity to butene. These results are consistent with the higher ethene selectivity for H-FER and H-FAU reported by Phung et al.[14] for ethanol dehydration on different zeolites. These authors also observed a higher ether yield for H-ZSM-5 under moderate reaction temperatures as used in our study.

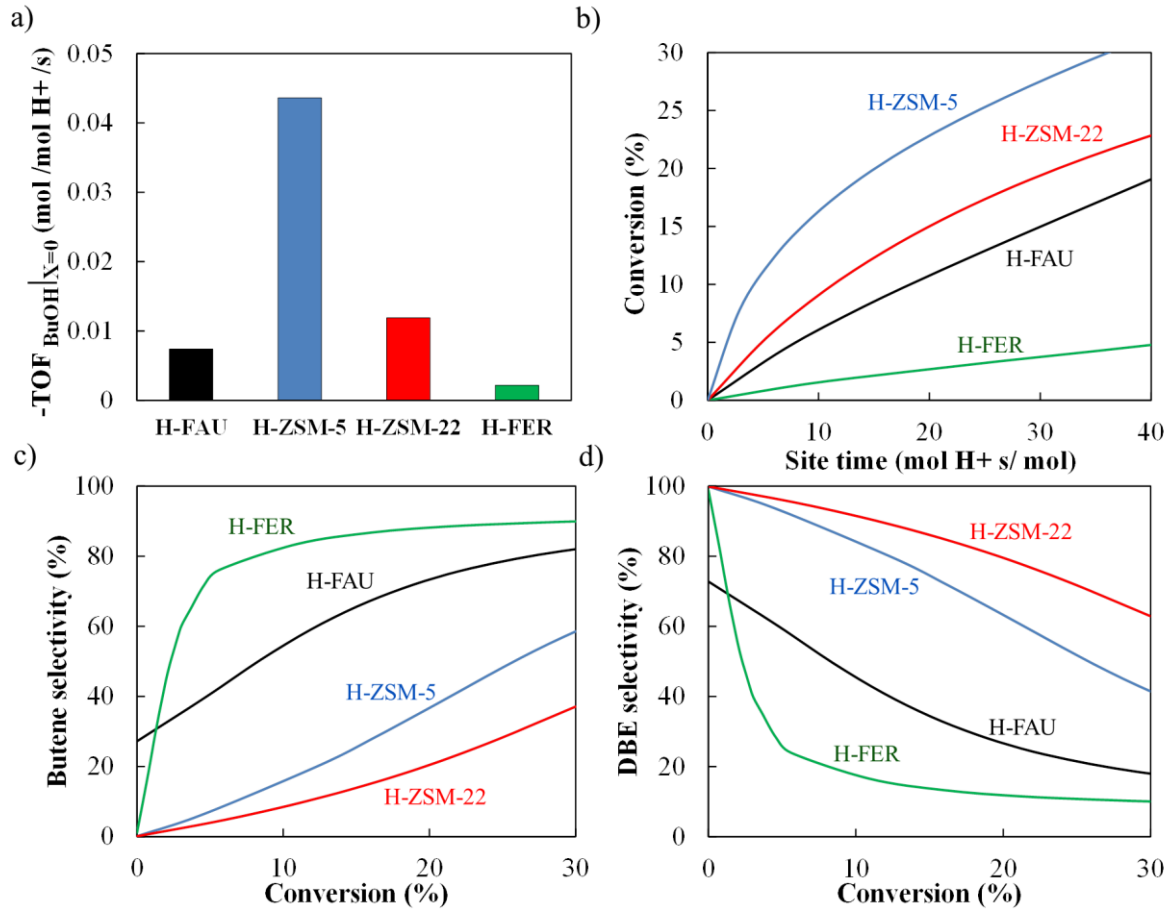

Figure 2: Comparison of different zeolites based on a) TOF for consumption of 1-butanol at zero conversion (X = 0), b) conversion as a function of site time, c) 1-butene selectivity as a function of conversion, d) DBE selectivity as a function of conversion. Reaction conditions: 450K, butanol feed partial pressure of 10 kPa. (these results correspond to plug-flow reactor simulations (Eqs. 3-5) with the ab-initio based microkinetic model. See Tables S6, S7, S8 and S9, for H-ZSM-5, H-FAU, H-ZSM-22 and H-FER, respectively, for the model parameters)

The TOFs for different reaction paths within different zeolites are used to explain the simulated and experimentally observed activity and selectivity profiles. Figure 3 depicts the TOFs as function of conversion for the different reaction paths (path A- direct dehydration of 1-butanol to butene, path B - dehydration of 1-butanol to DBE, path C – DBE decomposition) for H-FAU, H-ZSM-5, H-ZSM-22 and H-FER. For H-ZSM-5, H-ZSM-22 and H-FER, 1-butanol conversion mainly occurs via the path B mechanisms leading to DBE with a very limited contribution of the path A mechanisms leading to direct butene formation ($TOF_{pathB}/TOF_{pathA} < 10^2$). In contrast, in H-FAU the path A mechanisms, and in particular

mechanism m_3 (see Figure 4), significantly contribute to the butanol conversion which explains its higher butene selectivity even at extremely low conversion levels (X→0). Although, H-ZSM-5, H-ZSM-22 and H-FER follow an ether-mediated reaction scheme (path B followed by path C), these three zeolites differ in the conversion level at which the TOF for ether decomposition becomes comparable to the TOF for the ether formation (see Figure 3). For H-FER, the rate of ether formation becomes comparable to the rate of its decomposition from very low conversion (< 3%) onwards, which explains the higher butene selectivity of H-FER for butanol dehydration.

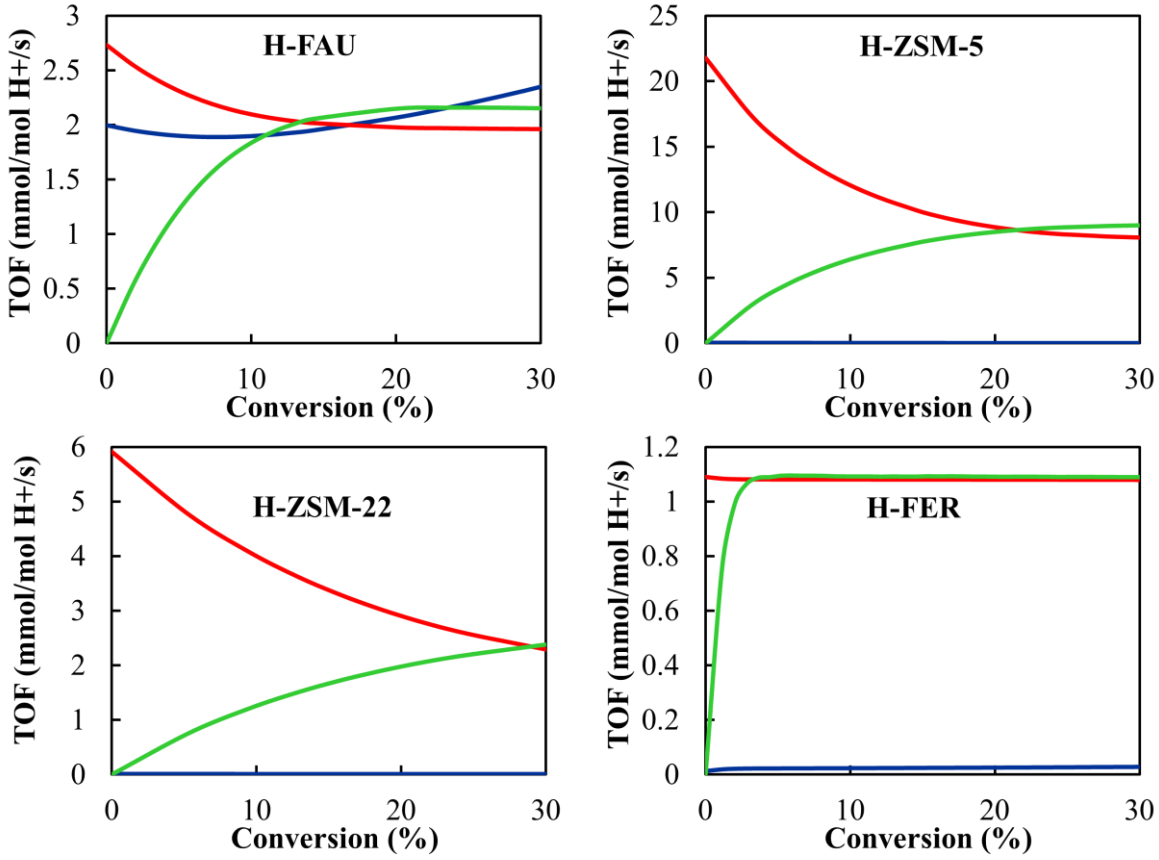

Figure 3: Comparison of 1-butanol dehydration paths for different zeolites (H-FAU, H-ZSM-5, H-ZSM-22 and H-FER) as a function of 1-butanol conversion at reaction temperature of 450K and 1-butanol feed partial pressure of 10 kPa. Reaction paths : direct dehydration path (path A —), DBE formation path (path B —) and DBE decomposition path (path C —). (These results correspond to plug-flow reactor simulations (Eqs. 3-5) with the ab-initio based microkinetic model. See Tables S6, S7, S8 and S9, for H-ZSM-5, H-FAU, H-ZSM-22 and H-FER, respectively, for the model parameters).

Understanding the influence of zeolite framework on the underlying reaction mechanism is important for identification of key intermediates and reaction steps. Moreover, it allows to rationalize why butene or DBE is the favored within a specific zeolite framework. Figure 4 depicts the TOFs for the different reaction mechanisms associated with path A (m_1, m_2, m_3, m_4, m_5), B (m_6, m_7, m_8) and C (m_9, m_{10}) as function of conversion for H-FAU, H-ZSM-5, H-ZSM-22 and H-FER. Figure 4 shows that the preferred mechanism for direct butene formation from butanol (path A) is not the same in the four zeolites. In H-FAU and H-ZSM-22, direct butanol dehydration to butene proceeds predominantly via the monomolecular mechanism m_3 involving anti-elimination (TS-3). For H-ZSM-5, the mechanism m_3 shows the highest TOF amongst the four monomolecular path A mechanisms (m_1-m_4), but due to the higher surface coverage of butanol dimer (see coverage for D1 in Figure S29 of Appendix B) direct butene formation via the dimer-mediated mechanism m_5 involving syn-elimination (TS-6) is favored. On the other hand, in H-FER steric constraints on the formation of the larger anti-elimination transition state (TS-3; see Figure of S15 of Appendix B) make the mechanism m_3 less favorable as compared to the butoxide-mediated mechanism m_4 involving an S_N2 type substitution (TS-4).

The DBE formation path (path B) remains dominant at low conversion levels (< 3%) for all zeolites owing to the higher concentration of butanol dimer D1 (see coverage for D1 in Figure S29 of Appendix B). For path B, the dimer-mediated mechanism m_6 involving S_N2 type substitution (TS-7) remains the dominant mechanism for all four zeolites. As expected, DBE decomposition (path C) gains importance with increasing conversion and proceeds predominantly via mechanism m_9 involving syn-elimination (TS-10) except for H-FAU, where comparable contributions are observed for mechanism m_9 and m_{10} that occurs via an anti-elimination (TS-11).

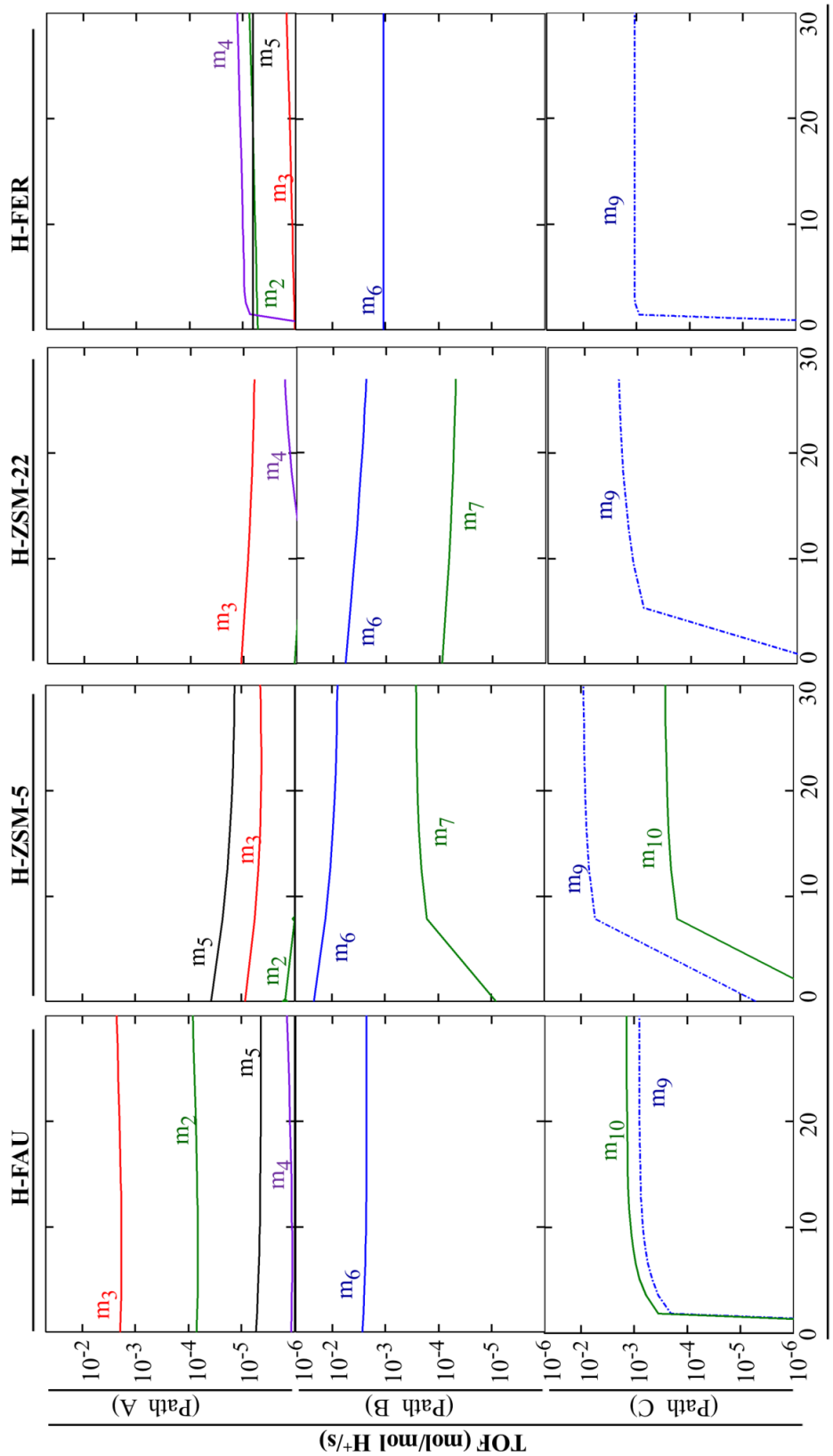

Figure 4: Turn over frequencies (TOF) for different reaction mechanisms (m_1-m_{10}, see Figure 1 and Table 1 for the elementary steps associated with each mechanism) as a function of 1-butanol conversion feed butanol partial pressure of 10 kPa and reaction temperature of 450K. (These results correspond to plug-flow reactor simulations (Eqs. 3-5) with the ab-initio based microkinetic model. See Tables S6, S7, S8 and S9, for H-ZSM-5, H-FAU, H-ZSM-22 and H-FER, respectively, for the model parameters. Mechanisms having TOF lower than 10^{-6} are not shown in the figure)

The difference in activity and selectivity for the different zeolites can be rationalized on the basis of the stabilization of the reaction intermediates/TS in the zeolite pores. To explain the simulated activity and selectivity trends, simplified standard free energy diagrams (see Figure 5) consisting of representative mechanisms, one from each reaction path (m_3, m_6 and m_9 for path A, B and C, respectively) are considered. The standard Gibbs free energies of transition states ($\Delta G^{0\ddagger}$) with respect to the relevant reactants contains an enthalpic ($\Delta H^{0\ddagger}$) and an entropic ($\Delta S^{0\ddagger}$) contribution that is shown in Figure S28 of Appendix B. At low conversion levels, D1 is the most abundant surface intermediate (MARI) (see Figure S29 in Appendix B), and the initial TOFs are governed by DBE formation. Hence, the zeolite which stabilizes better the transition state for DBE formation, would lead to the highest initial rates. The simulated activity trend (see Figure 2a) can be explained on the basis of the standard free energy diagrams (see Figure 5), comparing the stability of TS7 (mechanisms m_6) relative to D1. At 450 K, H-ZSM-5 offers the lowest standard free energy barrier for DBE formation followed by H-ZSM-22, H-FAU and H-FER ($\Delta G^{0o}{}_B{}^{\ddagger} = \Delta G^{0o}{}_{TS7\text{-}D1}{}^{\ddagger}$ = 126, 131, 136 and 137 kJ/mol, respectively), explaining the higher activity of H-ZSM-5 as compared to the other zeolites.

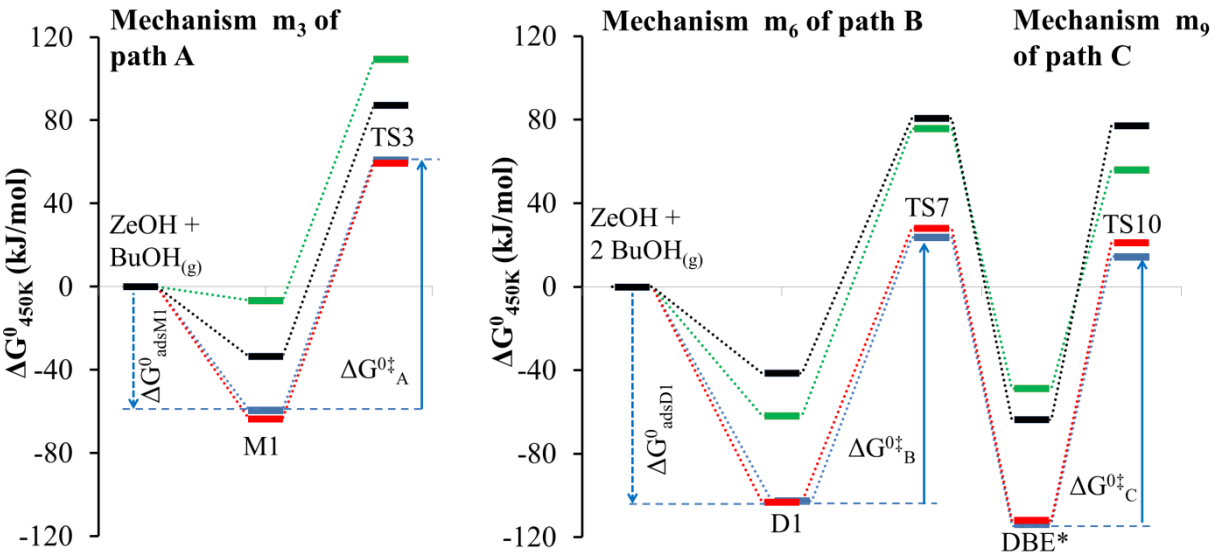

Figure 5: Standard Gibbs free energy profile for direct dehydration of butanol (via mechanism m_3, involving anti-elimination (TS3)), ether formation (via mechanism m_6, involving S_N2 type substitution (TS7)) and ether decomposition (via mechanism m_9, involving syn-elimination (TS10)) over different zeolites (H-FAU ─, H-ZSM-5 ─, H-ZSM-22 ─, H-FER ─) at 450K. $\Delta G^0_A{}^{\ddagger} = \Delta G^0_{TS3\text{-}M1}{}^{\ddagger}$, $\Delta G^0_B{}^{\ddagger} = \Delta G^0_{TS7\text{-}D1}{}^{\ddagger}$ and $\Delta G^0_C{}^{\ddagger} = \Delta G^0_{TS10\text{-}DBE}{}^{\ddagger}$. (These results are also listed in Table S10 of Appendix B)

Reaction path A and C lead to the production of butene and the zeolite providing higher TOFs for the mechanisms associated with these paths would provide higher butene selectivity. For mechanism m_3 (of path A), all the four zeolites have similar free energy activation barriers ($\Delta G^o_A{}^{\ddagger} = \Delta G^o_{TS3\text{-}M1}{}^{\ddagger}$ = 121, 120, 123 and 116 kJ/mol for H-FAU, H-ZSM-5, H-ZSM-22 and H-FER, respectively) and, hence, butene formation via this mechanism is governed by the surface coverage of butanol monomer (M1). As butanol monomer (M1) and dimer (D1) are quasi-equilibrated, the surface coverage of M1 is governed by the relative stability of M1 with respect to D1 and the reaction conditions (butanol partial pressure and reaction temperature). While at 450 K, D1 is some 20 kJ/mol more stable than M1 in H-FAU, the free energy difference between M1 and D1 is in the range of 40 to 55 kJ/mol for the other zeolites. This indicates a weaker stabilization of D1 in H-FAU and can be attributed to the relatively lower dispersive stabilization of adsorbed dimer in the large pore zeolite as compared to the medium pore zeolites. Moreover, the higher free energy barrier of 134 kJ/mol for DBE formation via mechanism m_6 ($\Delta G^o_{TS7\text{-}D1}$) as compared to 121 kJ/mol for direct dehydration via mechanism

m_3 ($\Delta G^{o}_{TS3\text{-}M1}$) in H-FAU indicates that in H-FAU the direct dehydration path (path A) can be preferred provided the surface coverages of M1 and D1 are of the same order of magnitude. In the considered simulation conditions, the M1 coverage in H-FAU is significantly higher than in the other zeolites explaining its preference for direct butene formation (path A) via mechanism m_3 and higher butene selectivity for 1-butanol dehydration. On the other hand, in H-ZSM-5, H-ZSM-22 and H-FER, which exhibit consecutive reaction involving 1-butanol dehydration to DBE followed by DBE decomposition, the product selectivity is governed by the free energy barrier for the DBE decomposition step ($\Delta G^{o}_{TS10\text{-}DBE}{}^{\ddagger}$ = 128,132 and 105 kJ/mol for H-ZSM-5, H-ZSM-22 and H-FER, respectively). Amongst all four zeolite, H-FER offers the lowest free energy barrier for DBE decomposition via m_9. Moreover, the steric constrains imposed by the partial confinement in the 8 MR in H-FER leads to a lower relative stability for DBE* ($\Delta G°_{adsDBE}$ of -32, -97 and -95 kJ/mol for H-FER, H-ZSM-5 and H-ZSM-22, respectively at 450 K), making it a reactive intermediate that decomposes readily which explains the higher butene selectivity for H-FER.

This first principles microkinetic modelling analysis thus provides the first theoretical explanation for the experimental observation[14] that H-FAU and H-FER with significantly differing pore sizes, dimensionality and channel structure yield a similar selectivity pattern and provide higher butene selectivity as compared to H-ZSM-5 and H-ZSM-22. In the large pore H-FAU, the weaker dispersive stabilization of the D1 dimer makes that the surface coverage of the M1 monomer becomes significant and that butene formation by direct butanol dehydration via a concerted anti elimination (m_3) can successfully compete with DBE formation and its further decomposition to butene. In H-FER, on the other hand, steric constraints imposed by the 8-MR channels decrease the stability of the protonated DBE favoring its further decomposition to butene via a concerted syn-elimination (m_9) of butanol.

Such insights on the effect of zeolite framework on the stability of reaction intermediates and transition states can provide guidelines for a rational catalyst design.

3.3.2.2. Effect of reaction temperature and butanol partial pressure

Reaction conditions can play an important role in determining the key surface species, dominant reaction mechanism and pathway[24]. Moreover, there can be significant differences in reaction conditions in experiments used for understanding different phenomena at different scales, which can lead to conflicting observations. Mechanistic insights from the DFT based microkinetic simulations in a wide range of conditions can serve as a tool to reconcile conflicting experimental observations. Accordingly, DFT based microkinetic simulations are used to study the effect of reaction temperature and butanol partial pressure for 1-butanol dehydration in different zeolites.

Effect of reaction temperature: The effect of temperature on product selectivity, surface coverage and TOFs is investigated in the temperature range of 400-460 K and compared at an iso-conversion level of 10%. For all four zeolites, DBE remains the dominant product at temperatures below 400K, and the selectivity shifts towards the production of butene with an increase in temperature (see Figure 6 a-b). This trend is consistent with the low temperature[12,13] and high temperature[78,79] experimental results reported in literature.

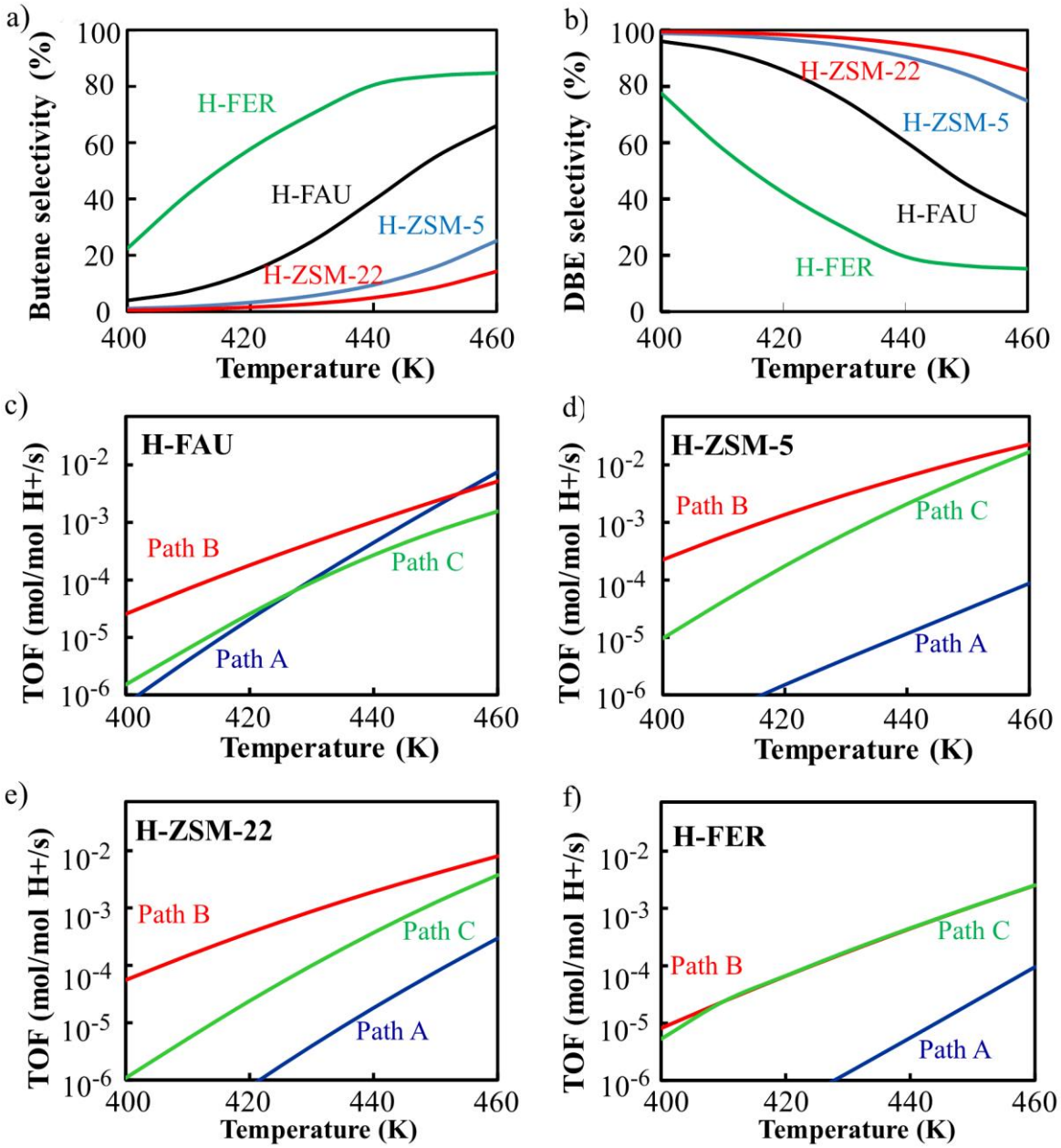

Figure 6: Effect of reaction temperature on a) 1-butene selectivity and b) DBE selectivity over different zeolites. Comparison of 1-butanol dehydration paths in c) H-FAU, d) H-ZSM-5, e) H-ZSM-22 and f) H-FER as function of reaction temperature. Inlet partial pressure of butanol: 10 kPa, site time adjusted in the range of 0-100 (mol/ mol H+ /s) so as to attain a conversion of 10%. Reaction paths: path A - direct dehydration, path B - DBE formation and path C - DBE decomposition. (These results correspond to plug-flow reactor simulations (Eqs. 3-5) with the ab-initio based microkinetic model. See Tables S6, S7, S8 and S9, for H-ZSM-5, H-FAU, H-ZSM-22 and H-FER, respectively, for the model parameters).

Figure 6 c-f shows the effect of reaction temperature on the TOFs for different reaction paths for the four zeolites at a conversion level of 10%. An increase in reaction temperature leads to a shift in the relative contributions from DBE formation (path B) to direct butene formation

(path A) which is particularly prominent for H-FAU, where mechanism m_3 (path A) tends to dominate at temperatures above 460 K (see Figure 7, $TOFm_3/TOFm_6 = 10^{-4}$, 0.8 and 1.4 at 400, 450 and 460K, respectively). This can be understood on the basis of the decrease in surface coverage of adsorbed dimer with increasing temperature[24], leading to a decrease in the relative contribution from the dimer mediated path B. The equilibrium coefficient for the formation of butanol dimer (D1) from adsorbed monomer (M1) and gas phase butanol (K_{11}), decreases from 175 to 2.8 $(kPa)^{-1}$ with an increase in temperature from 400 to 460 K. This, in turn, leads to a decrease in the surface coverage of butanol dimer (D1) and to the predominance of the direct dehydration from butanol monomer to butene in H-FAU at higher temperatures. For H-ZSM-5, H-ZSM-22 and H-FER, path A starts to contribute to butene formation at much higher temperatures as seen from the slope of TOF vs temperature curves in Figure 6 c-f. This difference associated with different zeolites is a consequence of differences in stability of butanol monomer (M1) and dimer (D1) within different zeolites as will be discussed later in more detail.

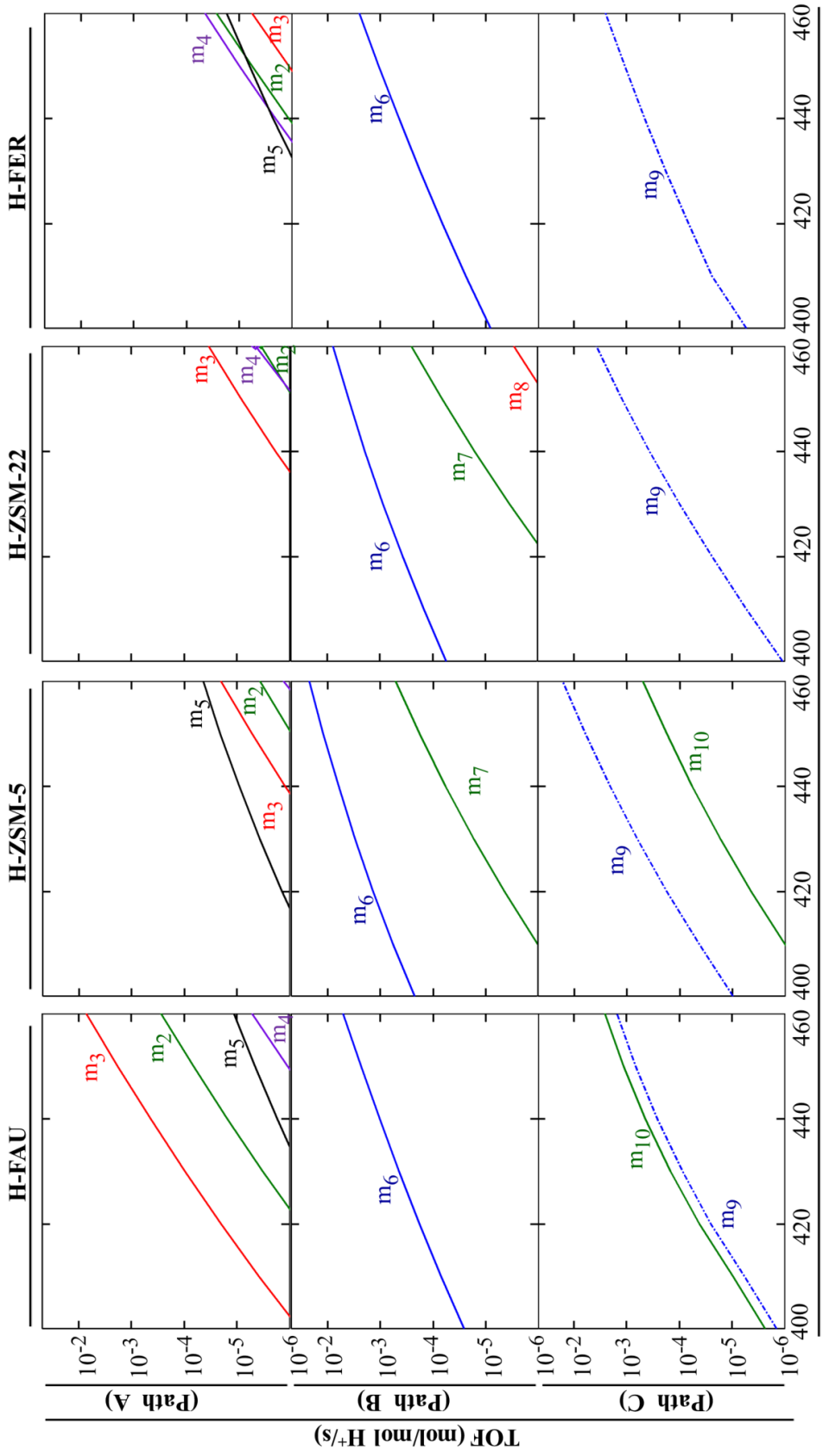

Figure 7. Turn over frequencies (TOF) for different reaction mechanisms (m1-m10, see Figure 1 and Table 1 for the elementary steps associated with each mechanism) as a function of reaction temperature at a constant conversion of 10% and feed butanol partial pressure of 10 kPa. (These results correspond to plug-flow reactor simulations (Eqs. 3-5) with the ab-initio based microkinetic model. See Tables S6, S7, S8 and S9, for H-ZSM-5, H-FAU, H-ZSM-22 and H-FER, respectively, for the model parameters. Mechanisms having TOF lower than 10^{-6} are not shown in the figure).

Figure 7 shows that in H-FAU and H-ZSM-22 the monomolecular mechanism m_3 remains dominant for the direct butene formation path over the entire temperature range. In H-ZSM-5, direct butene formation occurs mainly via the bimolecular mechanism m_5 over the entire temperature range, while in H-FER, m_4, m_5 and m_2 are contributing more or less equally to direct butane formation. Under the investigated temperature range, mechanism m_6 remains the dominant mechanism for DBE formation in the four zeolites. For DBE decomposition, the dominant mechanism (m_9, viz. m_{10}/m_9 in H_FAU) for the different zeolites remains the same as the ones discussed in section 3.3.1.

Effect of butanol partial pressure: Dehydration reaction is studied in a wide range of butanol partial pressure (10^{-3} to 100 kPa) so as to capture different possible experimental conditions. Figure 8 a-b depicts the effect of butanol feed partial pressure on DBE and butene selectivity for the four zeolites at a conversion of 10%. Higher butanol partial pressure leads to higher surface coverage for butanol dimer (D1), which prefers to dehydrate to ether via reaction path B. Likewise, lower butanol partial pressures favor butanol monomer (M1) leading to formation of 1-butene via monomolecular path A mechanisms. This dependence of the selectivity profile on the butanol partial pressure remains valid for all four zeolites and is consistent with the experimentally reported trend of decreased alkene yield with increasing alcohol partial pressure [13,29].

Figure 8 c-f shows that for all four zeolites, path A remains dominant at low butanol partial pressure ($P_{BuOH,0} < 10^{-2}$ kPa) and shifts in favor of path B with increasing butanol partial pressure. The effect of butanol feed partial pressure on TOFs for the different mechanism associated with path A, B and C for the four zeolites is shown in Figure 9.

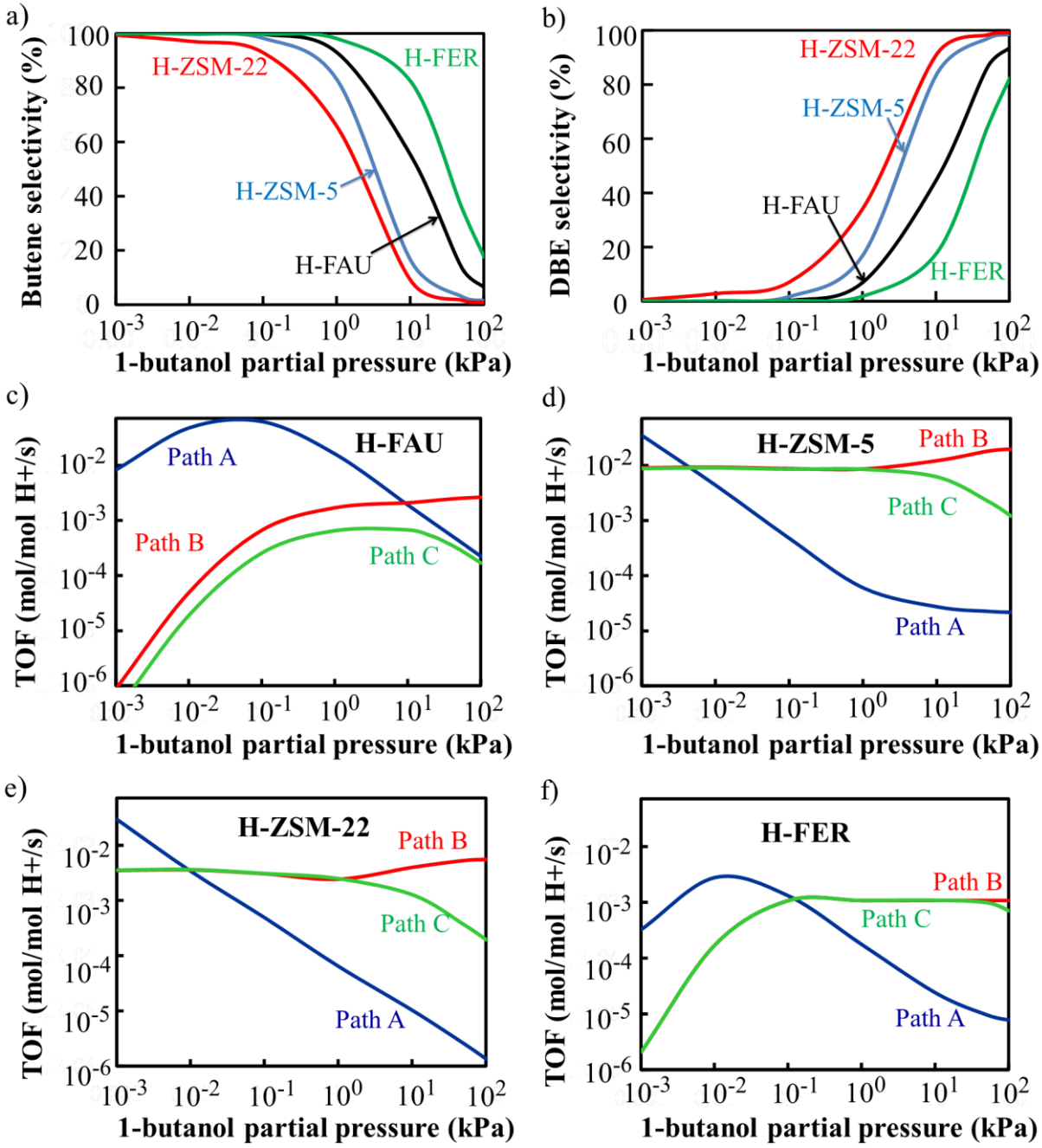

Figure 8: Effect of feed butanol partial pressure on a) 1-butene selectivity and b) DBE selectivity over different zeolites. Comparison of 1-butanol dehydration paths in c) H-FAU, d) H-ZSM-5, e) H-ZSM-22 and f) H-FER as function of feed butanol partial pressure. Reaction temperature: 450K, site time adjusted in the range of 0-100 (mol/ mol H+ /s) so as to attain a conversion of 10%. Reaction paths: path A-direct dehydration, path B -DBE formation and path C - DBE decomposition. (These results correspond to plug-flow reactor simulations (Eqs. 3-5) with the ab-initio based microkinetic model. See Tables S6, S7, S8 and S9, for H-ZSM-5, H-FAU, H-ZSM-22 and H-FER, respectively, for the model parameters).

For path A, mechanism m_3 remains the dominant mechanism (TOF_{m3} ~ 95% of $TOF_{path\ A}$) in H-FAU in the entire 1-butanol pressure range (10^{-3} to 10^{2} kPa) considered. In H-ZSM-5,

mechanism m_3 remains dominant up to a 1-butanol partial pressure of 1 kPa with m_3 contributing to about 53-75% to the TOF of path A. At 1-butanol partial pressures above 10 kPa, there is a significant decrease in contributions from all the monomolecular path A mechanisms (m_2-m_4) in favor of the bimolecular mechanism m_5, with a contribution of ~75-95 % to the TOF of path A. In H-ZSM-22, mechanism m_4 is dominant at 1-butanol partial pressures < 10^{-2} kPa (TOF_{m4} ~ 80% of TOF path A) which shifts in favor of mechanism m_3 with increasing butanol partial pressure (TOF_{m3} contributes to ~70-87 % to the TOF of path A in the P_{BuOH} range of 1-100 kPa). In H-FER at 1-butanol partial pressure below 1 kPa, TOF_{m2} and TOF_{m4} contribute to about ~34 % and ~57%, respectively, to the TOF of path A. With increase in 1-butanol partial pressure from 10 to 10^2 kPa, the preference shifts in favor of the bimolecular mechanism m_5 and the contribution of m_5 to path A increases from 27 to 82 %. For all the four zeolite, a regime of negative order pressure dependence is seen at moderate to high pressure (see Figure 8c-f) and is consistent with the experimental observation of Chiang and Bhan [13] for ethanol dehydration within zeolites and of Macht et al. for 2-butanol dehydration on POM[16]. Within the range of our simulation, a zero order pressure dependence is clearly seen for H-ZSM-5 above 10 kPa butanol partial pressure (see Figure 8d). Such a profile has been reported by Zhi et al. for 1-propanol dehydration in H-ZSM-5[29].

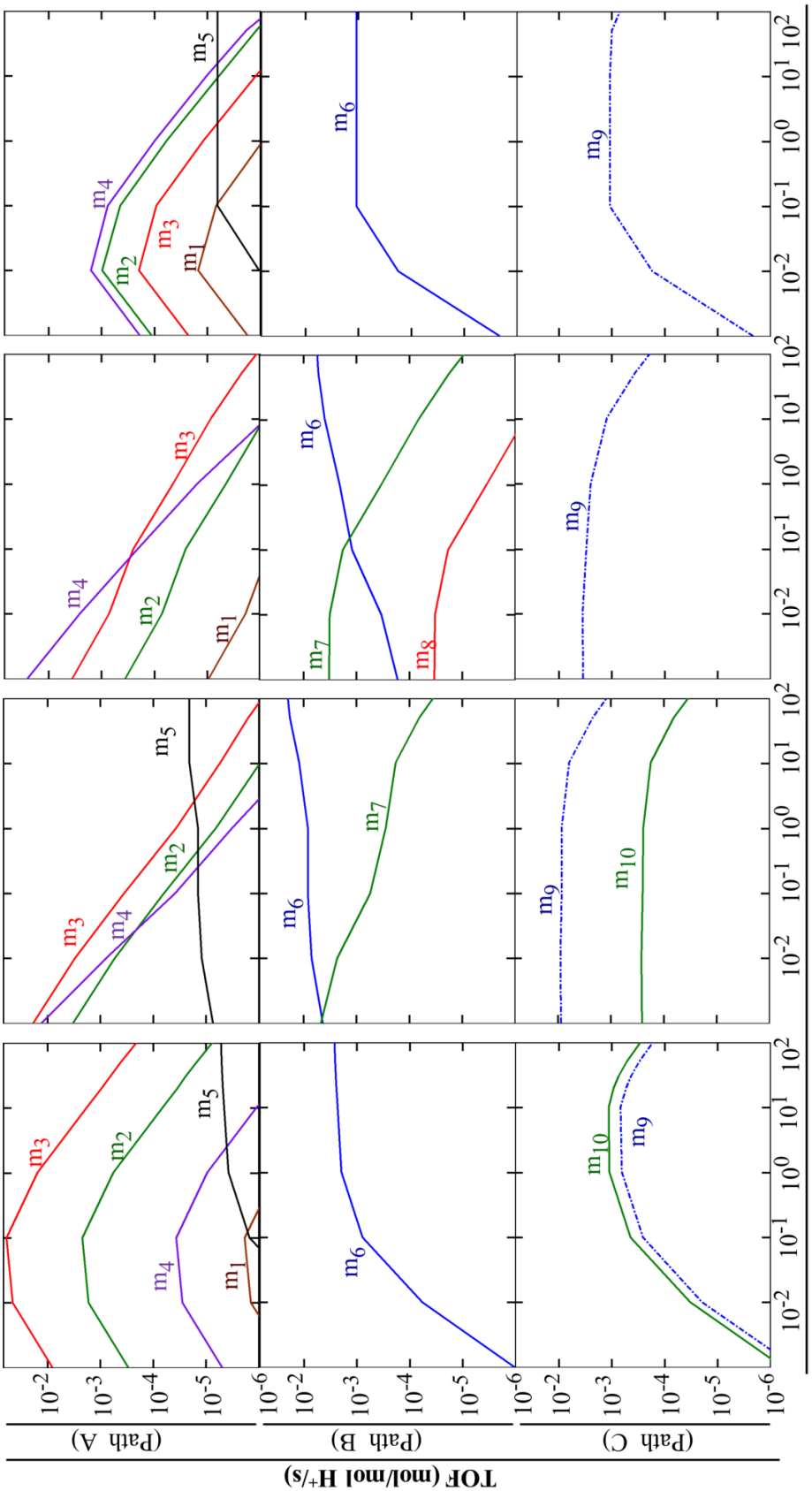

Figure 9: Turn over frequencies (TOF) for different reaction mechanisms (m_1-m_{10}, see Figure 1 and Table 1 for the elementary steps associated with each mechanism) as a function of feed butanol partial pressure at conversion of 10% and reaction temperature of 450K. (These results correspond to plug-flow reactor simulations (Eqs. 3-5) with the ab-initio based microkinetic model. See Tables S6, S7, S8 and S9, for H-ZSM-5, H-FAU, H-ZSM-22 and H-FER, respectively, for the model parameters. Mechanisms having TOF lower than 10^{-6} are not shown in the figure).

For path B, the dimer mediated mechanism m_6 remains dominant for H-FAU, H-ZSM-5 and H-FER with TOF_{m6} contributing ~100, 50-100 and 100 % to path B, respectively. For H-ZSM-22, the butoxide mediated mechanism m_7 is dominant at 1-butanol partial pressure below 0.1 kPa and the preference shifts in favor of the dimer mediated mechanism m_6 at 1-butanol partial pressures above 1 kPa. Such a shift in the dominant reaction mechanism with alcohol partial pressure can explain why the low pressure FTIR experiments suggest an alkoxide mediated mechanism[12] for ether formation, while moderate pressure kinetic experiments in micro-reactors support the dimer mediated mechanism[13] for ether formation during alcohol dehydration in zeolites. Thus, DFT based microkinetic simulations allow to reconcile these conflicting experimental observations.

For path C, the dominant mechanism does not change with a change in butanol partial pressure. The effect of feed butanol partial pressure on each of the reaction mechanisms is related to the changes in surface coverage of their corresponding surface species (see surface coverage in Figure S30 of Appendix B: M1 for mechanisms m_1 to m_4, D1 for mechanisms m_5 and m_6, C3 for mechanisms m_7 and m_8, DBE* for mechanisms m_9 and m_{10}). Finally, in order to allow a facile comparison of theoretical TOFs with that obtained from experimental measurements of initial reaction rates, analytical equations for the initial TOFs are provided in Appendix B.

Summary of effect of reaction conditions on 1-butanol dehydration in different zeolites: A pictorial summary of the effect of reaction conditions on the *MARI* and the dominant reaction path is shown in Figure 10. For the sake of simplicity, the surface species having the largest contribution to the surface coverage (instead of the standard definition of *MARI* of having significantly larger coverage than any other surface species) is defined as the "*MARI"*. In general for all four zeolites, an increase in reaction temperature and a decrease in butanol feed partial pressure leads to an increase in surface coverage of butanol monomer M1 (see Figure

S31 of Appendix B), which in turn leads to an increase in TOF for monomolecular path A mechanisms (m_2-m_4) and explains the dominance of path A for all four zeolites at 1-butanol partial pressure less than 10^{-3} kPa and reaction temperature above 440K (see Figure 10). On the other hand, a lower reaction temperatures and higher 1-butanol partial pressure lead to an increase in surface coverage of alcohol dimer D1 (see Figure S31 of Appendix B) and favors dimer mediated mechanism (m_6) for DBE formation (path B). Thus, the DBE forming path B remains dominant for all four zeolites at butanol partial pressure above 10 kPa and reaction temperature below 420 K (see Figure 10).

It is seen that reaction conditions play a pivotal role in determining the *MARI*, which in turn significantly influences the relative contribution of the various mechanisms to the reaction paths. In certain cases at low butanol pressure and higher temperature, path A can be dominant even when M1 is not MARI (see Figure 10), provided it is present in a high enough concentration (see Figure S31). This is explained on the basis of the lower free energy barrier for the dominant path A mechanism m_3 as compared to the path B mechanism m_6 (see Table S10 of Appendix B) as described in section 3.3.1. For H-ZSM-5 and H-ZSM-22, path C (or path B/C) is dominant only when DBE* is *MARI*. In case of H-FER DBE* does not need to be the *MARI* for path B/C to be dominant as DBE* behaves as a reactive intermediate.

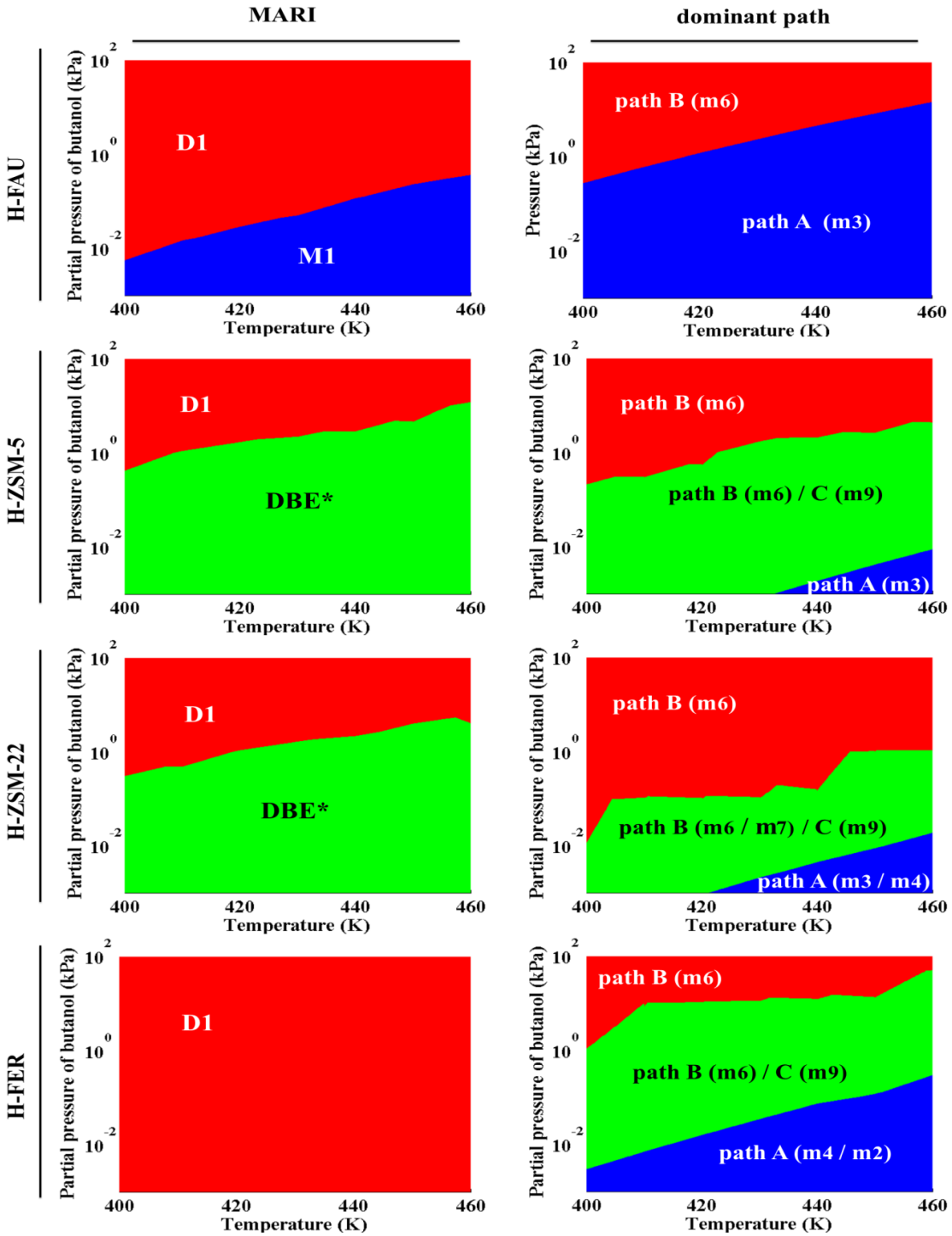

Figure 10: Effect of reaction temperature and butanol partial pressure on the most abundant reaction intermediate (*MARI*, left panels) for different zeolites and the dominant reaction paths and mechanism (right panels) for different zeolites at 1-butanol conversion of 10 %. (These results correspond to plug-flow reactor simulations (Eqs. 3-5) with the ab-initio based microkinetic model. See Tables S6, S7, S8 and S9, for H-ZSM-5, H-FAU, H-ZSM-22 and H-FER, respectively, for the model parameters).

More than the specific effect of reaction conditions on surface species, Figure 10 illustrates that under identical conditions different zeolites can have different *MARI*, dominant reaction

path and reaction mechanism. This is understood on the basis of differences in relative stability of the surface intermediates within different zeolites (see Appendix B Figure S3 and Tables S6, S7, S8 and S9). The larger void space offered by H-FAU provides a relatively lower dispersive stabilization to both monomer (M1) and dimer (D1) species. The difference in stability of M1 and D1 is further decreased with increasing temperature, favoring surface coverage with M1 at moderate and lower butanol partial pressure. Hence, at moderate and lower butanol partial pressure, path A is favored in H-FAU resulting in higher butene selectivity. On the other hand, DBE and butanol dimer are very well stabilized in the medium pore H-ZSM-5 and H-ZSM-22 which provide a very good fit for stabilizing these reaction intermediates and their corresponding transition states. Owing to the better stabilization of D1 in H-ZSM-5, H-ZSM-22 and H-FER, the butanol dehydration within these zeolites preferentially occurs via the dimer-mediated mechanism m_6 leading to DBE formation and the production of butene occurs mainly via DBE decomposition (via mechanism m_9). The steric constrains in the 8MR of H-FER, which partially confines DBE* significantly decreases its stability in H-FER, leading to a fast decomposition of DBE and a higher butene selectivity.

3. 4. Conclusions

In agreement with the literature reported experimental results for ethanol dehydration on different zeolites, our simulated results indicate highest TOF for 1-butanol dehydration in H-ZSM-5 and higher alkene selectivity for H-FAU and H-FER. Reaction path analysis shows that H-FAU and H-FER do not follow the same reaction paths but do provide similar selectivity profile. The higher 1-butene selectivity for H-FAU is attributed to its preference for monomolecular direct dehydration path (path A). This specific preference for monomolecular path A mechanisms in H-FAU is attributed to a relatively lower equilibrium coefficient for the formation of the butanol dimer (D1) from adsorbed monomer (M1) as compared to narrower zeolites. On the other hand, the higher 1-butene selectivity for H-

FER, which follows an ether-mediated consecutive reaction scheme, is rationalized on the basis of a lower stability for adsorbed ether and a lower activation barrier for ether decomposition. Similarly, at low and moderate temperatures, in H-ZSM-5 and H-ZSM-22 an ether-mediated reaction scheme for butene formation is preferred. But, unlike H-FER, the adsorbed ether is very well stabilized in these zeolite frameworks, which also exhibit a lower energy barrier for ether formation as compared to ether decomposition. This in turn explains the higher ether selectivity in H-ZSM-5 and H-ZSM-22. In general for all four zeolites, an increase in reaction temperature and a decrease in butanol feed partial pressure lead to an increase in butene selectivity. Under identical reaction conditions, different zeolites may have different *MARI*, which in turn leads to differences in pressure dependence (reaction order), preference for a specific reaction mechanism and product selectivity.

3.5. References

(1) Ragauskas, A. J.; Williams, C. K.; Davison, B. H.; Britovsek, G.; Cairney, J.; Eckert, C. A.; Frederick, W. J.; Hallett, J. P.; Leak, D. J.; Liotta, C. L.; Mielenz, J. R.; Murphy, R.; Templer, R.; Tschaplinski, T. *Science* **2006**, 311, 484-489.

(2) Willems, P. A. *Science* **2009**, 325, 707-708.

(3) Luque, R.; Herrero-Davila, L.; Campelo, J. M.; Clark, J. H.; Hidalgo, J. M.; Luna, D.; Marinas, J. M.; Romero, A. A. *Energ Environ Sci* **2008**, 1, 542-564.

(4) Haw, J. F.; Song, W. G.; Marcus, D. M.; Nicholas, J. B. *Accounts Chem Res* **2003**, 36, 317-326.

(5) Sun, J.; Wang, Y. *Acs Catal* **2014**, 4, 1078-1090.

(6) Savage, N. *Nature* **2011**, 474, S9-S11.

(7) Mascal, M. *Biofuel Bioprod Bior* **2012**, 6, 483-493.

(8) Li, Y.; Yu, J. H. *Chem Rev* **2014**, 114, 7268-7316.

(9) Van Santen, R. A.; Kramer, G. J. *Chem Rev* **1995**, 95, 637-660.

(10) Gounder, R.; Iglesia, E. *Accounts Chem Res* **2012**, 45, 229-238.

(11) Bhan, A.; Iglesia, E. *Accounts Chem Res* **2008**, 41, 559-567.

(12) Makarova, M. A.; Paukshtis, E. A.; Thomas, J. M.; Williams, C.; Zamaraev, K. I. *J Catal* **1994**, 149, 36-51.

(13) Chiang, H.; Bhan, A. *J Catal* **2010**, 271, 251-261.

(14) Phung, T. K.; Hernandez, L. P.; Lagazzo, A.; Busca, G. *Appl Catal a-Gen* **2015**, 493, 77-89.

(15) Norskov, J. K.; Bligaard, T.; Rossmeisl, J.; Christensen, C. H. *Nat Chem* **2009**, 1, 37-46.

(16) Macht, J.; Janik, M. J.; Neurock, M.; Iglesia, E. *J Am Chem Soc* **2008**, 130, 10369-10379.

(17) Janik, M. J.; Macht, J.; Iglesia, E.; Neurock, M. *J Phys Chem C* **2009**, 113, 1872-1885.

(18) Macht, J.; Carr, R. T.; Iglesia, E. *J Catal* **2009**, 264, 54-66.

(19) Vjunov, A.; Hu, M. Y.; Feng, J.; Camaioni, D. M.; Mei, D. H.; Hu, J. Z.; Zhao, C.; Lercher, J. A. *Angew Chem Int Edit* **2014**, 53, 479-482.

(20) Ensing, B.; Laio, A.; Gervasio, F. L.; Parrinello, M.; Klein, M. L. *J Am Chem Soc* **2004**, 126, 9492-9493.

(21) Kim, S.; Robichaud, D. J.; Beckham, G. T.; Paton, R. S.; Nimlos, M. R. *J Phys Chem A* **2015**, 119, 3604-3614.

(22) Konda, S. S. M.; Caratzoulas, S.; Vlachos, D. G. *Acs Catal* **2016**, 6, 123–133.

(23) Prestianni, A.; Cortese, R.; Duca, D. *React Kinet Mech Cat* **2013**, 108, 565-582.

(24) John, M.; Alexopoulos, K.; Reyniers, M. F.; Marin, G. B. *J Catal* **2015**, 330, 28-45.

(25) Makarova, M. A.; Williams, C.; Zamaraev, K. I.; Thomas, J. M. *J Chem Soc Faraday T* **1994**, 90, 2147-2153.

(26) Makarova, M. A.; Williams, C.; Thomas, J. M.; Zamaraev, K. I. *Catal Lett* **1990**, 4, 261-264.

(27) Makarova, M. A.; Williams, C.; Romannikov, V. N.; Zamaraev, K. I.; Thomas, J. M. *J Chem Soc Faraday T* **1990**, 86, 581-584.

(28) Makarova, M. A.; Paukshtis, E. A.; Thomas, J. M.; Williams, C.; Zamaraev, K. I. *Catal Today* **1991**, 9, 61-68.

(29) Zhi, Y.; Shi, H.; Mu, L.; Liu, Y.; Mei, D.; Camaioni, D. M.; Lercher, J. A. *J Am Chem Soc* **2015**, 137, 15781–15794.

(30) Blaszkowski, S. R.; vanSanten, R. A. *J Phys Chem B* **1997**, 101, 2292-2305.

(31) Blaszkowski, S. R.; vanSanten, R. A. *J Am Chem Soc* **1996**, 118, 5152-5153.

(32) Baerlocher, C.; Meier, W. M.; Olson, D.; Meier, W. M. *Atlas of zeolite framework types*; 5th rev. ed.; Elsevier: Amsterdam ; New York, 2001.

(33) Sierka, M.; Sauer, J. *Faraday Discuss* **1997**, 106, 41-62.

(34) Nguyen, C. M.; Reyniers, M. F.; Marin, G. B. *J Catal* **2015**, 322, 91-103.

(35) Nguyen, C. M.; De Moor, B. A.; Reyniers, M. F.; Marin, G. B. *J Phys Chem C* **2012**, 116, 18236-18249.

(36) Lonsinger, S. R.; Chakraborty, A. K.; Theodorou, D. N.; Bell, A. T. *Catal Lett* **1991**, 11, 209-217.

(37) Mentzen, B. F.; Sacerdoteperonnet, M. *Mater Res Bull* **1994**, 29, 1341-1348.

(38) Dedecek, J.; Lucero, M. J.; Li, C. B.; Gao, F.; Klein, P.; Urbanova, M.; Tvaruzkova, Z.; Sazama, P.; Sklenak, S. *J Phys Chem C* **2011**, 115, 11056-11064.

(39) Mazar, M. N.; Al-Hashimi, S.; Bhan, A.; Cococcioni, M. *J Phys Chem C* **2012**, 116, 19385-19395.

(40) Kresse, G.; Hafner, J. *Phys Rev B* **1993**, 47, 558-561.

(41) Kresse, G.; Hafner, J. *Phys Rev B* **1994**, 49, 14251-14269.

(42) Kresse, G.; Furthmuller, J. *Comp Mater Sci* **1996**, 6, 15-50.

(43) Blochl, P. E. *Phys Rev B* **1994**, 50, 17953-17979.

(44) Kresse, G.; Joubert, D. *Phys Rev B* **1999**, 59, 1758-1775.

(45) Perdew, J. P.; Chevary, J. A.; Vosko, S. H.; Jackson, K. A.; Pederson, M. R.; Singh, D. J.; Fiolhais, C. *Phys Rev B* **1992**, 46, 6671-6687.

(46) Grimme, S. *J Comput Chem* **2006**, 27, 1787-1799.

(47) Kerber, T.; Sierka, M.; Sauer, J. *J Comput Chem* **2008**, 29, 2088-2097.

(48) Tuma, C.; Sauer, J. *Phys Chem Chem Phys* **2006**, 8, 3955-3965.

(49) Goltl, F.; Gruneis, A.; Bucko, T.; Hafner, J. *J Chem Phys* **2012**, 137, 11411.

(50) Vener, M. V.; Rozanska, X.; Sauer, J. *Phys Chem Chem Phys* **2009**, 11, 1702-1712.

(51) Chiu, C. C.; Vayssilov, G. N.; Genest, A.; Borgna, A.; Rosch, N. *J Comput Chem* **2014**, 35, 809-819.

(52) Nguyen, C. M.; Reyniers, M. F.; Marin, G. B. *Phys Chem Chem Phys* **2010**, 12, 9481-9493.

(53) Nguyen, C. M.; Reyniers, M. F.; Marin, G. B. *J Phys Chem C* **2011**, 115, 8658-8669.

(54) Bucko, T.; Hafner, J. *J Catal* **2015**, 329, 32-48.

(55) Leydier, F.; Chizallet, C.; Costa, D.; Raybaud, P. *J Catal* **2015**, 325, 35-47.

(56) Grimme, S.; Antony, J.; Ehrlich, S.; Krieg, H. *J Chem Phys* **2010**, 132.

(57) Bader, R. F. W. *Atoms in molecules : a quantum theory*; Clarendon Press: Oxford, 1990.

(58) Henkelman, G.; Arnaldsson, A.; Jonsson, H. *Comp Mater Sci* **2006**, 36, 354-360.

(59) Henkelman, G.; Jonsson, H. *J Chem Phys* **2000**, 113, 9978-9985.

(60) Henkelman, G.; Jonsson, H. *J Chem Phys* **1999**, 111, 7010-7022.

(61) Heyden, A.; Bell, A. T.; Keil, F. J. *J Chem Phys* **2005**, 123, 224101 .

(62) Kaestner, J.; Sherwood, P. *J Chem Phys* **2008**, 128, 014106.

(63) De Moor, B. A.; Ghysels, A.; Reyniers, M. F.; Van Speybroeck, V.; Waroquier, M.; Marin, G. B. *J Chem Theory Comput* **2011**, 7, 1090-1101.

(64) Zhao, Y.; Truhlar, D. G. *Phys Chem Chem Phys* **2008**, 10, 2813-2818.

(65) Ribeiro, R. F.; Marenich, A. V.; Cramer, C. J.; Truhlar, D. G. *J Phys Chem B* **2011**, 115, 14556-14562.

(66) Grimme, S. *Chem-Eur J* **2012**, 18, 9955-9964.

(67) Jensen, J. H. *Phys Chem Chem Phys* **2015**, 17, 12441-12451.

(68) Piccini, G.; Sauer, J. *J Chem Theory Comput* **2014**, 10, 2479-2487.

(69) Piccini, G.; Alessio, M.; Sauer, J.; Zhi, Y. C.; Liu, Y.; Kolvenbach, R.; Jentys, A.; Lercher, J. A. *J Phys Chem C* **2015**, 119, 6128-6137.

(70) De Moor, B. A.; Reyniers, M. F.; Marin, G. B. *Phys Chem Chem Phys* **2009**, 11, 2939-2958.

(71) Cramer, C. J. *Essentials of computational chemistry : theories and models*; 2nd ed.; Wiley: Chichester Hoboken, NJ, 2004.

(72) Stepanov, A. G.; Maryasov, A. G.; Romannikov, V. N.; Zamaraev, K. I. *Magn Reson Chem* **1994**, 32, 16-23.

(73) Nishchenko, A. M.; Kolokolov, D. I.; Gabrienko, A. A.; Stepanov, A. G. *J Phys Chem C* **2012**, 116, 8956-8963.

(74) Stepanov, A. G.; Alkaev, M. M.; Shubin, A. A. *J Phys Chem B* **2000**, 104, 7677-7685.

(75) Sabbe, M. K.; Canduela-Rodriguez, G.; Reyniers, M. F.; Marin, G. B. *J Catal* **2015**, 330, 406-422.

(76) *NIST Chemistry WebBook, NIST Standard Reference Database Number 69*; National Institute of Standards and Technology, 2005.

(77) Hindmarsh, A. C. *IMACS transactions on scientific computation* **1983**, 1, 55-64.

(78) Zhang, D. Z.; Al-Hajri, R.; Barri, S. A. I.; Chadwick, D. *Chem Commun* **2010**, 46, 4088-4090.

(79) Zhang, D. Z.; Barri, S. A. I.; Chadwick, D. *Appl Catal a-Gen* **2011**, 403, 1-11.

Chapter 4

Mechanistic insights into formation of butene isomers from 1-butanol in H-ZSM-5: DFT based microkinetic modelling

Abstract

Besides being a renewable energy source, the catalytic conversion of bio-alcohols can serve as a sustainable means for the production of high-value chemicals. Butenes produced by dehydration of 1-butanol could serve as a building block for several essential compounds such as fuels and polymers. This study provides theoretical insights into the competing pathways for the formation of butene isomers (1-butene, cis/trans 2-butenes and iso-butene) during catalytic dehydration of 1-butanol in H-ZSM-5. As di-1-butyl ether (DBE) is one of the key products during low temperature dehydration of 1-butanol, a new mechanism for direct formation of trans-2-butene from DBE via E1 elimination is also envisaged along with the direct dehydration of 1-butanol to trans-2-butene. A 2-butoxide mediated stepwise mechanism and a concerted mechanism involving simultaneous protonation of the double bond by the Brønsted acid site and abstraction of the H_γ by the zeolite oxygen are considered for the double bond isomerization in H-ZSM-5. A monomolecular 2-butoxide and iso-butoxide mediated mechanism is considered for the skeletal isomerization. The transformation of 2-butoxide to iso-butoxide occurs via a π-bonded propene-methyl carbocationic transition state. DFT based microkinetic simulations show that, except for very low conversion levels where 2-butenes are produced via E1 elimination of 1-butanol from the protonated di-1-butyl ether (DBE*), the formation of 2-butenes occurs essentially via double bond isomerization mechanisms with comparable contributions of both concerted and 2-butoxide mediated stepwise mechanisms. Owing to the higher activation barrier for the skeletal isomerization, isobutene is not observed in the simulated temperature range of 450-500K. Simulation results indicate that low reaction temperature, low site time and high butanol pressure favor production of 1-butene and DBE, while high temperature and site time and low butanol pressure favor the consecutive reactions leading to production of butene isomers.

4.1. Introduction

Butene isomers produced from the dehydration of bio-butanol can serve as platform species for the sustainable production of fuels, specialty chemicals and petrochemicals [1]. Zeolite catalyzed dehydration of 1-butanol can be used to produce a butene mixture consisting of 1-butene, trans-2-butene (2t-butene) and cis-2-butene (2c-butene) along with di-1-butyl ether (DBE) at low temperatures [2]. On the other hand, a high temperature dehydration of 1-butanol can be used to produce iso-butene [3,4] along with other hydrocarbons. Although the butene mixtures produced by dehydration of 1-butanol can be directly used for certain applications such as production of fuel or fuel additives via alkylation reactions[5], most of the applications such as production of polymers or synthesis of specialty chemicals require pure butenes [1]. Hence, it would be interesting to explore the possibility of selectively producing a specific isomer so as to suit the desired application.

Detailed insights into the reaction mechanisms can guide the selection of appropriate catalyst and reaction conditions to increase selectivity for a specific isomer. The reaction mechanisms for the dehydration of bio-alcohols to alkene and ether in zeolites have been discussed in detail in recent theoretical work[6-9]. Although dehydration of 1-butanol to 1-butene and DBE in H-ZSM-5 has been studied both experimentally [2,10,11] and theoretically [6], the reaction mechanism for the formation of other butene isomers from 1-butanol is still not clear. The formation of 2-butenes (cis/trans) during 1-butanol dehydration has been suggested to occur via an E1-like elimination of water from 1-butanol accompanied by rearrangement of a primary carbenium ion (formed during elimination) to a secondary carbenium ion [12-14] or by double bond isomerization of the 1-butene formed during the dehydration of 1-butanol.

Standard organic chemistry text books[12] suggest that in acidic solutions the dehydration of 1-butanol to 2-butene occurs via E1 elimination of water from 1-butoxonium ($C_4H_9OH_2^+$) ion. This mechanism involves breakage of the C-O bond of the butoxonium eliminating water,

rearrangement of the produced primary carbocation to a secondary carbocation and deprotonation of the secondary carbocation producing 2-butene. A similar mechanism was proposed by Olaofe and Yue [13] for dehydration of 1-butanol to 2-butene in zeolites (X, 4A, ZNa), but the exact nature of the adsorbed alcohol species is not clear from their findings. They attributed the formation of 2-butene to the aforementioned E1 elimination accompanied by a hydride shift and the formation of 1-butene to E2 elimination of water from 1-butanol. Moreover, they considered double bond isomerization to be highly unlikely owing to the weaker adsorption of 1-butene in comparison to 1-butanol. Since adsorbed butanol dimer (D1) and adsorbed di-1-butyl ether (DBE*) are some of the key adsorbed species [6,15,16], it is imperative to look into the possibility of an E1 elimination with carbenium ion rearrangement for the formation of 2-butenes from these species.

On the other hand, a sizeable amount of literature is available on the reaction mechanisms of double-bond [17-22] and skeletal isomerization [23-31]. Kazansky [17] proposed a step-wise secondary alkoxide mediated mechanism for double-bond isomerization, while the experimental study by Kondo et al. [19,20] for 1-butene double-bond isomerization in deuterated ZSM-5 and MOR indicated a concerted mechanism without the formation of protonated intermediates. Boronat et al. [21] and Li et al. [22] studied the concerted mechanism for the double-bond isomerization of butenes in zeolites using a DFT cluster model. Monomolecular [25-29] and bimolecular mechanisms [30,31] have been proposed for the skeletal isomerization of butenes in zeolites. It is generally accepted that the monomolecular mechanism leads to a more selective production of iso-butene [26]. However, the presence of strongly adsorbed alcohol (M1, D1) and ether species (DBE*) can significantly influence the surface coverage of 1-butene and the rate of butene double bond and skeletal isomerization. Moreover, reaction conditions such as site time, reaction temperature and inlet butanol partial pressure can significantly alter the surface

coverages. Thus, it is essential to study the effect of these reaction conditions at different conversion levels.

In this work, a first principles based microkinetic modelling approach is used to study the reaction mechanism for formation of butene isomers, namely 1-butene, 2t-butene, 2c-butene and isobutene during 1-butanol dehydration in H-ZSM-5. This study provides theoretical insights into competing pathways for formation of 2-butene (cis/trans) isomers via E1 elimination of adsorbed butanol/DBE in addition to double bond and monomolecular skeletal isomerization reactions. The results of the microkinetic simulations emphasize the role of reaction conditions in governing the surface coverages of reaction intermediates and the relative contribution of each reaction path, which in turn defines the selectivity for butene isomers.

4.2. Theory

4.2.1. Catalyst model

The H-ZSM-5 framework structure with *Pnma* symmetry, unit cell composition– $HAlSi_{95}O_{192}$ and unit cell parameters: a = 2047.2 pm, b =2010.9 pm, c = 1357.6 pm, α = 89.97°, β = 89.88°, and γ = 89.99° [32] was used in this study. The zeolite acid site was created by replacing a Si atom with an Al atom and adding a proton to the adjacent oxygen atom. The location of the Al atom in the unit cell was reported to be non-random [33] and to depend on the zeolite synthesis conditions [34]. Previous theoretical studies specify the T12 site to be the preferred location for the Al atom associated with the Brønsted acid site [35,36]. Moreover, when the Al atom is located at the T12 site, the Brønsted acid site is accessible to molecules located in both the straight and sinusoidal channels and could accommodate larger species. Accordingly, the T12 tetrahedral site was selected for the replacement of a Si atom with Al, while the

zeolite proton is chosen to be located at the oxygen atom adjacent to the channel intersection [37].

4.2.2. Computational details

4.2.2.1. Electronic energy calculations

Dispersion corrected periodic DFT calculations were performed with the Vienna Ab Initio Simulation Package (VASP) using plane wave basis sets [38-40]. The electron-ion interactions were described using the projector–augmented wave (PAW) method [41,42] with a plane-wave energy cut-off of 600 eV. The exchange correlation energies were calculated on the basis of the generalized gradient approximation (GGA) according to Perdew, Burke and Ernzerhof (PBE) [43]. Brillouin zone sampling was restricted to the Γ-point. A maximum force convergence criterion of 0.02 eV $Å^{-1}$ was used and each self-consistency loop was iterated until a convergence level of 10^{-8} eV was achieved. Dispersive corrections for the van der Waals interactions were included by adding a pairwise interaction term to the Kohn–Sham energy using the DFT-D2 approach proposed by Grimme [44] and extended by Kerber et al. [45] for periodic PBE calculations. Although systematic deviations may be observed due to the overestimation of the dispersion interaction [46-49], DFT-D2 has been widely applied for the theoretical investigation of adsorption [32,50-52] and reaction in zeolites [52,53] and is known to provide reasonably accurate results [47,54]. The electronic charge on atoms and fragments were calculated using Bader analysis [55] as implemented by Henkelman et al. [56] Transition state search was performed using Nudged Elastic Band (NEB) [57] and dimer [58,59] calculations. The Nudged Elastic Band (NEB) method was used to find an initial guess for the minimal energy path (MEP), which was used as a starting point for the dimer calculations.

4.2.2.2. Frequency calculations

Normal mode analysis was performed using a Partial Hessian Vibrational Analysis (PHVA), relaxing the T5 cluster ($HAl(SiO_4)_4$) of the zeolite framework and the adsorbate molecule for the numerical Hessian calculation. Previous studies for physisorption and chemisorption in zeolites have shown that the partial Hessian approach leads to a marginal difference in the result as compared to a Full Hessian Vibrational Analysis (FHVA) [60]. Although very stringent optimization (maximum force criterion of 0.02 eV $Å^{-1}$) and electronic convergence (self-consistency loop convergence criterion of 10^{-8} eV and energy cut-off of 600 eV) criteria have been used, spurious imaginary frequencies were still present in very few cases. The low lying frequencies (<50 cm^{-1}) associated with the frustrated motions of the surface bound species (such as translation or rotation of the molecule within the zeolite pore structure) could lead to significant error in the entropy calculations [61-64]. A more accurate estimation of the entropic contributions could be obtained by accounting for anharmonicities by detailed scanning of the potential energy surface [65,66], but this would require significant computational efforts for large systems. Another approach to treat the low lying modes is the use of a frequency cutoff [50,61,62,67]. De Moor et al. [67] studied the entropy contributions of these frequencies for alkanes and alkenes in FAU zeolite and suggested the replacement of these spurious frequencies with 50 cm^{-1}. Therefore, in order to obtain consistent results, the spurious imaginary frequencies and low-lying frequencies were replaced by normal modes of 50 cm^{-1} [67].

4.2.2.3. Statistical thermodynamics

Standard enthalpies, entropies, Gibbs free energies and the corresponding adsorption and reaction equilibrium coefficients (K) are obtained from total partition functions by statistical thermodynamics calculations [68].

Reaction equilibrium coefficients, *K*, for elementary reactions are calculated as:

$$K(T) = \frac{\prod_i Q_i(N,V,T)}{\prod_j Q_j(N,V,T)} \exp\left(-\frac{\Delta E_r}{RT}\right) \qquad (1)$$

where *i* and *j* denote products and reactants respectively. ΔE_r is the change in electronic energy at 0 K (including the zero-point vibrational energy) of the reaction and *Q* the total partition function. The electronic energy from the DFT calculation along with the frequencies obtained from the vibrational analysis are used for the statistical thermodynamic calculation (see Appendix A). The total partition function for gas-phase species consists of translational, rotational and vibrational contributions. On the other hand, the surface bound complexes in the zeolite are modeled using either the *immobile* or the *mobile adsorbate* method, based on the vibrational analysis [60]. The *immobile adsorbate* method considers all degrees of freedom of the adsorbed species within the zeolite as frustrated motions, which are described by the harmonic oscillator approximation [67]. This *immobile adsorbate* approach has been applied for all surface–bound complexes except for the physisorbed butenes (1-butene, 2t-butene, 2c-butene and iso-butene). These loosely–bound physisorbed butenes are considered as *mobile adsorbates*, which retain certain rotational and translational degrees of freedom [67]. Harmonic frequencies associated with these rotational and translational motions were identified based on visual inspection of frequencies lower than 100 cm^{-1}. These frequencies are removed from the calculation of the vibrational partition function and are replaced by free translational or rotational contributions.

The reaction rate coefficients of elementary reaction steps are calculated on the basis of transition state theory:

$$k_{TST}(T) = \frac{k_B T}{h} \frac{Q_{TS}(N,V,T)}{Q_R(N,V,T)} \exp\left(-\frac{E^{\ddagger}}{RT}\right) \qquad (2)$$

where k_B is the Boltzmann constant, h is the Planck constant and $E^{\ddagger}$ the electronic activation barrier at 0 K (including the zero-point vibrational energy). Q_{TS} and Q_R denote the total partition functions of the transition and reactant state respectively. Arrhenius pre-exponential factors (A) and activation energies (E_a) are obtained by regression of the ab initio calculated rate coefficients with Eq. 2 in the temperature range of 300 – 800 K.

The adsorption occurs without any activation barrier. Hence, the reaction rate coefficient for the adsorption step is calculated as $k_{ads} = k_B T/h$, while the reaction rate coefficient for the desorption step is calculated from thermodynamic consistency as $k_{des} = k_{ads}/K_{ads}$.

4.2.3. Microkinetic model

In this work, an isothermal plug flow reactor model was used for the reactor simulations. The following continuity equations were applied for the gas-phase components i and surface species k along with a site balance:

$$\frac{d\theta_k}{dt} = \sum_j \nu_{jk} TOF_j = 0 \qquad (3)$$

$$\theta_* + \sum_k \theta_k = 1 \qquad (4)$$

$$\frac{dF_i}{dW} = R_i = C_t \sum_j \nu_{ji} TOF_j \qquad (5)$$

with $F_i = F_{i,0}$ at $W = 0$

where TOF_j is the turnover frequency of elementary step j (mol mol_{H+}^{-1} s^{-1}), ν_{ji} the stoichiometric coefficient of component i in the elementary step j, θ_k the fractional coverage of surface species k (mol mol_{H+}^{-1}), θ_* the fractional coverage of free acid sites (mol mol_{H+}^{-1}), C_t the acid site concentration (mol_{H+} kg^{-1}), F_i the molar flow rate of gas-phase component i

(mol s^{-1}), W the mass of the catalyst (kg), R_i the net production rate of gas-phase species i (mol kg^{-1} s^{-1}).

The microkinetic model assumes absence of any diffusion limitation for reactant and product species. This assumption is consistent with the experimental results of Makarova et al.[2], where they studied the effect of ZSM-5 crystallite size on the reaction rates for dehydration of 1-butanol and di-1-butyl ether. The above mentioned set of ordinary differential equations are (eq. 3 and 5) integrated using the LSODA module of ODEPACK [69]. The investigated reaction conditions are partial pressure of 1-butanol (0.001-100 kPa), site time ($N_{H+}/F_{BuOH,0}$ = 0-200 mol H+ s / mol $BuOH_0$) and reaction temperature (450-500 K). The calculation of TOF for each mechanism is shown in appendix C.

4.3. Results and discussion

4.3.1. Reaction paths for formation of butene isomers from 1-butanol in H-ZSM-5

Figure 1 shows the possible reaction paths for formation of butene isomers from 1-butanol in H-ZSM-5. The dehydration of 1-butanol to 1-butene and di-1-butyl ether has been discussed in detail in Chapter 2 / Ref.[6] As the adsorbed butanol dimer (D1) and di-1-butyl ether (DBE*) were found to be key surface species [6], the formation of 2t-butene from 1-butanol (via path D) and from DBE (via path E) has been considered. On the other hand, 1-butene produced from dehydration of 1-butanol (via path A or path B followed by path C) can undergo double bond isomerization to produce trans-2-butene (2t-butene) and cis-2-butene (2c-butene) via path F, G and H. These linear butenes (1-butene/2t-butene/2c-butene) can undergo skeletal isomerization reaction via path I, J and K.

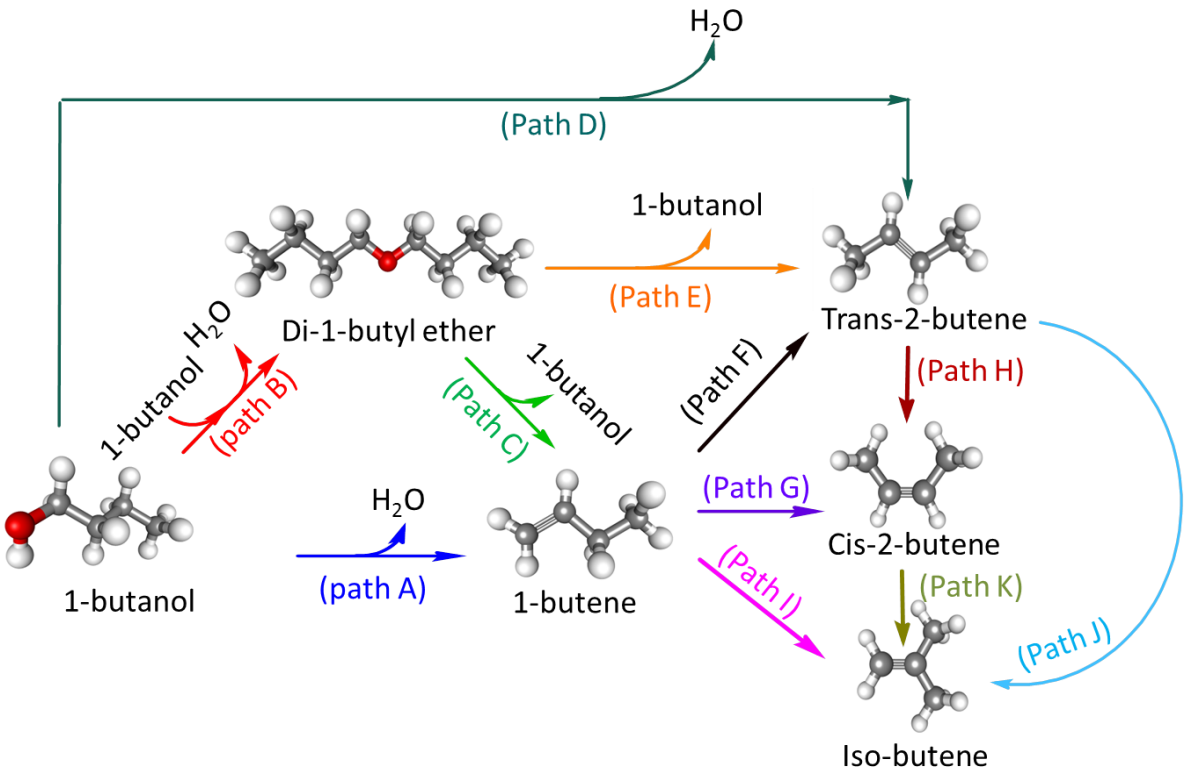

Figure 1. Reaction scheme for butanol dehydration and butene isomerization in H-ZSM-5

The reaction network for 1-butanol dehydration to 1-butene and DBE consisting of 23 elementary steps described in Chapter 2 / Ref [6] is extended for the production of 2t-butene, 2c-butene and iso-butene by inclusion of 11 extra elementary steps which are shown in Figure 2. Any further reference to a specific reaction step of the network and reaction path/mechanism is done as per the numbering used in Figure 2 and Table 1, respectively. The standard reaction enthalpy (ΔH_r^o), reaction entropy (ΔS_r^o), Arrhenius activation energies and pre-exponential factors, forward reaction rate coefficients and equilibrium coefficients for each elementary step are tabulated in Table 2. Carbon atoms are named according to their initial position w.r.t. the OH group, with the one connected to OH as C_α and the terminal carbon atom of 1-butanol as C_δ. In order to explain the transformations occurring during reaction their original naming scheme is retained throughout the text.

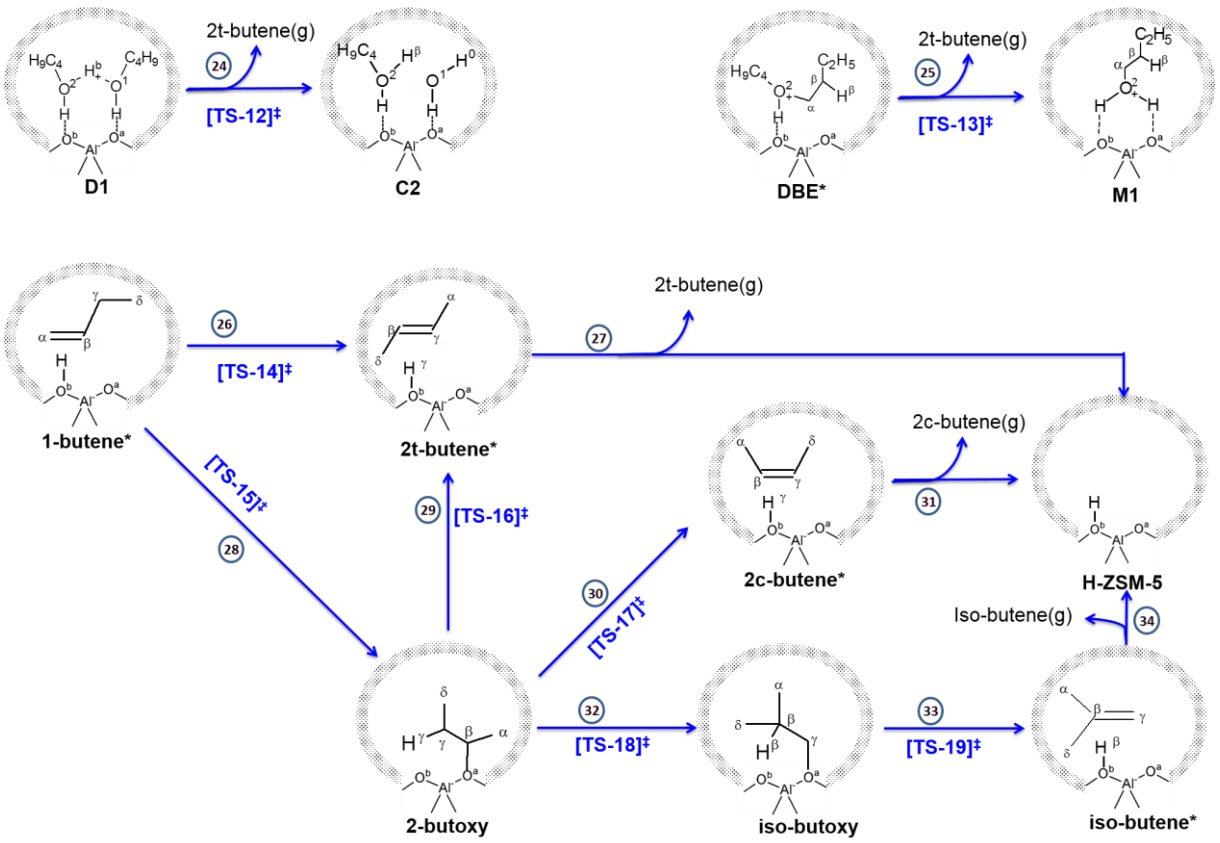

Figure 2. Reaction network for 2-butenes (cis/trans) and iso-butene formation from 1-butanol dehydration in H-ZSM-5. M1 and D1 are adsorbed monomer and dimer formed via adsorption of 1-butanol, DBE* (adsorbed di-1-butyl ether) and 1-butene* are formed during dehydration of 1-butanol (see Chapter 2 / Ref [6] for detailed reaction network for dehydration of 1-butanol to DBE and 1-butene) .

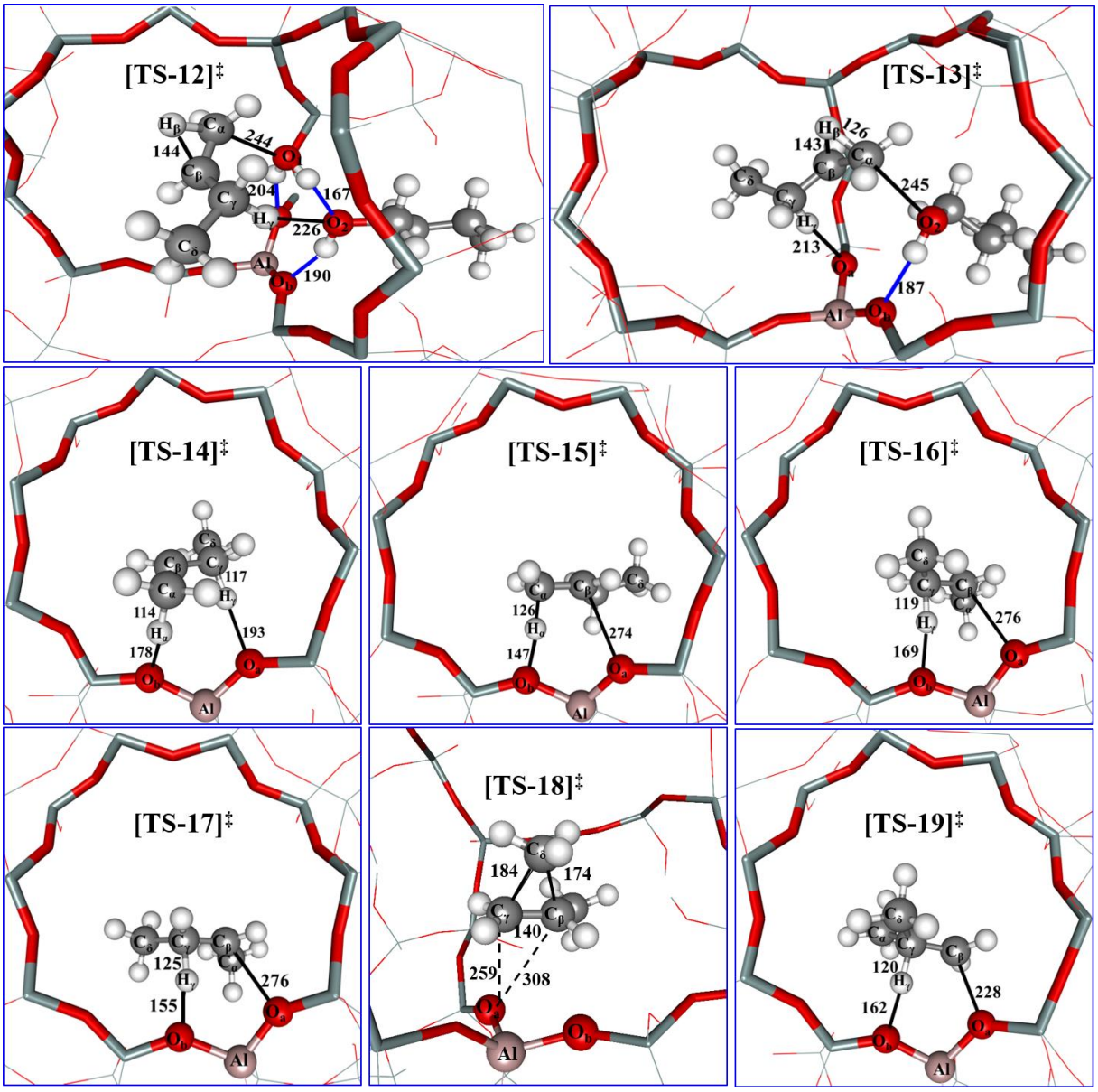

Figure 3. Transition state structures (TS-12, TS-13 and TS-18 view of the channel intersection, TS-14 to TS-17 and TS-19 view from the sinusoidal channel) for the production of 2t-butene, 2c-butene and isobutene during 1-butanol dehydration in H-ZSM-5. Color code: silicon – light blue, aluminum – pink, oxygen – red, hydrogen – white, carbon – gray, hydrogen bonds (distance < 250 pm) – blue lines, bond breaking/forming – black lines

Table 1. Elementary steps and reaction mechanisms for the butanol dehydration reaction. Non-equilibrated steps as found by microkinetic simulations are indicated with bold stoichiometric numbers.

	Path	D	E	F		G	H	I	J	K
	Mechanism	m_{11}	m_{12}	m_{13}	m_{14}	m_{15}	m_{16}	m_{17}	m_{18}	m_{19}
1[#]	M1↔1-$BuOH_{(g)}$+ ∗	0	1	0	0	0	0	0	0	0
8[#]	1-$butene_{(g)}$+ ∗↔ 1-butene*	0	0	1	1	1	0	1	0	0
11[#]	M1 + 1-$BuOH_{(g)}$ ↔ D1	1	0	0	0	0	0	0	0	0
14[#]	C2↔ M1 + $H_2O_{(g)}$	1	0	0	0	0	0	0	0	0
16[#]	$DBE_{(g)}$+ ∗ ↔ DBE*	0	1	0	0	0	0	0	0	0
24	D1↔ C2+2-t-$butene_{(g)}$	**1**	0	0	0	0	0	0	0	0
25	DBE*↔ M1+2-t-$butene_{(g)}$	0	**1**	0	0	0	0	0	0	0
26	1-butene* ↔ 2-t-butene*	0	0	**1**	0	0	0	0	0	0
27	2-t-butene*↔ 2-t-$butene_{(g)}$+ ∗	0	0	1	1	0	-1	0	-1	0
28	1-butene* ↔ 2-butoxy	0	0	0	**1**	**1**	0	**1**	0	0
29	2-butoxy ↔ 2-t-butene*	0	0	0	**1**	0	**-1**	0	**-1**	0
30	2-butoxy ↔ 2-c-butene*	0	0	0	0	**1**	**1**	0	0	**-1**
31	2-c-butene*↔ 2-c-$butene_{(g)}$+ ∗	0	0	0	0	1	1	0	0	-1
32	2-butoxy ↔ iso-butoxy	0	0	0	0	0	0	**1**	**1**	**1**
33	iso-butoxy ↔ iso-butene*	0	0	0	0	0	0	**1**	**1**	**1**
34	iso-butene*↔ iso-$butene_{(g)}$+ ∗	0	0	0	0	0	0	1	1	1

Path D (mechanism m11)	1-$BuOH_{(g)}$ ↔ 2-t-$butene_{(g)}$ + $H_2O_{(g)}$
Path E (mechanism m12)	$DBE_{(g)}$ ↔1-$BuOH_{(g)}$+ 2-t-$butene_{(g)}$
Path F (mechanism m13-m14)	1-$butene_{(g)}$ ↔ 2-t-$butene_{(g)}$
Path G (mechanism m15)	1-$butene_{(g)}$ ↔ 2-c-$butene_{(g)}$
Path H (mechanism m16)	2-t-$butene_{(g)}$↔ 2-c-$butene_{(g)}$
Path I (mechanism m17)	1-$butene_{(g)}$ ↔ iso-$butene_{(g)}$
Path J (mechanism m18)	2-t-$butene_{(g)}$↔ iso-$butene_{(g)}$
Path K (mechanism m19)	2-c-$butene_{(g)}$↔ iso-$butene_{(g)}$

[#]elementary step from reaction network for 1-butanol dehydration to DBE and 1-butene from Chapter 2/ Ref [6].

Table 2. Standard reaction enthalpy (kJ/mol), reaction entropy (J/mol/K), activation energy (kJ/mol), pre-exponential factor (s^{-1}), forward reaction rate coefficient k_f (s^{-1}) at 450K and equilibrium coefficient at 450K (10^{-2} kPa^{-1}, 10^2 kPa or dimensionless for adsorption, desorption and surface transformation, respectively) for the elementary steps (numbered as indicated in Figure 2)

	Elementary steps	**ΔH_r^o**	**ΔS_r^o**	**$E_{a(f)}$**	**A_f**	**$k_{f\ (450K)}$**	**$K_{eq\ (450K)}$#**
24	D1↔ C2+2-t-butene$_{(g)}$	97	164	201	$4.9\ 10^{15}$	$2.2\ 10^{-8}$	$2.4\ 10^{-4}$
25	DBE*↔ M1+2-t-butene$_{(g)}$	100	189	171	$3.8\ 10^{15}$	$5.6\ 10^{-5}$	$2.5\ 10^{-3}$
26	1-butene* ↔ 2-t-butene*	-23	-4	54	$4.6\ 10^{9}$	$2.8\ 10^{3}$	$2.5\ 10^{2}$
27	2-t-butene*↔ 2-t-butene$_{(g)}$+ *	97	116	–	–	–	$8.2\ 10^{-7}$
28	1-butene* ↔ 2-butoxy	-24	-80	48	$2.7\ 10^{9}$	$8.2\ 10^{3}$	$4.4\ 10^{-2}$
29	2-butoxy ↔ 2-t-butene*	1	75	68	$1.0\ 10^{14}$	$1.2\ 10^{6}$	$5.8\ 10^{3}$
30	2-butoxy ↔ 2-c-butene*	17	67	74	$5.5\ 10^{13}$	$1.4\ 10^{5}$	$3.3\ 10^{1}$
31	2-c-butene*↔ 2-c-butene$_{(g)}$+ *	85	126	–	–	–	$7.1\ 10^{-5}$
32	2-butoxy ↔ iso-butoxy	12	11	123	7.310^{14}	4.4	$1.5\ 10^{-1}$
33	iso-butoxy ↔ iso-butene*	-3	58	100	$1.1\ 10^{13}$	$2.7\ 10^{1}$	$2.3\ 10^{3}$
34	iso-butene*↔ iso-butene$_{(g)}$+ *	85	119	–	–	–	$3.9\ 10^{-5}$

elementary steps involving adsorption/ desorption corrected using NIST experimental data

The electronic energies for physisorption and chemisorption of 1-butene, 2t-butene and isobutene in H-ZSM-5 are compared with literature reported theoretical results and are listed in Table 3. In comparison to the QM-POT calculations[70], the periodic PBE –D2 calculations used in our study indicates 12-16 kJ/mol higher adsorption energy for the physisorbed 1-butene and 2t-butene. On the other hand, 2-butoxide formation from gas-phase butene is found to be ~20 kJ/mol less favorable when using periodic PBE–D2 in comparison to QM-POT calculations. For the physisorption and chemisorption of isobutene in H-ZSM-, the PBE–D2 results are much closer to the BEEF-vdW[71], while PW91+D2[72] results indicate a higher adsorption strength than that obtained from PBE–D2 and BEEF-vdW. In general, the

relative stability of the different adsorbed species depict trends similar to that reported in literature.

Table 3. Physisorption and chemisorption electronic energies (at 0 K and in kJ/mol) for the adsorption of 1-butene, 2t-butene and isobutene in H-ZSM-5

Adsorption step	PBE-D2 (this study)	BEEF-vdW[71]	PW91+D2[72]	QM-POT[70]
1-butene$_{(g)}$ + * → 1-butene*	-88	−	−	-72
1-butene$_{(g)}$ + * → 2-butoxy	-122	−	−	-147
2t-butene$_{(g)}$ + * → 2-butene*	-97	−	−	-83
2t-butene$_{(g)}$ + * → 2-butoxy	-108	−	−	-136
isobutene$_{(g)}$ + * →isobutene*	-84	-84	-88	−
isobutene$_{(g)}$ + * →isobutoxy	-95	-87	-103	−

4.3.1.1. Dehydration of 1-butanol to DBE and 1-butene (path A, B and C)

The reaction network for 1-butanol dehydration to DBE and 1-butene in H-ZSM-5[6] is used in the current study. Herein, five possible mechanisms are considered for the direct dehydration path (path A) of 1-butanol conversion to 1-butene, namely, m_1 (via E1 elimination), m_2 (via syn-elimination), m_3 (via anti-elimination), m_4 (via S_N2 substitution for the formation of 1-butoxide), and m_5 (via butanol-assisted syn-elimination). DBE formation (path B) occurs via 1-butanol dimer mediated mechanism m_6 (via S_N2 type substitution) and 1-butoxide mediated mechanism m_7 and m_8 (via S_N2 and S_N1 type substitution, respectively). The DBE decomposition to 1-butene (path C) proceeds via two possible mechanisms m_9 and m_{10} with the activated step following a syn-elimination and an anti-elimination of 1-butanol from DBE, respectively.

4.3.1.2. Formation of 2t-butene from adsorbed butanol and DBE (path D and E)

Mechanism m11 (path D) and m12 (path E) involve direct formation of 2t-butene from D1 and DBE, respectively. To the best of our knowledge, these mechanisms involving E1 elimination accompanied by a 1,2 hydride shift for direct formation of 2t-butene from D1 and DBE has not been considered in any of the previous theoretical studies for dehydration in zeolites. As the closest comparison, the mechanism m11 can be considered analogous to the E1 elimination of water from 1-butoxonium ion accompanied by rearrangement of the carbenium ion, as proposed by Olaofe and Yue [13] and reported in standard text-books[12] for dehydration of a primary alcohol in acidic solutions. An E1 elimination of water from chemisorbed butanol monomer M1 leading to direct formation of 2t-butene was also explored as a part of this study, but was found to have an electronic energy barrier similar to the E1 elimination step of mechanism m1 leading to formation of 1-butene. As the latter mechanism is known to have an insignificant contribution to the overall TOF[6] for the conversion of 1-butanol, the mechanism for formation of 2t-butene from M1 is also expected to have a negligible contribution and has not been considered for further study. The higher activation energy for these mechanisms is justified considering the lower stability of primary carbenium ions. On the other hand, as adsorbed butanol dimer (D1) and DBE* remain the key surface intermediates during 1-butanol dehydration, the possibility of the direct conversion of D1 and DBE* to 2t-butene is investigated in detail. Analogous reaction mechanisms for the direct formation of 2c-butene from D1 and DBE via E1 elimination may be operative but these mechanisms are not considered in the scope of the present study.

Mechanism m11 consists of adsorption of butanol on the adsorbed monomer M1 to form adsorbed dimer D1 (step 11), which undergoes water elimination accompanied by a hydride shift reaction (step 24) producing 2t-butene and C2 (co-adsorbed butanol and water), followed by desorption of water (step 14). Reaction step 24 for the conversion of D1 to C2 is activated.

Strictly speaking the conversion of D1 to C2 consists of two steps (see Figure 4a), namely an initial rearrangement of D1 followed by the elimination reaction, which are nonetheless considered as a single step in the microkinetic simulation in order to simplify the reaction network. In the initial rearrangement of the butanol dimer, the shared proton H_z moves closer to the oxygen atom O_1 increasing the positive charge on the alcohol and leading to elongation of the $C\alpha$-O_1 bond which facilitates its cleavage. The rearrangement of the butanol dimer also involves rotation of the alkyl chain of the protonated 1-butanol so that H_γ is positioned closer to the oxygen atom O_2 of the physisorbed 1-butanol. As seen in Figure 4a, the rearranged dimer undergoes a simultaneous 1,2-hydride shift of the H_β, cleavage of the C_α-O_1 bond, and H_γ abstraction by the oxygen atom (O_2) of the physisorbed butanol molecule leading to the formation of 2t-butene.

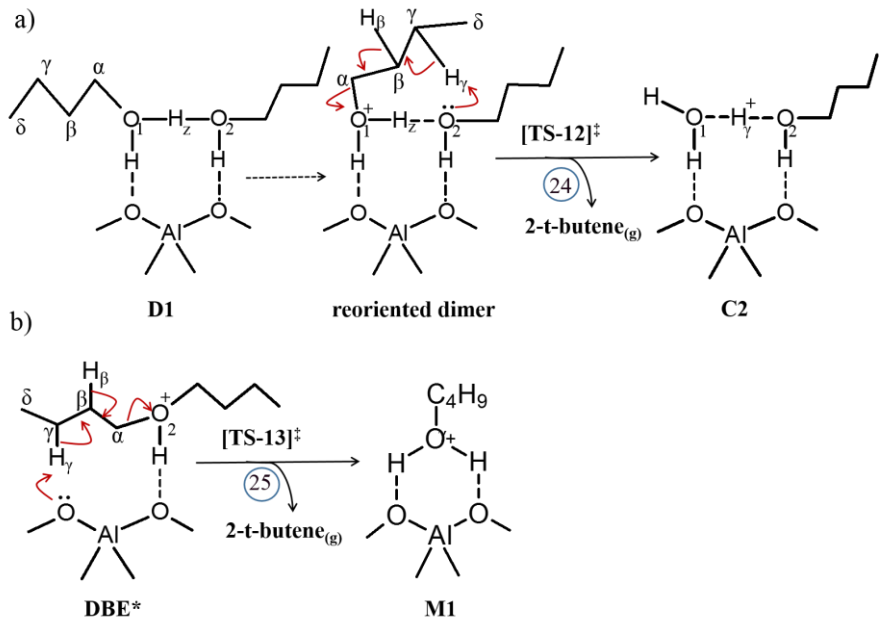

Figure 4: Electron flow diagram for conversion of (a) 1-butanol dimer (D1) to 2t-butene and butanol-water co-adsorbed species (C2), (b) adsorbed di-1-butyl ether (DBE*) to 2t-butene and adsorbed 1-butanol monomer (M1).

In the transition state (TS-12, Figure 3) geometry for 2t-butene formation from butanol dimer, C_α–O_1 and C_γ–H_γ interatomic distances are 244 and 112 pm, respectively. Therefore, the C–O bond is completely broken while the C_γ–H_γ still remains intact, indicating an E1-type

elimination. The 1,2 hydride shift is also evident from the C_β–H_β and C_α–H_β interatomic distances which are 144 and 127 pm, respectively. This transition state differs from the previously studied TS (TS-6 of m5 in Chapter 2 / Ref [6]) for 1-butene formation from butanol dimer in the following aspects. First, TS-12 for the formation of 2t-butene follows an E1 elimination while TS-6 for the formation of 1-butene follows a syn E2 elimination. This is understood from the extent of bond breakage in the TS geometry, namely the C_α–O_1 bond breakage is more pronounced in TS-12, while the C-H bond breakage due to the hydrogen abstraction by the zeolite oxygen is more pronounced in TS-6. Second, TS-12 involves a hydride shift reaction which is not seen in the case of TS-6. Third, different hydrogen atoms are abstracted by the zeolite oxygen in case of these two TS. H_β and H_γ atoms are abstracted by the zeolite oxygen in case of TS-6 and TS-12, respectively. In addition, reaction step 24 for the conversion of D1 to C2 and 2-butene has an activation energy of 201 kJ/mol in comparison to the activation energy of 161 kJ/mol for the conversion of D1 to C2 and 1-butene[6].

The direct mechanism for 2-butene formation from DBE decomposition (m12) can be of significant importance owing to the high surface coverage of DBE*. As seen from Table 1, mechanism m12 proceeds via a sequence of elementary steps namely, reaction step 16 (adsorption of DBE), step 25 (decomposition of DBE* to 2t-butene and adsorbed butanol monomer M1) and step 1 (desorption of 1-butanol). Reaction step 25 of mechanism m12 is activated and involves simultaneous 1,2-hydride shift, cleavage of the C_α-O_2 bond, and H_γ abstraction by the basic oxygen atom of the zeolite (see Figure 4b). Reaction step 25 has an activation barrier of 171 kJ/mol as compared to 140 kJ/mol for DBE* decomposition to C4 (co-adsorbed 1-butene and 1-butanol) [6]. In the transition state (TS-13, Figure 3) geometry of reaction step 25, C_α–O_1 and C_γ–H_γ interatomic distances are 245 and 112 pm, respectively. Therefore, the C–O bond is completely broken, while the C_γ–H_γ still remains intact, indicating

an E1-type elimination. The 1,2 hydride shift is also evident from the C_β–H_β and C_α–H_β interatomic distances which are 143 and 126 pm, respectively.

Moreover, it is worth mentioning that the Bader charge for the [C_4H_9] fragment is found to be +0.89 and +0.86 in TS-12 and TS-13, respectively. The charge on the [C_4H_9] fragment is comparable with the one reported for the cationic fragment (+0.85) in a DFT study on E1 elimination of water from 2-butanol in POM [73]. Thus, the TS geometry and the charge on the [C4H9] fragment confirm an E1 elimination with simultaneous 1,2-hydride shift for the elimination of water and 1-butanol from butanol dimer and protonated ether, respectively.

Figure 5 shows the standard Gibbs free energy profile for mechanisms m11 (path D) and mechanism m12 (path E) for production of 2t-butene from D1 and DBE* respectively, and compares them to mechanism m9 (path C) described in Chapter 2/ Ref [6] for production of 1-butene from DBE*. The free energy profile shows that TS-12 of mechanism m11 exhibits the highest free energy barrier followed by TS-13 of mechanism m12 and TS-10 of m9, indicating that the formation of 1-butene from DBE* is energetically favored over formation of 2t-butene from D1 and DBE*.

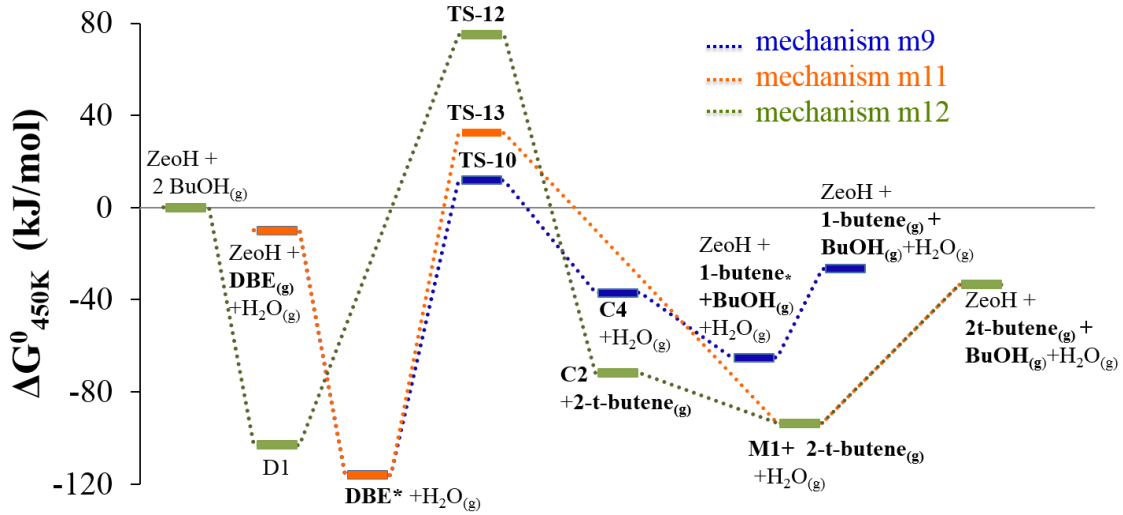

Figure 5. Comparison of standard Gibbs free energy profile for the conversion of 1-butanol to 2-t-butene (path D, mechanism m11) and DBE to 2-t-butene and 1-butanol (path E, mechanism m12) with the conversion of DBE to 1-butene and 1-butanol (mechanism m9 of path C) in H-ZSM-5 at 450 K.

4.3.1.3. Double bond isomerization (Path F, G and H)

The double bond isomerization of 1-butene to 2t-butene (path F) can proceed via a concerted mechanism (m13) [20,21] or a step-wise mechanism involving a 2-butoxide intermediate (m14) [17,18] as shown in Figure 6.

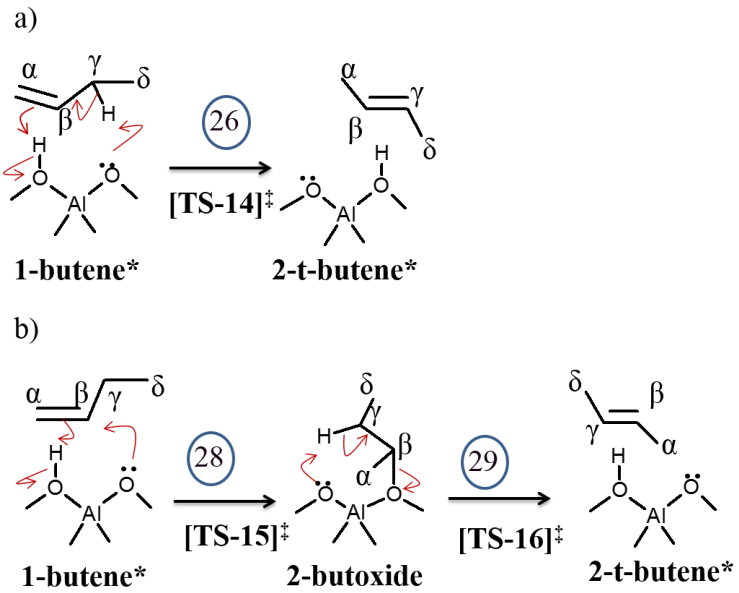

Figure 6: Electron flow diagram for conversion of 1-butene* to 2t-butene* via (a) concerted mechanism (b) 2-butoxide mediated step-wise mechanism.

As seen from Table 1, mechanism m13 consists of a sequence of steps namely, 8 (adsorption of 1-butene), 26 (conversion of adsorbed 1-butene to adsorbed 2t-butene) and 27 (desorption of 2t-butene). Step 26 of mechanism m13 is activated and involves the protonation of the double bond of 1-butene by the zeolite proton and a simultaneous abstraction of H_γ by the basic O-atom of the zeolite (see Figure 6a and TS-14 of Figure 3). Mechanism m14 consists of steps 8, 28, 29 and 27, of which steps 28 (TS-15) and 29 (TS-16) are activated. Reaction step 28 involves protonation of the double bond of 1-butene by the zeolite proton and bond formation between C_β and the zeolite oxygen atom (see Figure 6b and TS-15 of Figure 3) leading to formation of 2-butoxide. Reaction step 29 involves abstraction of H_γ by the basic O-atom of the zeolite and simultaneous breakage of the C_β–O_a bond (see Figure 6b and TS-16

of Figure 3) leading to formation of physisorbed 2t-butene. The free energy diagrams for path F mechanisms (see Figure 7) indicate comparable free energy barriers for the concerted (m13) and step-wise mechanism (m14) with the latter offering a slightly lower free energy barrier. Reaction step 26 of the concerted mechanism (m13) and reaction step 28 (physisorbed 1-butene to 2-butoxide) of mechanism m14 have activation energies of 54 and 48 kJ/mol respectively (see Table 2), which are in close agreement with the experimentally reported value of 49 ± 4 kJ/mol [20]. A previous quantum chemical calculation using a 3T zeolite cluster model for double bond isomerization of 1-butene to 2t-butene reports an activation energy of 84 kJ/mol w.r.t adsorbed 1-butene and an apparent activation energy of 59 kJ/mol [21]. The difference in activation energies between the present study and the previous small cluster calculation can be attributed to the absence of stabilizing interactions between the adsorbed species and the zeolite walls in the latter case.

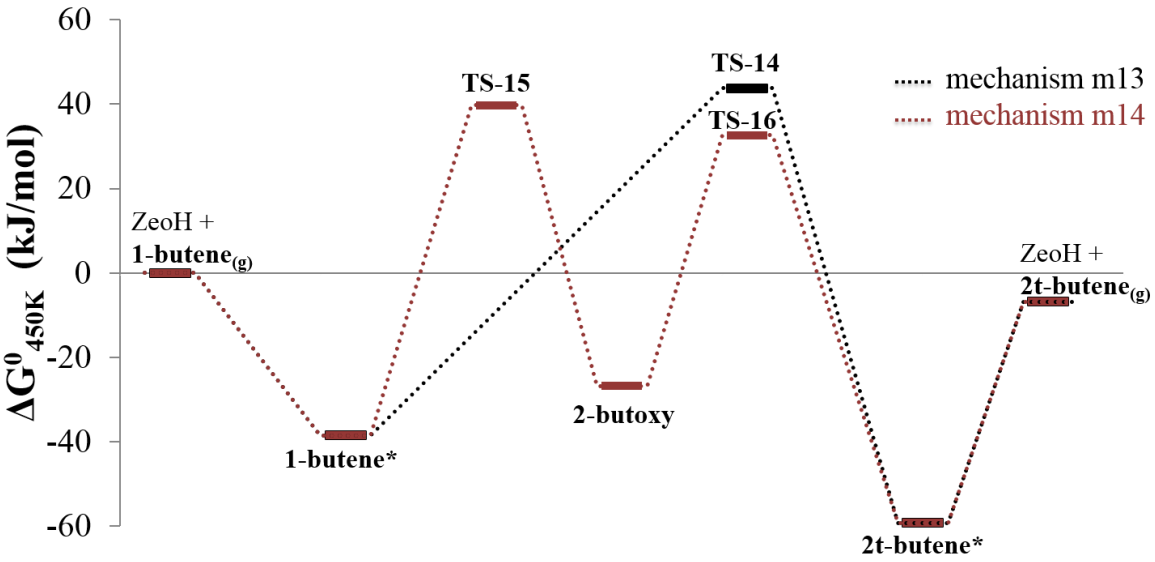

Figure 7. Standard Gibbs free energy profile for conversion of 1-butene to 2t-butene (path F via mechanisms m_{13} and m_{14}) in H-ZSM-5 at 450 K.

2c-butene can be produced via double bond isomerization of 1-butene (path G, via mechanism m15) and/or 2t-butene (path H, via mechanism m16) in a stepwise manner as shown in Figure 8. Alternatively, the small cluster (3T cluster) DFT studies by Li et al. [22] reported a

concerted mechanism for formation of 2c-butene from 1-butene, but our study indicates that steric repulsion from the zeolite walls prevented such a TS within the 10-MR ring of H-ZSM-5.

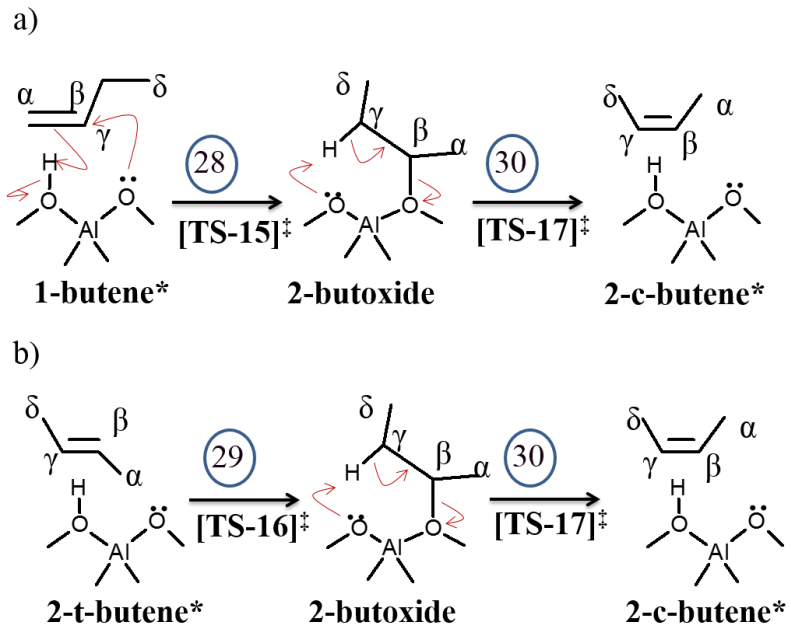

Figure 8: Electron flow diagram for conversion of (a) 1-butene* to 2c-butene* (b) 2t-butene* to 2c-butene*.

Both mechanisms m15 and m16 follow a 2-butoxide mediated route analogous to mechanism m14. As seen from Table 1, mechanism m15 consists of a sequence of steps, namely 8 (adsorption of 1-butene), 28 (protonation of adsorbed 1-butene to 2-butoxide), 30 (de-protonation of 2-butoxide to adsorbed 2c-butene) and 31 (desorption of 2c-butene), of which step 28 (TS-15) and 30 (TS-17) are activated. Mechanism m16 consists of a sequence of steps, namely 27 (adsorption of 2t-butene), 29 (protonation of adsorbed 2t-butene to 2-butoxide), 30 (de-protonation of 2-butoxide to adsorbed 2c-butene) and 31 (desorption of 2c-butene), of which step 29 (TS-16) and 30 (TS-17) are activated.

As seen from Figure 9, comparison of the free energy profile for path G and H for formation of 2c-butene indicates a slightly lower $\Delta G_0^{\ddagger}$ for the formation of 2-butoxide from 1-butene*

as compared to the formation of 2-butoxide from 2t–butene*. However, as the actual reaction rate is a complex function of reaction conditions, a conclusive result regarding the preferred reaction mechanism can only be obtained from a reaction path analysis in actual reaction conditions.

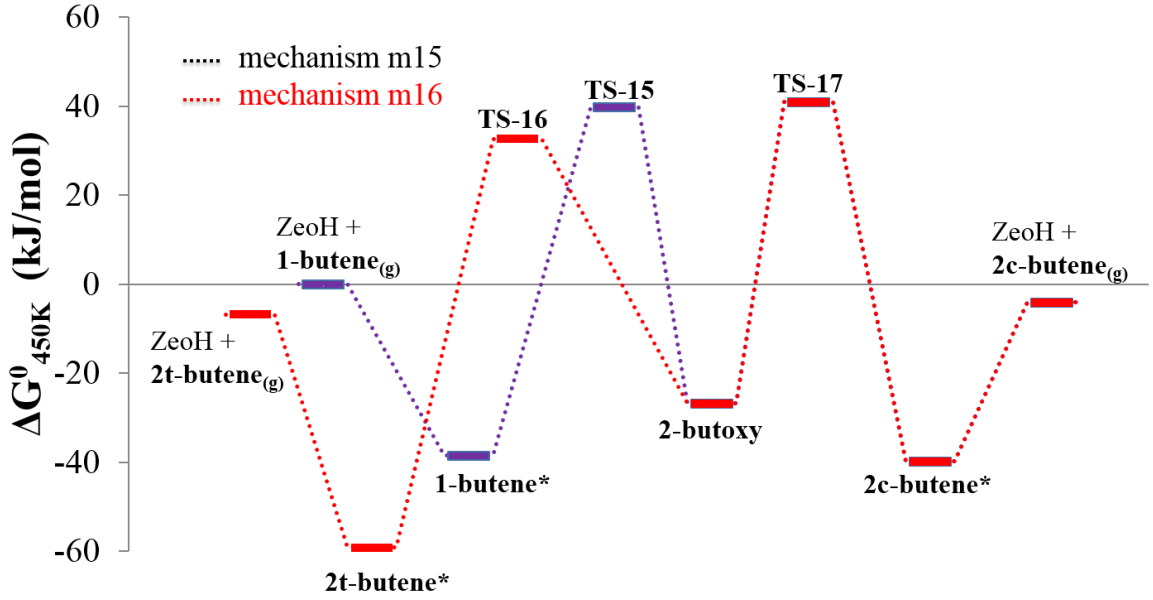

Figure 9. Standard Gibbs free energy profile for conversion of 1-butene to 2c-butene (path G, mechanism m_{15}) and 2t-butene to 2c-butene (path H, mechanism m_{16}) in H-ZSM-5 at 450 K.

4.3.1.4. Skeletal isomerization of linear butenes to isobutene (path I, J and K)

Both bimolecular [30,31] and monomolecular [25-29] mechanisms have been proposed for butene skeletal isomerization in zeolites. The bimolecular mechanism involves butene dimerization, isomerization, and cracking to produce isobutene. Although bimolecular mechanisms are reported to have lower activation barriers[31], they are known to be less selective and lead to production of several other side products[26]. Moreover, as the active sites are mostly occupied by strongly adsorbed 1-butanol and DBE, the possibility of a bimolecular skeletal isomerization is quite rare. Accordingly, the present study focuses only on the monomolecular skeletal isomerization of linear butenes to isobutene. The monomolecular mechanism can proceed via an alkoxide or carbenium ion intermediate. A hybrid quantum/molecular

mechanics study for skeletal isomerization of cis-2-butene in FER indicated the alkoxide mediated mechanism to be energetically favorable over the carbenium ion mediated mechanism[29].

In the present study, a monomolecular alkoxide mediated skeletal isomerization of linear butenes to isobutene has been investigated. Path I, J and K represent conversion of 1-butene, 2t-butene and 2c-butene to iso-butene via mechanism m17 (steps 8, 28, 32, 33, 34), m18 (steps 27, 29, 32, 33, 34) and m19 (steps 31, 30, 32, 33, 34). All three mechanisms involve reaction step 32 (2-butoxide to iso-butoxide), 33 (iso-butoxide to adsorbed iso-butene), and 34 (desorption of iso-butene), of which step 32 (via TS-18) and 33 (via TS-19) are activated. The electron flow diagram for the conversion of 1-butene* to isobutene* is shown in Figure 10.

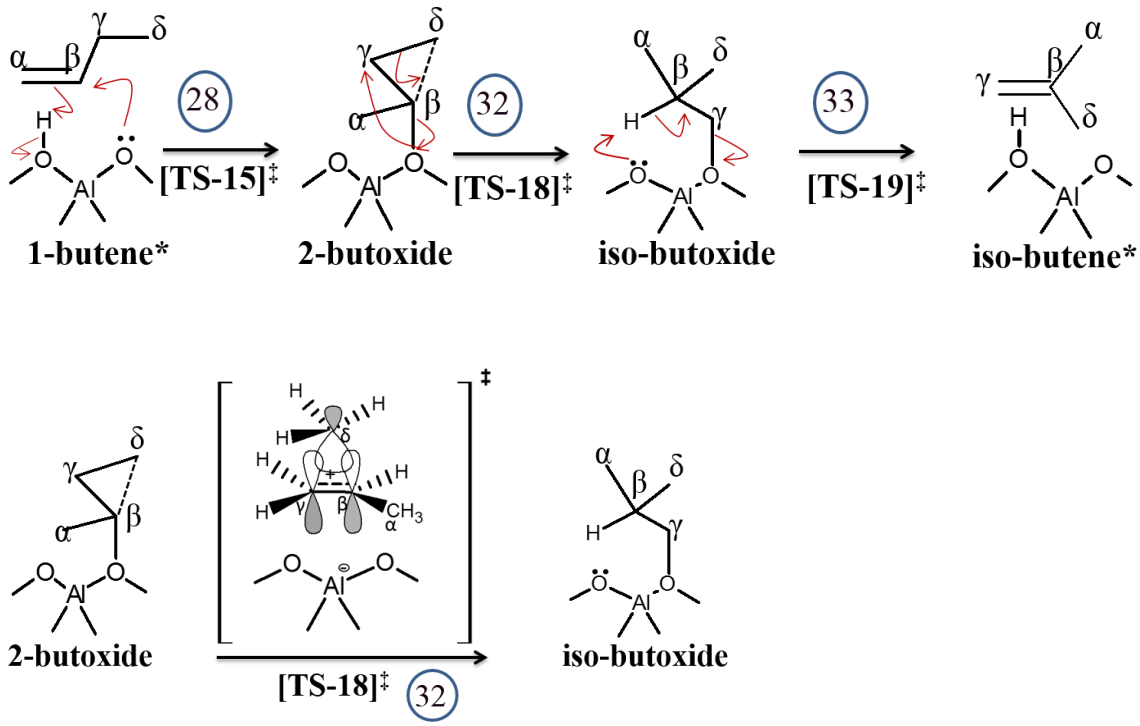

Figure 10: Electron flow diagram for conversion of 1-butene* to isobutene* and the π-bonded propene-methyl TS complex for conversion of 2-butoxide to iso-butoxide.

Reaction step 32 involves cleavage of the C_β–O_a and the C_γ–C_δ bond of 2-butoxide and formation of new C_β–C_δ and C_γ–O_a bonds leading to formation of iso-butoxide. In the

transition state (see TS-18 of Figure 3) geometry, the bond between C_β–O_a is completely broken (C_β–O_a interatomic distance of 308 pm), and the methyl group is bridged between C_β and C_γ (C_β–C_δ , C_γ–C_δ and C_β–C_δ interatomic distances of 174, 184 and 140 pm, respectively). These geometric parameters in TS-18 are characteristic of a π-bonded propene-methyl carbocationic TS[74,75] (see TS-18 in Figure 10) and are consistent with the interatomic distances reported for the TS of the skeletal isomerization of 1-butene in Theta-1 zeolite (i.e. C_β–C_δ , C_γ–C_δ and C_β–C_δ of 179, 180 and 139 pm, respectively)[24]. Furthermore, a Bader charge analysis indicates the cationic nature of the π-bonded propene-methyl complex in the TS with the [C_4H_9] fragment having a charge of +0.89, which is consistent with the reported charge of +0.85 on the same fragment of the TS for the skeletal isomerization of 1-butene in H-FER[76]. Finally, reaction step 33 involves abstraction of H_β by the basic O-atom of the zeolite and simultaneous breakage of C_γ–O_a bond (see Figure 10 and TS-19 of Figure 3) leading to formation of physisorbed isobutene.

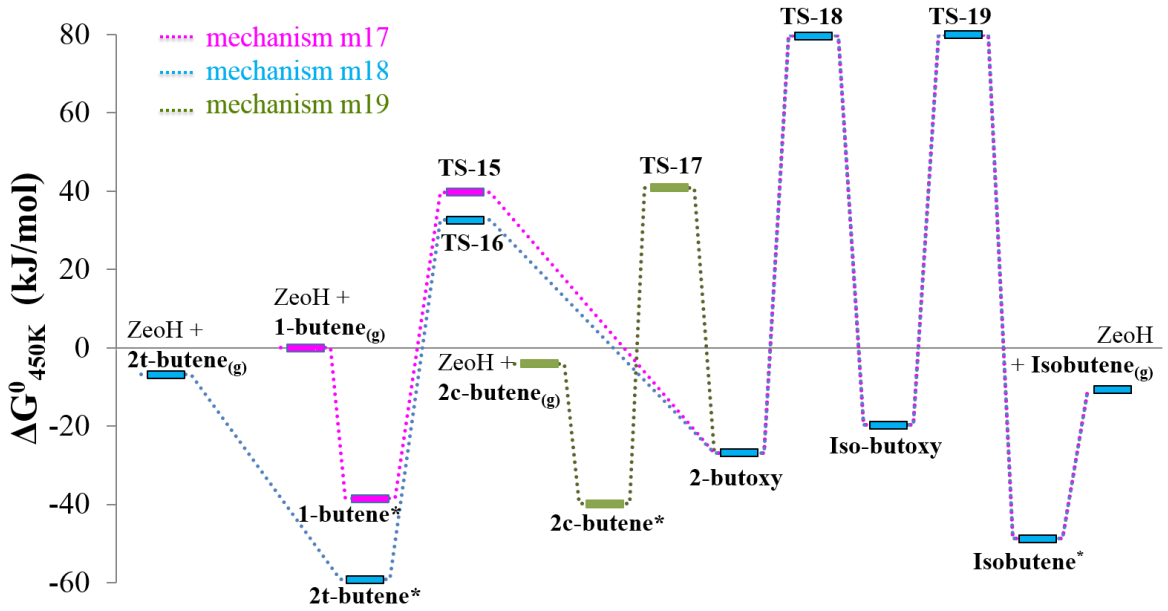

Figure 11. Standard Gibbs free energy profile for conversion of 1-butene to iso-butene (path I, mechanism m_{17}), 2t-butene to iso-butene (path J, mechanism m_{18}) and 2c-butene to iso-butene (path K, mechanism m_{19}) in H-ZSM-5 at 450 K.

The standard Gibbs free energy profiles for mechanisms m17–m19 leading to formation of isobutene are shown in Figure 11. The free energy diagram indicates a slightly higher stability of 2-butoxy over iso-butoxy. This relatively higher stability of 2-butoxy as compared to iso-butoxy is also in agreement with the B3LYP/6-31+G** level of calculation by Correa and Mota[77]. In comparison to their reported energy difference of 3 kJ/mol, a difference of 11 kJ/mol is found for the conversion of 2-butoxide to iso-butoxide in the present study.

Reaction steps 32 (via TS-18) and 33 (via TS-19) have much higher free energy barriers as compared to all other steps (see Figure 11) involved in the skeletal isomerization of butenes. The activation energies of reaction for conversion of 2-butoxide to iso-butoxide (step 32) and iso-butoxide to iso-butene (step 32)) are 123 and 100 kJ/mol respectively, which is in line with the experimentally reported value of 118 kJ/mol [25]. A previous quantum chemical calculation for skeletal isomerization of 1-butene to isobutene in a 20T cluster model of H-ZSM-22 reported an activation energy of 109 kJ/mol for the conversion of 2-butoxide to iso-butoxide [24]. A higher activation energy for skeletal isomerization of 1-butene in H-ZSM-5 as compared to H-ZSM-22 is in line with the experimentally reported higher isobutene selectivity in H-ZSM-22[3,4]. The 0 K electronic energy barrier for deprotonation of isobutoxide to form physisorbed isobutene in H-ZSM-5 is 112 kJ/mol (PBE-D2) which is comparable to the previously reported value 120 kJ/mol (PW91+D2)[72].

4.3.2 *Microkinetic modelling and reaction path analysis: 1-butanol dehydration and butene isomerization*

A detailed microkinetic model considering all 19 different reaction mechanisms, consisting of 34 elementary steps (23 steps for formation of 1-butene/DBE as described in Chapter 2/ Ref [6] and 11 extra steps as shown in Table 1 for formation of butene isomers) has been applied without making any assumption for the rate determining step. The effect of reaction conditions, viz., inlet partial pressure of 1-butanol (0.001-100 kPa) and reaction temperature

(450-500 K) at site times ranging from $N_{H+}/F_{BuOH,0}$ = 0 to 200 mol H^+ s / mol $BuOH_0$, is studied. A comparison of the forward, reverse and net reaction rates for the different elementary steps over a wide range of reaction conditions has been used to determine the equilibrated and non-equilibrated steps along each mechanism.

The DFT based microkinetic model used in this study has been validated with experimental observations [2] for dehydration of 1-butanol to 1-butene and DBE in H-ZSM-5 in Chapter 2/ Ref. [6] Moreover, as the calculated activation barriers for the double bond and skeletal isomerization are in good agreement with the experimentally reported values, the DFT based microkinetic model can be reliably used to identify key reaction mechanisms and to provide a detailed insight into the effect of reaction conditions.

4.3.2.1. Effect of site time and conversion

The influence of site time on conversion and product selectivity is studied at constant reaction temperature and pressure. Figure 12 shows the effect of site time on 1-butanol conversion, product selectivity and surface coverages. DBE selectivity decreases steadily with increasing site time, while the 1-butene selectivity was found to pass through a maximum as a function of site time. 2t-butene and 2c-butene were observed only at higher site time corresponding to higher conversions (above 50%), while no isobutene is observed in the entire 1-butanol conversion range. An increase in conversion leads to a decrease in surface concentration of adsorbed butanol dimer (D1) and an initial increase in DBE* surface coverage. As the 1-butanol conversion increases from 20% to 90%, there is a 100-fold increase in the surface coverage of 1-butene, which facilitates the subsequent double bond isomerization producing 2t-butene and 2c-butene. It is seen that at higher site time (above 100 mol H+ / mol), 1-butene, 2t-butene and 2c-butene tend to achieve the thermodynamic equilibrium composition of 10, 60 and 30%, respectively at 450K, and no isobutene is formed in these conditions.

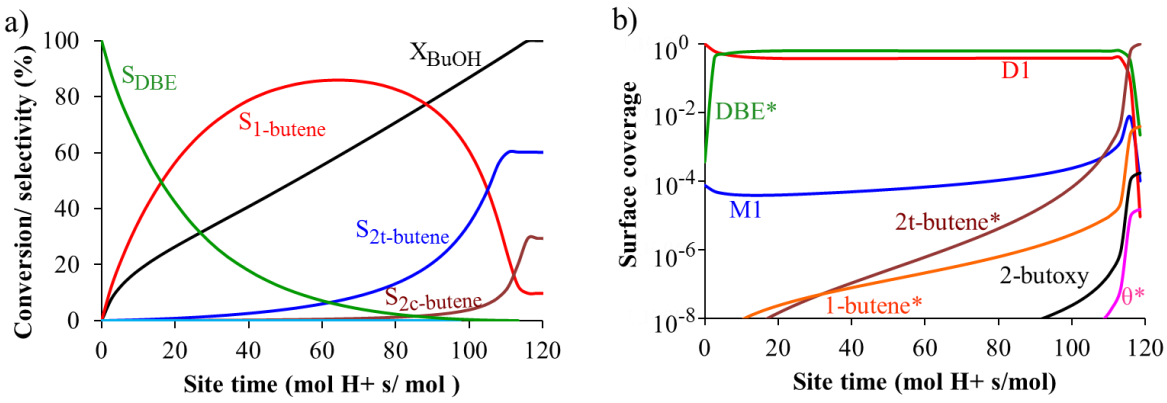

Figure 12. (a) 1-butanol conversion(X_{BuOH}) and product (1-butene, 2t-butene, isobutene and DBE) selectivity as a function of site time, (b) coverages for surface species as a function of site time. Reaction conditions: 450 K, 1-butanol inlet partial pressure of 10 kPa

At higher site time on complete conversion of 1-butanol, the surface coverage for butenes is high and alkylation of butenes is also expected to occur. However, alkylation of butenes is not included in the scope of the present study. Moreover, alkylation of alkenes is known to be significantly inhibited in presence of strongly adsorbing oxygenates such as alcohol and ether [78]. Accordingly, further discussions are restricted to site times which avoids complete conversion of butanol, ensuring that surface coverage of butanol /DBE is always higher than that of butenes.

Figure 13 shows the effect of conversion (X_{BuOH}) on the simulated selectivity profile, surface coverages and the TOFs for the different reaction mechanisms at 450K and 1-butanol inlet partial pressure of 10 kPa. An increase in conversion leads to a decrease in DBE selectivity and an increase in selectivity for 2t-butene and 2c-butene, while the 1-butene selectivity was found to pass through a maximum. The simulation results indicate no formation of isobutene in the entire butanol conversion range. For path A (Figure 13c), the preferred mechanism shifts from mechanism m5 (dimer mediated syn-elimination) to m3 (anti elimination) with increase in conversion. This shift in reaction mechanism is attributed to the changes in the surface coverage of M1 and D1 with increase in conversion as seen from Figure 13b. For path B (Figure 13d) and path C (Figure 13e), mechanism m6 (S_N2 substitution of butanol dimer

to DBE) and m9 (syn-elimination) remain the preferred mechanisms in the entire butanol conversion range. At low conversion levels (X_{BuOH} less than 5%), 2t-butene formation occurs via ether decomposition (mechanism m12 of path E), while the double bond isomerization mechanisms (m14, m13 and m15) tend to dominate at higher conversion levels (X_{BuOH} greater than 40%). Moreover, it is seen that the 2-butoxide mediated step-wise (m14) mechanism has a slightly higher contribution as compared to the concerted (m13) double bond isomerization.

Comparing Figures 13c-f, it is seen that with an increase in conversion the dominant path shifts from DBE formation (path B, mechanism m6) and 1-butene formation from DBE decomposition (path C, mechanism m9) to double bond isomerization reactions leading to formation of 2t-butene (path F via mechanisms m13 and m14) and 2c-butene (path G via mechanism m15) from 1-butene. This explains the occurrence of a maximum in the 1-butene selectivity profile. Hence, for a selective production 1-butene, it is advisable to operate at moderate conversion levels (50-60% at 450K and $P_{BuOH,0}$ of 10kPa), where 1-butene remains the key product and the surface is fully covered with strongly adsorbed 1-butanol and DBE species not allowing double bond isomerization reactions to occur.

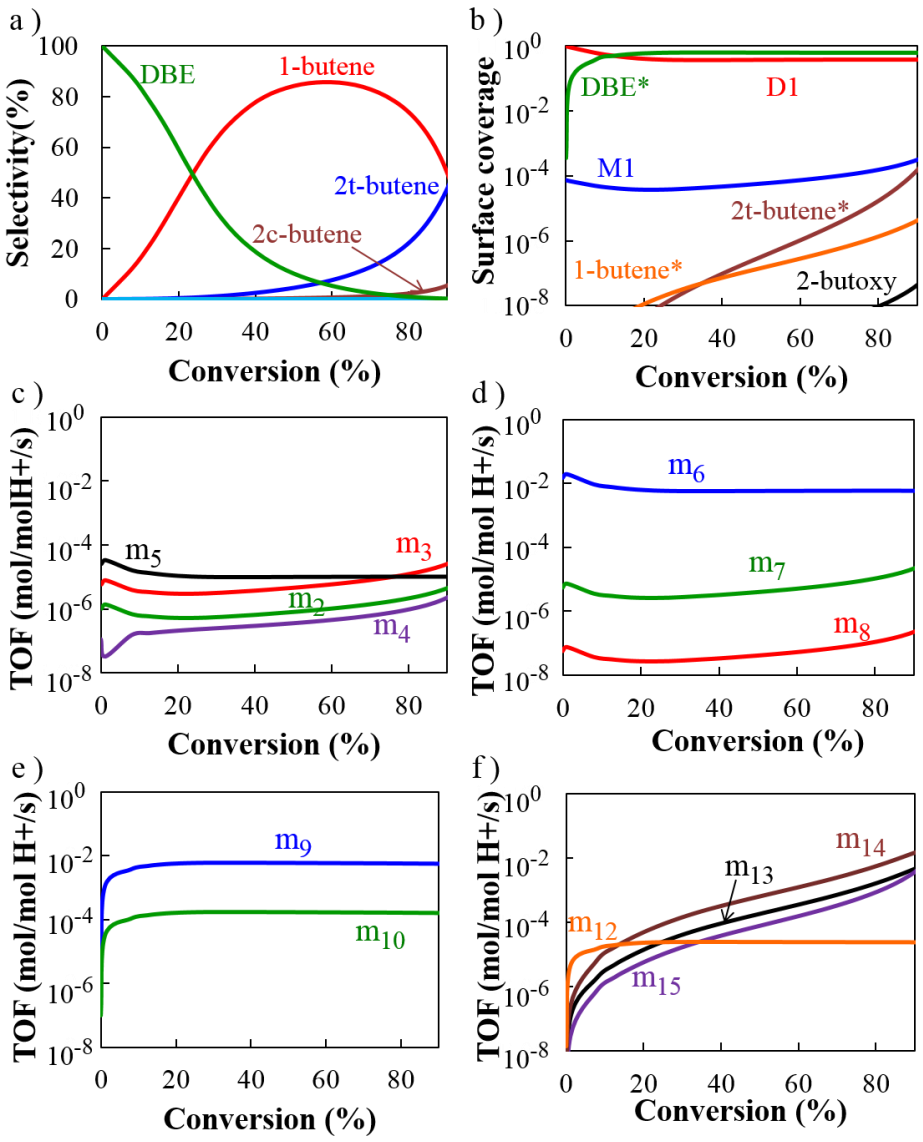

Figure 13. Effect of conversion on: (a) product selectivity, (b) surface coverages, (c) TOF for direct dehydration of 1-butanol to 1-butene (path A via mechanisms m_1-m_5), (d) TOF for dehydration of 1-butanol to di-1-butyl ether (path B via mechanisms m_6-m_8), (e) TOF for ether decomposition to 1-butene and 1-butanol (path C via mechanisms m_9-m_{10}), (f) TOF for conversion of 1-butanol to 2-t-butene (path D, mechanism m_{11}), DBE to 2-t-butene and 1-butanol (path E, mechanism m_{12}), double bond isomerization of 1-butene to trans-2-butene (path F via mechanisms m_{13}-m_{14}), double bond isomerization of 1-butene/2t-butene to cis-2-butene (path G/path H via mechanisms m_{15} /m_{16}), skeletal isomerization of 1-butene/2t-butene to iso-butene (path I/path J/ path K via mechanisms m_{17}/m_{18}/m_{19}). Reaction conditions: 450 K, butanol inlet partial pressure of 10 kPa. Mechanisms with TOF less than 10^{-8} s^{-1} are not shown in the figure.

4.3.2.2. Effect of reaction temperature

Earlier experimental studies [13] on 1-butanol dehydration in sodium exchanged X, 4A and ZNa zeolite indicated an increase in production of 2-butenes (trans/cis) with an increase in reaction

temperature. They ascribed this to a larger increase in the rate of formation of 2-butenes via E1 elimination relative to the rate of formation of 1-butene via E2 elimination with an increase in reaction temperature. Herein, the effect of reaction temperature on product selectivity, surface coverage and TOFs and the underlying reaction mechanism is investigated using microkinetic modelling in a temperature range of 450-500 K. An increase in reaction temperature is also associated with an increase in conversion which has a significant impact on the overall product selectivity. Therefore, selectivities, surface coverages and TOFs at different temperatures are compared at a fixed 1-butanol conversion of 70%, where one can expect significant production of 2-butenes (cis or trans), see e.g. Figure 13.

Figure 14 shows the effect of reaction temperature on the simulated selectivity profiles, surface coverages and TOFs for the different reaction mechanisms in a temperature range of 450-500K and butanol inlet partial pressure of 10 kPa, compared at 1-butanol conversion of 70 %.

As seen from Figure 14a, an increase in reaction temperature leads to a decrease in 1-butene selectivity and an increase in selectivity to 2t-butene and 2c-butene. This can be explained on the basis of the changes in the surface coverages with an increase in reaction temperature. The increase in reaction temperature leads to a larger decrease in ΔG^{o}_{ads} for the strongly adsorbed 1-butanol dimer and DBE, which have a much larger value of ΔS^{o}_{ads} as compared to the loosely bound butene isomers. This in turn leads to a relative increase in the surface coverage of butenes (see Figure 14b) with increasing reaction temperature, which increases the TOFs for double bond isomerization reactions, favoring the formation of 2t-butene and 2c-butene. Thus, the increase in production of 2-butenes with increase in reaction temperature is in line with the experimental observation of Olaofe and Yue [13] for 1-butanol dehydration in zeolites. Comparison of the relative slopes of TOF vs temperature (see Figure 14f) indicates that much

higher temperatures are required for the TOF of skeletal isomerization mechanism 17 to have a significant contribution.

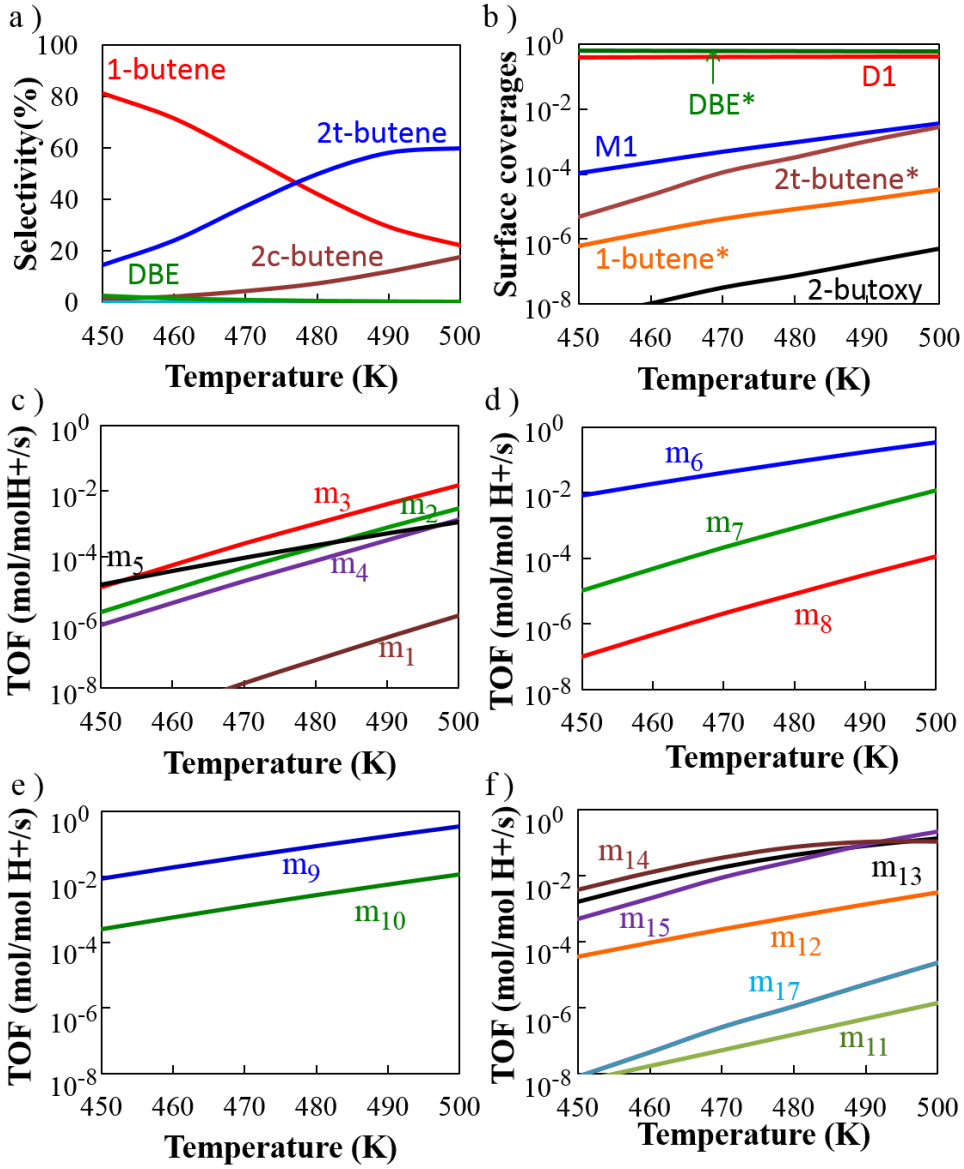

Figure 14. Effect of reaction temperature on: (a) product selectivity, (b) surface coverages, (c) TOF for direct dehydration of 1-butanol to 1-butene (path A via mechanisms m_1-m_5), (d) TOF for dehydration of 1-butanol to di-1-butyl ether (path B via mechanisms m_6-m_8), (e) TOF for ether decomposition to 1-butene and 1-butanol (path C via mechanisms m_9-m_{10}), (f) TOF for conversion of 1-butanol to 2-t-butene (path D, mechanism m_{11}), DBE to 2-t-butene and 1-butanol (path E, mechanism m_{12}), double bond isomerization 1-butene to trans-2-butene (path F via mechanisms m_{13}-m_{14}), double bond isomerization of 1-butene/2t-butene to cis-2-butene (path G/path H via mechanisms m_{15} /m_{16}), skeletal isomerization of 1-butene/2t-butene to iso-butene (path I/path J/ path K via mechanisms m_{17}/m_{18}/m_{19}). Reaction conditions: butanol inlet partial pressure of 10 kPa and site time adjusted to have a constant butanol conversion of 70%. Mechanisms with TOF less than 10^{-8} s^{-1} are not shown in the figure.

The effect of reaction temperature on the underlying reaction mechanisms is seen from Figures 14c-f. In line with Chapter 2 / Ref,[6] mechanism m3 (via anti elimination of water from chemisorbed monomer), m6 (via dimer mediated S_N2 mechanism) and m9 (via syn elimination of 1-butanol from DBE*) remain the preferred reaction mechanism for path A, B and C, respectively. At temperatures lower than 480 K, 2-butoxide mediated step-wise mechanism for formation of 2t-butene (m14) has a slightly higher contribution as compared to the concerted mechanism m13 and the step-wise mechanism for formation of 2c-butene (m15). At temperatures higher than 490K, all the three double bond isomerization mechanisms have comparable TOFs. Under the specified reaction conditions, the TOFs for mechanism m11 and m12 leading to the formation of 2t-butene from D1 and DBE* (via E1 elimination) are significantly lower than that of the concerted (m13) and 2-butoxide mediated step-wise (m14 and m15) mechanisms for double bond isomerization. Unlike the reaction mechanism proposed by Olaofe and Yue [13], which attributed the increase in production of 2-butenes to the shift in reaction mechanism from E2 to E1, i.e. form m3 to m11, our theoretical study shows that the increase in production of 2-butenes can be attributed to an increase of the TOFs for double bond isomerization, the latter resulting from the increase in butene coverage as discussed in the previous paragraph.

4.3.2.3. Effect of partial pressure of 1-Butanol

The influence of 1-butanol inlet partial pressure on the simulated product selectivity, surface coverages and TOFs of the underlying reaction mechanisms is studied at constant reaction temperature of 450K and constant 1-butanol conversion of 70 %. Figure 15a shows the effect of 1-butanol inlet partial pressure on product selectivity. The selectivity profile at low butanol inlet partial pressures indicate that the linear butene isomers (1-butene, 2t-butene and 2c-butene) are in thermodynamic equilibrium, while more of 1-butene and DBE are produced at higher 1-butanol partial pressures. This can be rationalized on the basis that at lower 1-butanol

inlet partial pressures ($P_{BuOH,0}$ less than 0.1 kPa), the TOFs for the double bond isomerization mechanisms (m13 and m14 of path F and m15 of path G) are comparable to the TOF for 1-butene formation from direct dehydration (path A) and DBE decomposition (path C). A decrease in $P_{BuOH,0}$ leads to a decrease in surface coverage of D1 and a marginal increase in the surface coverage of 1-butene. As the reaction rate coefficients for the double bond isomerization are ~4-5 orders of magnitude higher than that of 1-butanol dehydration (see Chapter 2 / Ref [6]), the TOF for double bond isomerization can still be comparable to that of 1-butene formation even at very low surface coverage of 1-butene. Thus, linear butenes tend to achieve the thermodynamic equilibrium composition for dehydration at lower 1-butanol partial pressures.

The influence of 1-butanol inlet partial pressure on the underlying reaction mechanisms is shown in Figures 15c-f. The TOFs for reaction mechanisms of path A, B and C follow a trend as reported in Chapter 2 / Ref,[6] with mechanism m3 (anti elimination mechanism of path A) being dominant at lower 1-butanol partial pressure which shifts in favor of mechanism m6 (dimer mediated S_N2 mechanism of path B) and m9 (syn elimination of path C) at higher 1-butanol partial pressures. For 1-butanol partial pressures less than 1 kPa, all three double bond isomerization mechanisms (m13, m14 and m15) have comparable contributions (see Figure 15f), while at higher 1-butanol partial pressures the 2-butoxide mediated step-wise mechanism for formation of 2t-butene (m14) has a slightly higher contribution as compared to the concerted mechanism m13 and the step-wise mechanism for formation of 2c-butene (m15).

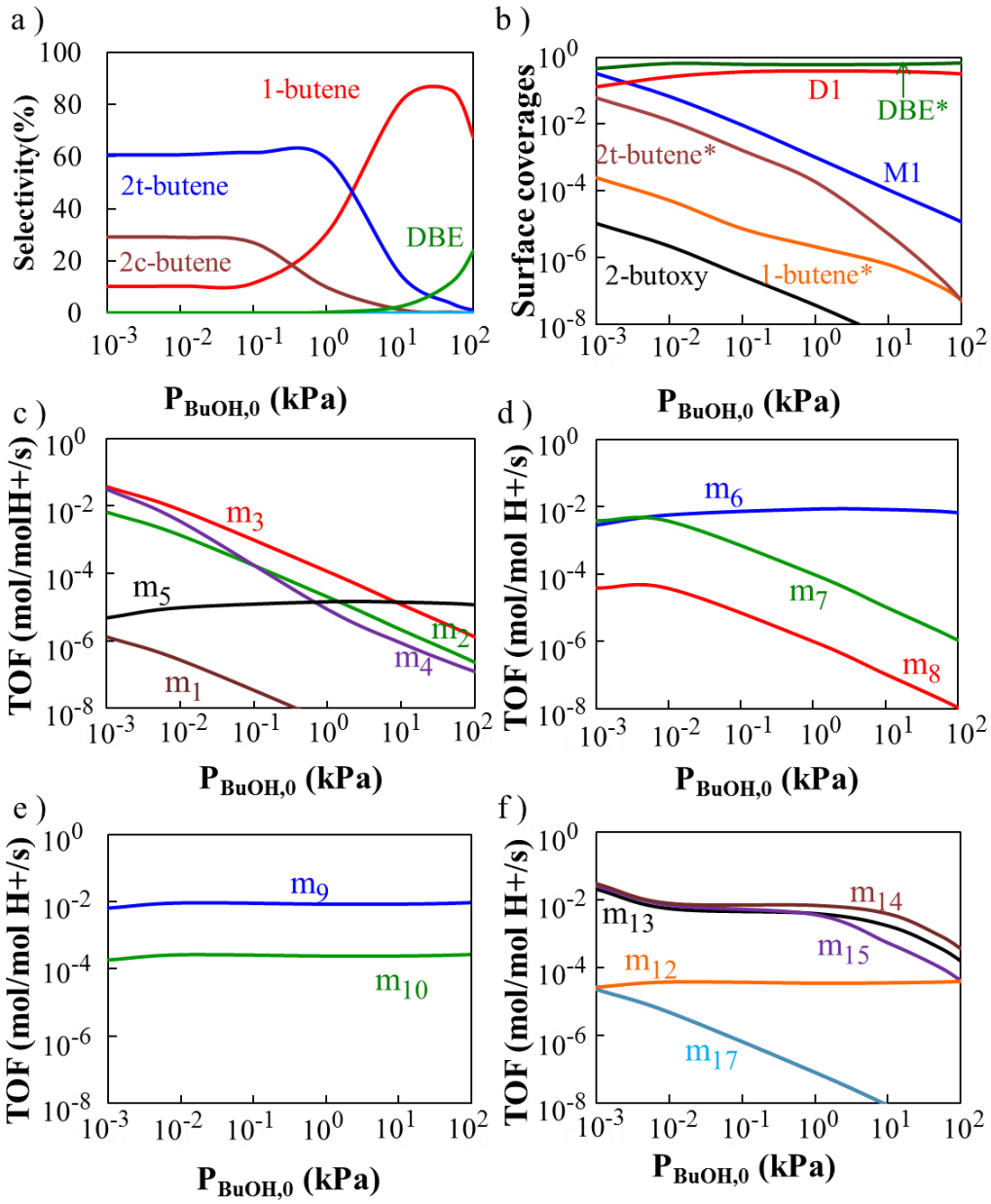

Figure 15. Effect of 1-butanol inlet partial pressure ($P_{BuOH,0}$) on: (a) product selectivity, (b) surface coverages, (c) TOF for direct dehydration of 1-butanol to 1-butene (path A via mechanisms m_1-m_5), (d) TOF for dehydration of 1-butanol to di-1-butyl ether (path B via mechanisms m_6-m_8), (e) TOF for ether decomposition to 1-butene and 1-butanol (path C via mechanisms m_9-m_{10}), (f) TOF for conversion of 1-butanol to 2-t-butene (path D, mechanism m_{11}), DBE to 2-t-butene and 1-butanol (path E, mechanism m_{12}), double bond isomerization 1-butene to trans-2-butene (path F via mechanisms m_{13}-m_{14}), double bond isomerization of 1-butene/2t-butene to cis-2-butene (path G/path H via mechanisms m_{15} /m_{16}), skeletal isomerization of 1-butene/2t-butene to iso-butene (path I/path J/ path K via mechanisms m_{17}/m_{18}/m_{19}). Reaction conditions: temperature of 450K and site time adjusted to have a constant butanol conversion of 70%. Mechanisms with TOF less than 10^{-8} are not shown in the figure.

In general for double bond isomerization mechanisms, the simulated TOF profile indicates three different regimes of 1-butanol partial pressure reaction order ($P_{BuOH,0} < 10^{-2}$ kPa, $10^{-2} <$

$P_{BuOH,0}$ < 1 kPa and $P_{BuOH,0}$ >10 kPa). For $P_{BuOH,0}$ < 1 kPa, the TOF for double bond isomerization is dependent only on the net formation rate of 1-butene from path A and path C. At extremely low 1-butanol partial pressure ($P_{BuOH,0}$ < 10^{-2} kPa), the TOF for 1-butene formation occurs essentially via monomolecular path A mechanisms (m3 and m4) which shows a negative reaction order in butanol partial pressure (see Figure 15c). Accordingly, a negative reaction order in butanol partial pressure is also seen for the double bond isomerization mechanisms (m13, m14 and m15) in this regime. Likewise, in the low to moderate 1-butanol partial pressure regime (10^{-2} < $P_{BuOH,0}$ < 1 kPa), 1-butene formation occurs essentially via path C mechanism m9, which shows a zero order in 1-butanol partial pressure in this regime (see Figure 15e) and consequently leads to zero order dependence for mechanisms m13, m14 and m15. Meanwhile at higher butanol pressures ($P_{BuOH,0}$ >10 kPa), the increase in 1-butanol partial pressure is associated with a decrease in surface coverage of butenes and again leads to a negative reaction order in butanol partial pressure for the double bond isomerization mechanism.

4.4. Conclusions

This study provides a detailed insight into the plausible reaction mechanisms for dehydration of 1-butanol to butene isomers in H-ZSM-5. The dehydration energetics indicate that the direct formation of 2-butenes from 1-butanol or DBE is highly activated in comparison to the formation of 1-butene. DFT based microkinetic modelling shows that, except for very low conversion levels where 2-butenes are produced via E1 elimination of water from the protonated di-1-butyl ether (DBE*), the formation of 2-butenes occur essentially via a double bond isomerization from 1-butene. This also explains the experimentally observed trend of increase in 2-butene selectivity with increase in reaction temperature, which was previously

attributed to an E2 to E1 shift in the mechanism for water elimination from 1-butanol. Increase in site time/conversion or reaction temperature and decrease in 1-butanol partial pressure leads to a relative increase in surface coverage of 1-butene, which favors double bond isomerization reactions and increases selectivity for 2-butenes. On the other hand, dehydration under conditions where the surface is completely covered with alcohol or DBE will favor the formation of 1-butene over other butene isomers. In H-ZSM-5 at moderate conversion levels, i.e. 50-60%, and at 450K and $P_{BuOH,0}$ of 10kPa, where the surface is fully covered with strongly adsorbed 1-butanol and DBE species, 1-butene is formed with 80 % selectivity. Owing to the relatively higher activation barrier for skeletal isomerization, higher temperatures are required for production of isobutene. This shows how reaction conditions can play a crucial role in determining the surface coverages of reaction intermediates, dominant reaction mechanism and in turn define the selectivity for butene isomers.

4.5. References

(1) Mascal, M. *Biofuel Bioprod Bior* **2012**, *6*, 483.

(2) Makarova, M. A.; Paukshtis, E. A.; Thomas, J. M.; Williams, C.; Zamaraev, K. I. *J Catal* **1994**, *149*, 36.

(3) Zhang, D. Z.; Barri, S. A. I.; Chadwick, D. *Appl Catal a-Gen* **2011**, *403*, 1.

(4) Zhang, D. Z.; Al-Hajri, R.; Barri, S. A. I.; Chadwick, D. *Chem Commun* **2010**, *46*, 4088.

(5) Wright, M. E.; Harvey, B. G.; Quintana, R. L. *Energ Fuel* **2008**, *22*, 3299.

(6) John, M.; Alexopoulos, K.; Reyniers, M. F.; Marin, G. B. *J Catal* **2015**, *330*, 28.

(7) Zhi, Y.; Shi, H.; Mu, L.; Liu, Y.; Mei, D.; Camaioni, D. M.; Lercher, J. A. *J Am Chem Soc* **2015**.

(8) Alexopoulos, K.; John, M.; Van der Borght, K.; Galvita, V.; Reyniers, M.-F.; Marin, G. B. *J Catal* **2016**, *339*, 173.

(9) John, M.; Alexopoulos, K.; Reyniers, M.-F.; Marin, G. B. *Acs Catal* **2016**, *6*, 4081.

(10) Makarova, M. A.; Williams, C.; Thomas, J. M.; Zamaraev, K. I. *Catal Lett* **1990**, *4*, 261.

(11) Makarova, M. A.; Paukshtis, E. A.; Thomas, J. M.; Williams, C.; Zamaraev, K. I. *Stud Surf Sci Catal* **1993**, *75*, 1711.

(12) Brown, W. H.; Foote, C. S.; Iverson, B. L.; Anslyn, E. V. *Organic chemistry* . *Cengage Learning*, ISBN 978-0-8400-5498-2, 2012.

(13) Olaofe, O.; Yue, P. L. *Collect Czech Chem C* **1985**, *50*, 1834.

(14) Noller, H.; Kladnig, W. *Catal Rev* **1976**, *13*, 149.

(15) Aronson, M. T.; Gorte, R. J.; Farneth, W. E. *J Catal* **1986**, *98*, 434.

(16) Aronson, M. T.; Gorte, R. J.; Farneth, W. E. *J Catal* **1987**, *105*, 455.

(17) Kazansky, V. B. *Accounts Chem Res* **1991**, *24*, 379.

(18) Corma, A. *Chem Rev* **1995**, *95*, 559.

(19) Kondo, J. N.; Shao, L. Q.; Wakabayashi, F.; Domen, K. *J Phys Chem B* **1997**, *101*, 9314.

(20) Kondo, J. N.; Domen, K.; Wakabayashi, F. *Micropor Mesopor Mat* **1998**, *21*, 429.

(21) Boronat, M.; Viruela, P.; Corma, A. *J Phys Chem A* **1998**, *102*, 982.

(22) Li, H. Y.; Pu, M.; Liu, K. H.; Zhang, B. F.; Chen, B. H. *Chem Phys Lett* **2005**, *404*, 384.

(23) Frash, M. V.; Kazansky, V. B.; Rigby, A. M.; vanSanten, R. A. *J Phys Chem B* **1997**, *101*, 5346.

(24) Boronat, M.; Viruela, P.; Corma, A. *Physical Chemistry Chemical Physics* **2001**, *3*, 3235.

(25) Domokos, L.; Lefferts, L.; Seshan, K.; Lercher, J. A. *J Catal* **2001**, *197*, 68.

(26) Houzvicka, J.; Hansildaar, S.; Ponec, V. *J Catal* **1997**, *167*, 273.

(27) Meriaudeau, P.; Tuan, V. A.; Le, N. H.; Szabo, G. *J Catal* **1997**, *169*, 397.

(28) Simon, M. W.; Suib, S. L.; Oyoung, C. L. *J Catal* **1994**, *147*, 484.

(29) Gleeson, D. *J Phys Chem A* **2011**, *115*, 14629.

(30) Guisnet, M.; Andy, P.; Gnep, N. S.; Benazzi, E.; Travers, C. *J Catal* **1996**, *158*, 551.

(31) Gleeson, D. *J Mol Catal a-Chem* **2013**, *368*, 107.

(32) Nguyen, C. M.; Reyniers, M. F.; Marin, G. B. *Phys Chem Chem Phys* **2010**, *12*, 9481.

(33) Olson, D. H.; Khosrovani, N.; Peters, A. W.; Toby, B. H. *J Phys Chem B* **2000**, *104*, 4844.

(34) Dedecek, J.; Balgova, V.; Pashkova, V.; Klein, P.; Wichterlova, B. *Chem Mater* **2012**, *24*, 3231.

(35) Lonsinger, S. R.; Chakraborty, A. K.; Theodorou, D. N.; Bell, A. T. *Catal Lett* **1991**, *11*, 209.

(36) Mentzen, B. F.; Sacerdoteperonnet, M. *Mater Res Bull* **1994**, *29*, 1341.

(37) Svelle, S.; Tuma, C.; Rozanska, X.; Kerber, T.; Sauer, J. *J Am Chem Soc* **2009**, *131*, 816.

(38) Kresse, G.; Hafner, J. *Phys Rev B* **1993**, *47*, 558.

(39) Kresse, G.; Hafner, J. *Phys Rev B* **1994**, *49*, 14251.

(40) Kresse, G.; Furthmuller, J. *Comp Mater Sci* **1996**, *6*, 15.

(41) Blochl, P. E. *Phys Rev B* **1994**, *50*, 17953.

(42) Kresse, G.; Joubert, D. *Phys Rev B* **1999**, *59*, 1758.

(43) Perdew, J. P.; Chevary, J. A.; Vosko, S. H.; Jackson, K. A.; Pederson, M. R.; Singh, D. J.; Fiolhais, C. *Phys Rev B* **1992**, *46*, 6671.

(44) Grimme, S. *J Comput Chem* **2006**, *27*, 1787.

(45) Kerber, T.; Sierka, M.; Sauer, J. *J Comput Chem* **2008**, *29*, 2088.

(46) Tuma, C.; Sauer, J. *Phys Chem Chem Phys* **2006**, *8*, 3955.

(47) Goltl, F.; Gruneis, A.; Bucko, T.; Hafner, J. *J Chem Phys* **2012**, *137*.

(48) Vener, M. V.; Rozanska, X.; Sauer, J. *Phys Chem Chem Phys* **2009**, *11*, 1702.

(49) Chiu, C. C.; Vayssilov, G. N.; Genest, A.; Borgna, A.; Rosch, N. *J Comput Chem* **2014**, *35*, 809.

(50) Nguyen, C. M.; Reyniers, M. F.; Marin, G. B. *J Catal* **2015**, *322*, 91.

(51) Nguyen, C. M.; Reyniers, M. F.; Marin, G. B. *J Phys Chem C* **2011**, *115*, 8658.

(52) Bučko, T.; Hafner, J. *J Catal* **2015**, *329*, 32.

(53) Leydier, F.; Chizallet, C.; Costa, D.; Raybaud, P. *J Catal* **2015**, *325*, 35.

(54) Grimme, S.; Antony, J.; Ehrlich, S.; Krieg, H. *J Chem Phys* **2010**, *132*.

(55) Bader, R. F. W. *Atoms in molecules : a quantum theory*; Clarendon Press: Oxford, 1990.

(56) Henkelman, G.; Arnaldsson, A.; Jonsson, H. *Comp Mater Sci* **2006**, *36*, 354.

(57) Henkelman, G.; Jonsson, H. *J Chem Phys* **2000**, *113*, 9978.

(58) Henkelman, G.; Jonsson, H. *J Chem Phys* **1999**, *111*, 7010.

(59) Heyden, A.; Bell, A. T.; Keil, F. J. *J Chem Phys* **2005**, *123*.

(60) De Moor, B. A.; Ghysels, A.; Reyniers, M. F.; Van Speybroeck, V.; Waroquier, M.; Marin, G. B. *J Chem Theory Comput* **2011**, *7*, 1090.

(61) Zhao, Y.; Truhlar, D. G. *Phys Chem Chem Phys* **2008**, *10*, 2813.

(62) Ribeiro, R. F.; Marenich, A. V.; Cramer, C. J.; Truhlar, D. G. *J Phys Chem B* **2011**, *115*, 14556.

(63) Grimme, S. *Chem-Eur J* **2012**, *18*, 9955.

(64) Jensen, J. H. *Phys Chem Chem Phys* **2015**, *17*, 12441.

(65) Piccini, G.; Sauer, J. *J Chem Theory Comput* **2014**, *10*, 2479.

(66) Piccini, G.; Alessio, M.; Sauer, J.; Zhi, Y. C.; Liu, Y.; Kolvenbach, R.; Jentys, A.; Lercher, J. A. *J Phys Chem C* **2015**, *119*, 6128.

(67) De Moor, B. A.; Reyniers, M. F.; Marin, G. B. *Phys Chem Chem Phys* **2009**, *11*, 2939.

(68) Cramer, C. J. *Essentials of computational chemistry : theories and models*; 2nd ed.; Wiley: Chichester Hoboken, NJ, 2004.

(69) Hindmarsh, A. C. *IMACS transactions on scientific computation* **1983**, *1*, 55.

(70) Nguyen, C. M.; De Moor, B. A.; Reyniers, M. F.; Marin, G. B. *J Phys Chem C* **2011**, *115*, 23831.

(71) Dai, W. L.; Wang, C. M.; Yi, X. F.; Zheng, A. M.; Li, L. D.; Wu, G. J.; Guan, N. J.; Xie, Z. K.; Dyballa, M.; Hunger, M. *Angew Chem Int Edit* **2015**, *54*, 8783.

(72) Nguyen, C. M.; De Moor, B. A.; Reyniers, M. F.; Marin, G. B. *J Phys Chem C* **2012**, *116*, 18236.

(73) Janik, M. J.; Macht, J.; Iglesia, E.; Neurock, M. *J Phys Chem C* **2009**, *113*, 1872.

(74) Dewar, M. J. S.; Ford, G. P. *J Am Chem Soc* **1979**, *101*, 783.

(75) Dewar, M. J. S.; Healy, E. F.; Ruiz, J. M. *J Chem Soc Chem Comm* **1987**, 943.

(76) Wattanakit, C.; Nokbin, S.; Boekfa, B.; Pantu, P.; Limtrakul, J. *J Phys Chem C* **2012**, *116*, 5654.

(77) Correa, R. J.; Mota, C. J. A. *Phys Chem Chem Phys* **2002**, *4*, 375.

(78) Van der Borght, K.; Batchu, R.; Galvita, V.; Alexopoulos, K.; Reyniers, M.-F.; Thybaut, J. W.; Marin, G. B. *Angew Chem Int Edit* **2016**, *55*, 12817.

Chapter 5

Effect of zeolite framework on the conversion of 1-butanol to butene isomers: mechanistic insights from DFT-based microkinetic modelling

Abstract

Ab initio based microkinetic modelling of 1-butanol dehydration to butene isomers is used to obtain mechanistic insights into the effect of zeolite framework on reaction kinetics and product selectivity. A detailed microkinetic model including double bond isomerization, skeletal isomerization and mechanisms for direct formation of 2t-butene from 1-butanol dimer and di-1-butyl ether (DBE) are considered for the dehydration study in H-ZSM-5, H-ZSM-22 and H-FER. H-FER favors the production of 2t-butene and H-ZSM-22 achieves thermodynamic equilibrium composition for linear butenes even at low conversion levels, while H-ZSM-5 exhibits an optimum conversion regime for maximizing 1-butene selectivity. However, significant differences are observed in the reaction mechanism leading to formation of 2t-butene. For H-ZSM-5 and H-ZSM-22, the formation of 2-butenes occurs via double bond isomerization of 1-butene produced from butanol dehydration. On the other hand for H-FER, 2t-butene is mainly produced from the butanol dimer via an E1 elimination accompanied by a 1,2-hydride shift. This in turn can be attributed to an increase in enthalpic stabilization of the E1 elimination transition state for the direct formation of 2t-butene from 1-butanol dimer when moving from H-ZSM-5 to H-FER.

Keywords: DFT, bio-butanol, dehydration, isomerization, reaction mechanism, zeolite confinement, microkinetic modelling

5.1. Introduction

Butene isomers namely 1-butene, 2-butenes and isobutene are important platform chemicals[1,2]. Conventionally, these butene isomers are produced from petroleum based feedstocks[3]. However, limited petroleum resources and growing environmental concerns have driven significant interest towards the development of a renewable bio-based alternative for production of butene isomers. Dehydration of bio-butanol to butene isomers can serve as one such promising alternative[4]. The key challenge for the development of such an alternative process for the selective production of butene isomers remains the design of a selective and active catalyst. Zeolites are excellent candidates for such a shape selective chemical transformation requiring high acid strength, surface area and well defined pore structure[5].

Zeolite catalyzed conversion of bio-alcohols to hydrocarbons is of significant importance for a sustainable future and has been studied extensively, both experimentally[6-13] and theoretically[10,13-16]. Makarova et al.[8] investigated low temperature (378-458 K) 1-butanol dehydration in H-ZSM-5 and amorphous aluminosilicate. Their study highlighted the role of confinement by ZSM-5 leading to its significant preference for di-butyl ether (DBE) formation in comparison to amorphous aluminosilicate. Zhang et al.[17,18] studied one-step conversion of 1-butanol to isobutene in different zeolites. Their study indicated that H-ZSM-22 and H-ZSM-23 provide much better selectivity for isobutene in comparison to H-ZSM-5 which was found to be a more active and less selective catalyst. Likewise, significant difference in turnover frequencies (TOF) and product selectivity was also reported in the case of ethanol dehydration in zeolites[11,12]. A recent theoretical study for dehydration of 1-butanol to DBE/1-butene in H-FAU, H-ZSM-5, H-ZSM-22 and H-FER indicated that differences in zeolite topology can alter the dominant reaction path by stabilizing or destabilizing reaction intermediates and/or transition states[16], thus resulting in differences in catalytic activity and selectivity. In general, activity and selectivity in zeolite catalyzed reactions are primarily

governed by zeolite acid strength and host-guest interactions [19-21] and a fundamental insight into the effect of zeolite properties on the underlying reaction mechanism is key to a rational catalyst design[22].

A first principles based microkinetic modelling approach was previously used to study the reaction mechanism for formation of butene isomers, namely 1-butene, 2t-butene, 2c-butene and isobutene during 1-butanol dehydration in H-ZSM-5[23]. The study of competing reaction pathways indicated that the formation of 2-butene (cis and trans) isomers in H-ZSM-5 occurs essentially via double bond isomerization of 1-butene produced during 1-butanol dehydration rather than direct formation of 2-butene from 1-butanol via an E1 like elimination accompanied by hydride shift. The simulation results also indicated absence of isobutene for reaction temperatures in the range of 450-500K. As indicated by experimental[17,18] and theoretical[16] studies for dehydration of 1-butanol in zeolites, different zeolites can follow different reaction mechanisms which can lead to differences in the product selectivity profile. For example, the one-dimensional H-ZSM-22 with 10 membered ring (MR) channels and two-dimensional H-FER with 10 and 8 MR channels can have quite different stabilization for the bulky TS of the direct formation of 2t-butene from 1-butanol dimer (D1) and adsorbed DBE (DBE*). Moreover, considering the fact that H-ZSM-22 and H-FER are known for their higher selectivity to 1-butene skeletal isomerization[18], it is imperative to look into important aspects of dehydration of 1-butanol to butene isomers in these zeolites.

In this work, we present a dispersion-corrected periodic density functional theory (DFT) study for 1-butanol dehydration to butene isomers in three industrially relevant medium pore zeolites i.e. H-ZSM-5, H-ZSM-22 and H-FER. Herein, the effect of zeolite framework on direct formation of 2t-butene from alcohol and DBE[23], concerted[24-26] and 2-butoxide mediated[27] double bond isomerization and monomolecular skeletal isomerization[28-32] have been investigated in conjunction with 1-butanol dehydration to DBE and 1-butene[14,16]. The

difference in catalytic performance of the investigated zeolites is rationalized on the basis of differences in stabilization of the reaction intermediates and transition state structures within the zeolite framework.

5.2. Theory

5.2.1. Catalyst models

The aluminum substitutions in the silicon-oxide structure of zeolite material give rise to the Bronsted acid sites. Here in, the optimized zeolite structure for H-ZSM-5 (Si/Al - 95 with Al atom at T12 site [14,33,34]) , H-ZSM-22 (Si/Al -35 with Al atom at T3 site [36,37]) and H-FER (Si/Al -71 with Al atom at T1b site[34,35]) reported in Chapter 3 / Ref [16] were used for the study. These three medium pore zeolites have different accessible dimensions (3-d , 2-d and 1-d for ZSM-5, H-FER and H-ZSM-22, respectively), pore sizes and framework type[36] making them ideal test set for assessing the effects of topological variation. The optimized zeolite geometry and unit cell parameters are available in Figure S1 and Table S1 of Appendix B. In addition to the T1b tetrahedral site (Al1O2) considered in Chapter 3 / Ref [16] , the acid site can also be located at the Al2O2 position (T2 tetrahedral site for Al atom)[34,35] in H-FER. Although H-FER, with the Al atom located at T2 (H-FER-T2) site, has been used in previous theoretical studies for isobutene protonation[37-39] and skeletal isomerization[32,40,41], Al at the T1b site has been reported to be most abundant (~ 80% of Al atoms occupying T1b site) in the case of the commercially available H-FER Zeolyst sample[34,35]. The narrow Al distribution offered by this sample for H-FER can facilitate a better comparison between experiments and DFT based microkinetic simulations. Accordingly, the present study focuses on the formation of butene isomers from 1-butanol and DBE in H-FER with the Al atom located at the T1b site. Nevertheless, thermodynamic and kinetic parameters of some of the reactions occurring at the H-FER-T2 site are also provided in Appendix D (see Table D1) for

comparison purposes. Henceforth, unless stated otherwise, all results presented in this work for H-FER refer to the ferrierite catalyst model with the Al atom located at the T1b site.

5.2.2. Computational details

5.2.2.1. Electronic energy calculations

Dispersion corrected periodic DFT calculations were performed with the Vienna Ab Initio Simulation Package (VASP) using plane wave basis sets [42-44]. The electron-ion interactions were described using the projector–augmented wave (PAW) method [45,46] with a plane-wave energy cut-off of 600 eV. The exchange correlation energies were calculated on the basis of the generalized gradient approximation (GGA) according to Perdew, Burke and Ernzerhof (PBE) [47]. Brillouin zone sampling was restricted to the Γ-point. A maximum force convergence criterion of 0.02 eV $Å^{-1}$ was used and each self-consistency loop was iterated until a convergence level of 10^{-8} eV was achieved. Dispersive corrections for the van der Waals interactions were included by adding a pairwise interaction term to the Kohn–Sham energy using the DFT-D2 approach proposed by Grimme [48] and extended by Kerber et al. [49] for periodic PBE calculations. Although systematic deviations may be observed due to the overestimation of the dispersion interaction [37,50-52], DFT-D2 has been widely applied for the theoretical investigation of adsorption [53-56] and reaction in zeolites [56,57] and is known to provide reasonably accurate results [50,58]. The electronic charge on atoms and fragments were calculated using Bader analysis [59] as implemented by Henkelman et al. [60] Transition state search was performed using Nudged Elastic Band (NEB) [61] and dimer [62,63] calculations. The Nudged Elastic Band (NEB) method was used to find an initial guess for the minimal energy path (MEP), which was used as a starting point for the dimer calculations. A qualitative depiction of the relative electrostatic stabilization of the adsorbed intermediates and transition states in different zeolite frameworks was obtained by using local potential (LOCPOT)

calculations as implemented in VASP. In this method, the electrostatic potential is evaluated from the interaction between a negative unit charge and the local charge density.

5.2.2.2. Frequency calculations

Normal mode analysis was performed using a Partial Hessian Vibrational Analysis (PHVA), relaxing the T5 cluster ($HAl(SiO_4)_4$) of the zeolite framework and the adsorbate molecule for the numerical Hessian calculation. Previous studies for physisorption and chemisorption in zeolites have shown that the partial Hessian approach leads to a marginal difference in the result as compared to a Full Hessian Vibrational Analysis (FHVA) [64]. Although very stringent optimization (maximum force criterion of 0.02 eV $Å^{-1}$) and electronic convergence (self-consistency loop convergence criterion of 10^{-8} eV and energy cut-off of 600 eV) criteria have been used, spurious imaginary frequencies were still present in very few cases. The low lying frequencies (<50 cm^{-1}) associated with the frustrated motions of the surface bound species (such as translation or rotation of the molecule within the zeolite pore structure) could lead to significant error in the entropy calculations [65-68]. A more accurate estimation of the entropic contributions could be obtained by accounting for anharmonicities by detailed scanning of the potential energy surface [69,70], but this would require significant computational efforts for large systems. Another approach to treat the low lying modes is the use of a frequency cutoff [53,65,66,71]. De Moor et al. [71] studied the entropy contributions of these frequencies for alkanes and alkenes in FAU zeolite and suggested the replacement of these spurious frequencies with 50 cm^{-1}. Therefore, in order to obtain consistent results, the spurious imaginary frequencies and low-lying frequencies were replaced by normal modes of 50 cm^{-1} [71].

5.2.2.3. Statistical thermodynamics

Standard enthalpies, entropies, Gibbs free energies, adsorption and reaction equilibrium coefficients (K) are obtained from total partition functions by statistical thermodynamics calculations [72].

Reaction equilibrium coefficients, *K*, for elementary reactions are calculated as:

$$K(T) = \frac{\prod_i Q_i(N,V,T)}{\prod_j Q_j(N,V,T)} \exp\left(-\frac{\Delta E_r}{RT}\right) \qquad (1)$$

where *i* and *j* denote products and reactants respectively. ΔE_r is the change in electronic energy at 0 K (including the zero-point vibrational energy) of the reaction and *Q* the total partition function. The electronic energy from the DFT calculation along with the frequencies obtained from the vibrational analysis are used for the statistical thermodynamic calculation (see Appendix A). The total partition function for gas-phase species consists of translational, rotational and vibrational contributions. On the other hand, the surface bound complexes in the zeolite are modeled using either the *immobile* or the *mobile adsorbate* method, based on the vibrational analysis [64]. The *immobile adsorbate* method considers all degrees of freedom of the adsorbed species within the zeolite as frustrated motions, which are described by the harmonic oscillator approximation [71]. This *immobile adsorbate* approach has been applied for all surface–bound complexes except for the physisorbed butenes (1-butene, 2t-butene, 2c-butene and iso-butene). These loosely–bound physisorbed butenes are considered as *mobile adsorbates*, which retain certain rotational and translational degrees of freedom [71]. Harmonic frequencies associated with these rotational and translational motions were identified based on visual inspection of frequencies lower than 100 cm^{-1}. These frequencies are removed from the calculation of the vibrational partition function and are replaced by free translational or rotational contributions. Details of this method are presented in Appendix B.

The reaction rate coefficients of elementary reaction steps are calculated on the basis of transition state theory:

$$k_{TST}(T) = \frac{k_B T}{h} \frac{Q_{TS}(N,V,T)}{Q_R(N,V,T)} \exp\left(-\frac{E^{\ddagger}}{RT}\right) \quad (2)$$

where k_B is Boltzmann constant, h is Planck constant and $E^{\ddagger}$ is the electronic activation barrier at 0 K (including the zero-point vibrational energy). Q_{TS} and Q_R denote the total partition functions of the transition and reactant state respectively. Arrhenius pre-exponential factors (A) and activation energies (E_a) are obtained by regression of Eq. 2 in the temperature range of 300 – 800 K.

The adsorption occurs without any activation barrier. Hence, the reaction rate coefficient for the adsorption step is calculated as $k_{ads} = k_B T/h$, while the reaction rate coefficient for the desorption step is calculated from thermodynamic consistency as $k_{des} = k_{ads}/K_{ads}$.

5.2.3. Microkinetic model

A microkinetic modelling approach has been used to carry out reaction path analysis and to study the effect of reaction conditions (temperature, site time and pressure). Here in, an isothermal plug flow reactor model was used for the reactor simulations. The following continuity equations were applied for the gas-phase components i and surface species k along with a site balance:

$$\frac{d\theta_k}{dt} = \sum_j \nu_{jk} TOF_j = 0 \quad (3)$$

$$\theta_* + \sum_k \theta_k = 1 \quad (4)$$

$$\frac{dF_i}{dW} = R_i = C_t \sum_j \nu_{ji} TOF_j \quad (5)$$

with $F_i = F_{i,0}$ at $W = 0$

where TOF_j is the turnover frequency of elementary step j (mol mol_{H+}^{-1} s^{-1}), ν_{ji} the stoichiometric coefficient of component i in the elementary step j, θ_k the fractional coverage of surface species k (mol mol_{H+}^{-1}), θ_* the fractional coverage of free acid sites (mol mol_{H+}^{-1}), C_t the acid site concentration (mol_{H+} kg^{-1}), F_i the molar flow rate of gas-phase component i (mol s^{-1}), W the mass of the catalyst (kg), R_i the net production rate of gas-phase species i (mol kg^{-1} s^{-1}).

The microkinetic model assumes absence of any diffusion limitation for reactant and product species. This assumption is consistent with the experimental results of Makarova et al.[8], where they studied the effect of ZSM-5 crystallite size on the reaction rates for dehydration of 1-butanol and di-1-butyl ether. The above mentioned set of ordinary differential equations is integrated using the LSODA module of ODEPACK [73]. The investigated reaction conditions are inlet partial pressure of 1-butanol (10^{-3}-10^{2}kPa), site time ($N_{H+}/F_{BuOH,0}$ = 0-100 mol H+ s / mol $BuOH_0$) and reaction temperature (450-500 K). The calculation of TOF for each mechanism is shown in appendix C.

5.3. Results and discussion

5.3.1. Reaction paths for formation of butene isomers from 1-butanol in zeolites

Figure 1 and Table 1 (see also Chapter 4) show the considered reaction paths for formation of butene isomers from 1-butanol in zeolites. The dehydration of 1-butanol to 1-butene has been discussed in detail in previous work [14]. As the adsorbed butanol dimer (D1) and di-1-butyl ether (DBE*) were found to be key surface species [14], the formation of 2t-butene from 1-butanol (via path D) and from DBE (via path E) has been considered. On the other hand, 1-butene produced from dehydration of 1-butanol (via path A or path B followed by path C) can undergo double bond isomerization to produce trans-2-butene (2t-butene) and cis-2-

butene (2c-butene) via path F, G and H. These linear butenes (1-butene/2t-butene/2c-butene) can undergo skeletal isomerization reaction via path I, J and K.

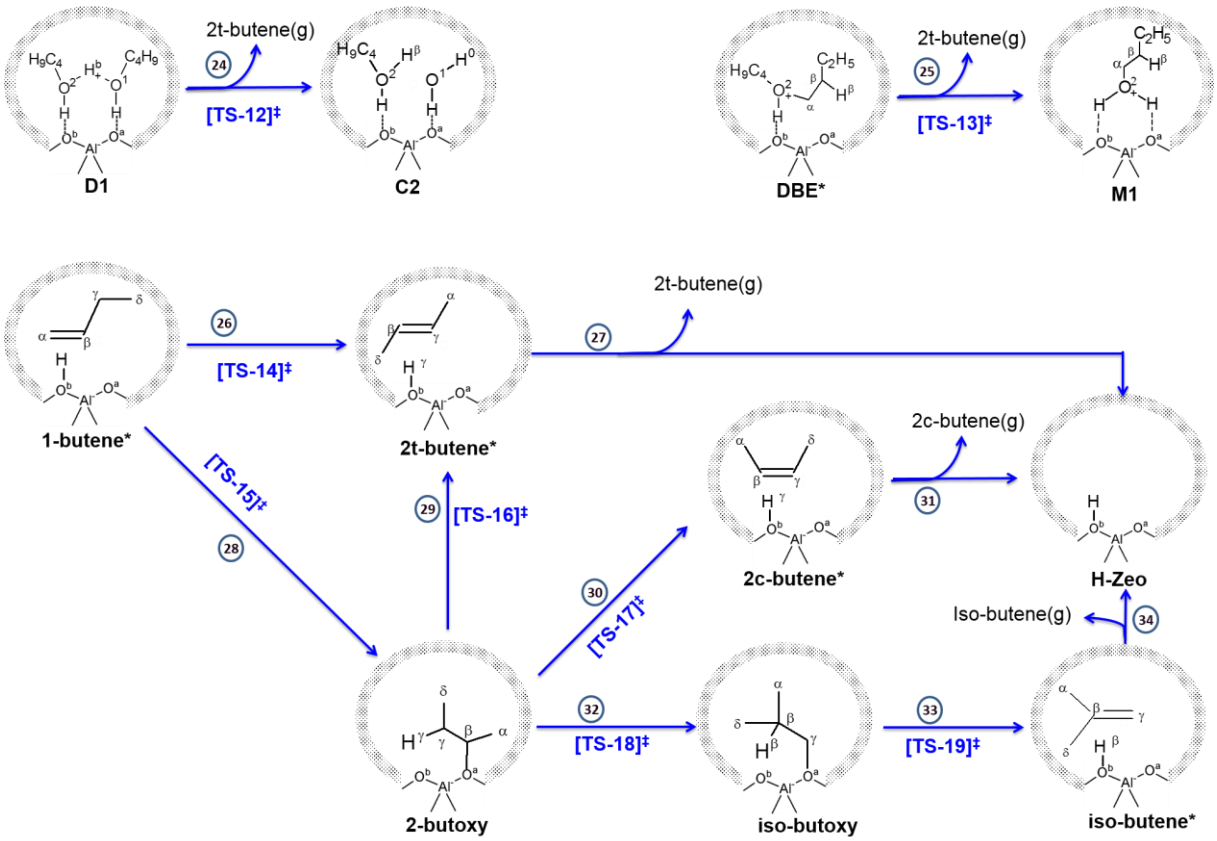

Figure 1. Reaction network for 2-butenes (cis/trans) and iso-butene formation from 1-butanol dehydration in zeolites (repeated from Chapter 4). M1 and D1 are adsorbed monomer and dimer formed via adsorption of 1-butanol, DBE* (adsorbed di-1-butyl ether) and 1-butene* are formed during dehydration of 1-butanol (see Chapter 3 for the detailed reaction network for dehydration of 1-butanol to DBE and 1-butene, Ref[14]).

The reaction network for 1-butanol dehydration to 1-butene and DBE consisting of 23 elementary steps as described in Chapter 2 / Ref [14] is extended for the production of 2t-butene, 2c-butene and iso-butene by inclusion of 11 extra elementary steps[23]. These steps are shown in Figure 1 which is taken from Chapter 4 and repeated here for convenience. Detailed electron flow diagrams and TS characteristics for the additional set of reaction mechanisms are described in detail in Chapter 4 on the theoretical study of 1-butanol conversion to butene isomers in H-ZSM-5[23]. Any further reference to a specific reaction step of the network and reaction path/mechanism is done as per the numbering used in Figure 1 and Table 1, respectively. The standard reaction enthalpy (ΔH_r^o), reaction entropy (ΔS_r^o), Arrhenius

activation energies and pre-exponential factors, forward reaction rate coefficients and equilibrium coefficients for each elementary step in H-ZSM-22 and H-FER are tabulated in Table 2 and 3, respectively. The thermodynamic and kinetic parameters for formation of butene isomers in H-ZSM-5[23] are taken from Chapter 4 and are used in the present study.

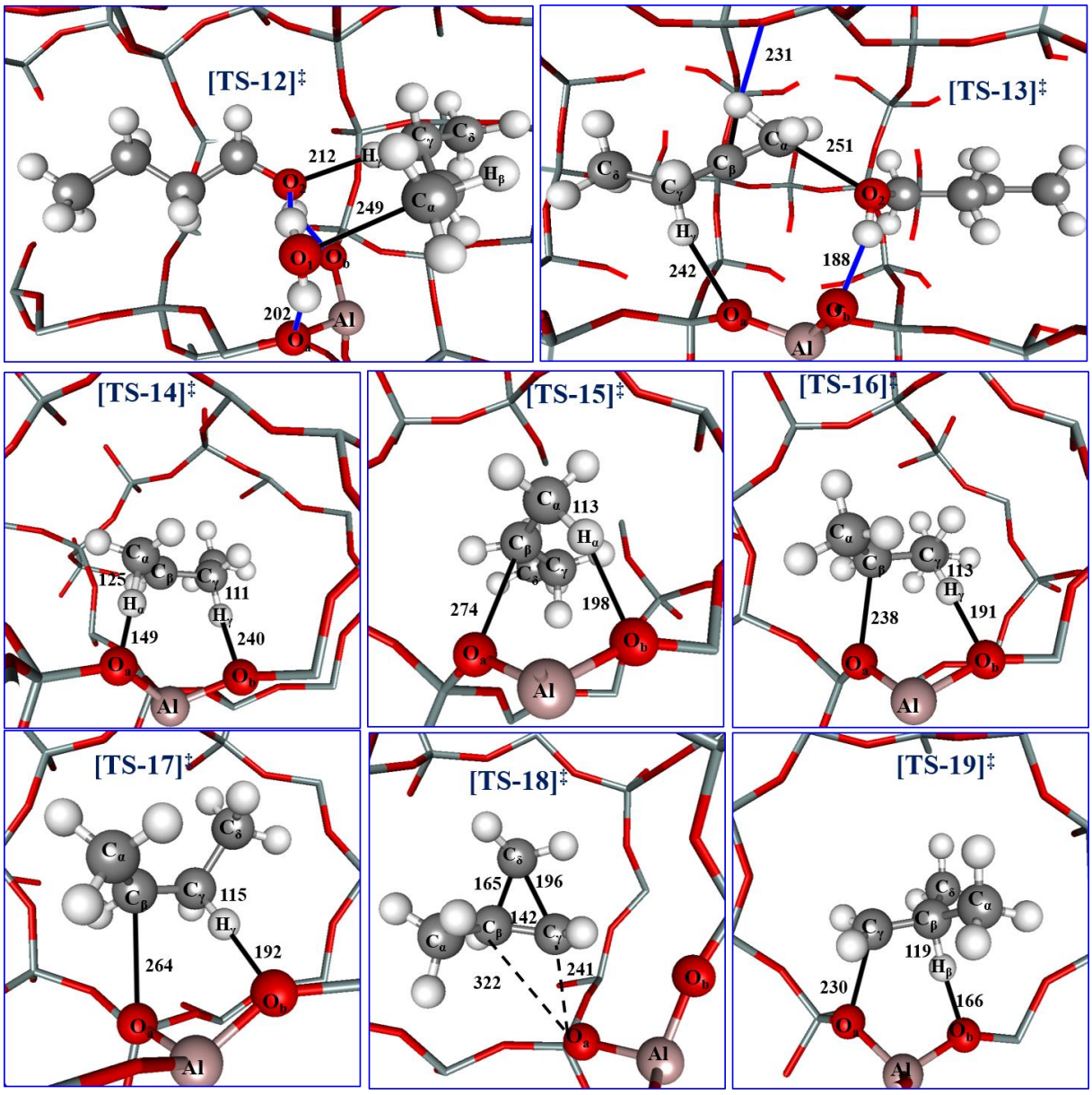

Figure 2: Transition state structures for the production of 2t-butene, 2c-butene and isobutene during 1-butanol dehydration in H-ZSM-22. Color code: silicon – light blue, aluminum – pink, oxygen – red, hydrogen – white, carbon – gray, hydrogen bonds (distance < 250 pm) – blue lines, bond breaking/forming – black lines.

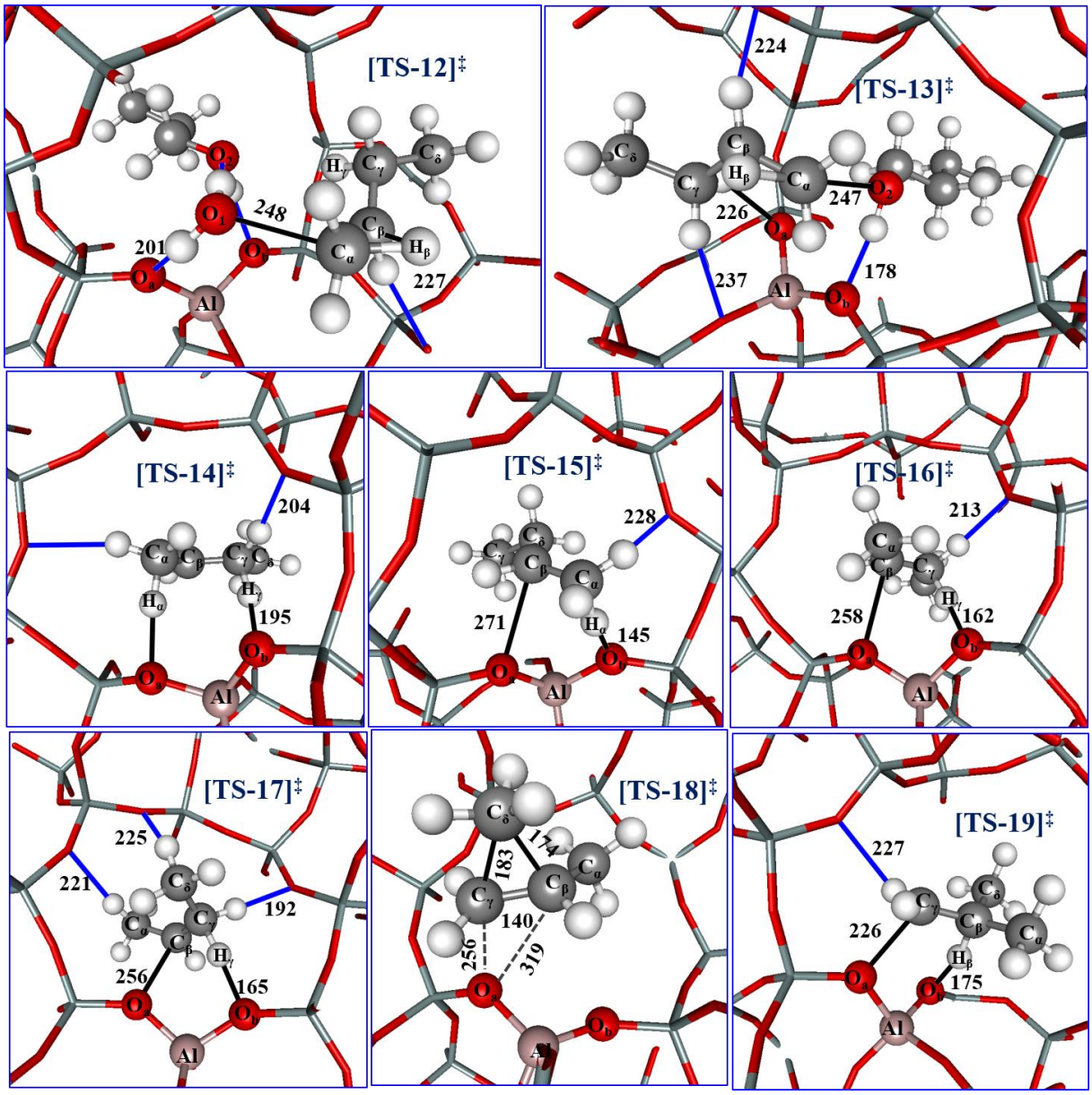

Figure 3: Transition state structures for the production of 2t-butene, 2c-butene and isobutene during 1-butanol dehydration in H-FER. Color code: silicon – light blue, aluminum – pink, oxygen – red, hydrogen – white, carbon – gray, hydrogen bonds (distance < 250 pm) – blue lines, bond breaking/forming – black lines.

Table 1. Elementary steps and reaction mechanisms for the butanol dehydration reaction. Non-equilibrated steps as found by microkinetic simulations are indicated with bold stoichiometric numbers (repeated from Chapter 4).

	Path	D	E	F		G	H	I	J	K
	Mechanism	m_{11}	m_{12}	m_{13}	m_{14}	m_{15}	m_{16}	m_{17}	m_{18}	m_{19}
1#	M1↔1-BuOH$_{(g)}$+ ∗	0	1	0	0	0	0	0	0	0
8#	1-butene$_{(g)}$+ ∗↔ 1-butene*	0	0	1	1	1	0	1	0	0
11#	M1 + 1-BuOH$_{(g)}$ ↔ D1	1	0	0	0	0	0	0	0	0
14#	C2↔ M1 + $H_2O_{(g)}$	1	0	0	0	0	0	0	0	0
16#	DBE$_{(g)}$+ ∗ ↔ DBE*	0	1	0	0	0	0	0	0	0
24	D1↔ C2+2-t-butene$_{(g)}$	**1**	0	0	0	0	0	0	0	0
25	DBE*↔ M1+2-t-butene$_{(g)}$	0	**1**	0	0	0	0	0	0	0
26	1-butene* ↔ 2-t-butene*	0	0	**1**	0	0	0	0	0	0
27	2-t-butene*↔ 2-t-butene$_{(g)}$+ ∗	0	0	1	1	0	-1	0	-1	0
28	1-butene* ↔ 2-butoxy	0	0	0	**1**	**1**	0	**1**	0	0
29	2-butoxy ↔ 2-t-butene*	0	0	0	**1**	0	**-1**	0	**-1**	0
30	2-butoxy ↔ 2-c-butene*	0	0	0	0	**1**	**1**	0	0	**-1**
31	2-c-butene*↔ 2-c-butene$_{(g)}$+ ∗	0	0	0	0	1	1	0	0	-1
32	2-butoxy ↔ iso-butoxy	0	0	0	0	0	0	**1**	**1**	**1**
33	iso-butoxy ↔ iso-butene*	0	0	0	0	0	0	**1**	**1**	**1**
34	iso-butene*↔ iso-butene$_{(g)}$+ ∗	0	0	0	0	0	0	1	1	1

Path D (mechanism m11)	1-BuOH$_{(g)}$ ↔ 2-t-butene$_{(g)}$ + $H_2O_{(g)}$
Path E (mechanism m12)	DBE$_{(g)}$ ↔1-BuOH$_{(g)}$+ 2-t-butene$_{(g)}$
Path F (mechanism m13-m14)	1-butene$_{(g)}$ ↔ 2-t-butene$_{(g)}$
Path G (mechanism m15)	1-butene$_{(g)}$ ↔ 2-c-butene$_{(g)}$
Path H (mechanism m16)	2-t-butene$_{(g)}$↔ 2-c-butene$_{(g)}$
Path I (mechanism m17)	1-butene$_{(g)}$ ↔ iso-butene$_{(g)}$
Path J (mechanism m18)	2-t-butene$_{(g)}$↔ iso-butene$_{(g)}$
Path K (mechanism m19)	2-c-butene$_{(g)}$↔ iso-butene$_{(g)}$

#elementary step from reaction network for 1-butanol dehydration to DBE and 1-butene [16].

Table 2. Standard reaction enthalpy (kJ/mol), reaction entropy (J/mol/K), activation energy (kJ/mol), pre-exponential factor (s^{-1}), forward reaction rate coefficient k_f (s^{-1}) at 500K and equilibrium coefficient at 500K (10^{-2} kPa^{-1}, 10^2 kPa or dimensionless for adsorption, desorption and surface transformation, respectively) for the elementary steps (numbered as indicated in Figure 1) in H-ZSM-22.

	Elementary steps	**ΔH_r^o**	**ΔS_r^o**	**$E_{a(f)}$**	**A_f**	**$k_{f\ (500K)}$**	**$K_{eq\ (500K)}$#**
24	D1↔ C2+2-t-butene$_{(g)}$	71	190	177	$4.7\ 10^{15}$	$1.5\ 10^{-3}$	$4.0\ 10^{1}$
25	DBE*↔ M1+2-t-butene$_{(g)}$	100	203	161	$4.7\ 10^{15}$	$7.0\ 10^{-2}$	$1.7\ 10^{-1}$
26	1-butene* ↔ 2-t-butene*	-29	-7	36	$1.2\ 10^{10}$	$2.1\ 10^{6}$	$4.8\ 10^{2}$
27	2-t-butene*↔ 2-t-butene$_{(g)}$+ *	103	123	–	–	–	$5.0\ 10^{-6}$
28	1-butene* ↔ 2-butoxy	-12	-76	47	$1.2\ 10^{10}$	$1.5\ 10^{5}$	$1.8\ 10^{-3}$
29	2-butoxy ↔ 2-t-butene*	-17	70	46	$6.1\ 10^{13}$	$1.0\ 10^{9}$	$2.7\ 10^{5}$
30	2-butoxy ↔ 2-c-butene*	-11	68	53	$9.5\ 10^{13}$	$3.0\ 10^{8}$	$4.9\ 10^{4}$
31	2-c-butene*↔ 2-c-butene$_{(g)}$+ *	101	126	–	–	–	$1.5\ 10^{-5}$
32	2-butoxy ↔ iso-butoxy	16	-7	93	$6.1\ 10^{13}$	$1.3\ 10^{4}$	$9.9\ 10^{-3}$
33	iso-butoxy ↔ iso-butene*	-25	28	66	$3.1\ 10^{13}$	$3.8\ 10^{6}$	$1.3\ 10^{4}$
34	iso-butene*↔ iso-butene$_{(g)}$+ *	91	168	–	–	–	$2.7\ 10^{-2}$

#- elementary steps involving adsorption/ desorption corrected using NIST experimental data

Table 3. Standard reaction enthalpy (kJ/mol), reaction entropy (J/mol/K), activation energy (kJ/mol), pre-exponential factor (s^{-1}), forward reaction rate coefficient k_f (s^{-1}) at 500 K and equilibrium coefficient at 500 K (10^{-2} kPa^{-1}, 10^2 kPa or dimensionless for adsorption, desorption and surface transformation, respectively) for the elementary steps (numbered as indicated in Figure 1) in H-FER.

	Elementary steps	**ΔH_r^o**	**ΔS_r^o**	**$E_{a(f)}$**	**A_f**	**$k_{f\ (500K)}$**	**$K_{eq\ (500K)}$#**
24	D1↔ C2+2-t-butene(g)	74	208	160	$5.2\ 10^{15}$	$1.0\ 10^{-1}$	$1.9\ 10^{2}$
25	DBE*↔ M1+2-t-butene(g)	85	184	138	$2.5\ 10^{15}$	$9.9\ 10^{0}$	$6.1\ 10^{-1}$
26	1-butene* ↔ 2-t-butene*	-20	8	50	$4.0\ 10^{11}$	$2.7\ 10^{6}$	$2.8\ 10^{2}$
27	2-t-butene*↔ 2-t-butene(g)+ *	48	143	–	–	–	$3.5\ 10^{1}$
28	1-butene* ↔ 2-butoxy	-45	-56	23	$9.7\ 10^{10}$	$4.2\ 10^{8}$	$6.6\ 10^{1}$
29	2-butoxy ↔ 2-t-butene*	26	64	74	$5.0\ 10^{14}$	$8.7\ 10^{6}$	$4.2\ 10^{0}$
30	2-butoxy ↔ 2-c-butene*	56	52	89	$6.2\ 10^{13}$	$3.3\ 10^{4}$	$7.5\ 10^{-4}$
31	2-c-butene*↔ 2-c-butene(g)+ *	22	157	–	–	–	$1.1\ 10^{5}$
32	2-butoxy ↔ iso-butoxy	1	-5	100	$4.4\ 10^{15}$	$1.5\ 10^{5}$	$3.8\ 10^{-1}$
33	iso-butoxy ↔ iso-butene*	-12	69	120	$2.1\ 10^{14}$	$5.8\ 10^{1}$	$7.0\ 10^{4}$
34	iso-butene*↔ iso-butene(g)+ *	80	140	–	–	–	$1.4\ 10^{-2}$

#- elementary steps involving adsorption/ desorption corrected using NIST experimental data,

Formation of 2t-butene from adsorbed butanol and DBE (path D and E): Two reaction paths have been envisaged for the direct formation of 2t-butene from adsorbed butanol and DBE (path D via mechanism m11 and path E via mechanism m12, respectively). Mechanism m11 consists of the sequence of steps 11, 24 and 14 (see Table 1). Reaction step 24 (see Figure 4a) of mechanism m11 is activated and involves simultaneous 1,2-hydride shift of the H_β and cleavage of the C_α-O_1 bond leading to formation of a secondary carbenium ion like TS (see TS-12 of Figure 2 and 3 for H-ZSM-22 and H-FER, respectively), followed by abstraction of H_γ by the oxygen atom (O_2) of the physisorbed butanol molecule. Reaction step 24 has an activation energy of 201, 177 and 160 kJ/mol for H-ZSM-5, H-ZSM-22 and H-FER,

respectively. The effect of confinement on the stability of the transition state is evident from the fact that the activation energy is decreasing with decreasing pore size from H-ZSM-5 to H-FER. A better insight on the role of zeolite confinement is obtained from the standard free energy profile shown in Figure 4a, which compares the stability of the reaction intermediate and TS for the direct formation of 2t-butene from D1 in different zeolites.

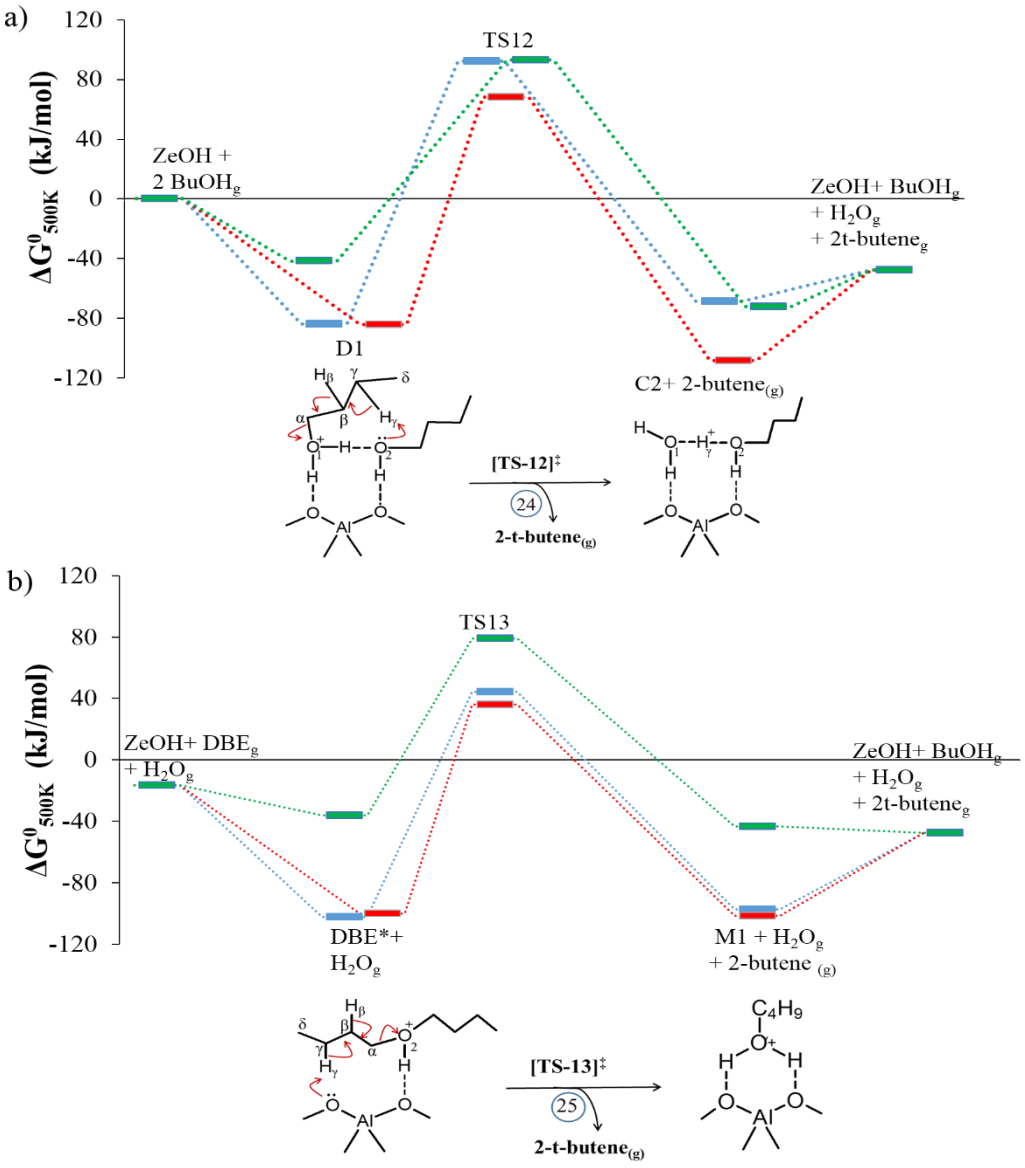

Figure 4. Standard Gibbs free energy profile (with respect to gas-phase butanol and zeolite) and electron flow diagram for the conversion of a) 1-butanol dimer (D1) to 2-t-butene and water-butanol co-adsorbed species (C2), path D, $\Delta G^0_{(D)}{}^{\ddagger} = \Delta G^0_{TS12\text{-}D1}{}^{\ddagger}$, (b) adsorbed di-1-butyl ether (DBE*) to 2-t-butene and adsorbed 1-butanol (M1), path E, $\Delta G^0_{(E)}{}^{\ddagger} = \Delta G^0_{TS13\text{-}DBE}{}^{\ddagger}$, in H-ZSM-5 (blue line), H-ZSM-22 (red line) and H-FER (green line), respectively.

Figure 4a shows that both H-ZSM-5 and H-ZSM-22 have comparable stability for the adsorbed dimer D1. With decreasing pore size from H-ZSM-5 to H-ZSM-22, there is a relative increase in the stability of TS-12 resulting in a higher rate coefficient for the direct formation of 2t-butene from D1 in the case of H-ZSM-22 as compared to H-ZSM-5. The free energy barrier and adsorption free energy of the key reaction intermediate for the direct formation of 2t-butene from D1 are listed in Table 4. As seen from Figure 4a and Table 4, although D1 has a lower stability in H-FER as compared to its stability in H-ZSM-5, both zeolites offer a comparable stability for TS-12. This is indicative of a better stabilization of TS-12 relative to D1 in the smaller pores of H-FER as compared to H-ZSM-5.

Table 4: Standard Gibbs free energy barriers and adsorption free energies for direct formation of 2t-butene from D1 and DBE* in H-ZSM-5, H-ZSM-22 and H-FER at 500K.

Zeolite	Path D (mechanism m11)		Path E (mechanism m12)	
	ΔG^0_{D1ads} (kJ/mol)	$\Delta G^0_{(D)^\ddagger} = G_{TS12} - G_{D1}$ (kJ/mol)	ΔG^0_{DBEads} (kJ/mol)	$\Delta G^0_{(E)^\ddagger} = G_{TS13} - G_{DBE*}$ (kJ/mol)
H-ZSM-5	-84	176	-86	147
H-ZSM-22	-84	152	-84	136
H-FER	-42	135	-20	116

As all three zeolites have similar pre-exponential factors (4.7-5.2 10^{15} s^{-1}) for the formation of 2t-butene from D1 (reaction step 24), the differences in reaction rate coefficient can be attributed to the differences in activation energy. A lower activation barrier for formation of 2t-butene from D1 in H-FER and H-ZSM-22 is attributed to better enthalpic stabilization of the TS in these zeolites. The better stabilization of TS can be attributed to dispersive interactions, hydrogen bonding (see Figure 2 and 3 for H-ZSM-22 and H-FER and Figure 3 of Chapter 4 for H-ZSM-5) and electrostatic interactions between the positively charged fragment of the TS and the zeolite framework, which all lead to lowering of the activation energy for H-FER and H-ZSM-22. For example, Figure 5 shows a more significant electrostatic stabilization of the TS-12 in H-ZSM-22 and H-FER as compared to H-ZSM-5.

The comparison of electrostatic potential maps when moving from D1 to TS-12 for different zeolite topologies (see Figure 5) indicates a better stabilization of the TS by electrostatic interactions relative to the respective adsorbed intermediate (D1). Figure 5 also depicts a much better stabilization of TS-12 relative to D1 in H-FER as compared to H-ZSM-5, which explains the much lower activation barrier in H-FER.

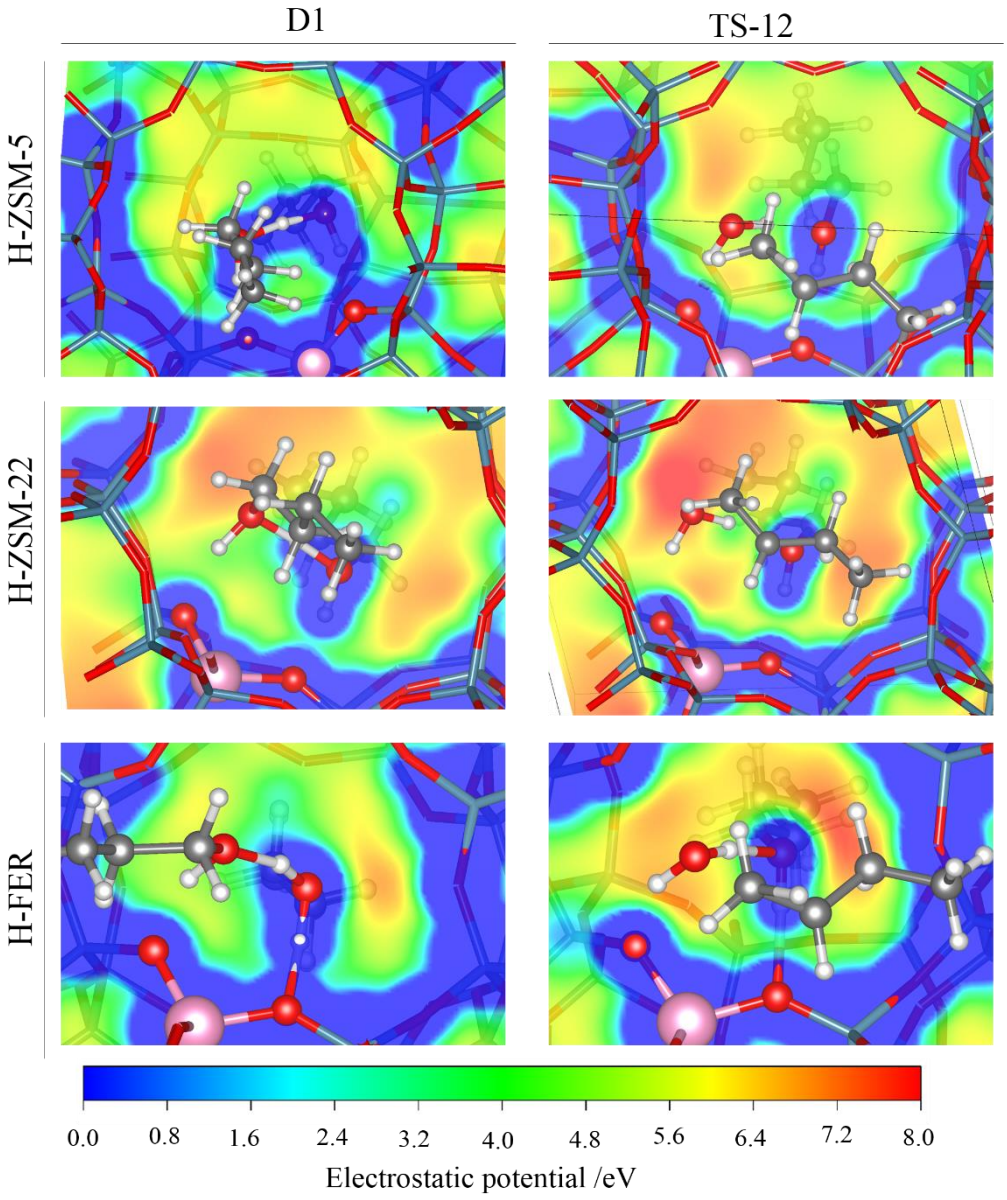

Figure 5. Electrostatic potential for the butanol dimer D1 and TS12 (for direct 2-butene formation from D1) mapped on planes that cross most atoms of the hosting ring of the acid site.

As seen from Table 1, mechanism m12 proceeds via a sequence of elementary steps 16, 25, 1. Reaction step 25 (see Figure 4b) of mechanism m12 is activated and involves simultaneous 1,2-hydride shift and cleavage of the C_α-O_2 bond leading to formation of a secondary carbenium ion like TS (see TS-13 of Figure 2 and 3 for H-ZSM-22 and H-FER, respectively), followed by abstraction of H_γ by the basic O-atom (O_b) of the zeolite. Reaction step 25 has an activation energy of 171, 161 and 138 kJ/mol for H-ZSM-5, H-ZSM-22 and H-FER, respectively. Again, decrease in zeolite pore size is found to stabilize the cationic transition state. A better stabilization of TS-13 relative to DBE* in smaller pores is also evident when moving from H-ZSM-5 to H-FER (see Figure 4b and $\Delta G^0_{(E)}{}^{\ddagger}$ in Table 4). Although H-FER offers a much lower free energy barrier for the direct formation of 2t-butene from DBE* as compared to H-ZSM-5 and H-ZSM-22, the contribution from mechanism m12 can still be lower in the case of H-FER, owing to its significantly lower stability of DBE*. The lower stability of the surface intermediate can result in a lower surface coverage for the intermediate which in turn results in a lower TOF for the reaction step. Thus, along with the free energy barriers, the stability of the reaction intermediate can also play an important role in determining the TOF, as will be illustrated later in this work by microkinetic simulations.

Analogous reaction mechanisms for the direct formation of 2c-butene from D1 and DBE via E1 elimination may be operative. As the direct formation of 2t-butene from D1 is found to be energetically favored in H-FER, an analogous mechanism for the direct formation of 2c-butene from D1 was also explored in H-FER. The activation barrier and pre-exponential factor for the direct formation of 2c-butene from D1 in H-FER is found to be 167 kJ/mol and $2.4\ 10^{15}\ s^{-1}$ in comparison to the 160 kJ/mol and $5.2\ 10^{15}\ s^{-1}$ for the direct formation of 2t-butene from D1. At 500K, the reaction rate coefficient for the direct formation of 2t-butene/2c-butene from D1 in H-FER is 1.0 10-1 (Table 3) and $8.1\ 10^{-3}\ s^{-1}$ (see Table D2 of Appendix D), respectively. The ratio of reaction rate coefficients for the formation of 2t-

butene to 2c-butene from D1 changes from 14 to 12 on increase in reaction temperature from 450 to 500 K. This is indicative of a higher preference for the direct conversion of D1 to 2t-butene in comparison to 2c-butene for the temperature range considered in this study. Thus, omitting this mechanism for the direct formation of 2c-butene during 1-butanol dehydration is expected to have an insignificant impact on the overall selectivity profile.

Double bond isomerization (Path F, G and H): The double bond isomerization of 1-butene to 2t-butene (path F) can proceed via a concerted mechanism (m13) [24,26] or a step-wise mechanism involving a 2-butoxide intermediate (m14) [27,74]. Mechanism m13 consists of a sequence of steps (see Table 1) namely, 8 (adsorption of 1-butene), 26 (conversion of adsorbed 1-butene to adsorbed 2t-butene) and 27 (desorption of 2t-butene). Step 26 of mechanism m13 is activated and involves the protonation of the double bond of 1-butene by the zeolite proton and a simultaneous abstraction of H_γ by the basic O-atom of the zeolite (see TS-14 of Figure 2 and 3 for H-ZSM-22 and H-FER, respectively). Reaction step 26 has an activation energy of 54, 36 and 50 kJ/mol for H-ZSM-5, H-ZSM-22 and H-FER, respectively. The activation energies for the concerted mechanism are thus comparable to the experimentally reported value of 49 ± 4 kJ/mol for double bond isomerization in H-ZSM-5[24]. Although H-ZSM-22 and H-FER have smaller activation energies in comparison to H-ZSM-5, they do not follow the trend of decreasing activation energy with pore size when moving from H-ZSM-22 to H-FER. This can possibly be attributed to steric constrains in the TS for H-FER, where the $[C_4H_9]^+$ fragment is too close to the zeolite walls (see TS-14 Figure 3).

Mechanism m14 consists of steps 8, 28, 29 and 27, of which step 28 (TS-15) and 29 (TS-16) are activated. Reaction step 28 involves protonation of the double bond of 1-butene by the zeolite proton and bond formation between C_β and the zeolite oxygen atom (see TS-15 of Figure 2 and 3 for H-ZSM-22 and H-FER respectively) leading to formation of 2-butoxide. Reaction step 29 involves abstraction of H_γ by the basic O-atom of the zeolite and

simultaneous breakage of the C_β–O_a bond (see TS-16 of Figure 2 and 3 for H-ZSM-22 and H-FER respectively) leading to formation of physisorbed 2t-butene. For both H-ZSM-22 and H-FER, the activation energy for 2-butoxide mediated double bond isomerization is higher than the concerted mechanism. This is also the case for H-ZSM-5 which has a slightly higher activation energy for the step-wise mechanism in comparison to the concerted mechanism[23].

2c-butene can be produced via double bond isomerization of 1-butene (path G, via mechanism m15) and/or 2t-butene (path H, via mechanism m16). Both these mechanisms follow a 2-butoxide mediated route analogous to mechanism m14. Mechanism m15 consists of a sequence of steps (see Table 1), namely 8, 28, 30 and 31, of which step 28 (TS-15) and 30 (TS-17) are activated. Mechanism m16 consists of a sequence of steps (see Table 1), namely 27, 29, 30 and 31, of which step 29 (TS-16) and 30 (TS-17) are activated.

Skeletal isomerization of linear butenes to isobutene (path I, J and K): The skeletal isomerization of linear butenes to isobutene via an alkoxide mediated mechanism[32,75] involving a π-bonded propene-methyl carbocationic TS[23] has been investigated. Path I, J and K represent conversion of 1-butene, 2t-butene and 2c-butene to iso-butene via mechanism m17 (steps 8, 28, 32, 33, 34), m18 (steps 27, 29, 32, 33, 34) and m19 (steps 31, 30, 32, 33, 34), respectively. All three mechanisms involve reaction step 32 (2-butoxide to iso-butoxide), 33 (iso-butoxide to adsorbed iso-butene), and 34 (desorption of iso-butene), of which step 32 (via TS-18) and 33 (via TS-19) are activated. Reaction step 32 involves cleavage of the C_β–O_a and the C_γ–C_δ bond of 2-butoxide and formation of new C_β–C_δ and C_γ–O_a bonds leading to formation of iso-butoxide. In the transition state (see TS-18 of Figure 2 and 3 for H-ZSM-22 and H-FER, respectively) geometry, the bond between C_β–O_a is completely broken (C_β–O_a interatomic distance of 322 and 319 pm for H-ZSM-22 and H-FER, respectively), and the methyl group is bridged between C_β and C_γ (C_β–C_δ , C_γ–C_δ and C_β–C_γ interatomic distances of 165, 196 and 142 pm for H-ZSM-22 and 174, 183 and 140 pm for H-FER, respectively).

These geometric parameters in TS-18 are characteristic of a π-bonded propene-methyl carbocationic TS [76,77]. Bader charge analysis indicates the cationic nature of the π-bonded propene-methyl complex in the TS, with the [C_4H_9] fragment having a charge in the range of +0.83 to +0.89 depending on the zeolite, which is consistent with the reported charge of +0.85 on the same fragment of the TS for the skeletal isomerization of 1-butene in H-FER[40]. Finally, reaction step 33 involves abstraction of H_β by the basic O-atom of the zeolite and simultaneous breakage of the C_γ–O_a bond (see TS-19 of Figure 2 and 3 for H-ZSM-22 and H-FER, respectively) leading to formation of physisorbed isobutene.

In line with a previous theoretical calculation[75], reaction step 32 is found to have a higher activation energy than reaction step 33 for skeletal isomerization in H-ZSM-22. However, the calculated activation energy of 93 kJ/mol for the conversion of 2-butoxide to iso-butoxide (step 32) in H-ZSM-22 is lower than the 109 kJ/mol for the 20T cluster model[75]. On the other hand, deprotonation of iso-butoxide to isobutene* (step 33, E_a =120 kJ/mol) is found to have a higher activation energy than 2-butoxide to iso-butoxide (step 32, E_a = 100 kJ/mol) for skeletal isomerization in H-FER. The higher activation energy for deprotonation of iso-butoxide to isobutene is in line with 37T ONIOM(MP2/6-311+G(2df,2p):M08-HX/6-311+G-(2df,2p))//ONIOM(MP2/6-31G(d,p):M08-HX/6-31G(d,p)) calculations[40]. Nevertheless, the calculated activation energy of 120 kJ/mol is much lower than the reported activation barrier of 151 kJ/mol for the 37T ONIOM calculation.[40] The calculated apparent activation energy w.r.t. to gas phase 1-butene is 34 kJ/mol, which is also lower than the experimentally reported apparent activation energy of 58 kJ/mol for skeletal isomerization in H-FER[31], possibly attributed to overestimation of the dispersive stabilization in the TS.[78]

5.3.2 *Microkinetic modelling and reaction path analysis: 1-butanol dehydration and butene isomerization*

A detailed microkinetic model considering all 19 different reaction mechanisms, consisting of 34 elementary steps (23 steps for formation of 1-butene/DBE[14] and 11 extra steps as shown in Table 1 for formation of butene isomers) has been applied without making any assumption for the rate determining step. The effect of reaction conditions, viz., partial pressure of 1-butanol (0.001-100 kPa), site time ($N_{H+}/F_{BuOH,0}$ = 0-100 mol H^+ s / mol $BuOH_0$) and reaction temperature (450-500 K), is studied. A comparison of the forward, reverse and net reaction rates for the different elementary steps over a wide range of reaction conditions has been used to determine the equilibrated and non-equilibrated steps along each mechanism. In what follows, a detailed reaction path analysis is used to identify the key reaction mechanisms and to provide an unpreceded insight into the effect of reaction conditions and zeolite framework.

5.3.2.1. Effect of site time

Catalytic activity and product selectivity for different zeolites are studied at different site times at constant temperature (500 K) and inlet butanol partial pressure (10 kPa). As seen from Figure 6, the investigated zeolites show significant differences in catalytic activity and product selectivity. Comparison of site time required to achieve an identical conversion shows that the catalytic activity for 1-butanol dehydration increases in the order H-FER ~ H-ZSM-22 < H-ZSM-5 (see Figure 6).

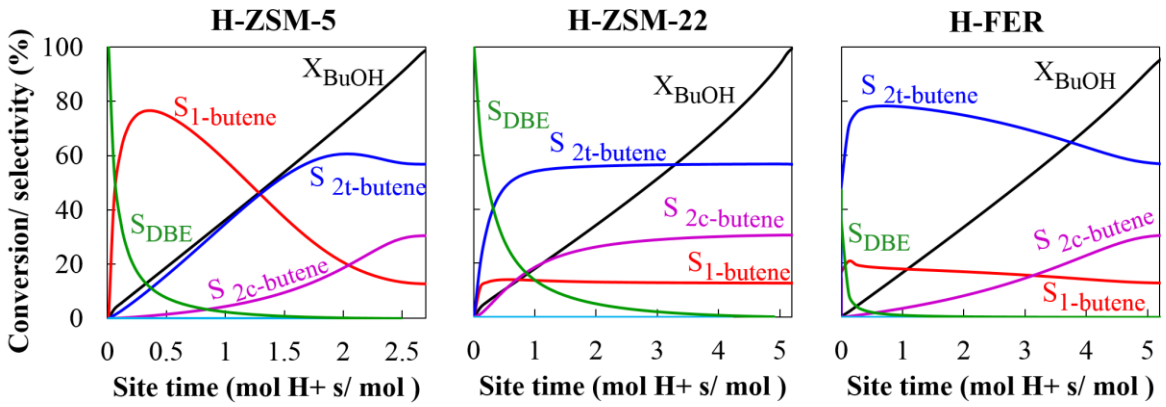

Figure 6. Simulated 1-butanol conversion and selectivity profile for formation of 1-butene, 2t-butene, 2c-butene, isobutene and DBE in H-ZSM-5, H-ZSM-22 and H-FER as a function of site time. Reaction conditions: 500 K, 1-butanol inlet partial pressure of 10 kPa.

The higher activity for H-ZSM-5 is in line with the previously reported trends on catalyst activity for alcohol dehydration [12]. For H-FER, the inclusion of the additional reaction mechanism for the direct formation of 2t-butene from butanol dimer results in a TOF_{BuOH} two times higher than in the previously reported theoretical study[16]. For all three zeolites, DBE selectivity decreases steadily with increasing site time, while significant differences are seen in the selectivity for butene isomers in the different zeolites. H-ZSM-5 shows a higher selectivity for DBE at very low site time, which shifts in favor of 1-butene at low-to-moderate site times and then to 2t-butene at higher site times. Likewise, H-ZSM-22 depicts a shift in selectivity from DBE to 2t-butene with increasing site time and conversion. On the other hand, H-FER exhibits a significant preference for 2t-butene starting from very low site times. No isobutene is formed under the investigated reaction conditions and higher site times lead to equilibrium composition within linear butenes for all three zeolites.

On complete conversion of 1-butanol, high butene surface coverages are expected to facilitate the oligomerization of butenes to higher hydrocarbons[79]. However, alkene oligomerization in zeolites is known to be significantly inhibited in the presence of strongly adsorbed oxygenates such as alcohol and ether[13]. Accordingly, further discussions are restricted to site time which avoids complete conversion of butanol, ensuring that the surface coverage of butanol /DBE is

always higher than that of butenes. Such reaction conditions also avoid the possibility of a bimolecular skeletal isomerization mechanism, which involves butene dimerization followed by skeletal isomerization and cracking[18]. This justifies the use of monomolecular reaction mechanism for skeletal isomerization of butene in the zeolites.

5.3.2.2. Effect of conversion

The influence of zeolite framework on product selectivity, TOFs and surface coverages are studied at identical conversion. The difference in zeolite performance is compared at several conversion levels by systematically varying the site time at constant temperature (500 K) and inlet butanol partial pressure (10 kPa). Figure 7 shows the effect of conversion (X_{BuOH}) on the simulated selectivity profile and surface coverages for the investigated zeolites at 500 K and 1-butanol inlet partial pressure of 10 kPa. At very low conversions ($X_{BuOH} \rightarrow 0$) DBE remains the key product for both H-ZSM-5 and H-ZSM-22, while with increasing conversion the selectivity shifts in favor of butene isomers. Interestingly, 1-butanol dehydration in H-FER depicts a significant 2t-butene selectivity even at extremely low conversion level ($X_{BuOH} \rightarrow 0$). This can be explained by a difference in the underlying reaction mechanism for formation of 2t-butene in H-FER as compared to H-ZSM-5 and H-ZSM-22.

As described previously[23], a maximum is observed for 1-butene selectivity in H-ZSM-5. It is pertinent to note that the 1-butene maximum for butanol dehydration in H-ZSM-5 at 450K was reported to be at X_{BuOH} ~50%, which shifts towards lower conversion (~20%) with increase in reaction temperature. This is indicative of the role of reaction conditions in determining the product selectivity. H-FER depicts a significant preference for 2t-butene starting from a very low conversion level. The selectivity profile for dehydration in H-ZSM-5 and H-FER indicate that linear butenes achieve thermodynamic equilibrium only at high conversions above 60%. On the other hand, 1-butanol dehydration in H-ZSM-22 does not

show any maximum for 1-butene and it attains thermodynamic equilibrium even at low conversion levels (less than 30%).

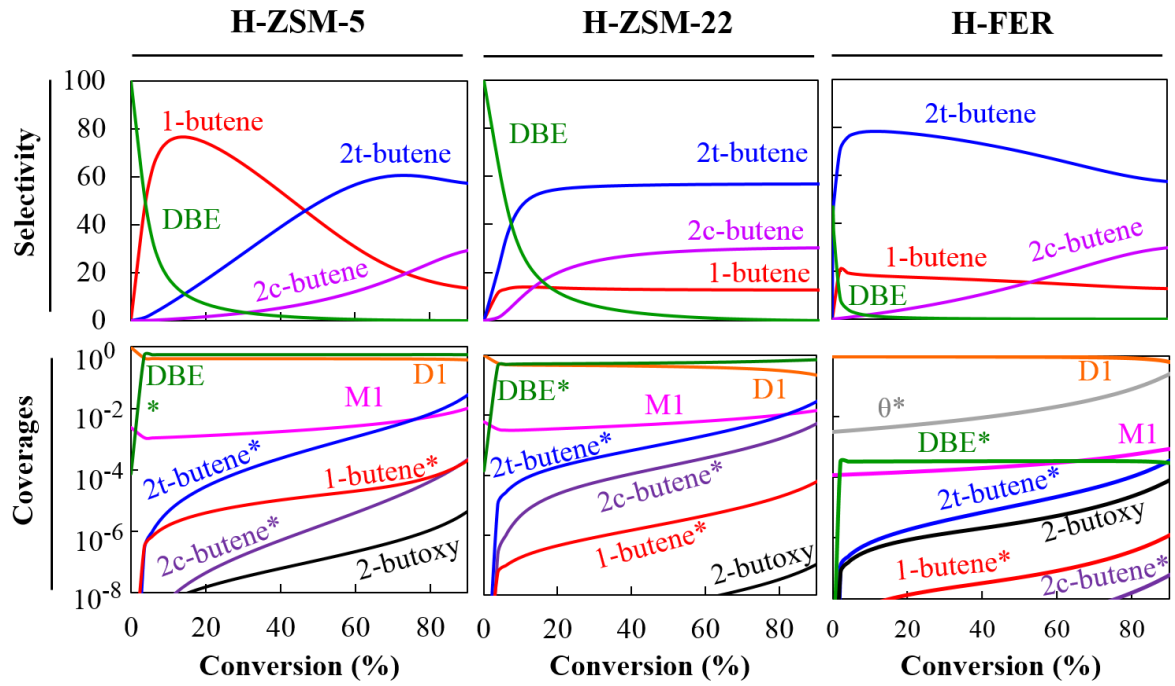

Figure 7. Comparison of simulated selectivity profile and surface coverages as function of 1-butanol conversion in H-ZSM-5, H-ZSM-22 and H-FER. Reaction conditions: 500 K, 1-butanol inlet partial pressure of 10 kPa and site time varied between 0 to 5.5 mol H^+ s / mol $BuOH_0$.

D1 remains the most abundant reaction intermediate (MARI) for H-FER in the entire butanol conversion range. For H-ZSM-5 and H-ZSM-22, D1 is MARI only at low conversions and DBE* starts gaining importance with increase in conversion. The differences in MARI for different zeolites are in line with the previous theoretical study.[16] For all three zeolites, increase in conversion is associated with an increase in surface coverage of linear butenes and 2-butoxide. Such changes in the surface coverage with conversion alters the rates of the elementary steps of the underlying reaction mechanisms and explains differences in product selectivity amongst different zeolites.

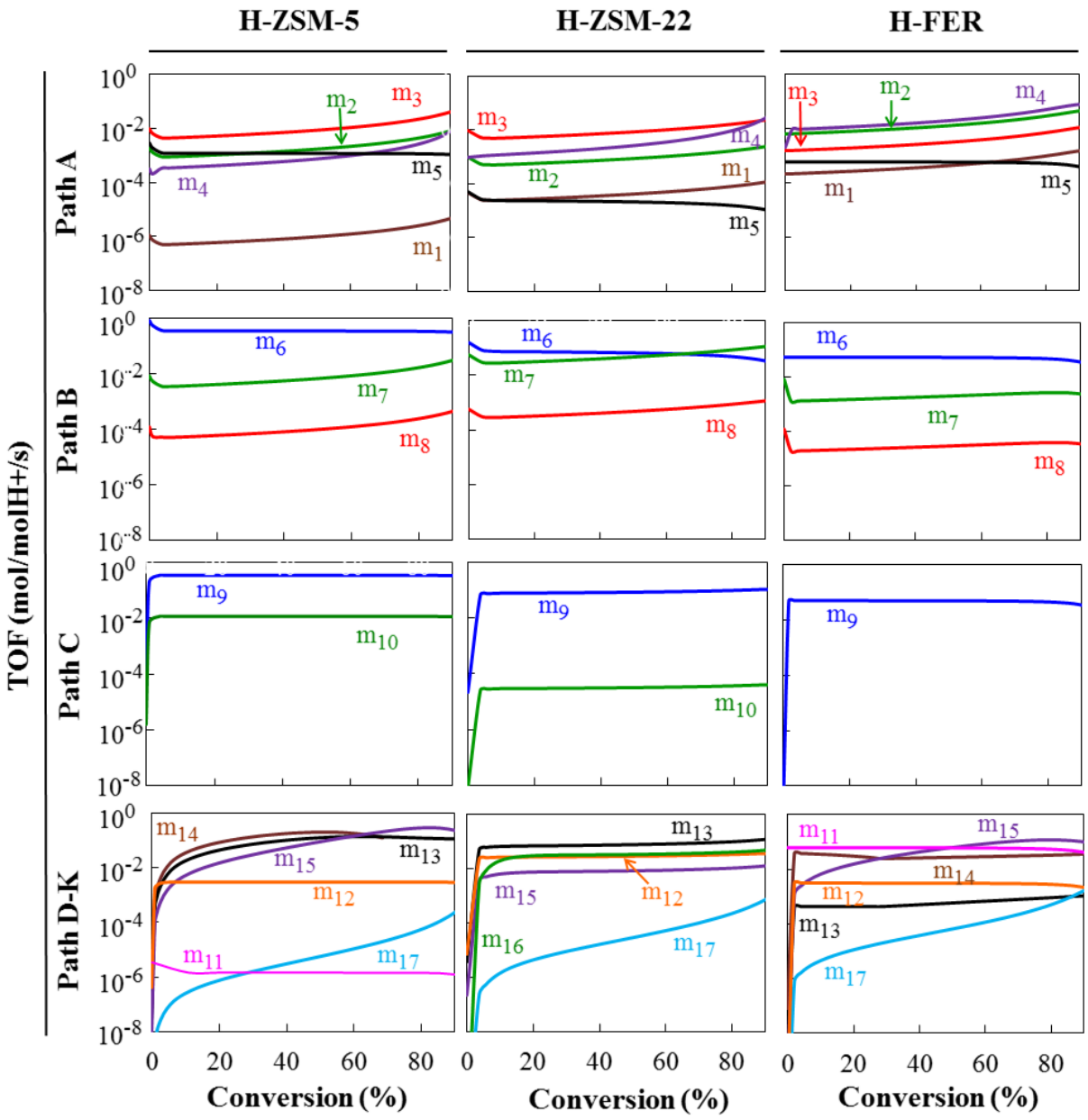

Figure 8. Turnover frequencies (TOF) for different reaction mechanisms (m_1-m_{19}) as a function of 1-butanol conversion at reaction temperature of 500 K and inlet 1-butanol partial pressure of 10 kPa. Reaction mechanism: m_1-m_5 for direct dehydration of 1-butanol to 1-butene (path A), m_6-m_8 for dehydration of 1-butanol to di-1-butyl ether (path B), m_9-m_{10} for DBE decomposition to 1-butene and 1-butanol (path C), m_{11}/m_{12} for direct formation of 2t-butene from D1/DBE (path D/E, respectively), m_{13}-m_{14} for double bond isomerization of 1-butene to trans-2-butene (path F), m_{15} and m_{16} for double bond isomerization of 1-butene/2t-butene to cis-2-butene (path G/H, respectively), m_{17}/m_{18}/m_{19} for skeletal isomerization of 1-butene/2t-butene/2c-butene to iso-butene (path I/ J/ K, respectively). Mechanisms with TOF less than 10^{-8} s^{-1} are not shown in the figure.

The TOFs for different reaction mechanisms within different zeolites are shown in Figure 8 and can be used to explain the simulated selectivity profile. For all three zeolites, a marginal increase in the TOF for monomolecular butanol dehydration mechanisms (m1-m4) is seen at higher 1-butanol conversions. This is attributed to the marginal increase in M1 coverage with decrease in the gas phase 1-butanol concentration, leading to conversion of D1 to M1 (see coverages of Figure 7).

Reaction mechanism m3 (anti-elimination) remains dominant for the direct dehydration of 1-butanol to 1-butene (path A) in H-ZSM-5 and H-ZSM-22. On the other hand, the steric constraints for the formation of the larger anti-elimination transition state in FER makes it less favorable in comparison to mechanism m4 (butoxide-mediated mechanism involving an S_N2 type substitution) and mechanism m2 (syn-elimination). For ether formation (path B) in H-ZSM-22, the dominant mechanism shifts from dimer mediated m6 to 1-butoxide mediated m7. Mechanism m6 remains the dominant path B mechanism for H-ZSM-5 and H-FER. For all three zeolites, mechanism m9 remains the dominant mechanism for DBE decomposition to 1-butene and 1-butanol (path C).

Significant differences are seen in the mechanism leading to formation of 2t-butene on dehydration of 1-butanol in zeolites (see Figure 8). For H-ZSM-5, the concerted mechanism m13 and 2-butoxide mediated step-wise mechanism m14 are found to provide a comparable contribution to the formation of 2t-butene. For the formation of 2t-butene in H-ZSM-22, the concerted mechanism m13 has the highest contribution to the TOF, followed by mechanism m12 for direct formation of 2t-butene from DBE. Hence for H-ZSM-5 and H-ZSM-22, the contribution from double bond isomerization is found to be significantly larger than direct formation of 2t-butene from D1 and DBE. In contrast, a significant contribution from mechanism m11 for direct formation of 2t-butene from D1 is observed for 1-butanol dehydration in H-FER. Moreover, the significantly higher surface coverage of D1 relative to

DBE* in H-FER (see Figure 7, D1/DBE* ~ 10^3) explains the preference for the direct formation of 2t-butene from D1 and not from DBE*, even though the former has a higher activation energy (E_a = 160 kJ/mol) than the latter (E_a = 138 kJ/mol). This highlights the key role of surface coverages in determining the dominant reaction mechanism.

For H-ZSM-5 and H-FER, formation of 2c-butene occurs essentially via step-wise double bond isomerization of 1-butene to 2c-butene (see Figure 8, mechanism m15) involving a 2-butoxide intermediate. On the other hand in H-ZSM-22, a higher TOF for 2t-butene formation and lower activation energy for formation of 2-butoxide from 2t-butene leads to production of 2c-butene essentially via mechanism m16 (isomerization of 2t-butene to 2c-butene).

For all three zeolites, no significant formation of isobutene is observed in the entire butanol conversion range (see Figure 8, mechanism 17). A marginal increase in TOF for isobutene formation via mechanism 17 is observed with increase in conversion. This is attributed to an increase in the surface coverage of 2-butoxide (an intermediate in skeletal isomerization mechanism) with increase in conversion (see coverages of Figure 7). In comparison to H-ZSM-5, the TOF for isobutene formation in H-ZSM-22 and H-FER are relatively higher (see Figure 8, mechanism 17), which is in line with the literature reported higher isobutene selectivity in H-ZSM-22 and H-FER[17,18]. Nevertheless, the TOF for isobutene formation at 500 K is too small to have a significant contribution in the product distribution (see selectivity profiles of Figure 7).

5.3.2.3. Effect of reaction temperature

Figure 9 shows that at 1-butanol conversion of 50 % , an increase in reaction temperature leads to a decrease in 1-butene selectivity and an increase in 2t-butene and 2c-butene selectivity for H-ZSM-5. For H-ZSM-22, only marginal changes are observed in 1-butene and 2t-butene selectivity, while a slight increase in 2c-butene selectivity is seen with increasing

temperature. Meanwhile, a slight decrease in 2t-butene selectivity and increase in 2c-butene selectivity is observed for H-FER with an increase in reaction temperature.

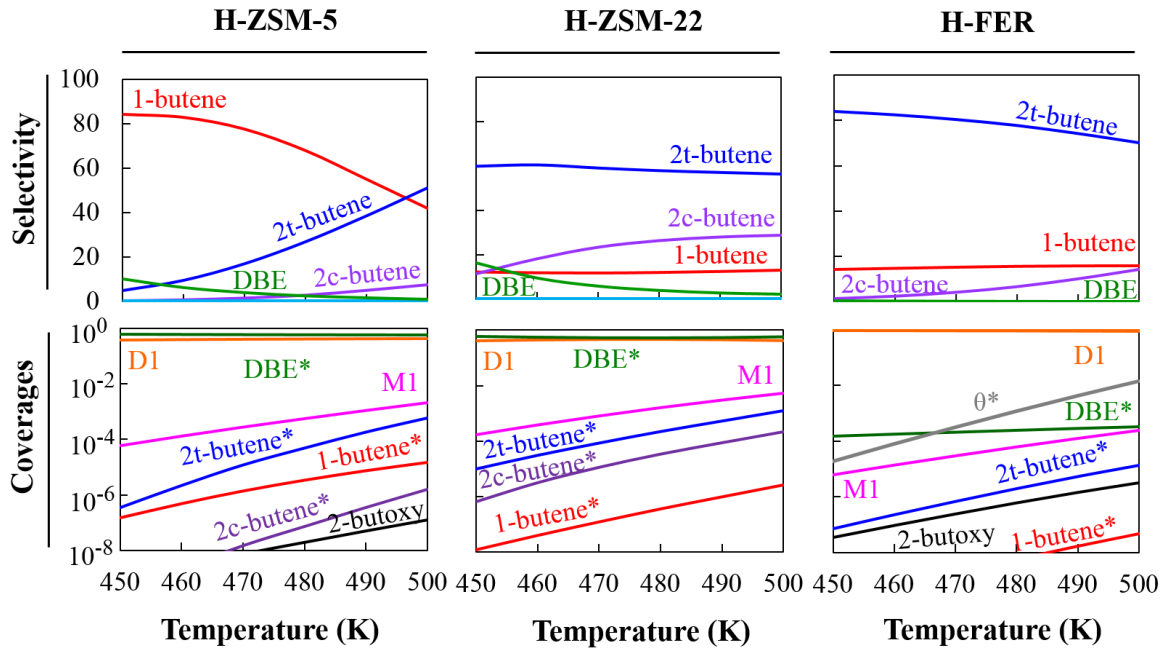

Figure 9. Effect of reaction temperature on simulated selectivity profile and surface coverages for the dehydration of 1-butanol in H-ZSM-5, H-ZSM-22 and H-FER at constant 1-butanol conversion of 50% and 1-butanol inlet partial pressure of 10 kPa.

As expected, an increase in reaction temperature leads to increase in TOF for all reaction mechanisms (see Figure 10) and this increase in TOF is more pronounced for reactions such as skeletal isomerization which have a relatively higher activation energy. The change in reaction temperature is also associated with a change in coverage of adsorbed reaction intermediates (see coverages of Figure 9) which can have different influence on different reaction mechanisms. For reaction path A, the relative contribution from the dimer-mediated mechanism (m5) is found to decrease in comparison to the monomolecular mechanism (m_1-m_4) in all three zeolites. This is ascribed to a relative increase in the surface coverage of M1 w.r.t to D1 with increase in temperature. For path B, the relative contribution from 1-butoxide mediated mechanism m7 is found to increase in comparison to the dimer-mediated mechanism (m6) which nevertheless remains dominant at low temperature conditions[16]. For

H-ZSM-22, the TOF for mechanism m7 becomes comparable to m6 at 500K. For path C, mechanism m9 remains dominant for all three zeolite. The increase in reaction temperature leads to an increase in the surface coverage of butene isomers and 2-butoxide intermediate (see Figure 9) which results in an increase in TOF for double bond and skeletal isomerization reaction. Thus, conversion of 1-butene to other butene isomers with increase in temperature explains the decrease in 1-butene selectivity for H-ZSM-5. On the other hand, a lower activation energy of 36 kJ/mol for the concerted double bond isomerization mechanism (m13) in H-ZSM-22 (as compared to 54 and 50 kJ/mol for H-ZSM-5 and H-FER, respectively), ensures a faster approach to the equilibrium composition for linear butene isomers (1-butene, 2t-butene and 2c-butene) in H-ZSM-22 even at relatively lower temperatures. Comparison of the relative slopes of TOF vs temperature (see Figure 10) indicates that much higher temperatures are required for the TOF of skeletal isomerization mechanism 17 to have a significant contribution. This is consistent with the temperature programmed surface reaction study by Zhang et al[18] for conversion of 1-butanol to isobutene in H-ZSM-22, where they observed an increase in isobutene yield from 4% to 34 % (at X_{BuOH} = 100%) on increasing the reaction temperature from 573 to 673 K. Their study also indicated that H-ZSM-22 and H-FER exhibit superior catalytic performance in terms of isobutene selectivity as compared to H-ZSM-5 at 673 K.

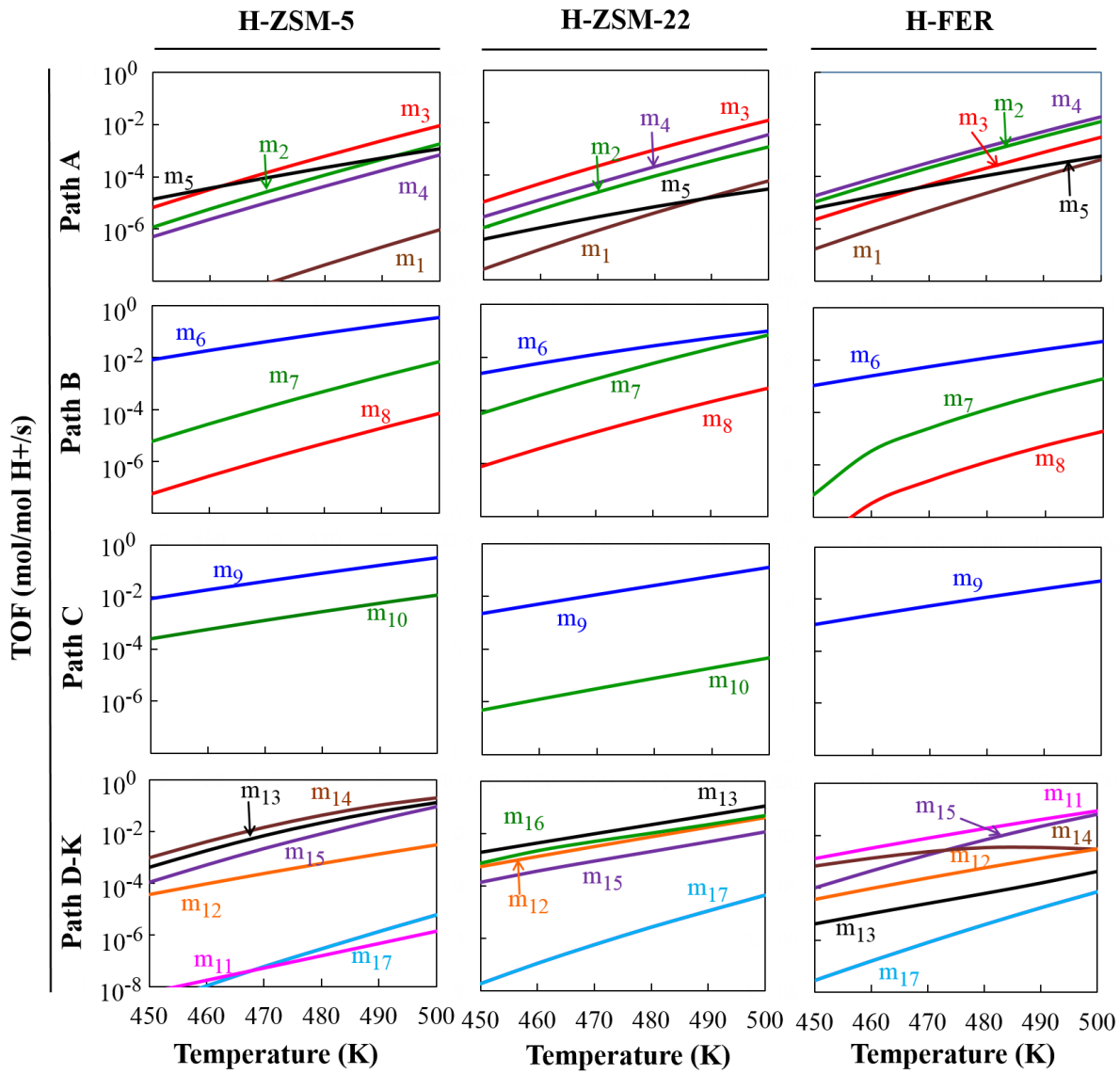

Figure 10. Turnover frequencies (TOF) for different reaction mechanisms (m_1-m_{19}) as a function of reaction temperature at a constant conversion of 50% and inlet 1-butanol partial pressure of 10 kPa. Reaction mechanism: m_1-m_5 for direct dehydration of 1-butanol to 1-butene (path A), m_6-m_8 for dehydration of 1-butanol to di-1-butyl ether (path B), m_9-m_{10} for DBE decomposition to 1-butene and 1-butanol (path C), m_{11}/m_{12} for direct formation of 2t-butene from D1/DBE (path D/E, respectively), m_{13}-m_{14} for double bond isomerization of 1-butene to trans-2-butene (path F), m_{15} and m_{16} for double bond isomerization of 1-butene/2t-butene to cis-2-butene (path G/H, respectively), m_{17}/m_{18}/m_{19} for skeletal isomerization of 1-butene/2t-butene/2c-butene to iso-butene (path I/ J/ K, respectively). Mechanisms with TOF less than 10^{-8} s^{-1} are not shown in the figure.

5.3.2.4. Effect of partial pressure of 1-Butanol

The influence of 1-butanol inlet partial pressure on the simulated product selectivity, surface coverages and TOFs of the underlying reaction mechanisms is studied at constant reaction temperature of 500 K and constant 1-butanol conversion of 50 %. Figure 11 shows the effect of 1-butanol inlet partial pressure on product selectivity and surface coverage.

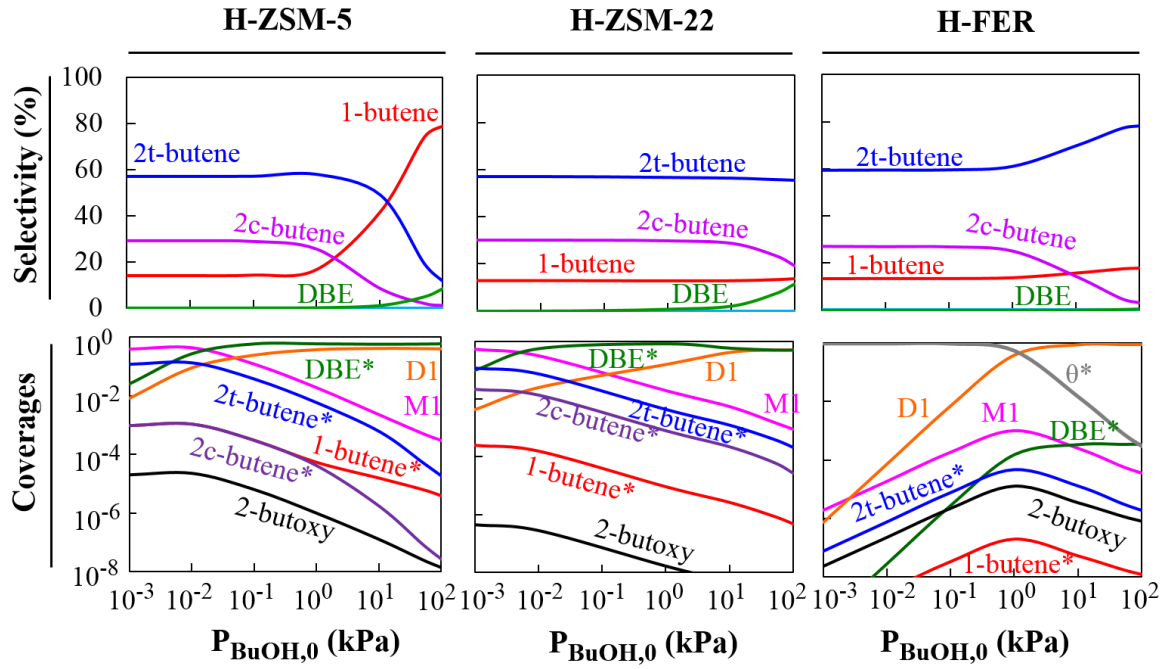

Figure 11. Effect of inlet 1-butanol partial pressure ($P_{BuOH,0}$) on the simulated selectivity profile and surface coverages for dehydration of 1-butanol in H-ZSM-5, H-ZSM-22 and H-FER at constant 1-butanol conversion of 50% and reaction temperature of 500 K.

At 1-butanol inlet partial pressures less than 1 kPa, linear butene isomers remain in thermodynamic equilibrium for all three zeolites. With increase in 1-butanol partial pressure from 10^{-1} to10^{2} kPa, 1-butene selectivity increases from 14 to 79 % for H-ZSM-5, while a slight increase in 2t-butene selectivity accompanied by decrease in 2c-butene selectivity is observed in the case of H-FER. On the other hand, 1-butanol dehydration in H-ZSM-22 shows no significant change in 1-butene and 2t-butene selectivity with increase in 1-butanol

partial pressures. A decrease in 2c-butene yield with increase in 1-butanol partial pressure from 10 to 100 kPa is seen in all three zeolites.

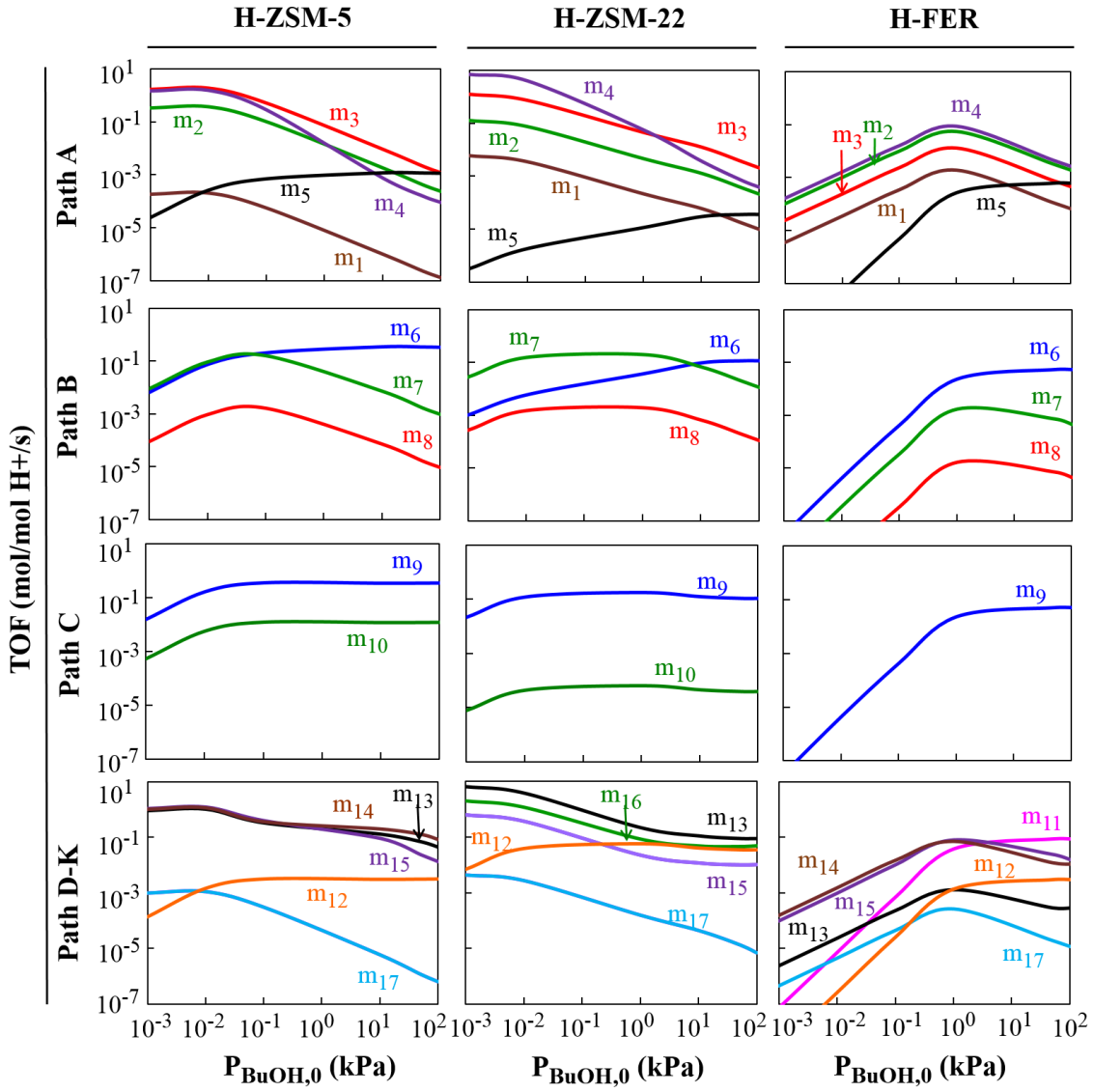

Figure 12. Turnover frequencies (TOF) for different reaction mechanisms (m_1-m_{19}) as a function of inlet butanol partial pressure ($P_{BuOH,0}$) at a constant conversion of 50 % and reaction temperature of 500 K. Reaction mechanism: m_1-m_5 for direct dehydration of 1-butanol to 1-butene (path A), m_6-m_8 for dehydration of 1-butanol to di-1-butyl ether (path B), m_9-m_{10} for DBE decomposition to 1-butene and 1-butanol (path C), m_{11}/m_{12} for direct formation of 2t-butene from D1/DBE (path D/E, respectively), m_{13}-m_{14} for double bond isomerization of 1-butene to trans-2-butene (path F), m_{15} and m_{16} for double bond isomerization of 1-butene/2t-butene to cis-2-butene (path G/H, respectively), m_{17}/m_{18}/m_{19} - for skeletal isomerization of 1-butene/2t-butene/2c-butene to iso-butene (path I/J/K, respectively). Mechanisms with TOF less than 10^{-8} s^{-1} are not shown in the figure.

In line with previous theoretical studies[14,16], there is an increase in DBE yield with increasing 1-butanol partial pressure for H-ZSM-5 and H-ZSM-22, while fast conversion of DBE to 1-butene* and 1-butanol leads to a negligible change in DBE selectivity in case of H-FER.

The effect of 1-butanol inlet partial pressure on the simulated TOFs for different reaction mechanisms (m1-m19) in different zeolites is shown in Figure 12. At low butanol pressures, formation of 1-butene occurs via monomolecular path A mechanisms, while, at high butanol partial pressures, formation of 1-butene occurs essentially via mechanism m9 (DBE decomposition, path C). For H-ZSM-5, the formation of 2-butenes occurs essentially via double bond isomerization mechanisms with both concerted m13 and 2-butoxide mediated stepwise m14 and m15 (for formation of 2t-butene and 2c-butene, respectively) having comparable contributions. For H-ZSM-22, the TOF for the concerted mechanism m13 for production of 2t-butene from 1-butene is slightly higher than the TOF for the stepwise m16 for formation of 2c-butene from 2t-butene. Lastly for H-FER, the formation of 2t-butene and 2c-butene occurs via stepwise mechanisms m14 and m15, respectively, at butanol pressures lower than 1 kPa. At butanol partial pressure above 10 kPa, the formation of 2t-butene in H-FER occurs essentially via mechanism m11 (direct formation of 2t-butene from D1). For all three zeolites, an increase in 1-butanol partial pressure above 1 kPa is associated with a decrease in the surface coverage for 1-butene and 2-butoxide (see Figure 11) and can result in a decrease in the TOF of the consecutive reactions for conversion of 1-butene to 2-butenes, as explained in the following paragraph.

A higher rate for the concerted double bond isomerization (mechanism 13, Figure 12) in H-ZSM-22 ensures that the rate of formation of 1-butene remains the rate controlling step for the formation of 2-butenes during 1-butanol dehydration in H-ZSM-22. Therefore, the double bond isomerization reaction in H-ZSM-22 exhibits an initial zero order dependence ($10^{-3} \leq$

$P_{BuOH,0} < 10^{-2}$ kPa), followed by a negative order dependence ($10^{-2} < P_{BuOH,0} < 1$ kPa) and then again a zero order pressure dependence ($1 < P_{BuOH,0} \leq 100$ kPa) according to the pressure dependence for the rate controlling path A mechanism m4 ($10^{-3} \leq P_{BuOH,0} < 1$ kPa) and path C mechanism m9 ($1 < P_{BuOH,0} \leq 100$ kPa). Meanwhile, four different regimes for 1-butanol pressure dependence are seen in the case of H-ZSM-5. In addition to the initial zero order ($10^{-3} \leq P_{BuOH,0} < 10^{-2}$ kPa), subsequent negative order ($10^{-2} \leq P_{BuOH,0} < 10^{-1}$ kPa) and later zero order ($10^{-1} \leq P_{BuOH,0} < 1$ kPa) butanol pressure dependence regimes (as seen in the case of H-ZSM-22), a fourth regime of negative order dependence is seen at butanol partial pressures above 1 kPa in the case of H-ZSM-5. The occurrence of such an additional regime is attributed to the decrease in the surface coverage of 1-butene and 2-butoxide with increase in butanol partial pressure (see Figure 11), making the TOF for 1-butene isomerization lower than the rate of formation of 1-butene via path C (see mechanism 9 vs. mechanisms 13-15 in Figure 12). Thus, a decrease in TOF for double bond isomerization with increase in butanol partial pressure results in a net positive rate of formation of 1-butene and explains the increase in 1-butene selectivity in H-ZSM-5 at butanol partial pressures above 1 kPa, (corresponding to the fourth regime see Figure 11). The point of onset of the high butanol pressure negative order dependence regime in a zeolite is defined by the butanol partial pressure at which the TOF for isomerization becomes lower than the TOF for formation of 1-butene. Overall, it is clear that a detailed insight into the butanol partial pressure dependence is needed in order to understand the cause for the differences observed in selectivity of butene isomers in different zeolites at high butanol partial pressures.

5.4. Conclusions

This study provides a detailed insight into the plausible reaction mechanisms for dehydration of 1-butanol to butene isomers in three different medium pore zeolites. Microkinetic simulation results indicate highest TOF for 1-butanol dehydration in H-ZSM-5 and significant

differences in product selectivity and dominant reaction mechanism for dehydration and isomerization in different zeolites. H-ZSM-5 exhibits a conversion regime which maximizes 1-butene selectivity, while butene isomers attain thermodynamic equilibrium in H-ZSM-22 even at low conversion levels, owing to the lower activation barrier for the concerted double bond isomerization in H-ZSM-22. For H-ZSM-5 and H-ZSM-22, the formation of 2-butenes occurs via double bond isomerization of 1-butene produced from butanol dehydration. On the other hand for H-FER, 2t-butene is mainly produced from the butanol dimer via an E1 elimination accompanied by a 1,2-hydride shift. The decrease in zeolite pore size from H-ZSM-5 to H-FER provides a significant enthalpic stabilization of the transition state of E1 elimination for the direct formation of 2t-butene from 1-butanol dimer and DBE. Although a slightly higher TOF for formation of isobutene is obtained in H-ZSM-22 and H-FER as compared to H-ZSM-5, no significant formation of isobutene is observed in all three zeolites in the investigated temperature range of 450 – 500 K.

5.5. References

(1) Mascal, M. *Biofuel Bioprod Bior* **2012**, *6*, 483.

(2) Wright, M. E.; Harvey, B. G.; Quintana, R. L. *Energ Fuel* **2008**, *22*, 3299.

(3) Kirk-Othmer; Seidel, A. *Kirk-Othmer encyclopedia of chemical technology*; John Wiley & Sons, 2007; Vol. 4.

(4) Savage, N. *Nature* **2011**, *474*, S9.

(5) Li, Y.; Yu, J. H. *Chem Rev* **2014**, *114*, 7268.

(6) Makarova, M. A.; Williams, C.; Thomas, J. M.; Zamaraev, K. I. *Catal Lett* **1990**, *4*, 261.

(7) Makarova, M. A.; Paukshtis, E. A.; Thomas, J. M.; Williams, C.; Zamaraev, K. I. *Stud Surf Sci Catal* **1993**, *75*, 1711.

(8) Makarova, M. A.; Paukshtis, E. A.; Thomas, J. M.; Williams, C.; Zamaraev, K. I. *J Catal* **1994**, *149*, 36.

(9) Vjunov, A.; Hu, M. Y.; Feng, J.; Camaioni, D. M.; Mei, D. H.; Hu, J. Z.; Zhao, C.; Lercher, J. A. *Angew Chem Int Edit* **2014**, *53*, 479.

(10) Zhi, Y.; Shi, H.; Mu, L.; Liu, Y.; Mei, D.; Camaioni, D. M.; Lercher, J. A. *J Am Chem Soc* **2015**.

(11) Chiang, H.; Bhan, A. *J Catal* **2010**, *271*, 251.

(12) Phung, T. K.; Hernandez, L. P.; Lagazzo, A.; Busca, G. *Appl Catal a-Gen* **2015**, *493*, 77.

(13) Van der Borght, K.; Batchu, R.; Galvita, V.; Alexopoulos, K.; Reyniers, M.-F.; Thybaut, J. W.; Marin, G. B. *Angew Chem Int Edit* **2016**, *55*, 12817.

(14) John, M.; Alexopoulos, K.; Reyniers, M. F.; Marin, G. B. *J Catal* **2015**, *330*, 28.

(15) Alexopoulos, K.; John, M.; Van der Borght, K.; Galvita, V.; Reyniers, M.-F.; Marin, G. B. *J Catal* **2016**, *339*, 173.

(16) John, M.; Alexopoulos, K.; Reyniers, M.-F.; Marin, G. B. *ACS Catal* **2016**, *6*, 4081.

(17) Zhang, D. Z.; Al-Hajri, R.; Barri, S. A. I.; Chadwick, D. *Chem Commun* **2010**, *46*, 4088.

(18) Zhang, D. Z.; Barri, S. A. I.; Chadwick, D. *Appl Catal a-Gen* **2011**, *403*, 1.

(19) Vansanten, R. A.; Kramer, G. J. *Chem Rev* **1995**, *95*, 637.

(20) Gounder, R.; Iglesia, E. *Accounts Chem Res* **2012**, *45*, 229.

(21) Bhan, A.; Iglesia, E. *Accounts Chem Res* **2008**, *41*, 559.

(22) Norskov, J. K.; Bligaard, T.; Rossmeisl, J.; Christensen, C. H. *Nat Chem* **2009**, *1*, 37.

(23) John, M. **2016**, *chapter 4, doctoral dissertation*.

(24) Kondo, J. N.; Domen, K.; Wakabayashi, F. *Micropor Mesopor Mat* **1998**, *21*, 429.

(25) Kondo, J. N.; Shao, L. Q.; Wakabayashi, F.; Domen, K. *J Phys Chem B* **1997**, *101*, 9314.

(26) Boronat, M.; Viruela, P.; Corma, A. *J Phys Chem A* **1998**, *102*, 982.

(27) Kazansky, V. B. *Accounts Chem Res* **1991**, *24*, 379.

(28) Houzvicka, J.; Hansildaar, S.; Ponec, V. *J Catal* **1997**, *167*, 273.

(29) Meriaudeau, P.; Tuan, V. A.; Le, N. H.; Szabo, G. *J Catal* **1997**, *169*, 397.

(30) Simon, M. W.; Suib, S. L.; Oyoung, C. L. *J Catal* **1994**, *147*, 484.

(31) Domokos, L.; Lefferts, L.; Seshan, K.; Lercher, J. A. *J Catal* **2001**, *197*, 68.

(32) Gleeson, D. *J Phys Chem A* **2011**, *115*, 14629.

(33) Lonsinger, S. R.; Chakraborty, A. K.; Theodorou, D. N.; Bell, A. T. *Catal Lett* **1991**, *11*, 209.

(34) Dedecek, J.; Lucero, M. J.; Li, C. B.; Gao, F.; Klein, P.; Urbanova, M.; Tvaruzkova, Z.; Sazama, P.; Sklenak, S. *J Phys Chem C* **2011**, *115*, 11056.

(35) Dedecek, J.; Balgova, V.; Pashkova, V.; Klein, P.; Wichterlova, B. *Chem Mater* **2012**, *24*, 3231.

(36) Baerlocher, C.; Meier, W. M.; Olson, D.; Meier, W. M. *Atlas of zeolite framework types*; 5th rev. ed.; Elsevier: Amsterdam ; New York, 2001.

(37) Tuma, C.; Sauer, J. *Physical Chemistry Chemical Physics* **2006**, *8*, 3955.

(38) Nieminen, V.; Sierka, M.; Murzin, D. Y.; Sauer, J. *J Catal* **2005**, *231*, 393.

(39) Dai, W. L.; Wang, C. M.; Yi, X. F.; Zheng, A. M.; Li, L. D.; Wu, G. J.; Guan, N. J.; Xie, Z. K.; Dyballa, M.; Hunger, M. *Angew Chem Int Edit* **2015**, *54*, 8783.

(40) Wattanakit, C.; Nokbin, S.; Boekfa, B.; Pantu, P.; Limtrakul, J. *J Phys Chem C* **2012**, *116*, 5654.

(41) Gleeson, D. *J Mol Catal a-Chem* **2013**, *368*, 107.

(42) Kresse, G.; Hafner, J. *Phys Rev B* **1993**, *47*, 558.

(43) Kresse, G.; Hafner, J. *Phys Rev B* **1994**, *49*, 14251.

(44) Kresse, G.; Furthmuller, J. *Comp Mater Sci* **1996**, *6*, 15.

(45) Blochl, P. E. *Phys Rev B* **1994**, *50*, 17953.

(46) Kresse, G.; Joubert, D. *Phys Rev B* **1999**, *59*, 1758.

(47) Perdew, J. P.; Chevary, J. A.; Vosko, S. H.; Jackson, K. A.; Pederson, M. R.; Singh, D. J.; Fiolhais, C. *Phys Rev B* **1992**, *46*, 6671.

(48) Grimme, S. *J Comput Chem* **2006**, *27*, 1787.

(49) Kerber, T.; Sierka, M.; Sauer, J. *J Comput Chem* **2008**, *29*, 2088.

(50) Goltl, F.; Gruneis, A.; Bucko, T.; Hafner, J. *J Chem Phys* **2012**, *137*.

(51) Vener, M. V.; Rozanska, X.; Sauer, J. *Phys Chem Chem Phys* **2009**, *11*, 1702.

(52) Chiu, C. C.; Vayssilov, G. N.; Genest, A.; Borgna, A.; Rosch, N. *J Comput Chem* **2014**, *35*, 809.

(53) Nguyen, C. M.; Reyniers, M. F.; Marin, G. B. *J Catal* **2015**, *322*, 91.

(54) Nguyen, C. M.; Reyniers, M. F.; Marin, G. B. *Phys Chem Chem Phys* **2010**, *12*, 9481.

(55) Nguyen, C. M.; Reyniers, M. F.; Marin, G. B. *J Phys Chem C* **2011**, *115*, 8658.

(56) Bučko, T.; Hafner, J. *J Catal* **2015**, *329*, 32.

(57) Leydier, F.; Chizallet, C.; Costa, D.; Raybaud, P. *J Catal* **2015**, *325*, 35.

(58) Grimme, S.; Antony, J.; Ehrlich, S.; Krieg, H. *J Chem Phys* **2010**, *132*.

(59) Bader, R. F. W. *Atoms in molecules : a quantum theory*; Clarendon Press: Oxford, 1990.

(60) Henkelman, G.; Arnaldsson, A.; Jonsson, H. *Comp Mater Sci* **2006**, *36*, 354.

(61) Henkelman, G.; Jonsson, H. *J Chem Phys* **2000**, *113*, 9978.

(62) Henkelman, G.; Jonsson, H. *J Chem Phys* **1999**, *111*, 7010.

(63) Heyden, A.; Bell, A. T.; Keil, F. J. *J Chem Phys* **2005**, *123*.

(64) De Moor, B. A.; Ghysels, A.; Reyniers, M. F.; Van Speybroeck, V.; Waroquier, M.; Marin, G. B. *J Chem Theory Comput* **2011**, *7*, 1090.

(65) Zhao, Y.; Truhlar, D. G. *Phys Chem Chem Phys* **2008**, *10*, 2813.

(66) Ribeiro, R. F.; Marenich, A. V.; Cramer, C. J.; Truhlar, D. G. *J Phys Chem B* **2011**, *115*, 14556.

(67) Grimme, S. *Chem-Eur J* **2012**, *18*, 9955.

(68) Jensen, J. H. *Phys Chem Chem Phys* **2015**, *17*, 12441.

(69) Piccini, G.; Sauer, J. *J Chem Theory Comput* **2014**, *10*, 2479.

(70) Piccini, G.; Alessio, M.; Sauer, J.; Zhi, Y. C.; Liu, Y.; Kolvenbach, R.; Jentys, A.; Lercher, J. A. *J Phys Chem C* **2015**, *119*, 6128.

(71) De Moor, B. A.; Reyniers, M. F.; Marin, G. B. *Phys Chem Chem Phys* **2009**, *11*, 2939.

(72) Cramer, C. J. *Essentials of computational chemistry : theories and models*; 2nd ed.; Wiley: Chichester Hoboken, NJ, 2004.

(73) Hindmarsh, A. C. *IMACS transactions on scientific computation* **1983**, *1*, 55.

(74) Corma, A. *Chem Rev* **1995**, *95*, 559.

(75) Boronat, M.; Viruela, P.; Corma, A. *Physical Chemistry Chemical Physics* **2001**, *3*, 3235.

(76) Dewar, M. J. S.; Ford, G. P. *J Am Chem Soc* **1979**, *101*, 783.

(77) Dewar, M. J. S.; Healy, E. F.; Ruiz, J. M. *J Chem Soc Chem Comm* **1987**, 943.

(78) Piccini, G.; Alessio, M.; Sauer, J. *Angewandte Chemie International Edition* **2016**, *55*, 5235.

(79) Coelho, A.; Caeiro, G.; Lemos, M. A. N. D. A.; Lemos, F.; Ribeiro, F. R. *Fuel* **2013**, *111*, 449.

Chapter 6

Conclusions and perspectives

Conclusions. In this work, a first principle based molecular modelling approach is employed to study the reaction mechanisms for 1-butanol and butene conversion in zeolites. DFT-derived energetics and vibrational analysis are used to obtain thermodynamic and kinetic parameters at relevant temperatures, which are fed to a microkinetic model. This ab initio microkinetic model is then used to obtain unprecedented fundamental mechanistic insights into the zeolite catalyzed conversion of bio-butanol to butene isomers and to illustrate the effect of zeolite framework and reaction conditions on competing reaction pathways.

For dehydration of 1-butanol to di-1-butyl ether (DBE) and 1-butene in H-ZSM-5, several plausible reaction mechanisms, involving elimination (E1, syn- and anti-E2) and substitution

(S_N1 and S_N2) reactions, are studied. Useful insights into the dominant reaction mechanism and its dependence on reaction conditions are derived using reaction path analysis. The present study reveals the importance of alcohol protonation, which helps in the advancement of the dehydration reaction, as it leads to an elongation of the C-O bond, facilitating the cleavage of the C-O bond in a later step. The reasonable agreement between the simulated and literature reported experimental turnover frequencies (TOFs) demonstrates the reliability of the DFT-based microkinetic model. Reaction conditions play a pivotal role in defining the dominant reaction mechanism and pathway. For direct dehydration of 1-butanol to 1-butene (path A), increase in 1-butanol partial pressure leads to a shift in the preferred reaction mechanism from an anti-elimination to 1-butanol assisted 1,2-syn-elimination. The DBE formation (path B) reaction proceeds via S_N2-type nucleophilic substitution, while the DBE decomposition (path C) reaction predominantly occurs via 1,2-syn-elimination. Any shift in the preferred reaction mechanism or path with reaction conditions is explained based on the changes in surface coverages. Lastly, it is seen that under industrially relevant conditions, the presence of water has a negligible influence on the TOFs and the product selectivity.

Next, the effect of zeolite framework on the catalytic performance for 1-butanol dehydration to 1-butene and DBE has been investigated. In line with the experimentally observed trends for ethanol dehydration on different zeolites, the simulation results indicate higher TOFs for H-ZSM-5 in comparison to H-ZSM-22, H-FER and H-FAU and a higher alkene selectivity for H-FAU and H-FER. Interestingly, H-FAU and H-FER follow different reaction mechanisms to achieve this higher 1-butene selectivity. In case of H-FAU, the higher 1-butene selectivity is attributed to its higher preference for the monomolecular direct dehydration path A. On the other hand, the higher 1-butene selectivity in H-FER is attributed to the lower stability of adsorbed DBE which decomposes readily upon its formation. The differences in underlying reaction mechanism, TOFs and product selectivity are rationalized

on the basis of differences in stabilization of reaction intermediates and transition states within different zeolites. This work further highlights the role of reaction conditions in determining the most abundant reaction intermediate, dominant reaction paths, and underlying reaction mechanisms.

After the successful study of 1-butanol dehydration to 1-butene and DBE in H-ZSM-5, this study has also been extended to the formation of other butene isomers, namely trans- and cis-2-butene and isobutene, by including additional reaction mechanisms for concerted and stepwise double bond isomerization, skeletal isomerization and novel mechanisms for direct conversion of adsorbed 1-butanol and di-1-butyl ether to 2-butene. DFT-based microkinetic modelling in H-ZSM-5 shows that, except for very low conversion levels where 2-butenes are produced via E1 elimination of water from the protonated di-1-butyl ether (DBE*), the formation of 2-butenes occurs essentially via a double bond isomerization from 1-butene. This also explains the experimentally observed trend of increase in 2-butene selectivity with increase in reaction temperature, which was previously attributed to a E2 to E1 shift in the mechanism for water elimination from 1-butanol. Increase in site time/conversion or reaction temperature and decrease in 1-butanol partial pressure leads to a relative increase in surface coverage of 1-butene, which favors double bond isomerization reactions and increases selectivity for 2-butenes. Owing to the relatively higher activation barrier for skeletal isomerization, higher temperatures are required for production of isobutene. These results show how reaction conditions can play a crucial role in determining the surface coverages of reaction intermediates and the dominant reaction mechanism, which in turn define the selectivity for butene isomers.

As seen in the dehydration of 1-butanol to 1-butene and DBE, different zeolites can exhibit differences in their catalytic activity and selectivity. Accordingly, the conversion of 1-butanol to butene isomers has been investigated in three industrially relevant medium pore zeolites,

namely H-ZSM-5, H-ZSM-22 and H-FER. Microkinetic simulations indicate significant differences in product selectivity and dominant reaction mechanism for dehydration and isomerization in different zeolites. Once again, a higher TOF is found for H-ZSM-5 in comparison to H-ZSM-22 and H-FER. H-ZSM-5 exhibits a conversion regime which maximizes 1-butene selectivity, while butene isomers attain thermodynamic equilibrium in H-ZSM-22 even at low conversion levels. For H-ZSM-5 and H-ZSM-22, the formation of 2-butenes occurs via double bond isomerization, with both concerted and stepwise mechanisms having comparable contributions for H-ZSM-5, while the concerted mechanism has a greater contribution for H-ZSM-22. On the other hand for H-FER, 2t-butene is mainly produced from the 1-butanol dimer via an E1 elimination accompanied by a 1,2-hydride shift. A decrease in zeolite pore size from H-ZSM-5 to H-FER is found to provide a significant enthalpic stabilization of the transition state for the direct formation of 2t-butene from 1-butanol dimer and DBE. In general, no formation of isobutene is observed for the reaction temperatures (less than 500K) considered in the present study.

Perspectives. In this thesis, it has been shown how DFT-based kinetic parameters can be used in microkinetic models to elucidate changes in the underlying reaction mechanism with reaction conditions and to explain conflicting experimental observations. Despite these successes in explaining the observed trends under low-to-moderate reaction temperatures, these models require the inclusion of additional reactions to capture mechanisms operative at higher reaction temperatures. The present model shows that, at low-to-moderate reaction temperatures, the surface is fully covered with strongly bound alcohol and DBE species, which hinders butene oligomerization and bimolecular skeletal isomerization reactions under these conditions. At higher temperatures, the presence of free sites can allow oligomerization, skeletal isomerization, cracking and hydride shift reactions. These reactions can be further

investigated by using the presented DFT-based approach. Alternatively, a single-event concept might be used to describe these reactions occurring at higher temperatures, thus reducing significantly the number of kinetic parameters needed for the microkinetic model.

Experimental studies can be used to assess the accuracy of the simulation results. The ab initio based microkinetic model predicted a shift in dominant reaction mechanism with the change in the reaction conditions. Although the changes in reaction order at different butanol partial pressures are consistent with the reported experimental trends for ethanol and propanol dehydration in zeolites, an experimental assessment of the partial pressure dependency for 1-butanol dehydration in zeolites is worth investigating. Simulation results also indicate that the dimer mediated mechanism has significantly higher TOF as compared to the butoxide mediated mechanism for DBE formation. 1-Butene co-feed experiments can be devised to assess the contribution from the butoxide mediated mechanism towards DBE formation. If DBE formation follows the butoxide mediated mechanism, then it is expected to show an increase in TOF for DBE formation with increase in 1-butene partial pressure, since it is expected to increase the surface coverage of butoxide species.

For the investigation of the underlying reaction mechanisms in different zeolite frameworks, a specific location of the Al atom and the proton is selected in this work. However, the location of Brønsted acid sites within the zeolite channels can influence the reactivity and selectivity owing to the differences in the spatial constraints associated with the different locations, as seen by the differences in the equilibrium and reaction rate coefficients for the two different acid sites in H-FER. Since the Brønsted acid sites can have several possible spatial distributions in a zeolite, a detailed investigation of these possibilities may be required to obtain a more accurate representation of the catalytic performance. Moreover, for low Si/Al ratio zeolites, the presence of several acid sites per unit cell may result in a situation where one adsorbed molecule can have interaction with two or more Brønsted acid sites, if they are

close enough. However, considering all these possibilities would require significant computational efforts.

Apart from the acid site location, another possible source of error in the present approach is the use of the harmonic oscillator approximation for the calculation of the entropic contributions. In this respect, molecular dynamics can be used for a better description of the potential energy surface. However, since the availability of accurate force fields is rather limited for the investigated reactive systems, ab initio molecular dynamic methods are the natural choice for performing such simulations, which are highly challenging due to the high computational cost of a single trajectory. With increase in computational resources, these methods are expected to gain more importance.

Nevertheless, the present state-of-the-art DFT approach provides an optimum balance between computational cost and accuracy, allowing an unprecedented understanding of several possible reaction mechanisms for 1-butanol dehydration in different zeolites. Such mechanistic insights can also be obtained with this approach for the conversion of other bio-based alcohols and polyols to value added chemicals. Depending on the available experimental and computational resources, it would be interesting to study these reactions in the liquid/aqueous phase, where adsorption isotherms are first used to obtain the loading in the zeolite and molecular dynamics are then used to study the ensemble of possible reactants, transition states and products.

List of Publications

Journal Papers

1. M. John, K. Alexopoulos, M.F. Reyniers, G.B. Marin, Reaction path analysis for 1-butanol dehydration in H-ZSM-5 zeolite: Ab initio and microkinetic modeling, **J Catal**, 330 (2015) 28-45.
2. K. Alexopoulos, M. John, K. Van der Borght, V. Galvita, M.-F. Reyniers, G.B. Marin, DFT-based microkinetic modeling of ethanol dehydration in H-ZSM-5, **J Catal**, 339 (2016) 173-185.
3. M. John, K. Alexopoulos, M.-F. Reyniers, G.B. Marin, First-Principles Kinetic Study on the Effect of the Zeolite Framework on 1-Butanol Dehydration, **ACS Catal**, 6 (2016) 4081-4094.

Oral Presentations

1. M. John, K. Alexopoulos, M.F. Reyniers, G.B. Marin, Bio-butanol dehydration in zeolites: Mechanistic insights from DFT-based microkinetic modeling, **AIChE Annual Meeting**, Salt Lake City, Utah , USA, 2015.

Poster Presentations

1. M. John, K. Alexopoulos, M.F. Reyniers, G.B. Marin, Theoretical study of butanol dehydration on Zeolites, Methusalem International Advisory Board Meeting, Abstracts, 2014.

Glossary

Ab Initio	Latin term for "from first principles"; ab initio methods determine the energy of the electrons and nuclei of a system based on the Schrödinger equation accounting for the interactions between them. In its most strict meaning, no parameters other than the fundamental constants, such as Planck constant, the mass and charge of an electron, etc. are used in ab initio calculations.
Active site	A region on substrate surface where molecules bind and undergo a chemical reaction.
Adsorption	Adhesion of atoms, ions, or molecules from a gas, liquid, or dissolved solid onto a surface.
Activation energy	Minimum energy needed for reactants to result in a chemical reaction.
Anti elimination	An E2-type elimination which requires the atoms or groups involved in the reaction to be in the same plane making a torsional angle $\theta = 180°$, i.e. anti-periplanar orientation of the leaving group and the β-hydrogen (hence called as anti-elimination).
Chemical reaction	A process that leads to the transformation of one set of chemical substances to another.
Density Functional Theory	Computational quantum mechanical modeling method used to investigate the electronic structure of many-body systems, in particular atoms, molecules, the condensed phases and their interactions.

Dispersive interactions Attractive interactions between any pair of molecules, including non-polar atoms, arising from instantaneous induced dipole-induced dipole forces.

Dispersion correction A practical approach in which a damped interatomic potential is included within DFT calculations to account for *dispersive van der Waals interactions.*

E1 reaction In E1 reaction (elimination, monomolecular), the rate determining step involves a heterolytic cleavage of the bond between the leaving group and the carbon atom leading to formation of a carbenium ion. The second step involves deprotonation of an adjacent hydrogen by a base.

E2 reaction E2 (elimination, bimolecular) reaction is a concerted reaction involving a simultaneous deprotonation and departure of the leaving group. E2-type elimination requires the atoms or groups involved in the reaction to be in the same plane.

Electronic energy Energy of a system obtained from the molecular simulation program, not including any temperature correction.

Elementary reaction step A chemical reaction in which one or more species react to products in a single step, without passing through another reaction intermediate.

Enthalpy Thermodynamic quantity that is calculated from the internal energy U as $H = U + pV$, in which p is the pressure and V is the volume.

Entropy Thermodynamic quantity that measures the disorder of a system.

Hydrogen bond Electrostatic attraction between polar molecules that occurs when a hydrogen atom bound to a highly electronegative atom such as nitrogen, oxygen or fluorine

	experiences attraction to some other nearby highly electronegative atom.
Mechanism	Step by step sequence of elementary reactions by which an overall reaction occurs.
Molecular Dynamics	A technique by which one generates the atomic trajectories of a system of N particles by numerical integration of Newton's equation of motion, for a specific interatomic potential, with certain initial and boundary conditions.
Partial Hessian vibrational Analysis	A partial Hessian vibrational analysis (PHVA) is performed if the Hessian is calculated numerically from the positive and negative displacements along the x, y and z coordinate for a *subset of atoms* in the studied system.
Periodic boundary conditions	A set of boundary conditions which are often chosen for approximating a large (infinite) system by using a small part called a unit cell.
Reactant	A substance that is consumed in the course of a chemical reaction.
Reaction barrier	Energy barrier to chemical reaction.
Reaction path analysis	Analysis of the reaction rates that contribute to the rate of production or disappearance of a selected species, which allows to determine actual reaction path to form intermediates and products
SN1 type reaction	In SN1 (substitution, unimolecular) reaction, the rate determining step involves a heterolytic cleavage of the bond between the leaving group and the carbon atom leading to formation of a carbenium ion which undergoes a substitution reaction with the nucleophile.
SN2 type reaction	SN2 (substitution, bimolecular) reaction is a concerted reaction involving simultaneous bond breaking (between the carbon atom and leaving group) and bond formation(between carbon atom and the attacking

	nucleophile). The transition state for a SN2 type substitution involves a penta-coordinated carbon atom with a trigonal bipyramidal geometry with the incoming nucleophile and the leaving group occupying the axial positions (bond angle Nu--C--X ≈ 180°).
Syn elimination	This is a concerted elimination mechanism, where the leaving group and the hydrogen atom are in the same plane and have a syn coplanar orientation (torsional angle θ≈ 0°; eclipsed or near eclipsed conformation)
Steric constraint	steric strain of a molecular entity or transition state structure, i.e. distortions relative to a reference (real or hypothetical) 'strainless' structure with the standard bond lengths, bond angles and dihedral angles.
Transition state	Configuration of highest potential energy along the path of lowest energy between reactants and products. Strictly speaking in the formalism of transition state theory, the transition state of an elementary reaction is that set of states (each characterized by its own geometry and energy) in which an assembly of atoms, when randomly placed there, would have an equal probability of forming the reactants or of forming the products of that elementary reaction.
van der Waals interactions	the attractive or repulsive interactions between molecular entities (or between groups within the same molecular entity) other than those due to bond formation or to the electrostatic interaction of ions or of ionic groups with one another or with neutral molecules. The term includes: dipole–dipole, dipole-induced dipole and dispersive (instantaneous induced dipole-induced dipole) interactions.
Zero-point Energy	Energy of the ground vibrational state. All quantum mechanical systems undergo fluctuations even in their ground state and have an associated zero-point vibrational energy.

Appendices

Appendix A for Chapter 2 is available online:
http://dx.doi.org/10.1016/j.jcat.2015.07.005

Appendix B for Chapter 3 is available online:
http://pubs.acs.org/doi/suppl/10.1021/acscatal.6b00708

Appendix C

Contents. Expression for the TOFs of individual reaction mechanisms

Expression for the TOFs of individual reaction mechanisms

For reaction mechanism involving a unique activated step, the TOF for that mechanism is equal to the TOF of the corresponding unique activated step. For e.g.

$TOF_{m1} = TOF_{R2}$ .....(1)

$TOF_{m2} = TOF_{R4}$ .....(2)

$TOF_{m3} = TOF_{R7}$ .....(3)

$TOF_{m4} = TOF_{R10}$ .....(4)

$TOF_{m5} = TOF_{R13}$ .....(5)

$TOF_{m6} = TOF_{R15}$ .....(6)

$TOF_{m7} = TOF_{R18}$ .....(7)

$TOF_{m8} = TOF_{R19}$ .....(8)

$TOF_{m9} = TOF_{R20}$ ..... (9)

$TOF_{m10} = TOF_{R23}$ .....(10)

$TOF_{m11} = TOF_{R24}$ .....(11)

$TOF_{m12} = TOF_{R25}$.....(12)

$TOF_{m13} = TOF_{R26}$.....(13)

For reaction mechanisms not having a unique activated step, a case specific algorithm is used for calculation of TOF. For e.g.

$TOF_{R29} > 0$, indicates $TOF_{m16} = TOF_{m18} = 0$

$TOF_{R29} < 0$, indicates $TOF_{m14} = 0$

$TOF_{R30} > 0$ indicates $TOF_{m19} = 0$

$TOF_{R30} < 0$ indicates $TOF_{m15} = TOF_{m16} = 0$

Under most of the reaction conditions used in the present study the conversion of 2-butoxide to 2t-butene* (R29) and 2c-butene* (R30) have a net positive value for their TOF.

If ($TOF_{R29} > 0$ and $TOF_{R30} > 0$)

$TOF_{m14} = TOF_{R29}$ ……(14)

$TOF_{m15} = TOF_{R30}$ ……(15)

$TOF_{m16} = 0$ ……(16)

$TOF_{m17} = TOF_{R28} - TOF_{m14} - TOF_{m15}$ ……(17)

$TOF_{m18} = 0$ ……(18)

$TOF_{m19} = 0$ ……(19)

When the gas phase and surface concentration of 2t-butene is very high, 2t-butene* can get converted into 2-butoxide (1.e $TOF_{R29} < 0$)

If ($TOF_{R29} < 0$ and $TOF_{R30} > 0$)

$TOF_{m14} = 0$ ……(20)

$TOF_{m19} = 0$ ……(21)

In order to obtain the TOF for reaction mechanisms m15-18, we have to solve for a linear set of algebraic equations

$TOF_{m14} + TOF_{m15} + TOF_{m17} = TOF_{R28}$ ……(22)

as TOF_{m14} =0 equation 22 becomes

TOF_{m15}+ TOF_{m17} = TOF_{R28}……..(13)

TOF_{m16}+ TOF_{m18} = -TOF_{R29}……..(24)

TOF_{m15}+ TOF_{m16}= TOF_{R30}……..(25)

TOF_{m17}+ TOF_{m18} + TOF_{m19} = TOF_{R32}= TOF_{R33}……..(26)

as TOF_{m19} =0 equation 26 becomes

TOF_{m17}+ TOF_{m18} = TOF_{R32}……..(27)

The above set of equations (eqns. 23-25 and 27) can be directly solved to obtain TOF for mechanisms m15-18.

Alternatively, when TOF for the formation of isobutene is negligible (TOF_{m17} →0 and TOF_{m18} →0), equation reduces to a much simplified form.

TOF_{m15} = TOF_{R28}……..(28)

TOF_{m16} = -TOF_{R29}……..(29)

Lastly, a scenario involving a net positive TOF for conversion of 2c-butene* to 2-butoxy (i.e., TOF_{R30} <0) is not observed under reaction conditions used in the present study.

Appendix D

Contents. Appendix D includes A1 siting in H-FER zeolite (Figure D1) and the Arrhenius activation energies and pre-exponential factors, forward reaction rate coefficients and equilibrium coefficients for elementary steps associated with conversion of 1-butanol to DBE, 1-butene and isobutene in H-FER-T2 as tabulated in Table D1. Also, TS geometry (Figure D2), thermodynamic and kinetic parameters (Table D2) for direct formation of 2c-butene from butanol dimer in H-FER-T1b is presented

Al siting in H-FER zeolite :

There are different distinct tetrahedral sites in the FER framework[1] (see Figure D1) and the Al distribution can vary depending upon the synthesis procedure[2,3]. Amongst them, T1b and T2 site are reported to be the most preferred location of Al in H-FER[3,4]. A detailed study is performed for H-FER with Al at the T1b site (FER-T1b) as Al at this site is most abundant in commercially available H-FER from Zeolyst[3,4]. On the other hand, H-FER with Al at the T2 site (FER-T2) may also be of importance and has been used for several theoretical studies[5-9].

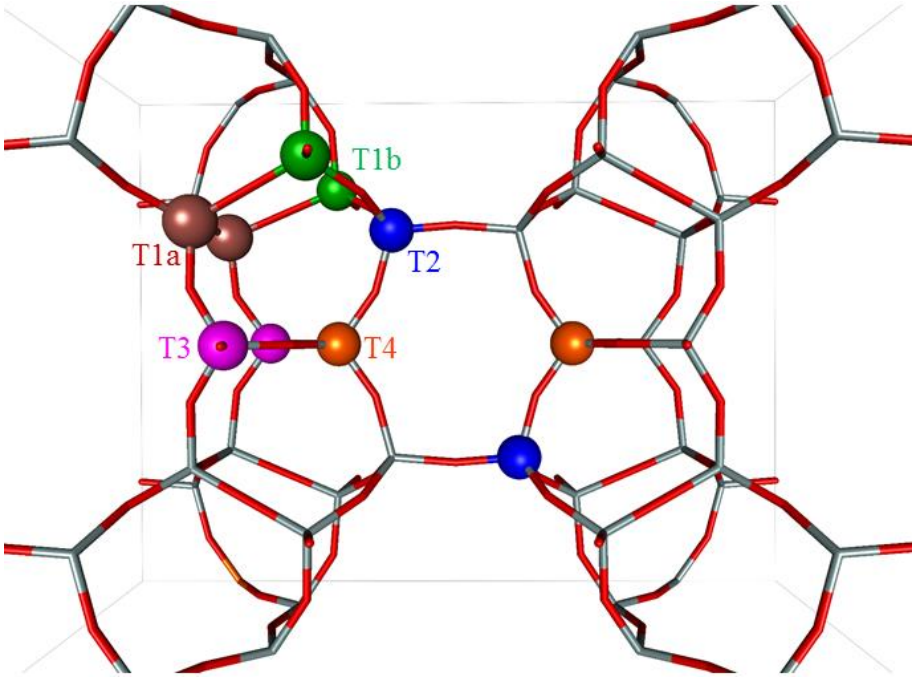

Figure D1. The tetrahedral positions for location of Al atom in FER framework.

Arrhenius activation energies and pre-exponential factors, forward reaction rate coefficients and equilibrium coefficients for elementary steps associated with conversion of 1-butanol to DBE, 1-butene and isobutene in H-FER-T2 are tabulated in Table D1.

Table D1. Standard reaction enthalpy (kJ/mol), reaction entropy (J/mol/K), activation energy (kJ/mol), pre-exponential factor (s^{-1}), forward reaction rate coefficient k_f (s^{-1}) at 500 K and equilibrium coefficient at 500 K (10^{-2} kPa^{-1}, 10^{2} kPa or dimensionless for adsorption, desorption and surface transformation, respectively) for the elementary steps (numbered as indicated in Figure 1) in H –FER –T2.

	Elementary steps	**ΔH_r^o**	**ΔS_r^o**	**$E_{a(f)}$**	**A_f**	**$k_{f\,(500K)}$**	**$K_{eq\,(500K)}$**
1	1-BuOH(g) + * ↔ M1	-148	-199	—	—	—	1.1E+05
6	M1 ↔ M2	43	-14	47	5.0E+12	6.8E+07	6.2E-06
7	M2↔ 1-Butene*+ H2O(g)	52	255	75	2.5E+15	3.7E+07	8.2E+07
8	1-Butene* ↔ 1-Butene(g) + *	96	109	—	—	—	4.7E-05
9	M2↔ Butoxy + H2O(g)	35	167	87	4.0E+14	3.6E+05	1.4E+05
10	Butoxy ↔ 1-Butene*	17	88	123	1.6E+13	2.0E+00	6.0E+02
11	M1 + BuOH(g) ↔ D1	-137	-182	—	—	—	6.7E+04
12	D1 ↔ D2	55	7	—	—	—	3.9E-06
15	D2 ↔ DBE* + H2O(g)	10	151	86	9.4E+12	9.7E+03	8.6E+06
16	DBE* ↔ DBE(g) + *	197	210	—	—	—	3.1E-11
20	DBE* ↔ C4	104	37	158	1.8E+13	5.2E-04	1.2E-09
21	C4 ↔ 1-Butene*+ BuOH(g)	66	235	—	—	—	2.1E+05
28	1-butene* ↔ 2-butoxy	-18	-90	57	3.2E+09	3.5E+03	1.6E-03
32	2-butoxy ↔ iso-butoxy	16	-7	124	3.3E+14	3.7E+01	8.8E-03
33	iso-butoxy ↔ iso-butene*	2	33	106	6.1E+13	5.5E+02	3.3E+01
34	iso-butene*↔ iso-butene(g)+ *	77	172	—	—	—	1.1E+00

elementary steps involving adsorption/ desorption corrected using NIST experimental data

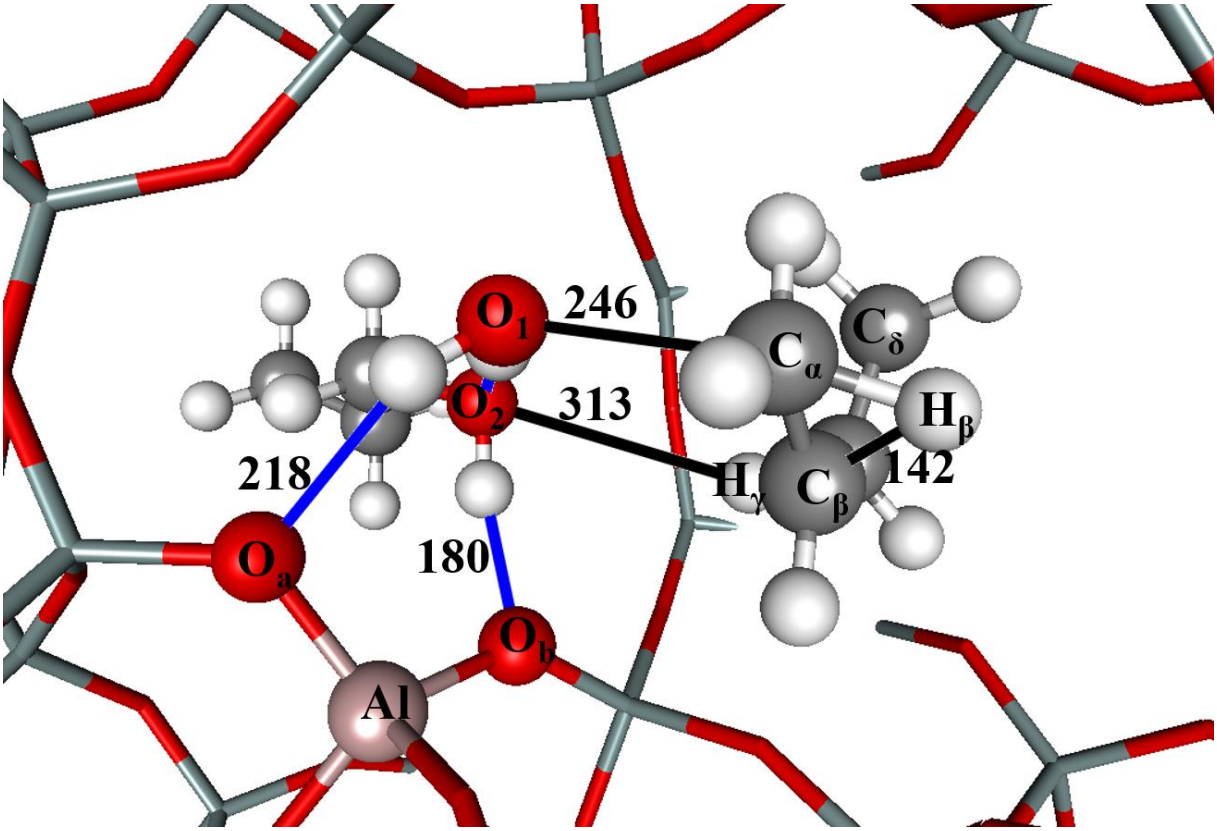

Figure D2. Transition state geometry for formation of 2c-butene from butanol dimer (D1) in H –FER –T1b.

Table D2. Standard reaction enthalpy (kJ/mol), reaction entropy (J/mol/K), activation energy (kJ/mol), pre-exponential factor (s^{-1}), forward reaction rate coefficient k_f (s^{-1}) at 500 K and equilibrium coefficient at 500 K (10^2 kPa) for formation of 2c-butene from butanol dimer (D1) in H –FER –T1b.

	Elementary steps	ΔH_r^o	ΔS_r^o	$E_{a(f)}$	A_f	$k_{f\,(500K)}$	$K_{eq\,(500K)}$
35	D1↔ C2+2-c-butene(g)	74	210	167	$2.4\ 10^{15}$	$8.1\ 10^{-3}$	$9.4\ 10^{1}$

References

(1) Baerlocher, C.; Meier, W. M.; Olson, D.; Meier, W. M. *Atlas of zeolite framework types*; 5th rev. ed.; Elsevier: Amsterdam ; New York, 2001.

(2) Dedecek, J.; Balgova, V.; Pashkova, V.; Klein, P.; Wichterlova, B. *Chem Mater* **2012**, *24*, 3231.

(3) Dedecek, J.; Sobalik, Z.; Wichterlova, B. *Catal Rev* **2012**, *54*, 135.

(4) Dedecek, J.; Lucero, M. J.; Li, C. B.; Gao, F.; Klein, P.; Urbanova, M.; Tvaruzkova, Z.; Sazama, P.; Sklenak, S. *J Phys Chem C* **2011**, *115*, 11056.

(5) Nieminen, V.; Sierka, M.; Murzin, D. Y.; Sauer, J. *J Catal* **2005**, *231*, 393.

(6) Wattanakit, C.; Boekfa, B.; Nokbin, S.; Pantu, P.; Limtrakul, J. *Abstr Pap Am Chem S* **2010**, *239*.

(7) Wattanakit, C.; Nokbin, S.; Boekfa, B.; Pantu, P.; Limtrakul, J. *J Phys Chem C* **2012**, *116*, 5654.

(8) Gleeson, D. *J Mol Catal a-Chem* **2013**, *368*, 107.

(9) Gleeson, D. *J Phys Chem A* **2011**, *115*, 14629.